



Newcastle University Biosciences Institute

**Using Induced Pluripotent Stem Cells to Discover
Advanced Therapies for Pre-mRNA Processing
Factor linked Retinitis Pigmentosa**

Robert Atkinson

A thesis submitted to Newcastle University for the degree of Doctor
of Philosophy (PhD)

December 2022

Abstract

Retinitis pigmentosa (RP) is an inherited retinal disease that affects 1 in 4000 people. Over one-third of cases are caused by autosomal dominant inheritance. Of these, ~20% are caused by mutations in pre-mRNA processing factors (PRPFs). This retinal phenotype is interesting as PRPFs are ubiquitously expressed and are core components of the spliceosome. Studies of mice harbouring RP-causing PRPF mutations identified retinal pigmented epithelial (RPE) cells as the most affected cell type. Each RPE cell possesses a primary cilium which is necessary for RPE function, this includes the diurnal phagocytosis of photoreceptor outer segments and the formation of a tight blood-retina-barrier. Both functions are recapitulated by RPE cells derived from induced pluripotent stem cells (iPSCs). Moreover, previous work from the Lako lab has shown iPSC-RPE cells that harbour *PRPF31* mutations exhibit reduced phagocytosis and barrier function, as well as ciliary abnormalities. This makes iPSC derived RPE cells a useful tool during pre-clinical evaluation of new therapies. There are currently no treatments for *PRPF31* or *PRPF8* linked RP. However, there is evidence to suggest that *PRPF31*-linked RP is caused by a loss of wild type *PRPF31* protein expression. There is no evidence to suggest that *PRPF8* mutations reduce protein expression. This study aims to generate an iPSC-RPE cell model of *PRPF31*- and *PRPF8*-linked RP and evaluate the potential of gene-therapies for the treatment of these diseases.

To achieve this, we generated iPSC-RPE cells from a donor with *PRPF31* mutations and supplemented *PRPF31* transcript using an adeno-associated virus (AAV). In parallel, iPSCs from three donors with *PRPF8*-linked RP underwent CRISPR/Cas9 mediated gene editing to correct the pathogenic mutation before differentiation to iPSC-RPE. Efficacy of these treatments was assessed using a combination of techniques including flow cytometry, transepithelial electrical resistance (TEER), immunofluorescent microscopy and electron microscopy.

This thesis shows that *PRPF31* supplementation can rescue phagocytic function of iPSC-RPE cells that were derived from a patient with *PRPF31*-linked RP. Cilia length was also rescued but the reduced cilia incidence and barrier function persisted following *PRPF31*-AAV transduction. Next, the effect of *PRPF8* gene editing is presented. Phagocytosis and barrier function of iPSC-RPE cells was not affected by *PRPF8* mutation. Quantitative ARL13B immunofluorescent microscopy showed cilia length is increase by *PRPF8* mutation but cilia incidence is unaffected. Quantitative ultrastructural analysis revealed ciliary swelling and fewer mitochondria in iPSC-RPE cells harbouring pathogenic *PRPF8* mutations. Furthermore, immunofluorescent microscopy of markers of both apical and basal epithelial polarity suggests epithelial cell polarity is reduced by RP-causing *PRPF8* mutations.

This thesis identifies several features that are caused by both *PRPF31* and *PRPF8* mutations. These include altered cilia length, cilia swelling, and reduced epithelial polarity. Additional evidence suggests *PRPF31*- and *PRPF8*-linked RP can be treated through gene supplementation and gene editing, respectively. These results highlight the potential of such therapies in the future treatment of RP and more broadly, retinal disease.

Acknowledgements

Thank you to my supervisors Prof. Majlinda Lako, Prof. Colin Johnson, Dr Joseph Collin and Prof. David Elliot for all their guidance, advice and suggestions. This PhD thesis was made possible by them.

Thank you to the university technical staff for their assistance. Special thanks to Lisa Hodgson, Mr Ross Laws, Dr Glyn Nelson, Dr Veronika Boczonadi, and Carly Knill.

Sincere thanks to Dr Maria Georgiou, Dr Chunbo Yang, Dr Katarzyna Szymanska, Dr Sina Mozaffari-Jovin, Dr Sander Smith, Dr Emma West, Prof. Robin Ali, Prof. Sushma Nagaraja Grellscheid, Dr Albert Lahat, Dr Elton Vasconcelos, Prof. David Steel, Dr Helen Phillips, Abhijit Saxena, Chia Beh, and Dr Marzena Kurzawa-Akanbi for their important work and contributions.

Specifically, I would like to thank Dr Georgiou for her assistance with the acquisition of immunofluorescence data. Dr Yang, who reprogrammed the fibroblasts into iPSCs, performed off-target sequencing of the CRISPR clones and performed CRISPR editing of *PRPF8* in $\frac{3}{4}$ of the cell lines used. And Miss Chia Beh and Mr Abhijit Saxena who segmented the transmission electron microscopy images.

Thank you also to Avril Watson, Alice Coomer, Chileleko Siachisumo, Robert Jackson, Rodrigo Cerna-Chavez, Jack Thornton, and Madeline Carter for their support and friendship during the last 4 years.

My deepest gratitude to all my friends and family who always supported me- thank you!

COVID Impact Statement

Long term cell cultures set up in January 2020 had a planned collection date of June 2020. Forced closure of the university meant these differentiations were terminated prematurely. In August 2020 I returned to the lab and began new differentiations which were collected in March 2021. This collection was 9 months after the planned collection date. This has an impact on time available for characterisation of the cells and has eliminated the prospect of testing gene therapy in these cultures.

Contents

Chapter 1. Introduction.....	1
1.1 The Retina	1
1.1.1 Photoreceptors and the Retinal Pigment Epithelium (RPE).....	4
1.1.2 The Retinal Pigment Epithelium	4
1.1.3 Photoreceptors.....	5
1.1.4 Phototransduction and Regeneration of Visual Pigment.....	7
1.2 Blindness	12
1.2.1 Retinal Degenerations	12
1.2.2 Retinitis Pigmentosa	12
1.2.3 Clinical Presentation	13
1.2.4 Inheritance.....	14
1.2.5 Treatments	17
1.3 CRISPR/Cas9 Gene Editing	21
1.4 Stem Cells.....	24
1.4.1 Induced Pluripotent Stem Cells	24
1.4.2 Differentiation to Retinal Cells	25
1.5 Pre-mRNA Splicing	30
1.5.1 The Splicing Cycle	30
1.5.2 Pre-mRNA Processing Factors (PRPFs) and Retinitis Pigmentosa	36
1.6 Cilia.....	42
1.7 Attempts to explore <i>PRPF</i> -linked Retinitis Pigmentosa.....	45
1.8 Project Aims	47
Chapter 2. Materials and Methods	48
2.1 Patient Information and Ethics	48
2.2 iPSC Culture.....	48

Introduction

2.3	Spontaneous Differentiation of iPSCs to RPE.....	48
2.4	Directed Differentiation of iPSC to RPE.....	49
2.5	Measurement of Transepithelial Electrical Resistance (TEER).....	51
2.6	Transduction of iPSC-RPE Cells with Adeno-Associated Virus	51
2.7	Assessment of Transduction Efficiency by Quantitative Polymerase Chain Reaction (qPCR).....	52
2.8	Assessment of Transduction Efficiency by Western Blot.....	55
2.9	Mutation Validation	56
2.10	CRISPR/Cas9 Guide RNA (gRNA) Synthesis and Validation	57
2.11	CRISPR/Cas9 Mediated Homology Directed Repair in RP13-1B iPSCs	58
2.12	Assessment of Pluripotency by PluriTest Assay	60
2.13	Assessment of Chromosomal Stability	60
2.14	Analysis by Immunohistochemistry.....	61
2.14.1	Cilia Length and Frequency measurements in RPE Cells	62
2.15	Phagocytosis Assay by Flow Cytometry.....	62
2.15.1	Fluorescent Labelling of POS.....	62
2.15.2	Phagocytic Challenge and Preparation for Flow Cytometry.....	63
2.16	Transmission Electron Microscopy	63
2.17	Serial Block Face Scanning Electron Microscopy (SBF-SEM)	64
2.18	Data Analysis.....	64
2.19	Summary of Methods	67
Chapter 3.	Evaluating the Potential of <i>PRPF31</i> -AAV Gene Therapy.....	70
3.1	Introduction.....	70
3.2	Aims.....	74
3.3	AAV2-[7m8] (AAV) Transduces iPSC-RPE	75
3.4	<i>PRPF31</i> -AAV Increases <i>PRPF31</i> mRNA Expression.....	76

3.5	<i>PRPF31</i> -AAV Does Not Affect <i>PRPF31</i> Protein Expression	77
3.6	Cilia Length but not Cilia Incidence is Rescued by <i>PRPF31</i> -AAV.....	79
3.7	iPSC-RPE Phagocytic Function is Rescued by <i>PRPF31</i> -AAV.....	80
3.8	<i>PRPF31</i> -AAV Treatment Reduces Protein Aggregation	82
3.9	AAV Treatment Reduces Barrier Function but does not Cause Cell Death	85
3.10	Discussion.....	87
Chapter 4. Generating Isogenic Controls of RP13 Patient-Derived iPSCs Using CRISPR/Cas9 Technology 91		
4.1	Introduction	91
4.2	Aims	94
4.3	RP13 Patient Background	94
4.4	RP13 Patient-Derived iPSCs do not acquire genomic abnormalities during the reprogramming and expansion process.....	96
4.5	RP13 Patient-Derived iPSCs and RP13-Cas9 iPSCs Differentiate into RPE.....	98
4.6	Lack of Off-Targeting Effects in the Gene Edited Isogenic Controls.....	107
4.7	Gene Edited Cells are Pluripotent and Have Not Acquired Genomic Instabilities During Gene Editing and Culture.....	110
4.8	Discussion	113
Chapter 5. Characterisation of RP13 and RP13-Cas9 iPSC-RPE Cells		
5.1	Introduction	117
5.2	Aims	120
5.3	RP13 and RP13-Cas9 iPSC-RPE cells have characteristics of human RPE	121
5.4	<i>PRPF8</i> Mutation Does not Impact Photoreceptor Outer Segment Phagocytosis <i>in vitro</i> 122	
5.5	Ultrastructural Analysis of RP13 and RP13-Cas9 iPSC-RPE cells.....	124
5.5.1	Cell Area.....	125
5.5.2	Melanosomes and Melanosome Complexes	126

Introduction

5.5.3	Stress Vacuoles	128
5.5.4	Basal Deposits	129
5.5.5	Basal Membrane Linearity	132
5.5.6	Mitochondrial Shape and Number	133
5.6	RP13 iPSC-RPE cells have Altered Ciliary Structure.....	135
5.7	Epithelial Polarisation is reduced in RP13 RPE.....	140
5.8	Discussion.....	142
Chapter 6.	Conclusions and Future Directions	149
References.....		156

List of Figures

Figure 1.1: Laminated organisation of the retina..	3
Figure 1.2: Retinal image obtained using optical coherence tomography and depicts the foveal pit (white arrow), the foveal slope and the parafovea..	4
Figure 1.3: Illustration of rod (blue) and cone (red) photoreceptors.	6
Figure 1.4: Illustration of the photo transduction cascade.....	9
Figure 1.5: Transmission electron microscopy (TEM) image showing the intimate association of RPE with photoreceptor outer segments (OS).....	11
Figure 1.6: Fundus of healthy retina and of retina from patient with retinitis pigmentosa (RP).	13
Figure 1.7: As RP progresses the field of vision decreases.	14
Figure 1.8: Schematic of the domain organisation of human PRPF31 and PRPF8.....	17
Figure 1.9: Illustration showing regulation of <i>PRPF31</i> expression by MSR1 repeats and CNOT3.	19
Figure 1.10: Illustration of the mechanisms by which Cas9, base editors, and prime editors install DNA edits.....	21
Figure 1.11: Cartoon of Cas9 mediated genomic cleavage.....	23
Figure 1.12: Timeline showing the emergence of different cell types during retinal development	26
Figure 1.13: Cartoon of the splicing cycle illustrating the role of five uridine rich snRNPs as well as pre-mRNA processing factor 31 (PRPF31) and PRPF8.	35
Figure 1.14: Ribbon diagram showing the interaction between the C-terminal domain of yeast Prp8 and N-terminal domain of Brr2.....	40
Figure 1.15: Structure of an RPE primary cilium	42
Figure 1.16: Ciliary disorganisation of patients with PRPF-linked retinitis pigmentosa	44
Figure 2.1: Schematic illustrating iPSC differentiation to RPE, purification and maturation on transwell inserts.....	50
Figure 2.2: Cartoon illustrating functional regions of the <i>PRPF31</i> -AAV.....	52
Figure 2.3: Guide RNA (gRNA) sequences that were tested using genomic cleavage detection.....	58
Figure 2.4: Schematic showing how the gRNA DNA template is assembled during the PCR reaction.	57
Figure 2.5: Schematic showing how one corrected iPSC clone was isolated following nucleofection with Cas9/gRNA ribonucleoprotein..	59
Figure 3.1: Efficiency of <i>GFP</i> -AAV2-[7m8] transduction in F018 (WT) iPSC-RPE cells.....	75
Figure 3.2: Expression level of <i>PRPF31</i> in RP11S1 iPSC-RPE measured using qPCR following treatment with <i>GFP</i> -AAV and <i>PRPF31</i> -AAV. Treatment with 5×10^4 MOI <i>PRPF31</i> -AAV did not affect <i>PRPF31</i> expression	76

Introduction

Figure 3.3: PRPF31 western blot following AAV transduction in RP11S1 iPSC-RPE cells and quantification	77
Figure 3.4: Quantification of cilia length and incidence using ARL13B immunofluorescent images....	79
Figure 3.5: Effect of <i>PRPF31</i> -AAV treatment on iPSC-RPE phagocytosis of FITC-labelled photoreceptor outer segments (POS).....	81
Figure 3.6: Representative images showing cytoplasmic aggregates present within the cytoplasm of RP13 and RP13-Cas9 iPSC-RPE cells.....	84
Figure 3.7: AAV treatment negatively affects barrier function but does not induce apoptosis	85
Figure 4.1: Cartoon to illustrate heterogeneity amongst iPSCs	91
Figure 4.2: Cartoon illustrating how heterogeneity is acquired by iPSC-derived samples	93
Figure 4.3: Chromosomal copy numbers of different cell lines are plotted	97
Figure 4.4: Photographs to illustrate progression of RPE differentiation over 12 weeks.....	99
Figure 4.5: Photographs to show RPE differentiation efficiency using a guided differentiation protocol	100
Figure 4.6: Photographs showing iPSC-RPE differentiation and purified iPSC-RPE cells.....	101
Figure 4.7: Schematic of gRNA and single stranded donor oligonucleotide (ssODN) design and in vitro cleavage detection of PRPF8 amplicon	104
Figure 4.8: Restriction digest of <i>PRPF8</i> following nucleofection with Cas9/gRNA.....	106
Figure 4.9: The heterozygous H2309P PRPF8 mutation is present in all four patient lines.....	108
Figure 4.10: The pathogenic PRPF8 mutation present in all patient lines was edited to the wildtype sequence.....	109
Figure 4.11: Sequences of possible off-target gRNA/cas9 cleavage sites	110
Figure 4.12: The right y-axis corresponds to the copy number (n = 3) produced by each probe on the microarray	111
Figure 4.13: Pluripotency plot that provides a visual representation of the results in table below...	112
Figure 5.1: RP13 and RP13-Cas9 iPSC-RPE cell cultures form monolayers of pigmented epithelial cells	121
Figure 5.2: Quantified phagocytosis of FITC-labelled photoreceptor outer segments (POS) by iPSC-RPE cells.....	123
Figure 5.3: Quantification of cross-sectional cell surface area and example TEM images	125
Figure 5.4: Quantification of melanosomes, melanosome-complexes, and example TEM images....	127
Figure 5.5: TEM image quantification of stress vacuoles and example TEM images.....	128
Figure 5.6: TEM image quantification of number and area of basal deposits, and example images .	130

Figure 5.7: TEM image quantification of basal membrane linearity, example TEM image and diagrammatic explanation of measurement.....	132
Figure 5.8: Quantification of mitochondrial number per cell and representative TEM images.....	133
Figure 5.9: Quantification of mitochondrial aspect ratio, example TEM image and explanation of measurement.....	134
Figure 5.10: Quantification of cilia length and incidence using ARL13B immunofluorescent images	136
Figure 5.11: Comparison of iPSC-RPE ciliary ultrastructure visible using TEM and SBF-SEM	138
Figure 5.12: Analysis of ciliary volume and length and three-dimensional reconstruction of selected cilia using SBF-SEM data.....	139
Figure 5.13: Detection of apical and basal polarity in iPSC-RPE cells by immunocytochemistry	141
Figure 5.14: The rhythmicity of phagocytosis is affected in RP13 mice.....	146

List of Tables

Table 1: Table summarising the main causative genes of autosomal recessive, autosomal dominant, and X-linked retinitis pigmentosa.....	16
Table 2: Brief history of research that successfully differentiated RPE from stem cells.....	28
Table 3: Brief history of research that successfully generated neural retina from stem cells.....	29
Table 4: Eight splicing factors were linked to retinitis pigmentosa.....	31
Table 5: Key Resources used in this study.....	66
Table 6: Oligonucleotide sequences of the PCR primers, guide RNAs (gRNA), and single stranded oligodeoxynucleotide (ssODN) used in this study.....	53
Table 8: The cell lines used throughout this study were derived from four patients and one unaffected patient	95

Table of Abbreviations

5'SS	5' splice site
3'SS	3' splice site
AMD	Age-related macular degeneration
ANOVA	Analysis of variance
BBS	Bardet-Biedl syndrome
BCA	Bicinchoninic acid
BMP	Bone morphogenetic protein
BPS	Branch point sequence
cGMP	Cyclic guanosine monophosphate
CLIP	cross-linking and immunoprecipitation
CMV	Cytomegalovirus
CNV	Copy number variant
CRISPR	Clustered regularly interspaced short palindromic repeats
DMEM	Dulbecco's Modified Eagle Medium
DNA	Deoxyribonucleic acid
DSB	Double-stranded DNA break
EDTA	Ethylenediaminetetraacetic acid
EM	Electron Microscopy
FACS	Flow assisted cell sorting
FBS	Foetal bovine serum
FDA	U.S. Food and drug administration
FGF	Fibroblast growth factor
FITC	Fluorescein isothiocyanate
GC	Guanylyl cyclase
GCAP	Guanylyl cyclase activating proteins
GCD	Genome cleavage detection
GDP	Guanosine diphosphate
GFP	Green fluorescent protein
GTP	Guanosine triphosphate
HDR	Homology directed repair
HRP	Horseradish peroxidase
IF	Immunofluorescence
IFT	Intraflagellar transport
IGF	Insulin growth factor
INL	Inner nuclear layer
IPL	Inner plexiform layer
IPSC	Induced pluripotent stem cell
LCA2	Leber congenital amaurosis 2
LDS	Lithium dodecyl sulphate
MEM	Modified Eagle Medium
MFI	Median Fluorescence intensity
MIB	Microscopy image browser

MOI	Multiplicity of infection
MSR1	Minisatellite repeat element
NCKX	Sodium/calcium potassium exchanger
NEAA	Non-essential amino acids
NHEJ	Non-homologous end joining
NTC	Non-treated control
NTP	Nucleoside triphosphate
ONL	Outer nuclear layer
OPL	Outer plexiform layer
OS	Outer segment
PAGE	Polyacrylamide Gel Electrophoresis
PAM	Protospacer adjacent motif
PBS	Phosphate buffered saline
PCR	Polymerase chain reaction
PDE	Phosphodiesterase
PET	Polyethylene terephthalate
PFA	Paraformaldehyde
PIS	Photoreceptor inner segment
POS	Photoreceptor outer segment
PRPF	Pre-mRNA processing factor
PSC	Pluripotent stem cell
PVDF	Polyvinylidene difluoride
RCF	Relative centrifugal force
RCS	Royal college of surgeons
RDH	Retinal dehydrogenase
RNA	Ribonucleic acid
RNP	Ribonucleoprotein
ROCK	Rho-kinase
RP	Retinitis Pigmentosa
RP11	Retinitis pigmentosa type 11
RP13	Retinitis pigmentosa type 13
RPC	Retinal progenitor cell
RPE	Retinal pigment epithelium
RPMI	Roswell Park Memorial Institute Medium
SBF	Serial block face scanning electron microscopy
SD	Standard deviation
SEM	Standard error of the mean
SNP	Single nucleotide polymorphism
snRNP	small nuclear ribonucleoprotein
ssODN	single stranded oligodeoxynucleotide
SV40	Simian virus 40
TBS	Tris-buffered saline
TBST	Tris-buffered saline with TWEEN-20
TEER	Transepithelial electrical resistance

TEM	Transmission electron microscopy
TESR	a defined medium for human ES cell culture
TGF	Transforming growth factor
WHO	World health organisation
WT	Wild-type

Chapter 1. Introduction

1.1 The Retina

The retina is a multi-layered organ that contains layers of neurons and glial cells necessary for function. In brief, the retinal pigment epithelium (RPE) sits at the back of the eye and makes extensive contacts with photoreceptor outer segments via its apical surface. Upon sufficient light-induced depolarisation of photoreceptors, action potentials are elicited and then propagated across the retina via 2nd order neurons and then to ganglion cells that innervate the brain. There are various cells that support this tissue and function to increase visual acuity such as horizontal, amacrine, and Müller cells (**Figure 1.1**). This review will give a brief account of retinal structure and topology before focusing on two cell types: RPE and rod photoreceptors. This section is a review of retinal biology for more detail please refer to (Lee Ann, 2012; Kolb, Fernandez and Nelson, 2016).

During fundoscopic inspection of the retina a blood vessel-free reddish spot called the fovea can be identified. This structure defines the centre of the retina. Beyond 6 mm from this area is the peripheral retina, which extends to the *ora serrata* 21 mm from the centre of the retina. The retina is ~0.5 mm thick overall with the thickness varying radially. A radial cross-section reveals ganglion cells that transmit visual information to the brain lie closest to the vitreous whilst photoreceptors lie at the back of the eye against the RPE. Vertebrate retinas are composed of five layers, three nuclear layers of nerve cell bodies and two plexiform layers of synapses (**Figure 1.1**). The outer nuclear layer (ONL) contains cell bodies of the photoreceptors (rods and cones); the inner nuclear layer (INL) contains cell bodies of the retinal interneurons (bipolar, amacrine, Müller and horizontal cell types). The outer plexiform layer (OPL) separates the ONL and INL where photoreceptors, bipolar cells, and horizontal cells connect. Glutamatergic synapses between photoreceptors and bipolar cells transmit visual towards the inner surface of the retina. The inner plexiform layer is where bipolar cells synapse with ganglion cells. The ganglion cell layer is the third and innermost nuclear layer of the retina. A variety of amacrine cells form networks that integrate ganglion cell signals. These signals travel to the brain along the optic nerve.

Introduction

The central retina contains a significantly higher proportion of cones than rods. The converse is true in the peripheral retina. The central retina close to the fovea is thicker than the peripheral retina due to an increased density of photoreceptors (ONL) and a thickened INL that contains the associated interneurons.

The centre of the fovea is called the foveal pit and contains the maximum density of cones found within the retina. The other layers of retina are displaced, making the foveal pit the thinnest part of the retina. The associated neurons are radially distorted and appear gradually along the edge of the foveal pit, making this region, the parafovea, the thickest portion of the retina. The fovea and parafovea make up the macula of the human eye. The relative thickness of the IPL and ganglion cell layer is also increased in the parafovea (**Figure 1.2**), due to an increased density of ganglion cells in cone pathways and displacement from the foveal pit.

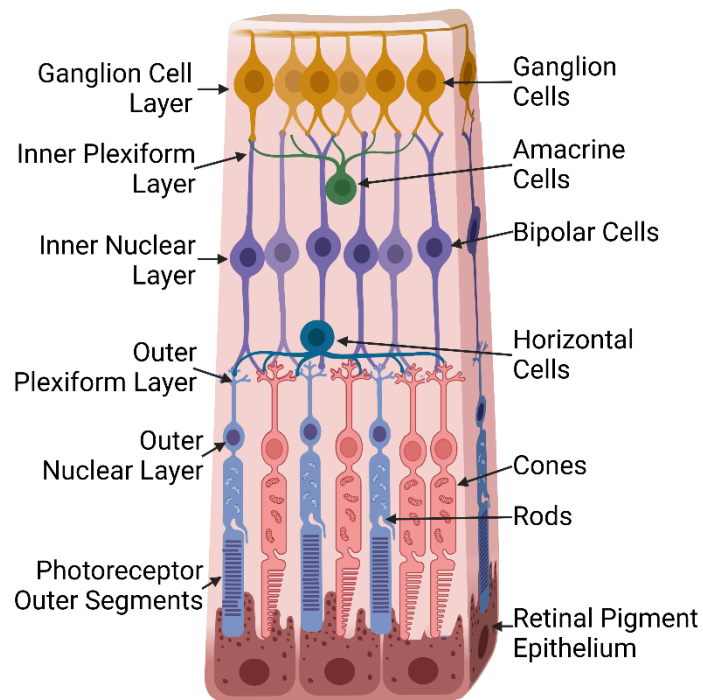


Figure 1.1: Laminated organisation of the retina. This figure illustrates all the cell types in the neural retina and the retinal pigment epithelium. Ganglion cells form the ganglion cell layer on the inner surface of the retina. Synaptic connections in the inner plexiform layer connect ganglion cells with amacrine and bipolar cells. Bipolar cell bodies make up the inner nuclear layer. Bipolar cells, horizontal cells, and photoreceptor cells form synapses in the outer plexiform layer. There are two types of photoreceptor cells: rods and cones. Photoreceptor cell bodies are present in the outer nuclear layer. Adjacent to the outer nuclear layer are the photoreceptor outer segments, which interdigitate with the retinal pigment epithelium. Image created using Biorender.com.

1.1.1 Photoreceptors and the Retinal Pigment Epithelium (RPE)

Light is focused onto the retina by the cornea and the lens (Nickells, 1999). Light is important for the function of several cell types within the eye (Buhr *et al.*, 2015) including photoreceptors and photosensitive ganglion cells. The RPE absorbs excess light, recycles 11-*cis* retinal (the photosensitive pigment in photoreceptors), and phagocytoses photoreceptor outer segments (POS) (Strauss, 2005).

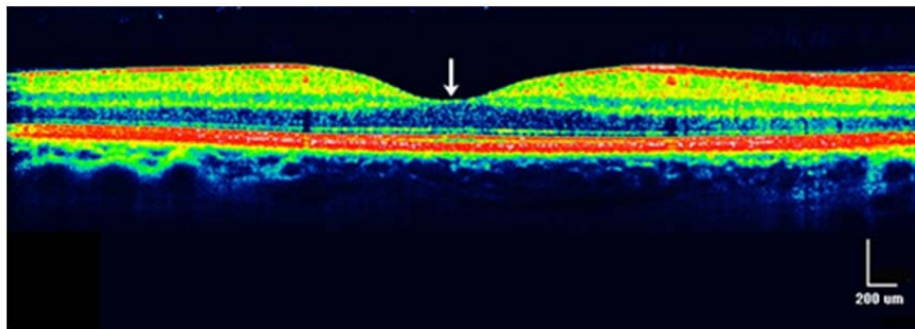


Figure 1.2: Retinal image obtained using optical coherence tomography and depicts the foveal pit (white arrow), the foveal slope and the parafovea. Taken from (Kolb, 2019). The image shows how the thickness of the retina is lowest in the fovea and highest in the parafovea. The intensity of reflected light is shown using colour, with warm colours (red) indicating more reflection than cold colours (blue).

1.1.2 The Retinal Pigment Epithelium

The RPE apical membrane is adjacent to POS and the basal membrane is next to the Bruch's membrane and blood vessels (Bok, 1993; Nag and Wadhwa, 2012). Surface contact between the RPE and POS is maintained by an elaborate network of microvilli. Depending on the location within the retina, 20-40 POS project towards a single RPE cell (Gao and Hollyfield, 1992).

Two RPE functions are the most significant in the context of photoreceptor support. First, the RPE is required for constant renewal of POS. POS membranes contain unsaturated lipids (Bazan, 2006) that are prone to oxidation in the physiological conditions of the retina (Caprara and Grimm, 2012; Lange and Bainbridge, 2012). To prevent accumulation of oxidised lipids, photoreceptors shed their outer segments and regenerate 10% of outer segment (OS) volume shed daily. The POS are phagocytosed by adjacent RPE cells (Kevany and Palczewski, 2010). Thus, each RPE cell phagocytoses hundreds of thousands of OS disks over a lifetime

(Anderson, Fisher and Steinberg, 1978). Dysfunction of processes associated with phagocytosis, such as mutations in Mer tyrosine kinase (*MERTK*) which prevent binding of POS to RPE lead to retinal degeneration (D’Cruz *et al.*, 2000). Over time, chronic exposure to POS makes the RPE susceptible to damage due to oxidative stress (Brown *et al.*, 2019). As a result, loss of protection against this stress leads to a loss of RPE function and subsequent photoreceptor death (Brown *et al.*, 2019). The second function is to supply photoreceptors with visual pigment. The outer segments also act as a source of visual pigment that is recycled and delivered back to photoreceptors by the RPE. Mutations that affect this recycling of visual pigment, such as mutations in retinal pigment epithelium-specific 65 kDa (*RPE65*), also cause retinal degeneration (Veske *et al.*, 1999) (**Section 1.1.4.2**).

1.1.3 Photoreceptors

The following section covers the foundational knowledge of photoreceptor structure and function, adapted from (Kolb, Fernandez and Nelson, 2016).

Photoreceptors consist of four sections (**Figure 1.3**): an outer segment that is filled with stacks of membrane discs containing the components required for phototransduction, an inner segment (PIS) that contains cellular organelles required for basic cellular function such as ribosomes and mitochondria, a nucleus, and a short axon that synapses with second order neurons (bipolar and horizontal cells). There are four broad classes of photoreceptor in the human eye: rods that express the opsin rhodopsin (most sensitive to 500 nm light) and three types of cones: blue/short (most sensitive to 437 nm), medium/green (533 nm) and long/red (564 nm). The POS and PIS of cones are generally thicker than those of rods in human retina.

Photoreceptors are packed in a mosaic pattern; different types of photoreceptors are packed at different densities around the retina. In the fovea, cones are very tightly packed in a hexagonal pattern to maximise cell density. Outside of this area, cones are more diffuse and are surrounded by rings of rod photoreceptors. There is a ring around the fovea where rod photoreceptors reach their greatest density.

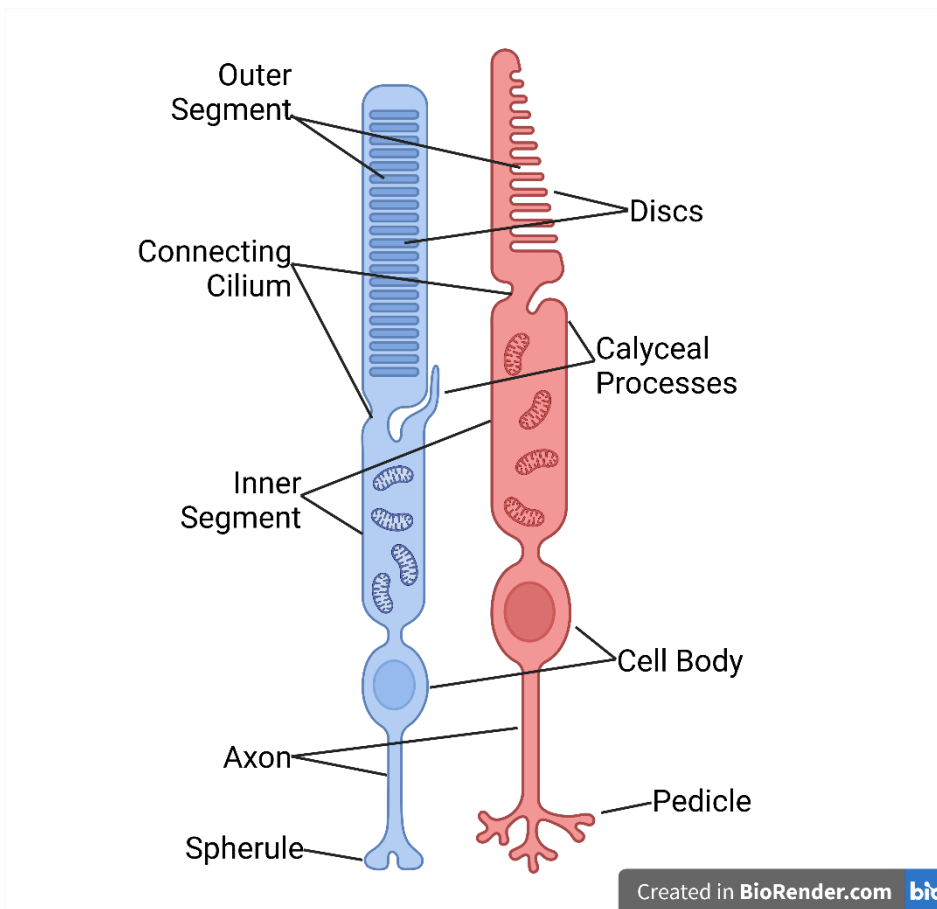


Figure 1.3: Illustration of rod (blue) and cone (red) photoreceptors. Key differences structural between rods and cones indicated include morphology of the photoreceptor outer segment and axon terminals. Image created in Biorender.com.

The POS connects to the PIS by a thin connecting cilium through which proteins required for phototransduction are trafficked. Outer segments are generated from the base of the cilium, where membrane invaginations and evaginations give rise to the outer segment (Steinberg, Fisher and Anderson, 1980).

The presynaptic region of rod photoreceptors is called the spherule; the cone equivalent is the pedicle. Cone pedicles form connections on the outer edge of the outer plexiform layer (OPL), the spherules are located above and below the pedicles. Both these structures form specialised synapses called synaptic ribbons that release glutamate onto the invaginated postsynaptic surfaces of second order neurons. Cones synapse with almost 10-fold more secondary neurons than rods. Each cone pedicle forms triad connections with second order neurons a vertical bipolar cell element and two lateral horizontal cell elements.

1.1.4 Phototransduction and Regeneration of Visual Pigment

Photoreceptors depend on the RPE for removal of toxic products produced by phototransduction and for supply of the visual pigment, 11-*cis* retinal, which is required for phototransduction (reviewed in (Baylor, 1996; Baylor and Burns, 1998; Pugh and Lamb, 2000; Parker and Crouch, 2010; Kiser, Golczak and Palczewski, 2014)). This section will focus on RPE and rod photoreceptors as these are the primary cell types affected in RP. In addition, Muller glia cells are required for efficient visual pigment recycling.

1.1.4.1 The Phototransduction Cascade

The phototransduction cascade is the molecular process by which light is converted to an electrochemical signal (synaptic transmission). It is best considered as two stages: activation and termination/regulation of the membrane current.

1.1.4.1.1 Activation

The opsins (R) are a group of 7-transmembrane domain containing G-protein coupled receptors capable of binding retinal, a light-sensitive visual pigment (Hargrave, 2001). 11-*cis*-retinal is covalently bound to a Lys residue in the seventh transmembrane helix of R via a Schiff-base linkage. 11-*cis*-retinal is isomerised to all-*trans*-retinal upon exposure to visible light. The change in conformation from *cis* to *trans* causes opsin activation (R*). This facilitates binding of R* with transducin-GDP (G), a membrane-bound inactive heterotrimeric G-protein. Binding facilitates the release of GDP (Sprang, 1997; Hamm, 1998; Iiri, Farfel and Bourne, 1998) and leaves the complex available to bind cytoplasmic GTP (Bornancin, Pfister and Chabre, 1989). Binding of GTP causes transducin dissociation into α and $\beta\gamma$ subunits, and the GTP-bound α (G*) subunit acts as an effector. This step amplifies the signal because one activated opsin receptor can form thousands of GTP- α complexes (Kahlert and Hofmann, 1991; Pugh and Lamb, 1993). GTP- α increases cyclic GMP (cGMP) phosphodiesterase (PDE, E*) activity by interacting with the γ subunit of this enzyme. Activated PDE converts cGMP in the cytoplasm to GMP, reducing the cytoplasmic concentration of cGMP in the outer segment (Beavo, 1995).

1.1.4.1.2 Photoreceptor Membrane Current

The photoreceptor outer segment contains two classes of ion channel: cyclic nucleotide gated channels (CNGCs) and $\text{Na}^+/\text{Ca}^{2+}$, K^+ exchangers (NCKX) (Schnetkamp, 1989, 1995; Finn, Grunwald and Yau, 1996). CNGCs transduce the cytoplasmic concentration of cGMP into an electrical current (Fesenko, Kolesnikov and Lyubarsky, 1985). Incredibly, ~4% of the open CNGCs are closed upon isomerisation of a single 11-*cis*-retinal molecule thus allowing rod photoreceptors to respond to single photons (Baylor, Lamb and Yau, 1979; Baylor, Nunn and Schnapf, 1984). Under dark conditions, cGMP concentration is relatively high and a small number of CNGCs are held open (**Figure 1.4**). This results in a CNGC mediated current in the POS, which is balanced by an outwards current in the inner segment of photoreceptors. This results in the formation of a continuous looping current between the outer and inner segment, known as the dark current. When cGMP concentration drops, CNGCs close. This stimulates an inward current mediated by NCKX, caused by influx of Na^+ and efflux of Ca^{2+} and K^+ (**Figure 1.4**). This reduces the outwards current of the inner segment. The inner segment then hyperpolarises and decreases synaptic release of glutamate.

The subsequent effect on bipolar cell firing can be broadly categorised in two ways: on centre, off surround or off centre, on surround. Central bipolar cells synapse directly with the ganglion cell whereas surrounding bipolar cells synapse with horizontal cells. Horizontal cell excitation inhibits ganglion cell firing. On centre off surround bipolar cells express inhibitory postsynaptic glutamate receptors and so firing rate is increased when glutamate release from photoreceptors is decreased. This inhibition is followed by a burst of post-inhibitory rebound firing when the membrane potential rises following hyperpolarisation. Off centre on surround bipolar cells express excitatory postsynaptic glutamate receptors and so the firing rate is decreased if presynaptic glutamate release is decreased. Therefore, off centre bipolar cells reduce ganglion cell firing immediately after photoreceptor glutamate release whereas their surround counterparts increase ganglion cell firing. The converse effect on ganglion cell firing is true for on bipolar cell pathways.

1.1.4.1.3 Termination and Modulation

Termination and modulation of the photo transduction cascade is regulated by intracellular Ca^{2+} concentration ($[\text{Ca}^{2+}]_i$) and is therefore indirectly regulated by the NCKX current. Two key mechanisms of signal inactivation target the receptor (R^*) and effector (E). Rhodopsin kinase (RK) is a serine/threonine kinase that phosphorylates R^* (Zhao, Palczewski and Ohguro, 1995; Palczewski, 1997; Hurley, Spencer and Niemi, 1998). The calcium-bound conformation of recoverin inhibits RK in a calcium-dependent manner (Kawamura, 1993). Upon efflux of Ca^{2+} , inhibition of recoverin is relieved and RK activity increases. RK phosphorylates R^* and promotes the association of arrestin with R^* , this inhibits the catalytic activity of R^* (Wilden, Hall and Kuhn, 1986). The association of R^* with arrestin prevents the formation of G^* . As well as R^* , E^* is regulated. E^* activity is regulated by Regulator of G-protein Signalling 9 (RGS9) and its cofactor type 5 G-protein β subunit ($\text{G}\beta 5$), which promote hydrolysis of bound GTP to GDP (He, Cowan and Wensel, 1998; Makino *et al.*, 1999). Hydrolysis of GTP terminates E^* catalytic activity.

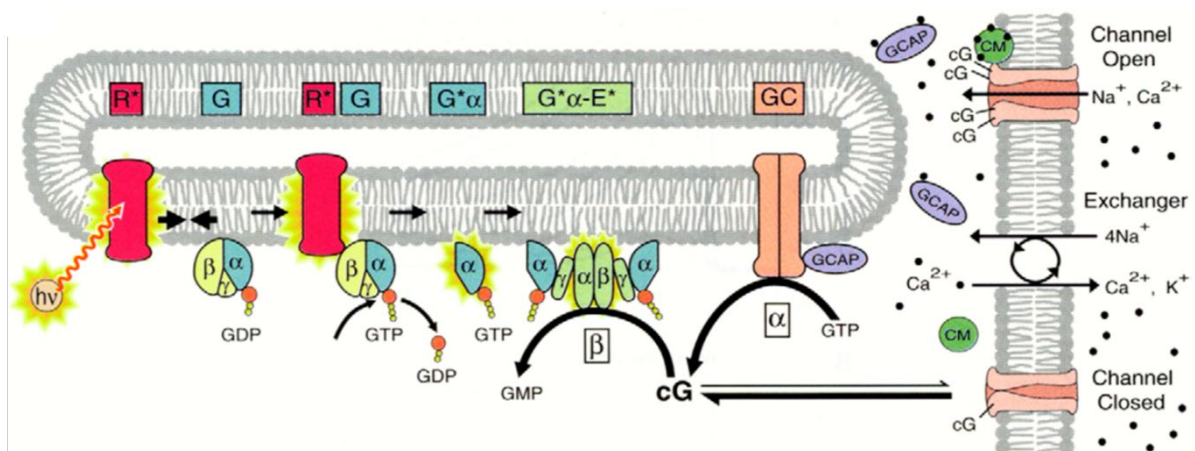


Figure 1.4: Illustration of the photo transduction cascade. Opsin (R) is activated (R^*) by light which allows it to bind transducin (G) and produce $\text{G}^*\alpha$ which acts as an effector. Transducin dissociates and the $\text{G}^*\alpha$ subunit interacts with phosphodiesterase (E) to activate the enzyme (E^*) and promote hydrolysis of cGMP to GMP. This decreases cGMP concentration and causes cGMP gated channels to close, leading to an inward current mediated by the $\text{Na}^+/\text{Ca}^{2+}$, K^+ exchanger (NCKX) and photoreceptor hyperpolarisation. The concurrent decrease in intracellular Ca^{2+} promotes association of GCAP with guanylyl cyclase (GC) to promote formation of cGMP. Figure taken from Pugh and Lamb (2000).

Introduction

During photo-transduction cytoplasmic cGMP are depleted by E*. The enzyme guanylyl cyclase (GC) restores the cGMP concentration. This restores cGMP depleted during phototransduction, using energy from hydrolysis of GTP. GC is activated by GC activating proteins (GCAPs) (Palczewski *et al.*, 1994; Gorczyca *et al.*, 1995), which are Ca²⁺ binding proteins. During photoreceptor depolarisation, [Ca²⁺]_i and GC adopts an active conformation that stimulates GC activity. Subsequently, cGMP production restores cytoplasmic cGMP levels.

1.1.4.2 Pigment Regeneration

George Wald was the first to characterise the recycling of visual pigment in the retina, and this work earned him a Nobel Prize (Wald, 1968). His work built on observations by Böll and Kühne, who discovered that visual pigment is regenerated in the dark and requires multiple cell types (Ripps, 2008). More recently, interest in this cycle has intensified (reviewed in (Parker and Crouch, 2010; Kiser, Golczak and Palczewski, 2014)).

All-*trans* retinal is reduced to all-*trans*-retinol by the retinol dehydrogenases (RDH) *RDH8* and *RDH12* (Haeseleer *et al.*, 1998; Rattner, Smallwood and Nathans, 2000; Maeda *et al.*, 2005, 2006). All-*trans*-retinol moves out of photoreceptors into the interphotoreceptor space, which is packed with interphotoreceptor retinoid binding protein (IRBP). IRBP is a large glycoprotein capable of binding multiple retinoid molecules. All-*trans*-retinol entry to the RPE is dependent on CRBP1/RBP1 (Saari *et al.*, 2002) and once inside the RPE all-*trans*-retinol is esterified by Lecithin Retinol Acyl Transferase (LRAT). This non-polar retinoid is a major storage form and the first retinoid metabolite produced by the RPE. It readily associates with lipid droplets called retinosomes that can be imaged using 2-photon microscopy (Imanishi *et al.*, 2004) and locate close to the plasma membrane (Wu, Chen and Koutalos, 2006; Palczewska *et al.*, 2010; Orban, Palczewska and Palczewski, 2011). These retinyl-esters are also the substrate of RPE65 (MacDonald and Ong, 1988; Moiseyev *et al.*, 2003; Batten *et al.*, 2004), a retinol isomerase localised to the endoplasmic reticulum that catalyses the formation of 11-*cis*-retinol. Before moving into photoreceptors 11-*cis*-retinol is oxidised to 11-*cis* retinal by RDH5 (Simon *et al.*, 1995; Cideciyan *et al.*, 2000; Kim *et al.*, 2005), RDH11 (Haeseleer *et al.*, 2002; Kasus-Jacobi *et al.*, 2005; Kim *et al.*, 2005) and potentially RDH10 (Farjo *et al.*, 2009).

11-cis-retinal transport is dependent on CRALBP/RLBP1 binding (Futterman and Saari, 1977; Futterman, Saari and Blair, 1977; Bunt Milam and Saari, 1983; Stecher *et al.*, 1999).

There is evidence that the isomerisation of retinal can be facilitated by light. Despite relatively early observations that this process is mediated by retinal G protein coupled receptor (RGR), the mechanism of this process is unclear (Radu *et al.*, 2008). Another gap in the understanding of visual pigment regeneration is how retinoids are trafficked within RPE and photoreceptors.

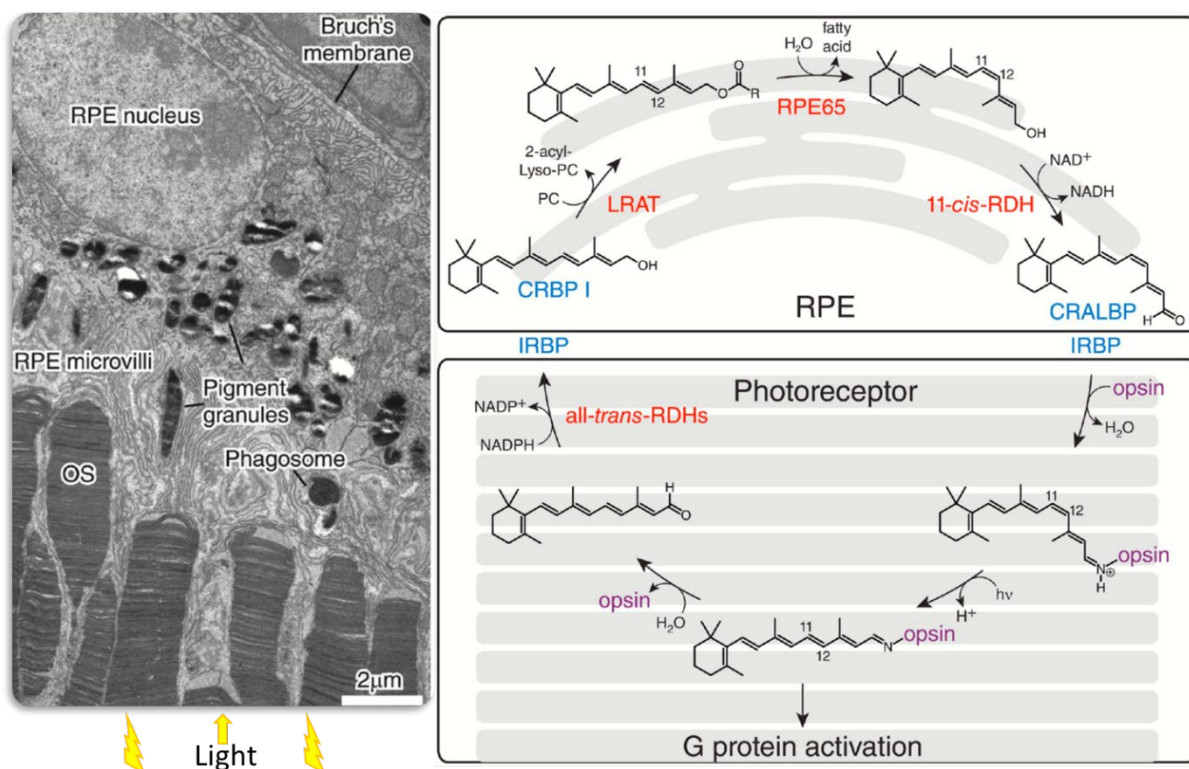


Figure 1.5: Left- Transmission electron microscopy (TEM) image showing the intimate association of RPE with photoreceptor outer segments (OS). Right- schematic of the visual cycle showing how retinoids are processed within the RPE and photoreceptors. Figure taken from (Kiser, Golczak and Palczewski, 2014).

1.2 Blindness

Globally, 36 million people were estimated to be blind in 2015 and 216.6 million people visually impaired (Flaxman *et al.*, 2017). Preventable causes in adults aged 50 years and older make up the majority of cases and are being addressed by the World Health Organisation (WHO) Vision 2020 global initiative (Flaxman *et al.*, 2017).

1.2.1 Retinal Degenerations

Degeneration of the retina underlies many cases of blindness, particularly in the ageing population. It has been estimated that 20% of the global population have age-related macular degeneration (AMD), the most common retinal dystrophy (Lim *et al.*, 2012). There are two forms of AMD and treatment exists for the “wet” form that is characterised by retinal neovascularisation but not for the “dry” form. There are many other forms of retinal degeneration such as diabetic retinopathy, Stargardt disease and Retinitis Pigmentosa (RP). There are limited treatments that can reduce disease progression such as gene therapy for Leber congenital amaurosis type 2 (Luxturna™) and optogenetic therapy for RP (Sahel *et al.*, 2021). However, these are not available to most patients because the disease is too advanced and/or the patient does not possess a treatable mutation. There is some evidence to suggest that the rate of disease progression may be slowed e.g. through vitamin supplementation (Berson *et al.*, 1993, 2010) but overall there are no cost-effective treatments available at a large scale.

1.2.2 Retinitis Pigmentosa

RP is a group of hereditary disorders with similar phenotypes and heterogeneous underlying causes. The wide heterogeneity of RP makes it challenging to describe the pathogenesis, although there are broad similarities in the way the disease progresses (Verbakel *et al.*, 2018). Typically, night blindness (nyctalopia) presents within the first decades of life. This is caused by a loss of rod photoreceptors which may or may not be accompanied by RPE cell dysfunction. This in turn can affect cone viability later in the disease, as rod photoreceptors promote cone photoreceptor survival (Aït-Ali *et al.*, 2015). Loss of peripheral vision typically

occurs for 2-3 decades; this can be followed by a gradual loss of central vision that leads to many patients being diagnosed legally blind later in life.

Given the conservation of symptoms and disease progression in this disease it is remarkable that over 100 genes have been linked to disease onset. Some cases of RP are caused by mutations in genes that expressed exclusively in the retina (for example, rhodopsin, phosphodiesterase 6a (*PDE6A*) and retinal G-protein coupled receptor (*RGR*) (Verbakel *et al.*, 2018)). However, many are caused by mutations in genes that are expressed in many tissues. For example, mutations in some ciliary components can cause Bardet-Biedl syndrome (BBS) that includes RP as one of the symptoms. This is understandable as primary cilia are important for retinal function, photoreceptor outer segments are highly specialised primary cilia. Another cause of RP is mutations in ubiquitously expressed pre-mRNA processing factors (PRPFs). This is interesting because PRPFs are ubiquitously expressed and yet mutations are linked to a retinal phenotype.

1.2.3 Clinical Presentation

RP diagnosis is confirmed through assessment of fundus topography or electroretinogram. The fundus of RP patients exhibits a waxy pallor and bone spicule-like deposits of pigment that lend the disease its name (**Figure 1.6**).

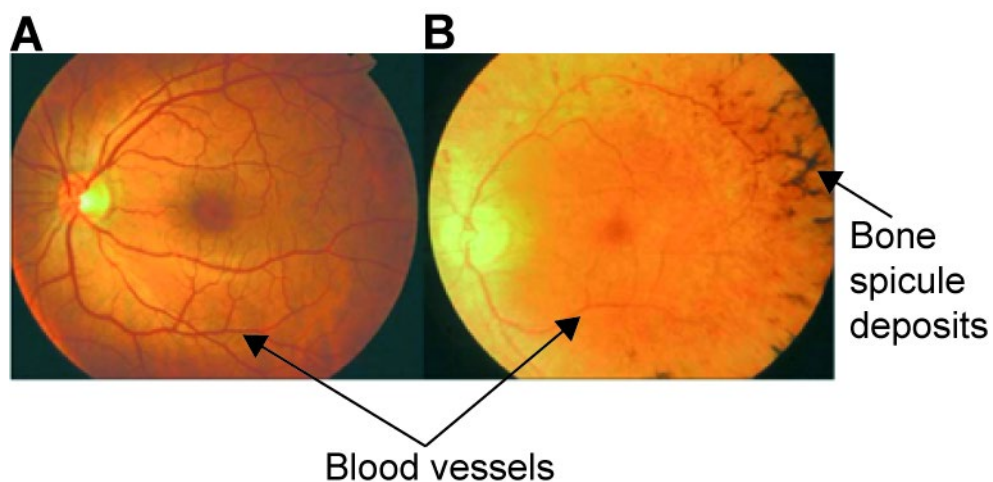


Figure 1.6: A) Fundus of healthy retina and B) of retina from patient with retinitis pigmentosa (RP). In RP, the retina adopts a waxy pallor, blood vessels are thinner and there are black pigment deposits in the retina. Figure taken from Hartong, Berson and Dryja (2006).

Introduction

The peripheral retina contains a relatively high number of rod photoreceptor cells, which are responsible for night vision. These rod cells are generally affected more severely in RP and this eventually leads to loss of peripheral vision (**Figure 1.7**). This can prevent patients from being able to drive.

Visual symptoms are highly variable between patients and the age of diagnosis ranges from less than 10 to over 40 years of age. Diagnosis is often facilitated by a family history of the disease. Once vision is lost in RP it cannot be replaced, as photoreceptors and RPE cells are not capable of regenerating *in vivo*. Early diagnosis is useful because therapies target disease progression in patients with residual vision.



Figure 1.7: As RP progresses the field of vision decreases. This results in ‘tunnel vision’, which restricts patient mobility and ability to drive.

1.2.4 Inheritance

Retinitis pigmentosa is inherited through all Mendelian modes of inheritance, as well as oligogenic inheritance (Hartong, Berson and Dryja, 2006). There are over 100 genes implicated in inheritance of RP (Hartong, Berson and Dryja, 2006).

50-60% of cases are caused by autosomal-recessive inheritance, the inheritance of an affected allele from each parent. Autosomal recessive RP is the only symptom for some individuals, whereas for others it is one feature of a syndromic disorder. For example, individuals with Usher's syndrome may be born deaf and have severe balance problems but then go on to develop to RP. Similarly, individuals with Bardet-Biedl syndrome may be born with additional fingers and/or toes (polydactyly), exhibit learning disabilities and later develop RP. Despite this phenotypic variability in autosomal recessive RP there is some conservation

in the biological function of those genes that cause this disease. Many are important for retinal function e.g., retinal specific genes such as *PDE6A* and *RPE65*. Others are implicated in ciliary biogenesis and function e.g., Usherin (*USH2A*) and *BBS1*. Most tissues in the human body contain ciliated cells but the retina is particularly sensitive to ciliary mutations. The most frequent causes of RP are summarised in **(Table 1)**.

5-15% of cases are X-linked, most of these cases are caused by mutations in RP GTPase regulator (*RPGR*) (Hartong, Berson and Dryja, 2006). The second most common mutation underlying X-linked RP is in *RP2*, which accounts for 7-10% of cases. *RP2* was the second gene found to cause an RP phenotype, hence the RP2 phenotype **(Table 1)**. Digenic inheritance is uncommon but is caused by inheritance of mutations in the *RDS* (peripherin) and retinal outer segment membrane protein 1 (*ROM1*) genes (Kajiwara, Berson and Dryja, 1994). Mitochondrial inheritance of RP is relatively rare but occurs in Kearns-Sayre syndrome (MIM identifier #530000).

Gene	% of Cases	Note	Phenotype
Autosomal recessive, 50-60% of cases			
<i>USH2A</i>	17%	Mutations can cause Usher's syndrome	RP39/USH2A
<i>PDE6B</i>	4-5%	Component of phototransduction cascade	RP40
<i>PDE6A</i>	3-4%	Component of phototransduction cascade	RP43
<i>MYO7A</i>	4%	Mutations cause Usher's syndrome	USH1B
<i>CDH23</i>	3.5%	Mutations cause Usher's syndrome	USH1D
<i>RPE65</i>	2%	Visual cycle component	RP20
<i>ABCA4</i>	5-6%	Required for photoreceptor function	RP19
<i>BBS1</i>	2.3%	Cilia component	BBS1
<i>CNGB1</i>	4%	Component of phototransduction cascade	RP45
<i>BBS10</i>	2%	Cilia component	BBS10
<i>USH3A</i>	2%	Mutations cause Usher's syndrome	USH3A
Autosomal-dominant, 30-40% of cases			
<i>RHO</i>	25%	Component of phototransduction cascade	RP4
<i>RP1</i>	5.5%	Required for photoreceptor function	RP1
<i>PRPF31</i>	5%	Pre-mRNA processing factor	RP11
<i>PRPF3</i>	4%	Pre-mRNA processing factor	RP18
<i>PRPF8</i>	2%	Pre-mRNA processing factor	RP13
<i>IMPDH1</i>	2%	Required for photoreceptor function	RP10
X-linked, 5-15% of cases			
<i>RPGR</i>	70-80%	Required for photoreceptor function	RP3
<i>RP2</i>	7-10%	Required for photoreceptor function	RP2

Table 1: Table summarising the main causative genes of autosomal recessive, autosomal dominant, and X-linked retinitis pigmentosa. Some of these genes cause the syndromic diseases such as Usher's syndrome (USH) and Bardet-Biedl syndrome (BBS). Data taken from Hartong, Berson, and Dryja., 2006. The RP number indicates the order in which the genes were discovered to cause RP.

30-40% of RP cases are autosomal-dominant (adRP) and are caused by the inheritance of a single affected allele. 25% of cases of adRP are caused by mutations in rhodopsin (*RHO*), a component of the phototransduction cascade (Hartong, Berson and Dryja, 2006). The second most common cause of adRP are mutations in PRPFs, these represent over 10% of the adRP cohort (**Table 1**). Similar to ciliary genes, these are ubiquitously expressed genes where mutations cause a retinal phenotype. It is not known why the retina is particularly susceptible to mutations in these genes. However, there is some evidence suggesting cilia biogenesis is sensitive to loss of PRPF function (Whewey *et al.*, 2015a). Six PRPF genes are implicated in adRP: *PRPF3*, *PRPF4*, *PRPF6*, *PRPF8*, *PRPF31* and small nuclear ribonucleoprotein U5 subunit 200 kDa (*SNRNP200*). The patterns of inheritance vary between these genes. For example, *PRPF31* shows characteristic non-penetrance through affected families (Rose and Bhattacharya, 2016). Non-penetrance means that individuals can inherit pathogenic mutations but not display symptoms. Symptom onset in these individuals is modified by other genetic loci (described in section 1.1.5). RP causing mutations have been found throughout the *PRPF31* gene and so it appears that modification of *PRPF31* expression, rather than structure, determines symptom onset (**Figure 1.8**). Symptomatic individuals have been shown to have lower *PRPF31* mRNA expression compared to asymptomatic individuals who also harbour known pathogenic *PRPF31* mutations (Rivolta *et al.*, 2006). This has led to the suggestion that *PRPF31* mutations cause disease through haploinsufficiency, that is, mutations reduce the level of functional PRPF31 protein. Interestingly this makes treatment of *PRPF31*-linked RP with adeno-associated virus (AAV) mediated gene supplementation a possibility. This contrasts the strong penetrance *PRPF8* mutations in affected families. The clustering of adRP-linked mutations in the C-terminal Jab1 or Mpr1, Pad1 N-terminal (MPN) domain of *PRPF8* suggests that these mutations have a dominant negative effect on the gene (**Figure 1.8**) (Grainger and Beggs, 2005). It is likely that gene supplementation of wild-type *PRPF8* would have limited clinical efficacy.

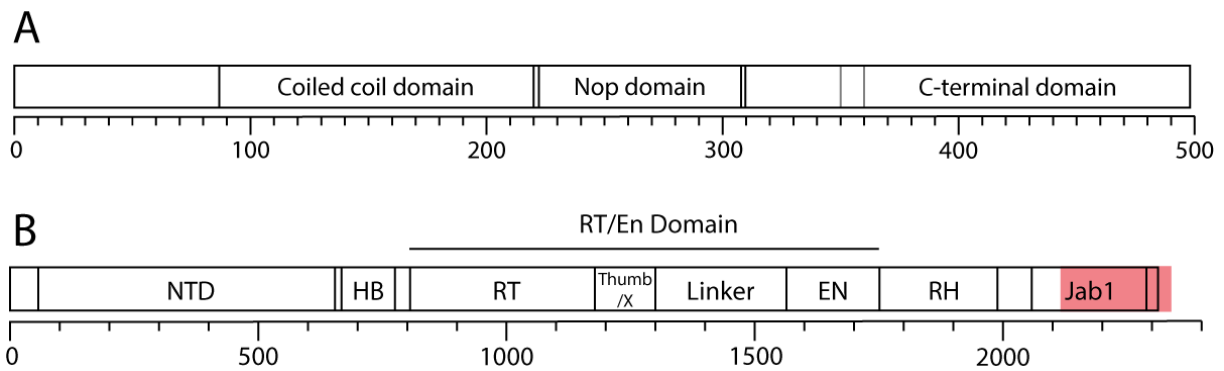


Figure 1.8: A) Schematic of the domain organisation of human PRPF31. B) Schematic of the domain organization of human PRPF8. PRPF8 contains an amino-terminal domain (NTD), helical bundle (HB), reverse transcriptase-like (RT) domain, and thumb/X domain, followed by a Linker region and an endonuclease-like (En) domain, plus carboxy (C)-terminal RNase-H-like (RH) and Jab1/MPN domains. The RT, En, RH, and Jab1 domains are deconstructed enzymes that do not show enzymatic activities.

1.2.5 Treatments

There have been 158 clinical trials looking at treatments of RP. Three have completed phase 3 evaluation. These investigated the effect of nutritional supplements (vitamin A, vitamin E and lutein) on disease progression (Clinical Trial identifiers: NCT00346333, NCT00000116, NCT00000114). The overall low success rate of these trials suggest that vitamin nutritional supplementation and small molecules are not cures but can potentially slow disease progression.

1.2.5.1 Gene Therapy

Over the last twenty years the application of gene therapy in the treatment of inherited blindness has been an area of intense study (Boye *et al.*, 2013; Kumar *et al.*, 2016). This was stimulated by a proof-of-concept study that used viral delivery of a gene to prevent blindness in dogs with inherited retinal disease (Acland *et al.*, 2001). Seven years later, the safety of this approach was confirmed in humans through three separate phase 1/2 clinical trials (Bainbridge *et al.*, 2008; Hauswirth *et al.*, 2008; Maguire *et al.*, 2008; Jacobson *et al.*, 2012). All trials (clinical trial identifiers NCT00643747, NCT00481546, and NCT00516477) used AAV2 serotypes with different promoters (*RPE65*, cytomegalovirus/chicken β -actin, and chicken β actin). Despite the differences between these studies, all the trials concluded gene

Introduction

supplementation had a positive effect on vision. Following an accelerated approval in both the USA and Europe, gene therapy was approved in 2017 and 2018 for a specific form of inherited retinal degeneration- Leber's congenital amaurosis type 2 (LCA2). This is the first gene therapy approved for non-lethal disease and the first treatment of an inherited blinding disease.

Luxturna™ treatment involves a sub-retinal injection of voretigene neparvovec. This is a solution containing non-replicating AAVs that encode the *RPE65* gene. Autosomal recessive mutations in *RPE65* are the cause of LCA2 (Hauswirth *et al.*, 2008) and this extra copy of the gene restores protein function. Patients treated with the therapy show significantly improved visual acuity compared to the control group. This is proof-of-concept that gene therapy can supplement the retina with functional protein, suggesting that this is a possible treatment for other inherited retinal disorders such as RP.

There is good evidence to suggest that *PRPF31* mutations cause disease through haploinsufficiency. This evidence also suggests that RP11 patients could benefit from gene supplementation. Mutations in *PRPF31* do not cluster in a specific region of the gene but are scattered throughout its full length, including non-coding regions (Whewey *et al.*, 2020). This suggests that mutations in non-coding and protein coding regions have similar genetic effects. And that *PRPF31* mutations, regardless of location, cause disease by a common effect on gene expression. Interestingly, non-penetrance is observed in *PRPF31* families. This is where two siblings can inherit identical mutations but only one of the siblings goes on to develop RP11. Symptomatic patients have a greater reduction in wildtype *PRPF31* expression compared to their asymptomatic counterparts (Rivolta *et al.*, 2006). This susceptibility to disease has been shown to be affected by modifiers of *PRPF31* expression including the trans-acting CCR4-NOT transcription complex subunit 3 (*CNOT3*) and cis-acting microsatellite repeat 1 (*MSR1*) (Venturini *et al.*, 2012; Rose and Bhattacharya, 2016). *CNOT3* negatively regulates *PRPF31* expression by interacting with the promoter region of the gene (**Figure 1.9**). *MSR1* repeats are present in the same promoter region. Four *MSR1* elements are associated with higher *PRPF31* expression than three elements (**Figure 1.9**) (Rose *et al.*, 2016). This data suggests that the phenotype of RP11 induced pluripotent stem cell (iPSC) derived RPE could be rescued

through *PRPF31* supplementation using AAV. Further evidence suggesting that *PRPF31* supplementation can slow vision loss in RP11 was recently shown in *PRPF31*^{+/-} iPSC-RPE cells (Brydon *et al.*, 2019). In brief, iPSC-RPE cells were transduced with AAV2-Anc80 with a chicken beta-actin (CASI) promoter that drives *PRPF31* expression. This led to an increase in photoreceptor outer segment (POS) phagocytosis 2 hours after challenge and an increase in iPSC-RPE cilia length. One potential limitation of this study was the use of a genetically engineered *PRPF31*^{+/-} iPSC line rather than a patient-derived iPSC line. This heterozygous knockout lacks any mutant protein that has been shown to contribute to disease progression (Georgiou *et al.*, 2022).

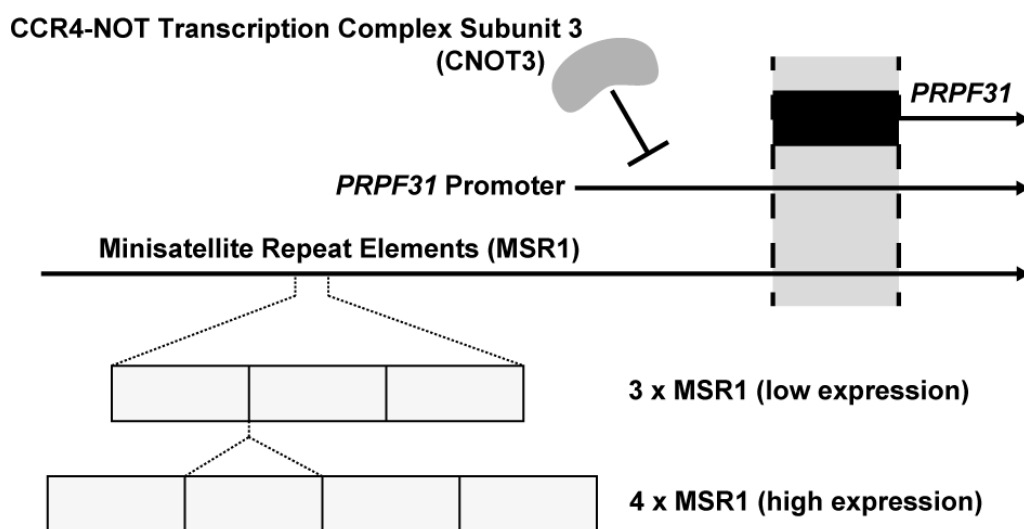


Figure 1.9: Illustration showing regulation of *PRPF31* expression by MSR1 repeats and CNOT3. CNOT3 binds to the promoter region of *PRPF31* and inhibits transcription. Adjacent to the *PRPF31* promoter are several minisatellite repeat (MSR1) elements. The presence of three MSR1 elements is associated with lower expression of *PRPF31* compared to when four MSR1 elements are present.

Gene supplementation is a viable treatment for disorders where the mechanism of disease is haploinsufficiency. However, this represents a fraction of genetic diseases overall. For example, dominant negative mutations can produce toxic protein isoforms. The effect of these mutations could be nullified through post-transcriptional gene silencing e.g., using synthetic oligonucleotides such as small interfering RNA (siRNA) or morpholino oligomers. However, these molecules have a limited half-life within cells and may have limited selectivity

Introduction

between transcripts that differ by a single nucleotide. Given that administration of treatments to the retina requires patients be under general anaesthesia, repeated administrations are not desirable. Instead, one-off treatments such as that offered by base editing and prime editing technologies are more suitable, in theory (Gaudelli *et al.*, 2017; Anzalone *et al.*, 2019; Ballios, Pierce and Huckfeldt, 2021). These are advantageous over classic Cas9 mediated editing which is inefficient and frequently creates short insertions and deletions at the target site through a process called non-homologous end joining (**Figure 1.10**). Base editing ribonucleoproteins fuse an enzyme such as cytidine deaminase to the Cas9 protein. The enzyme typically targets a single nucleotide such as cytosine and convert it to another base such as uracil which is then converted to thymine through DNA mismatch repair (**Figure 1.10**). One limitation of base editing is that the enzyme can install bystander edits in proximal nucleotides. Prime editing ribonucleoproteins efficiently target a series of <12 nucleotides and can install specific edits, albeit at a lower efficiency than base editors (**Figure 1.10**) (Kim *et al.*, 2020). Given that RP causing *PRPF8* mutations cluster within exon 42 of *PRPF8*, prime editing is a possible approach for treatment of RP13. However, the reliability of these technologies *in vivo* remains to be confirmed (Jang *et al.*, 2021; Suh *et al.*, 2022).

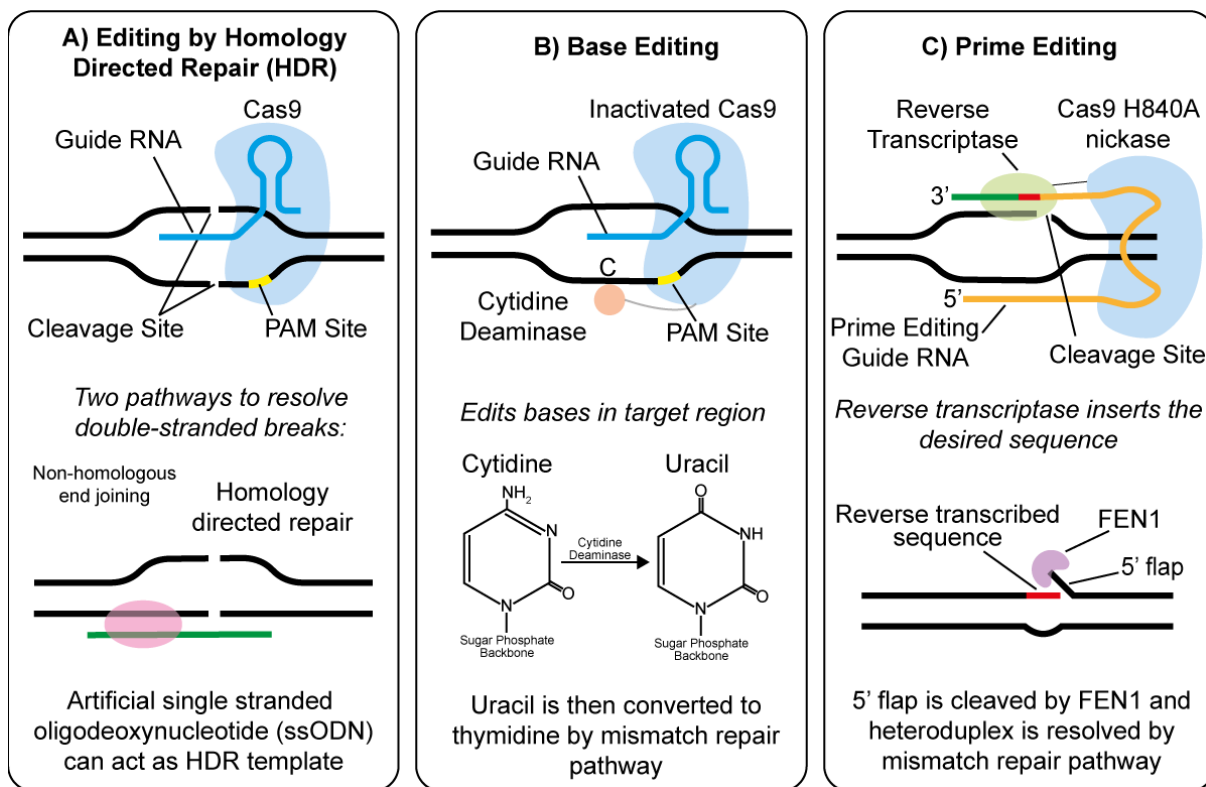


Figure 1.10: Illustration of the mechanisms by which Cas9, base editors, and prime editors install DNA edits. A) Cas9-gRNA ribonucleoprotein interacts with target site and creates a double stranded break in the DNA. The break is then resolved by either non-homologous end joining (NHEJ) or homology directed repair (HDR). NHEJ can install short insertions and deletions at the target site whilst HDR repairs the sequence using the sequence in the homologous chromosome as a template. The efficiency of HDR can be increased by introducing additional template along with the ribonucleoprotein. B) Catalytically inactive Cas9 protein fused to cytidine deaminase does not cut the DNA and converts all cytosines in the target region to uracil. Uracil is then converted to thymidine during DNA mismatch repair. C) Cas9 nickase protein fused to reverse transcriptase cleaves one strand of the DNA. The prime editing guide RNA recognises the cleaved strand and serves as a template for reverse transcriptase. The newly transcribed sequence anneals to the DNA and the 5' flap is degraded by FEN1. Mismatches between the new sequence and old sequence are resolved during DNA mismatch repair.

1.3 CRISPR/Cas9 Gene Editing

Cas9 mediated editing of genes is a technique that allows high-fidelity alterations of the genetic code (Cong *et al.*, 2013) (reviewed in (Doudna and Charpentier, 2014; Hsu, Lander and Zhang, 2014; Sander and Joung, 2014)). Whilst the technology arose from the biological CRISPR/Cas9 system (Barrangou *et al.*, 2007), the Cas9 protein in complex with a single RNA

Introduction

strand (guide RNA, or gRNA) is sufficient to perform editing (Kim *et al.*, 2014). The RNA strand contains two domains, a scaffold domain that interacts with the Cas9 protein and a target specific domain, which recognises the target nucleotide sequence (**Figure 1.11**) (Nishimasu *et al.*, 2014). Effective gRNA design requires specific recognition of a region of interest by the gRNA, a task for which multiple online platforms are available. A second consideration during gRNA design is the requirement for an adjacent protospacer adjacent motif (PAM). This is a conserved three-nucleotide sequence that must be recognised by the Cas9 protein for cleavage to occur. After initial discovery of the Cas9 protein, bioengineers have optimised the protein for *in vitro* use (Liang *et al.*, 2017).

There are two mechanisms of DNA damage repair that resolve Cas9-mediated DNA cleavage. The most common and most error prone is non-homologous end joining (NHEJ). This mechanism is prone to the formation of insertions and deletions to the gene of interest. Thus, NHEJ limits the efficiency of genome editing. There are pharmacological inhibitors of NHEJ which can reduce NHEJ efficiency (Srivastava *et al.*, 2012).

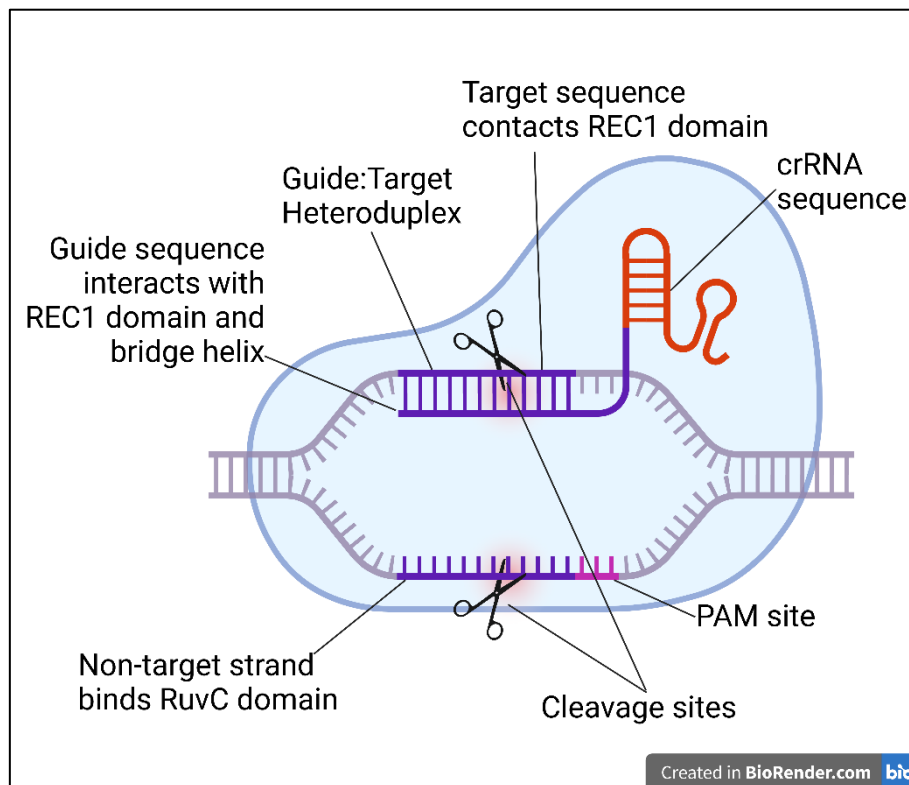


Figure 1.11: Cartoon of Cas9 mediated genomic cleavage. The guide RNA (gRNA) contains a crRNA sequence that interacts with Cas9 and a 20-nucleotide region that interacts with the target sequence. These sequences interact with recognises the target strand of DNA and its cognate protein, Cas9, binds to the adjacent PAM site. The non-target strand is stabilised by the HNH/RuvC groove of Cas9. Following recognition of the target site Cas9 cleaves both strands of the DNA. Image produced using BioRender and Nishimasu et al., 2014.

The second mechanism of DNA damage repair is homology directed repair (HDR). Following double-stranded cleavage, the 5' ends of the break are resected to create single strands. This allows invasion of a complementary nucleotide strand, for example from a homologous chromosome or an artificial oligonucleotide. This complex, called a D-loop, facilitates DNA synthesis and repair of the break. To facilitate genome editing, a single stranded donor oligonucleotides (ssODN) is incubated with the cells as well as the Cas9-gRNA ribonucleoprotein. This interacts with the resected DNA strands and facilitates DNA synthesis of a pre-designed sequence.

1.4 Stem Cells

Stem cells are cells capable of differentiating into other cell types and can self-renew. Stem cells can be categorised according to 'potency', which refers to a capacity to differentiate into other cell types. Only zygotes and blastomeres can differentiate into whole organisms (including placenta) and are "totipotent". Cells that give rise to all embryonic tissues (endoderm, mesoderm, and ectoderm) are "pluripotent". Within most adult tissues, there exist cells that can differentiate into tissue-specific cell types, and these are termed "multipotent" or "unipotent". The existence of stem cells was first proposed in the 19th century following two observations. The first observation, made by Driesch, was that a bisected sea urchin blastocyst could give rise to two whole organisms (Robinton and Daley, 2012). This suggested that the blastocyst contains cells capable of giving rise to a whole organism. The second observation was made by Virchow, who saw that teratocarcinomas are tumours made up of both embryonic and mature cell types from multiple tissues (Sell, 2010). Since then, a huge amount of research has gone into investigating how these cells work and whether they can be cultured *in vitro*, reviewed in (Weissman, 2000; Stadtfeld and Hochedlinger, 2010).

Evidence that cells retain the ability to regain potency came from work by John Gurdon. Somatic cell nuclear transfer of nuclei from differentiated cells into enucleated oocytes (a totipotent cell type) demonstrated that differentiated cells retained the genetic information required to generate new, albeit abnormal, frogs (Gurdon, 1962). Thirty-five years later the same technique was used to clone Dolly the sheep (Wilmut *et al.*, 1997). This was followed by the discovery of embryonic stem cell (ESC) lines from mouse embryos in 1981 and then subsequently from human embryos in 1998 (Evans and Kaufman, 1981; Thomson, 1998).

1.4.1 Induced Pluripotent Stem Cells

Murine embryonic stem cells were first derived in 1981 (Evans and Kaufman, 1981; Martin, 1981) and 17 years later this result was replicated using human blastocysts (Thomson, 1998). However, due to ethical considerations around the use of human embryos, the scientific community was slow to adopt these techniques on a large scale. Then in a 2006 publication

Takahashi and Yamanaka demonstrated that mouse fibroblasts could be reprogrammed into a stem cell-like state (mouse iPSCs) through the induction of four pluripotency factors (Takahashi and Yamanaka, 2006). One year later the result was replicated using human fibroblasts (Takahashi *et al.*, 2007). These results culminated in John Gurdon and Shinya Yamanaka being awarded the Nobel Prize for Physiology or Medicine in 2012. Within three years, research showing that patient-derived iPSCs could recapitulate cellular abnormalities seen in disease were published (Ebert *et al.*, 2009; Lee *et al.*, 2009). The number of articles in a Scopus search for “iPSC” has increased 10-fold from 156 in 2010 to 1554 in 2021, demonstrating a rapidly growing interest in this technology.

As more people have adopted iPSC technology several limitations have been identified. These limitations include the requirement of iPSCs to be maintained over weekends as well as high cost of reagents required to culture stem cells. Most concerning is the high genetic and epigenetic variability that can affect the reproducibility of experiments (Volpato and Webber, 2020). The source of this variability has been studied and arises depending on culture techniques and chromosomal aberrations that iPSCs acquire during reprogramming and culture (Kilpinen *et al.*, 2017). However, the single greatest source of variability between iPSC lines is the donor. This reflects genetic variability that exists across the population (Kilpinen *et al.*, 2017). This has led to widespread interest in combining iPSC technology with CRISPR/Cas9 to faithfully model genetic disease. Gene editing with CRISPR/Cas9 controls facilitates creation of isogenic iPSC lines that vary by as little as a single nucleotide and thereby controls for the effect of donor variability.

1.4.2 Differentiation to Retinal Cells

The retina derives from retinal progenitor cells (RPCs), a multipotent neuroepithelial cell population that proliferates and differentiates to give rise to the retina in a temporally ordered sequence (Swaroop et al 2010). The process begins with the formation of bilateral apically concave optic vesicles, which evaginate from the developing neural tube. The apical surface then invaginates to form the optic cup, a bilayered structure. The outer layer of cells become the RPE monolayer whilst the inner layer proliferates to generate cell types: retinal

Introduction

ganglion cells are formed first, then horizontal cells, cone photoreceptors, amacrine cells, rod photoreceptors, bipolar and Muller glia cells are formed last (**Figure 1.12**: Timeline showing the emergence of different cell types during retinal development. The cell types on the left (ganglion cells and horizontal cells) are the first to commit to their cell fates.) (Mellough, Bauer, *et al.*, 2019). There is conservation between retinogenesis *in vivo* and *in vitro* (Collin *et al.*, 2019). During this process, there are six major families of signalling molecules that govern key events: Sonic Hedgehog (Shh), transforming growth factor beta (TGF β), bone morphogenetic protein (BMP), Wnt, FGF, Notch and IGF-1. This knowledge has been incorporated into differentiation protocols (Mellough *et al.*, 2014).

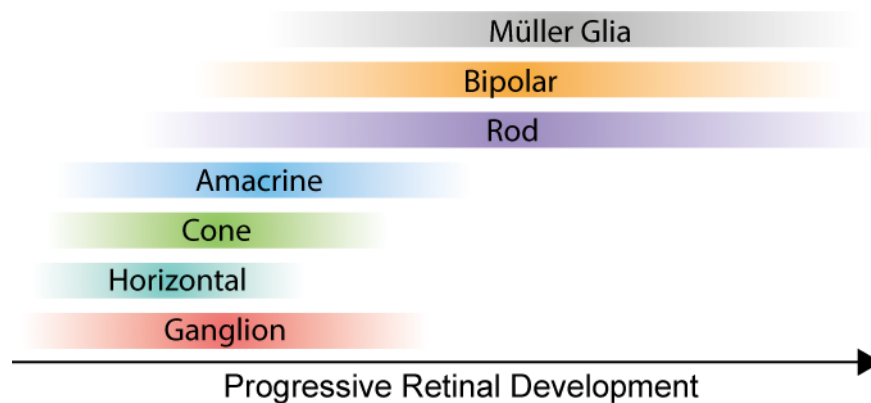


Figure 1.12: Timeline showing the emergence of different cell types during retinal development. The cell types on the left (ganglion cells and horizontal cells) are the first to commit to their cell fates. During retinal development, the number of differentiated cell types increases. Muller glia, bipolar, and rod photoreceptor cells are the last to emerge.

The number of differentiation protocols that can generate different cell types has grown. In 2011 retinal organoids and in 2014 retinal pigment epithelium (RPE cells) were derived from pluripotent stem cells (Eiraku *et al.*, 2011; Kamao *et al.*, 2014; Zhang *et al.*, 2017). Many of these protocols vary subtly but key advancements in the differentiation of iPSC to RPE are given in **Table 2**. In general, they mimic the signals that guide differentiation *in vivo* through the addition of exogenous growth factors. Whilst many molecules have been reported to increase RPE differentiation, a review of RPE differentiation protocols revealed that there were five classes of molecules used. The timing of supplementation varied significantly across different protocols. In brief: during the first week two protocols reported using SMAD

inhibitors (such as SB431542) (Choudhary *et al.*, 2017; Buskin *et al.*, 2018). During the first week activators of BMP signalling (such as noggin) were used in three protocols (Choudhary *et al.*, 2017; Foltz and Clegg, 2017; Buskin *et al.*, 2018). The addition of WNT signalling modulators (such as CHIR99021) were used in three protocols, usually during the second or third weeks after differentiation initiation (Iwasaki *et al.*, 2016; Foltz and Clegg, 2017; Buskin *et al.*, 2018). Activin A, an activator of TGF β signalling, was used in four protocols, generally in the second week of differentiation (Idelson *et al.*, 2009; Choudhary *et al.*, 2017; Foltz and Clegg, 2017; Buskin *et al.*, 2018). MEK/ERK inhibitors (such as SU5402) were added during the second week (Idelson *et al.*, 2009; Iwasaki *et al.*, 2016; Foltz and Clegg, 2017). There is no consensus on a single superior protocol for RPE differentiation.

In two landmark papers, the laboratory of Yoshiki Sasai showed that both murine embryonic stem cells (mESCs) and human embryonic stem cells (hESCs) can generate self-organising optic cups when cultured under 3D minimal culture conditions (Eiraku *et al.*, 2011; Nakano *et al.*, 2012). These optic cups can generate fully laminated neural retina containing all classes of retinal cells by following the normal sequence of retinal development. Over time, many protocols that facilitate retinal organoids development have been published. A summary of key papers is given in **Table 3** and a comprehensive review is provided by (Mellough *et al.*, 2014; Morizur *et al.*, 2020).

Introduction

Cell Type	RPE Derivation	Method
hESC	Pure RPE (Klimanskaya <i>et al.</i> , 2004)	Monolayer/spontaneous differentiation
hiPSC/miPSC	RPE and retinal progenitor cells (Hirami <i>et al.</i> , 2009)	Floating embryoid bodies followed by plating onto coated tissue culture surfaces. First protocol using small molecules to guide RPE differentiation in hiPSCs.
hiPSC	Pure RPE (Buchholz <i>et al.</i> , 2009)	Monolayer/spontaneous differentiation
hESC and hiPSC	Pure RPE (Buchholz <i>et al.</i> , 2013)	Monolayer/small molecules and defined media
hiPSCs	Pure RPE (Ferrer <i>et al.</i> , 2014)	Floating embryoid body formation followed by 2D culture. RPE are then replated to improve purity.
hiPSCs	Pure RPE (Hallam <i>et al.</i> , 2017)	2D differentiation incorporating small molecules including B27
hESC and hiPSC	Pure RPE (Regent <i>et al.</i> , 2019)	2D differentiation incorporating small molecules (not B27)

Table 2: Brief history of research that successfully differentiated RPE from stem cells. Acronyms: hESC (human embryonic stem cell), mESC (mouse embryonic stem cell), hiPSC (human induced pluripotent stem cell) and miPSC (mouse induced pluripotent stem cell).

Cell Type	Neural Retina Derivation	Method
mESC/hESC	optic cup-like structures <i>in vivo</i> (Aoki <i>et al.</i> , 2009)	Transplanted hESCs into adult mouse eyes
mESC	optic cup-like structures <i>in vitro</i> (Eiraku <i>et al.</i> , 2011)	Floating embryoid bodies and small molecules on Matrigel coated plates
hESC	optic cup-like structures (Nakano <i>et al.</i> , 2012)	Floating embryoid bodies and small molecules
hiPSC	laminated neural retina (Phillips <i>et al.</i> , 2012)	Floating embryoid bodies followed by culture in chemically defined media. Included dissection of organoid from monolayers followed by suspension culture
hiPSC	optic cup-like structures (Zhong <i>et al.</i> , 2014)	Floating embryoid bodies and small molecules
hESC/hiPSC	optic-cup like structures (Mellough <i>et al.</i> 2015)	Treatment of embryoid bodies with IGF-1 to increase efficiency of optic cup formation
hiPSC	optic-cup like structures (Hallam <i>et al.</i> 2018)	Adapted conditions for culture in 96 well plate
hESC/hiPSC	optic-cup like structures (West <i>et al.</i> 2022)	Antioxidant and lipid supplementation improves formation of photoreceptor outer segments

Table 3: Brief history of research that successfully generated neural retina from stem cells.

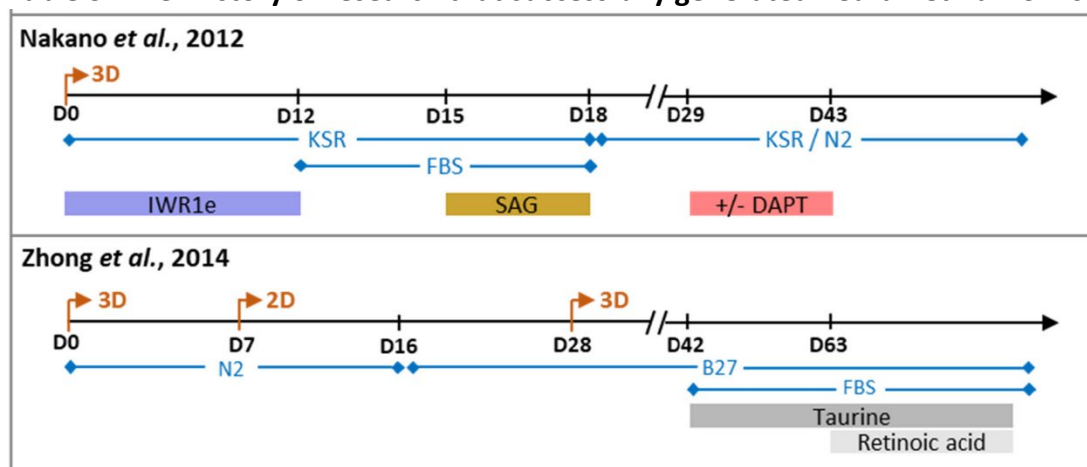


Figure 1.13: Summary schematic of retinal organoid differentiation protocols taken from Morizur et al., 2020.

1.5 Pre-mRNA Splicing

1.5.1 The Splicing Cycle

The majority of pre-mRNA can be simplified to being either exon or intron. Following transcription, in a process called splicing, exon identification and intron removal yields mature mRNA (Herzel *et al.*, 2017). Splicing is orchestrated by the spliceosome, a macromolecular machine that assembles stepwise onto pre-mRNA (Abelson, 2008). This process is of greater significance in higher eukaryotes as most genes give rise to 'alternatively spliced' transcripts, a mechanism believed to ###maximise the information stored within DNA.

Splicing is performed by the spliceosome, a macromolecular ribonucleoprotein. The spliceosome contains five ribonucleoproteins (RNPs) composed of five uridine-rich small nuclear RNAs (snRNAs) U1, U2, U4, U5, and U6 and a large number of proteins (reviewed in (Wahl, Will and Lührmann, 2009)). Purification of spliceosome complexes at different stages of the splicing cycle have revealed how the protein composition changes at different stages of spliceosome assembly (Hartmuth *et al.*, 2002; Makarov *et al.*, 2002; Makarova *et al.*, 2004; Deckert *et al.*, 2006; Behzadnia *et al.*, 2007; Bessonov *et al.*, 2008). These studies indicate that there are approximately 170 spliceosome-associated proteins with around 125 proteins associated with the spliceosome at each stage of the splicing cycle. Large changes to protein content of spliceosome (both to the core proteins and in the additional accessory proteins) occur between successive stages of the splicing cycle. The function of these proteins is an area of active research and is revealing that amongst other things, they are involved with coupling splicing with transcription and quality control (reviewed in (Maniatis and Reed, 2002; Jurica and Moore, 2003; Herzel *et al.*, 2017)). Interestingly, these studies reveal that many proteins are present in sub-stoichiometric amounts, indicating that they may only be weakly associated with the spliceosome (Wahl, Will and Lührmann, 2009; Papasaikas and Valcárcel, 2016).

Gene	Percent of adRP cohort	RetNet	Tri-snRNP Function
<i>PRPF3</i> (Vaclavik <i>et al.</i> , 2010; Zhong <i>et al.</i> , 2016)	1.5	English and Danish families; early onset night blindness; recurrent Thr494Met mutation	U4/U6 associated (Heng, Wang and Hu, 1998; Maita <i>et al.</i> , 2005; Liu <i>et al.</i> , 2015; Bertram, Agafonov, Dybkov, <i>et al.</i> , 2017)
<i>PRPF31</i> (Vithana <i>et al.</i> , 2001)	8.9	Incomplete penetrance and bimodal severity result from variable expression of alleles in trans; large deletions in <i>PRPF31</i> , not detectable by sequencing, account for 2.5% of dominant RP	Bridge U4/U6 and U5 snRNPs (Makarova <i>et al.</i> , 2002)
<i>PRPF8</i> (Townes <i>et al.</i> , 2010)	2.6	South African and European families	U4/U6 unwinding (Maeder, Kutach and Guthrie, 2009)
<i>SNRNP200</i> (Zhao <i>et al.</i> , 2009; Liu <i>et al.</i> , 2012; Bowne <i>et al.</i> , 2013)	1.5	Chinese and European families	U4/U6 unwinding (Zhao <i>et al.</i> , 2009)
<i>PRPF6</i> (Tanackovic, Ransijn, Ayuso, <i>et al.</i> , 2011)		Missense mutation in one dominant RP family among 188 screened; mutation affects PRPF6 protein localization in patient-derived cells	Bridge U4/U6 and U5 snRNPs (Lützelberger <i>et al.</i> , 2009; Bertram, Agafonov, Dybkov, <i>et al.</i> , 2017)
<i>PRPF4</i> (Chen <i>et al.</i> , 2014)		Heterozygous <i>PRPF4</i> missense mutation identified in a dominant RP family and an isolated case, respectively; a functional null mutation in <i>PRPF4</i> suggests haploinsufficiency as a disease mechanism	U4/U6 associated (Chen <i>et al.</i> , 2014; Linder <i>et al.</i> , 2014; Bertram, Agafonov, Dybkov, <i>et al.</i> , 2017)

Table 4: Eight splicing factors were linked to retinitis pigmentosa in a recent review (Růžicková and Staněk, 2017). However, some of these are very rare. Four splicing factors were detected in a sample of 270 families affected by autosomal dominant RP (Daiger, Bowne and Sullivan, 2015). The proportion of this sample is indicated in the top table. Alongside gene names are references in which mutations in these genes

Introduction

were linked to RP. Relevant information from RetNet and OMIM is presented along with functional information relevant to common genes affected in PRPF-linked adRP.

Owing to the complexity of spliceosome assembly, the mechanics of its function are difficult to elucidate experimentally. Some progress has been made in recent publications using cryo-electron microscopy, which elucidate how the tri-snRNP conformation shifts between stages of the splicing cycle (Agafonov *et al.*, 2016; Bertram, Agafonov, Dybkov, *et al.*, 2017; Bertram, Agafonov, Liu, *et al.*, 2017; Zhang *et al.*, 2018). There are six tri-snRNP proteins and two spliceosomal proteins linked to adRP (**Table 4**). The complexity itself provides insights into spliceosome function, as can be demonstrated by describing pre-spliceosome formation. During pre-spliceosome assembly (complex A formation), the U1 snRNP associates with pre-mRNA as does the U2 snRNA. U2 associates with the branch point signal (BPS) which is a conserved intron motif (**Figure 1.14**). This interaction is stabilized by multiple protein components of the U2 snRNP, (Gozani, Feld and Reed, 1996; Valcárcel *et al.*, 1996). U2 snRNA association displaces proteins that were previously associated with the BPS and these are replaced by other proteins which interact with the BPS (Will *et al.*, 2001). These newly associated proteins stabilise the conformation by interacting with the U2 snRNP (Gozani, Potashkin and Reed, 1998). These steps demonstrate a significant and recurring principle seen through spliceosome assembly: “functionally important binary interactions in the spliceosome are often weak but are enhanced by a combination of multiple interactions” (Wahl, Will and Lührmann, 2009). Identifying principles such as this are important and assist understanding of subsequent reconfigurations of the spliceosome, which are significantly less well understood (Wahl, Will and Lührmann, 2009).

Progression from the A complex to the B complex involves recruitment of 25 proteins and three snRNAs (U4/U6 and U5 snRNAs) which form a complex known as the tri-snRNP (**Figure 1.14**) (Gottschalk *et al.*, 1999). Many non-snRNP proteins such as the Prp19/CDC5 complex (NTC) (Makarova *et al.*, 2004) and NTC-related proteins (Chen *et al.*, 1999, 2002; Ajuh *et al.*, 2000) also associate at this stage. Recently, high-resolution structures of the tri-snRNP were resolved by cryo-EM (Agafonov *et al.*, 2016; Bertram, Agafonov, Liu, *et al.*, 2017; Zhang *et al.*, 2018). These provide insight into structural remodelling of the tri-snRNP during the splicing cycle and corroborate the wealth of existing biochemical data. These structures are limited by the lack of non-snRNP (such as the NTC) components required during splicing.

1.5.1.1 B Complex Activation

The U4 and U6 snRNAs of the tri-snRNP are extensively base paired with each other prior to B complex activation. During B complex activation these interactions are disrupted and allow the U6 snRNA to interact with U2 snRNA (Wahl, Will and Lührmann, 2009). This unwinding requires energy from ATP hydrolysis and the DExD/H-box 'unwindase' SNRNP200 (**Table 4**), one of eight ATPases that drive large conformational changes during the splicing cycle (Staley and Guthrie, 1998). The disrupted RNA-RNA interaction destabilizes the tri snRNP and U4/U6 proteins dissociate from the spliceosome (**Figure 1.14**). This includes several PRPFs that have been linked to RP including PRPF3, PRPF4, PRPF6, and PRPF31 (**Table 4**). This conformational change stabilises the association between the U5 snRNP and the NTC (Makarov *et al.*, 2002). The U5 snRNP contains PRPF8 and SNRNP200, these are the only two tri-snRNP proteins that have been linked to RP that are present in the spliceosome after B complex activation. PRPF8 is an important regulator of SNRNP200 unwindase activity (**Table 4**) (Grainger and Beggs, 2005). It contains a Jab1/MPN domain at the C-terminal end of the protein (Pena *et al.*, 2007; Zhang *et al.*, 2007). This region of PRPF8 interacts with SNRNP200 to stimulate its U4/U6 helicase activity during B-complex activation (Maeder *et al.*, 2009). The activated B complex (B*) was recently purified and its structure studied using cryo-electron microscopy (Haselbach *et al.*, 2018). The results suggested that the activated B-complex is a flexible structure that transitions through eight distinct conformations (Haselbach *et al.*, 2018). As with all conformation changes in the spliceosome, transitioning between these conformations is thought to be dependent on interactions between tri-snRNP components and more peripheral components of the spliceosome (Wahl, Will and Lührmann, 2009; Haselbach *et al.*, 2018).

Following B complex activation, two subsequent changes in spliceosome conformation and configuration catalyse the first and second transesterification reactions. The first transesterification reaction cleaves the 5' splice site and the pre-mRNA forms a lariat structure. The resulting ribonucleoprotein complex incorporates an additional 9 C complex proteins to form the C-complex (**Figure 1.14**) (Will and Lührmann, 2011). During the second transesterification reaction the 3'SS is cleaved and then ligates with the 5'SS. The intron lariat structure is no longer covalently bound to the mRNA. Finally, the post-spliceosome complex dissociates (**Figure 1.14**), the intron lariat is degraded and the snRNPs and NTC are trafficked

to nuclear speckles where they are recycled and stored before re-use (Chen *et al.*, 2006; Staněk *et al.*, 2008; Maréchal *et al.*, 2014).

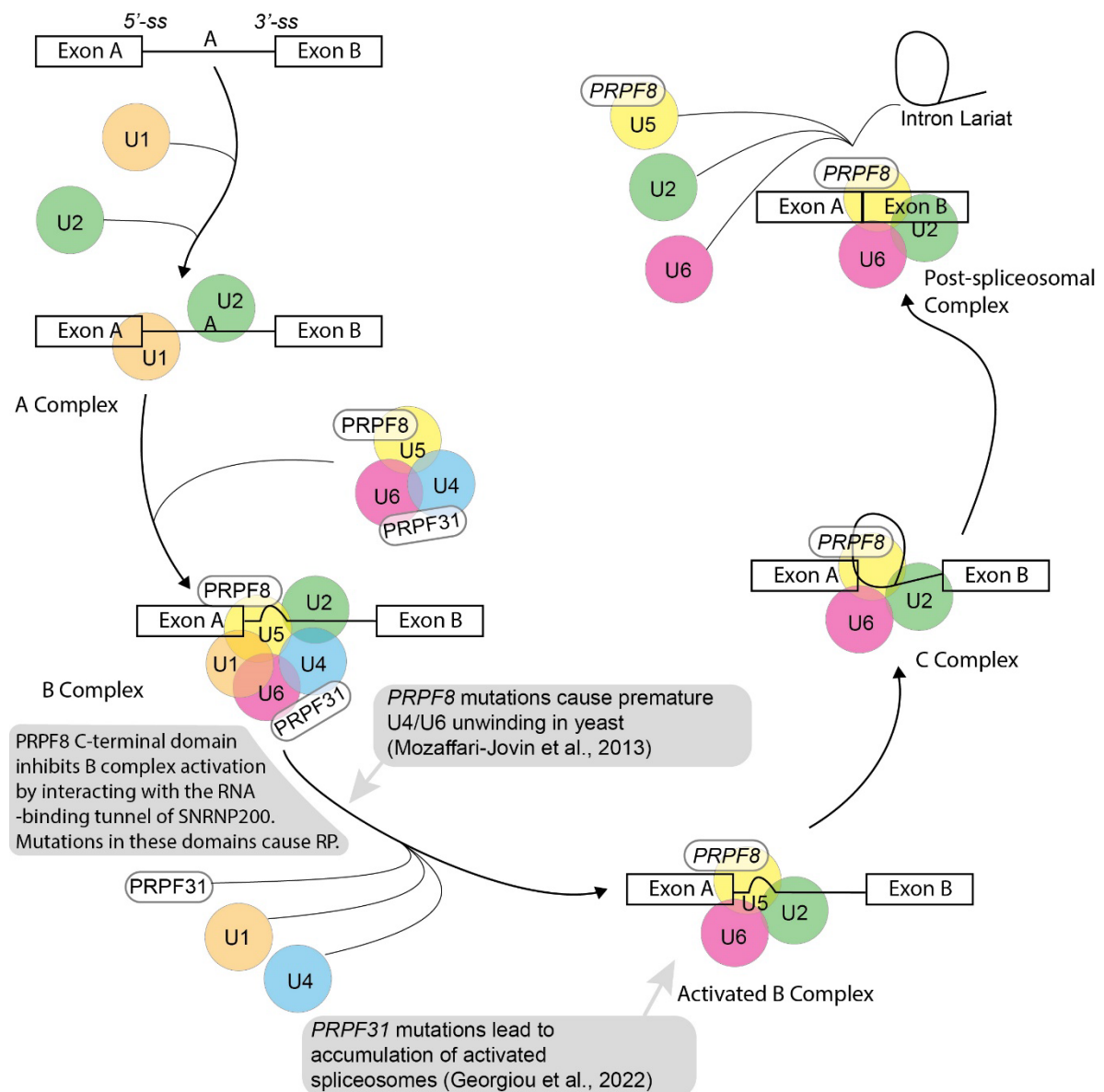


Figure 1.14: Cartoon of the splicing cycle illustrating the role of five uridine rich snRNPs as well as pre-mRNA processing factor 31 (PRPF31) and PRPF8. 5' splice site (5'-ss) 3' splice site (3'-SS). The U1 snRNP recognises the 5'-ss and U2 snRNP recognises the intron branch-point adenosine (complex A). The tri-snRNP particle formed by conjugation of the U4/U6 duplex bound to PRPF31 and U5 bound to PRPF8 interacts with U1 and U2 (complex B). ATP and GTP are required for activation of this complex, which involves release of U1, U4 and PRPF31. Figure adapted from (Rose et al. 2017).

1.5.2 Pre-mRNA Processing Factors (PRPFs) and Retinitis Pigmentosa

PRPFs implicated in RP are components of the tri-snRNP (**Table 4**). They are expressed ubiquitously and so it is interesting that mutations lead to a tissue-specific disease. Some studies have used bulk RNA sequencing to investigate genome-wide aberrant splicing events. These have proved that there are generalised splicing defects (Tanackovic, Ransijn, Thibault, *et al.*, 2011; Kurtovic-Kozaric *et al.*, 2015; Buskin *et al.*, 2018). However, only 10% of these are reflected by changes in protein expression (Buskin *et al.*, 2018) and splicing defects are observed in unaffected tissues (Kurtovic-Kozaric *et al.*, 2015; Buskin *et al.*, 2018). Therefore, it is still unclear why these mutations specifically affect the retina.

PRPF mutations associated with adRP cause splicing defects in multiple cell lines (Wilkie *et al.*, 2008; Huranová *et al.*, 2009; Tanackovic, Ransijn, Thibault, *et al.*, 2011; Vihandha O Wickramasinghe *et al.*, 2015; Papasaikas and Valcárcel, 2016). Some of these studies used PCR technology and manual selection of primers to identify alternatively spliced transcripts. These revealed that housekeeping genes and pre-mRNA processing factors were frequently mis-spliced. The development of unbiased RNA sequencing technology has allowed the entire population of cellular RNA to be sequenced (Vihandha O. Wickramasinghe *et al.*, 2015; Buskin *et al.*, 2018). These studies reveal global changes in alternative splicing in cell with *PRPF31* adRP mutations in both retinal and non-retinal cells (Buskin *et al.*, 2018).

1.5.2.1 PRPF31

Zebrafish and murine models of *Prpf31* linked adRP (RP11) have revealed that retinal degeneration caused by *PRPF31* mutations is conserved across species. Zebrafish expressing adRP *prpf31* mutations exhibit prominent photoreceptor degeneration and decreased visual response (Linder *et al.*, 2011; Yin *et al.*, 2011). Analysis of zebrafish photoreceptors indicated an accumulation of protein in rod photoreceptors (Yin *et al.*, 2011) and decreased expression of multiple components of the photo transduction cascade (Linder *et al.*, 2011). The phenotype of *prpf31* knockdown in these models can be restored by increasing expression of wild type *prpf31*, although the retinal phenotype following *prpf31* rescue was not examined in detail.

Generation of *Prpf31* mutant mice which recapitulate the retinal phenotype seen in RP is difficult due to complexities of *PRPF31* inheritance (Bujakowska *et al.*, 2009; Rose *et al.*, 2017). However, *Prpf3*^{+/^{T494M}, *Prpf8*^{+/^{H2309P} and *Prpf31*^{+/-} mice have been developed (Graziotto *et al.*, 2011; Farkas *et al.*, 2014). Photoreceptor cells of these mice do not die but do show signs of stress, whereas the RPE cells are the most affected cell type. A study of wildtype mice identified higher expression of snRNAs and snRNPs in the retina compared to other tissues (Cao *et al.*, 2011). This suggests retinal cells have a greater need for these splicing components. Ultrastructural analysis of the RPE cells of PRPF-mutant mice identified abnormalities including stress vacuoles and basal deposits (**Figure 1.15**) (Graziotto *et al.*, 2011). Therefore, RPE defects precede photoreceptor degeneration in mice and suggest that photoreceptor degeneration in RP11 is caused by dysfunctional RPE. Specific anomalies included appearance of vacuole-like structures, loss of basal infoldings and accumulation of material between the RPE and Bruch's membrane (**Figure 1.15**) (Graziotto *et al.*, 2011). There is also a loss of RPE polarity across all cell lines and a significant decrease of rod function (measured through electroretinogram) in *Prpf3*^{+/^{T494M} retina. Lastly, there is a loss of rhythmicity in the phagocytosis of POS (Mao and Finnemann, 2012; Farkas *et al.*, 2014). In wild type mice, two hours after light onset there is a peak in the number of phagosomes observed in the RPE. This peak in RPE phagocytic activity is absent from PRPF mutant mice (Farkas *et al.*, 2014).}}}

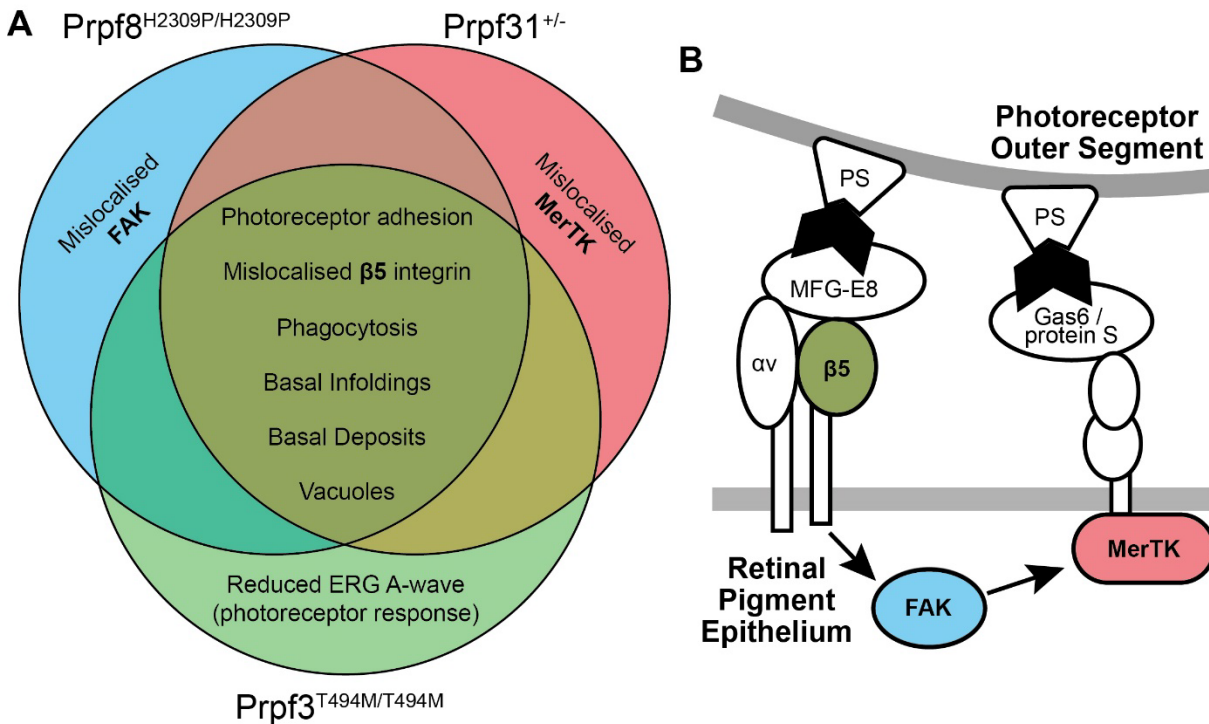


Figure 1.15: Summary of the retinal phenotypes observed in murine models of PRPF-linked retinitis pigmentosa. A) Venn diagram showing the overlapping features presented in Farkas et al., 2014 and Graziotto et al., 2011. Many features were present in all PRPF-models including decreased adhesion between photoreceptors and the RPE, decreased phagocytosis of photoreceptor outer segments, numerous ultrastructural changes, and mislocalisation of $\beta 5$ integrin, which is involved in POS phagocytosis initiation. Reduced photoreceptor response to light was detected in Prpf3^{T494M/T494M} mice only. B) Schematic showing location and role in initiation of proteins mis-localised in murine PRPF-models $\beta 5$ -integrin (all), focal adhesion kinase (FAK, Prpf8^{H2309P/H2309P}), and Mer tyrosine kinase (MerTK, Prpf31^{+/-}). Adapted from Mao and Finnemann (2012).

These results were followed up in a human disease model of iPSC-derived retinal organoids and RPE cells (Buskin *et al.*, 2018). This study identified multiple features that are conserved across species following *PRPF31* mutation. For example, transmission electron microscopy (TEM) analysis of iPSC-RPE cells derived from RP11 patients showed the presence of amorphous material beneath the monolayer, and similar deposits were reported in mice with PRPF mutations (Graziotto *et al.*, 2011; Buskin *et al.*, 2018). In addition, the iPSC-RPE cells contained numerous stress vacuoles that resemble those present in the mice (Graziotto *et al.*, 2011; Buskin *et al.*, 2018). Immunofluorescent staining against markers of epithelial cell polarity indicated that this characteristic was lost in both iPSC-RPE and mouse RPE cells that

harbour *PRPF31* mutations (Farkas *et al.*, 2014; Buskin *et al.*, 2018). Functional analysis of the patient-derived iPSC-RPE cells revealed a phagocytosis defect, similar to that which was observed in mice 2 hours after light onset (Farkas *et al.*, 2014; Buskin *et al.*, 2018).

More recently, studies of *PRPF31* models that harbour missense mutations and small deletions rather than heterozygous knockouts have revealed a propensity for mutant PRPF31 to aggregate in RPE cell cytoplasm. Three mutations that promote aggregation of PRPF31 have been identified: two missense mutations in the coiled-coil domain c.590T>C and c.646G>C (L197P and A216P, respectively) as well as a small deletion in the C-terminal domain c.1115_1125del11 (p.Arg372Glnfs*99) (Vithana *et al.*, 2001; Bryant *et al.*, 2019; Valdés-Sánchez *et al.*, 2019; Georgiou *et al.*, 2022). It is not clear how much this protein aggregation contributes to vision loss in RP11. However, one study showed that clearance of these aggregates through activation of autophagy can promote cell survival (Georgiou *et al.*, 2022).

1.5.2.2 PRPF8

PRPF8 is the largest protein in the spliceosome and coordinates zinc ions that are essential for transesterification reactions during the splicing cycle (Grainger and Beggs, 2005). RP-causing mutations are clustered at the C-terminal end of the Jab1 or MPN domain (Townes *et al.*, 2010). Mutations in other regions of the gene have been linked to other human diseases. For example, mutations in the N-terminal domain (p.P13L and p.M25T) increase risk of glaucoma (Micheal *et al.*, 2018). Mutations elsewhere in the gene can cause neurodevelopmental disorders and have also been identified in myeloid malignancies (Kurtovic-Kozaric *et al.*, 2015; O'Grady *et al.*, 2022).

The C-terminal region affected in RP13 interacts with other tri-snRNP components including the RNA-binding domain of SNRNP200 (**Figure 1.16**). This interaction regulates dissociation of the U4 snRNA from the spliceosome that occurs during B complex activation. The unwinding of U4 from U6 is impaired by mutations in the C-terminal domain of PRPF8 and the RNA-binding domain of SNRNP200 (Maeder, Kutach and Guthrie, 2009). The presence of RP-causing mutations in these contiguous domains implicate this interaction in the aetiology of RP (Maeder, Kutach and Guthrie, 2009; Zhao *et al.*, 2009).

In vitro studies using immortalised cell lines suggest *PRPF8* mutations affect splice site recognition (Wickramasinghe *et al.*, 2015) and splicing efficiency (Mayerle and Guthrie, 2016). However, this broadly affects the transcriptome, which raises the obvious question of why only the retina is affected. *PRPF8* and other RP-related *PRPFs* have been shown to localise to the cilia (Wheway *et al.*, 2015b). As mutations in ciliary proteins frequently cause human retinal disease, *PRPF8* mutations could cause RP by impairing ciliary function in retinal and RPE cells, either directly or indirectly through mis-splicing of ciliary transcripts. Whilst *PRPF8* is necessary for ciliogenesis, this process is not affected by mutations that cause RP (Wheway *et al.*, 2015b; Shen *et al.*, 2022). It is not clear whether RP-causing *PRPF8* mutations affect cilia structure or function.

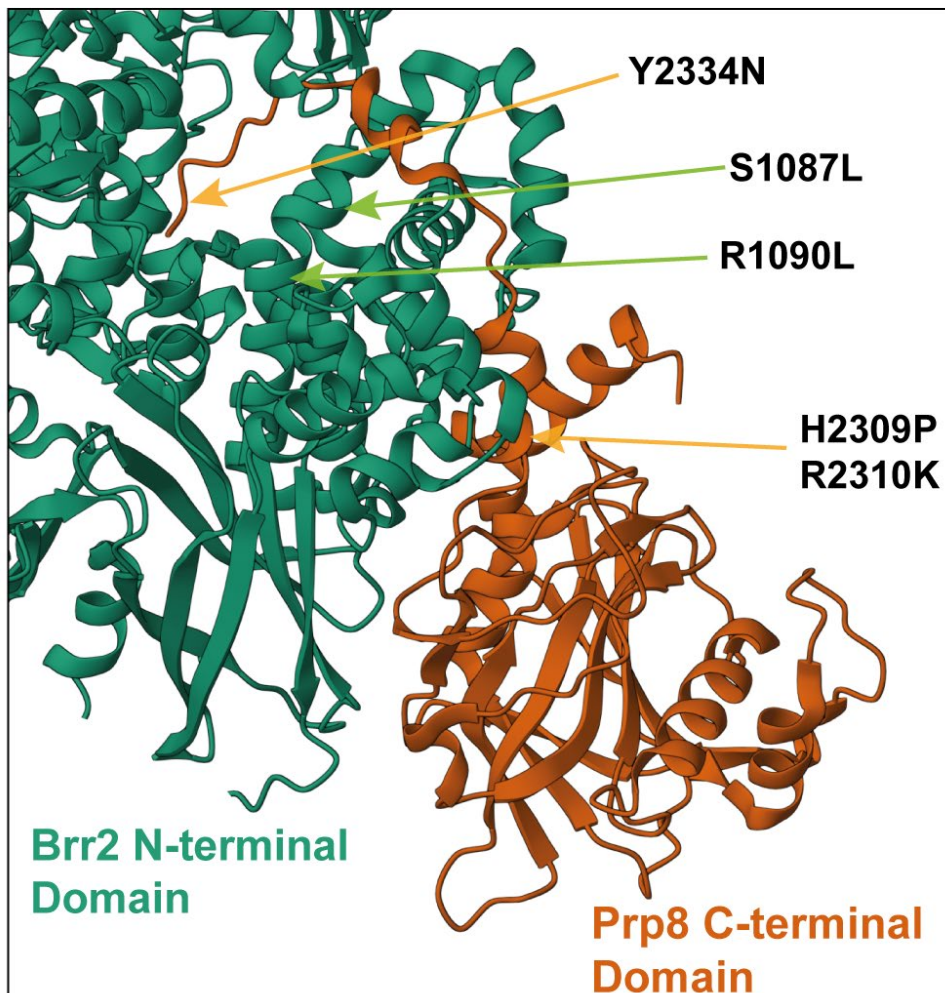


Figure 1.16: Ribbon diagram showing the interaction between the C-terminal domain of yeast Prp8 and N-terminal domain of Brr2 (yeast homologue of SNRNP200). The C-terminal

of Prp8 shown comprises a Jab1 domain and tail that inserts into a tunnel in Brr2. Mutations in Prp8 correspond to residues at the base of this tail (e.g., H2309P and R2310K) and within the tail (e.g., Y2334N). Mutations in Brr2 are found in the corresponding interacting domain (e.g., S1087L and R1090L). Figure created using data from Mozaffari-Jovin et al., 2013.

Studies of mice that harbour *PRPF8* and *PRPF31* mutations show no photoreceptor death occurs during their lifespan of 2 years. This could be because the disease is not recapitulated in mice, or because the relatively short 2-year lifespan of laboratory mice is insufficient for comparison with the 10 years that precede symptom onset in humans. Evidence to support the latter view comes from the observation that the RPE cells of mice harbouring RP-causing *PRPF31* and *PRPF8* mutations share some characteristics with other retinal diseases. For example, RPE cells in mice with PRPF mutations have increased presence of electron lucent inclusions, sometimes called stress vacuoles, that have previously been associated with diseased states of the RPE (Farkas *et al.*, 2014). For example, electron lucent inclusions are also abundant in the RPE of mice and dogs with *RPE65* mutations (Wrigstad, Nilsson and Narfström, 1992; Veske *et al.*, 1999; Redmond *et al.*, 2005). Another similarity between the reports of *RPE65* and *PRPF8* mice RPE is the impaired phagocytosis of photoreceptor outer segments, as has also been seen in rats with *MERTK* mutations (another model of RP) (Bok and Hall, 1971; Farkas *et al.*, 2014).

RP13 patient-derived iPSCs can differentiate and express classical RPE markers such as ZO-1, CRALBP, and BEST1 (Foltz *et al.*, 2018; Arzalluz-Luque *et al.*, 2021). The RP13 RPE cells have no obvious ultrastructural changes nor is there a reduction in phagocytic ability (Arzalluz-Luque *et al.*, 2021). Western blot and immunofluorescent microscopy of PRPF8 in RP13-RPE cells suggests that protein abundance and nuclear location are not affected by mutation (Arzalluz-Luque *et al.*, 2021). PEDF concentration was higher in RP13 iPSC-RPE compared to isogenic control, indicating a potential effect of *PRPF8* mutation on apico-basal polarity, as was observed in RP13 mouse RPE cells (Farkas *et al.*, 2014; Foltz *et al.*, 2018). Analysis of differential exon usage identified the splicing of spliceosome and mitochondrial transcripts to be particularly affected in RP13 iPSC-RPE cells, as was also identified in RP11 iPSC-RPE cells (Buskin *et al.*, 2018; Arzalluz-Luque *et al.*, 2021).

1.6 Cilia

Cilia are evolutionarily conserved organelles that are formed when cells exit the cell cycle, and the mother centriole docks onto the plasma membrane to form the basal body. Microtubules extend from the basal body outwards from the cell plasma membrane to form the ciliary axoneme (**Figure 1.17**). Trafficking of molecules into this specialised membrane compartment is regulated by the transition zone at the base of the axoneme (O'Toole *et al.*, 2003). The assembly and function of the cilia is dependent on the specialised protein trafficking system which exists within the cilia: the intraflagellar transport (IFT) system (Taschner and Lorentzen, 2016).

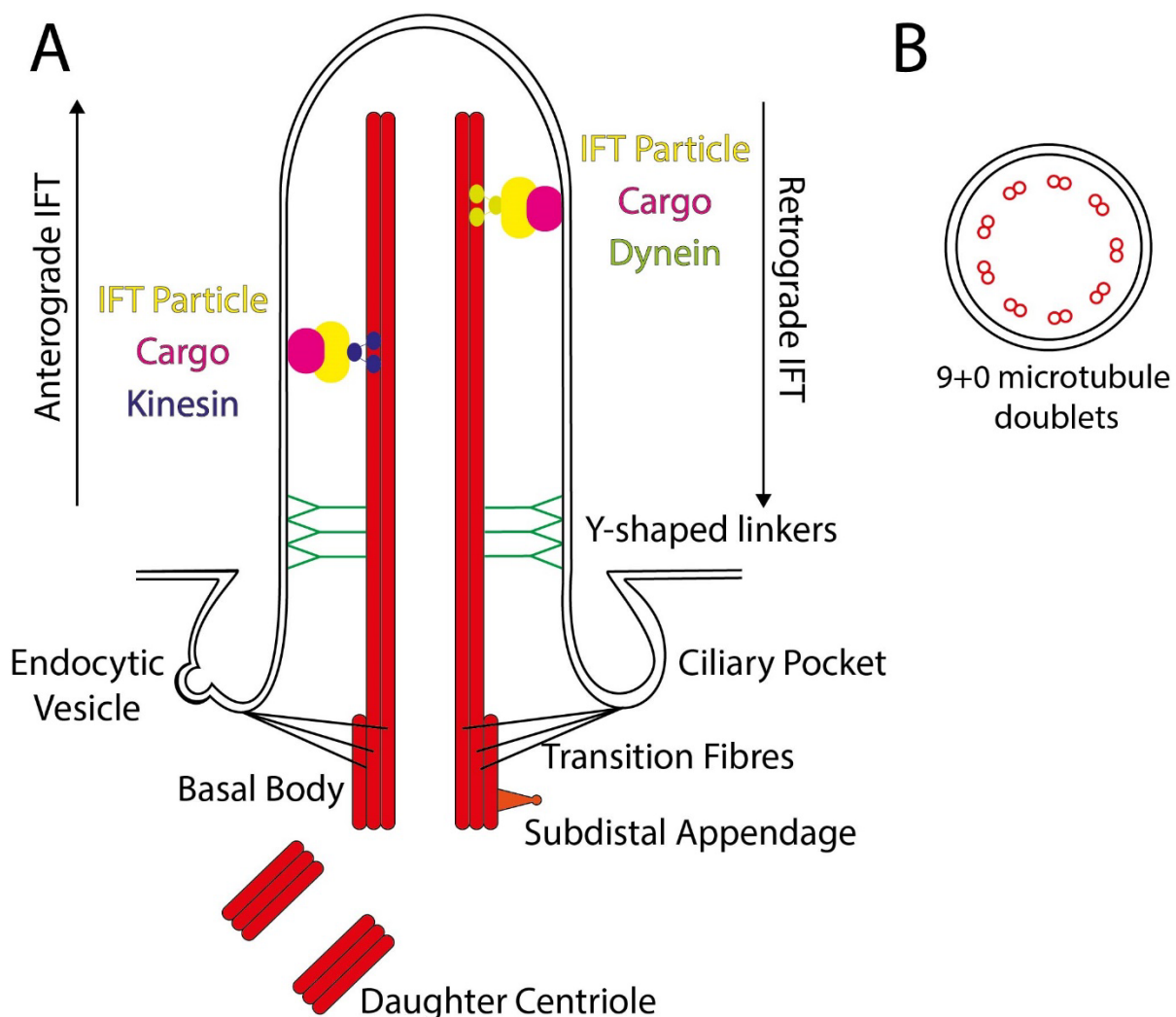


Figure 1.17: Structure of an RPE primary cilium. A) The primary cilium forms when the mother centriole docks with the apical cell surface and forms the basal body. The daughter centriole does not dock to the membrane but remains close to the basal body. The apical

membrane is depressed around the base of the cilia, this structure is an endocytic hotspot called the ciliary pocket. The basal body is connected to the apical cell surface membrane by transition fibres. Microtubules are anchored to the basal body by subdistal appendages. The region where the microtubule doublets extend away from the basal body to form the base of the ciliary axoneme is called the transition zone. In this region, Y-shaped linkers connect the ciliary axoneme to the ciliary membrane. The transition zone regulates the cargo that enters the cilium, once inside cargo is trafficked to the ciliary tip by intraflagellar transport (IFT) particles and kinesin (anterograde IFT). Cargo being trafficked from the cilia tip towards the ciliary base (retrograde IFT) is moved by dynein. **B) Transverse cross-section of the ciliary axoneme showing the 9+0 arrangement of microtubule doublets. Figure redrawn from Wheway et al., 2018.**

There are two broad classes of cilia: primary and motile. The defining characteristic is the organisation of microtubules that constitute the ciliary axoneme. Motile cilia comprise a ring of nine microtubule doublets that encircle two central microtubules (9+2 configuration) whereas primary cilia lack the central pair (9+0 configuration, **Figure 1.17 B**). Primary cilia are non-motile and act as cellular 'antennae' that can sense extracellular stimuli and regulate many cell signalling processes such as the hedgehog signalling pathway which is important for normal development (Goetz and Anderson, 2010; Malicki and Johnson, 2017).

The photoreceptor outer segment is a highly developed structure that is capable of transducing light into an electrochemical gradient. There are several structural features that are conserved between the POS and other primary cilia. At the base of outer segment is the transition zone, or connecting cilium, through which all components of the POS are trafficked. At the base of the transition zone, in the inner segment, is the basal body. The axoneme extends from the transition zone along the length of the POS. Structural and sensory components of the POS are trafficked by the IFT system.

RPE cells also possess primary cilia on the apical cell surface. The transition fibres and transition zone separate the internal space of the cilia and the ciliary membrane from the cytoplasm and plasma membrane (Garcia-Gonzalo and Reiter, 2017). Localisation of transition zone proteins within RPE cilia was disrupted in iPSC-derived retinal cells using RP11 patient lines (**Figure 1.18**). Similar results were observed upon knockdown of the ciliary components ARL3 and RP2 (Evans *et al.*, 2010; Wei *et al.*, 2012; Schwarz *et al.*, 2017).

Both the RPE and photoreceptors possess primary cilia, and, specifically, the photoreceptor outer segments are a highly specialised primary cilium. The importance of ciliary signalling in RPE function was recently investigated and it was shown that WNT and PKC delta signalling mediated by the cilia are required for the formation of tight junctions and apical-basal polarity (May-Simera *et al.*, 2018a). An interesting feature of RPE cilia is the abundance of ciliary pockets (Molla-Herman *et al.*, 2010; Ghossoub *et al.*, 2011). The ciliary pocket is associated closely with the actin cytoskeleton, transition fibres, and is enriched with proteins involved in clathrin-mediated vesicle formation (**Figure 1.17**) (Molla-Herman *et al.*, 2010). In addition, this domain closely resembles the flagellar pocket present in Trypanosomes, where it is the only membrane domain capable of endocytosing and exocytosing vesicles across the cell membrane (Ghossoub *et al.*, 2011). Given the importance of endocytosis and endoplasmic-reticulum-to-plasma-membrane transport in RPE (POS phagocytosis and visual pigment

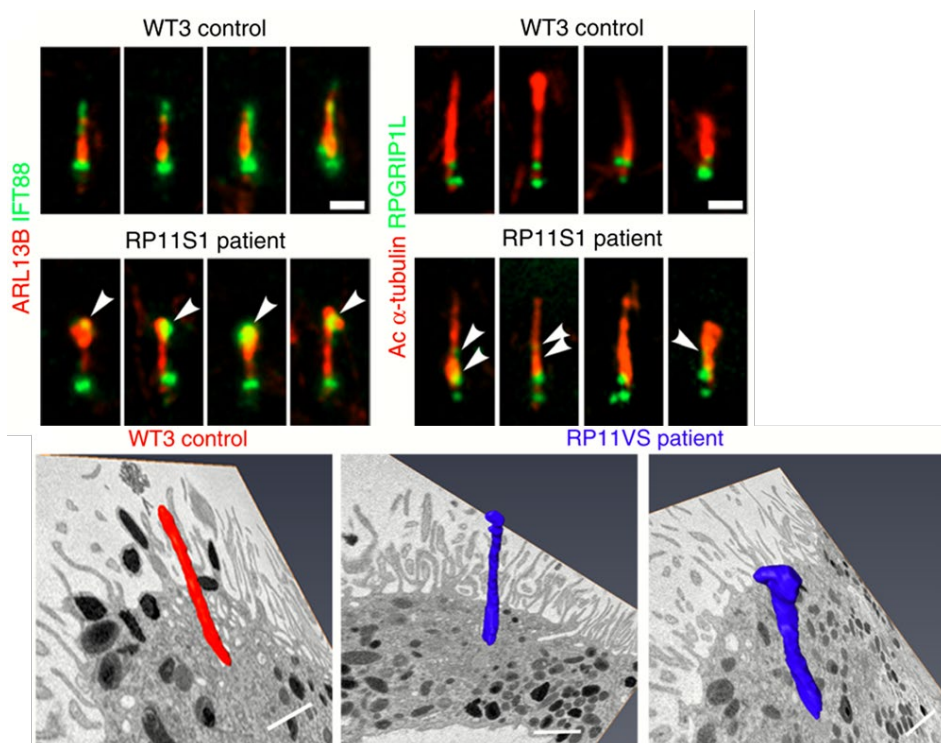


Figure 1.18: Taken from Buskin et al (2018). Ciliary disorganisation patients with PRPF-linked retinitis pigmentosa. Top panel of four shows accumulation of intraflagellar transport 88 (IFT88) at the ciliary tip and mis-localisation of retinitis pigmentosa GTPase interacting protein 1 like (RPGRIP1L) to the axoneme in patient photoreceptors. Bottom panel of three indicates similar accumulation of material at the tip of patient RPE cilia. Scale bars are 1 μ m.

recycling) and photoreceptors (trafficking of photo transduction proteins), this represents a potential function of retinal and RPE cilia that distinguishes them from other ciliated cell types.

1.7 Attempts to explore *PRPF*-linked Retinitis Pigmentosa

Early attempts to understand the mechanism by which *PRPF8* mutations lead to retinal disease were made using yeast. *PRPF8* is highly conserved from yeast to man, as is the interaction between the Jab1 domain of *PRPF8* and Brr2. Mutations in yeast *PRPF8* lead to reduced functional tri-snRNP present in the cells. More specifically, the U4/U6 RNA duplex was prematurely unwinding in tri-snRNPs containing mutant *PRPF8* C-terminal domains (Mozaffari-Jovin *et al.*, 2013). These studies suggest that RP-linked *PRPF8* mutations affect spliceosome function, but it is not clear why the retina is more susceptible to these defects.

Mouse models of *PRPF*-linked RP were reported in 2011 and 2014 (Graziotto *et al.*, 2011; Farkas *et al.*, 2014). Conservation of *PRPFs* is greater between mice and humans than between yeast and humans, perhaps contributing to these models reflecting more features of the human disease than yeast. Importantly, mice harbouring heterozygous pathogenic mutations did not display retinal degeneration or visual defects (Graziotto *et al.*, 2011). This may reflect the onset of disease seen in humans which is not observed until around ten years of life, much longer than the lifespan of laboratory mice. Mice harbouring homozygous pathogenic mutations *Prpf8*^{H2309P/H2309P} or heterozygous knockout of *Prpf31* showed evidence of retinal degeneration after 2 years of life, but no visual defect was detected (Graziotto *et al.*, 2011). Analysis of retinal ultrastructure in these mice revealed numerous abnormalities in the RPE cell layer whilst the photoreceptor cells were relatively unaffected. These abnormalities included the presence of large electron-lucent vacuoles within the RPE cells as well as an accumulation of material beneath the RPE cell layer (Graziotto *et al.*, 2011). A subsequent more detailed characterisation of the RPE cell layer revealed additional defects including a loss of epithelial cell polarity and impaired phagocytosis of POS (Farkas *et al.*, 2014).

The limited lifespan of laboratory mice may be the reason that heterozygous mutations in *PRPF8* do not cause a retinal phenotype. To address this, large animals such as pigs and non-human primates could be generated and the effect of heterozygous mutations over a longer

Introduction

time could be assessed. However, large animal models are characteristically expensive and require many ethical considerations.

Species-specific differences in the underlying mechanism of *PRPF8*-linked retinal degeneration could also explain the lack of retinal phenotype observed in mice with heterozygous *PRPF8* mutations. This can be addressed using iPSC technology which can generate human models of retinal cells with different genotypes. One limitation of this technology is genetic variability that makes it difficult to compare cultures derived from different individuals (Kilpinen *et al.*, 2017). Fortunately, recent advances in gene editing technology mean that multiple genotypes can be generated using iPSCs derived from a single individual. This approach was previously used to characterise iPSC-RPE derived from an individual with *PRPF31*-linked RP (Buskin *et al.*, 2018). These results corroborated many of the results reported in the murine model of *PRPF31* linked disease including loss of epithelial polarity, appearance of electron-lucent vacuoles and changes to phagocytosis of POS (Buskin *et al.*, 2018). There is now interest in using these models to discover new treatment for PRPF-linked RP (Brydon *et al.*, 2019)

The hypothesis of this thesis is that *PRPF8*-linked RP can be modelled using iPSC technology and the existing model of *PRPF31*-linked RP can be used to evaluate the potential of gene supplementation as a treatment.

1.8 Project Aims

- 1) Evaluate the utility of gene therapy for the treatment of *PRPF31*-linked retinitis pigmentosa using patient specific RPE. If gene therapy can rescue the RP11 phenotype *in vitro* then individuals with RP11 could benefit significantly from clinical assessment of this treatment.
- 2) From *PRPF8* patient derived iPSCs, create isogenic control cells using CRISPR/Cas9 technology. Validate all iPSCs and differentiate them to iPSC-RPE. CRISPR/Cas9 can control for genetic variability between cell donors and thus increase confidence in iPSC-based disease models.
- 3) Characterise iPSC derived RPE cells that harbour *PRPF8* mutations and identify characteristics shared with cultures harbouring *PRPF31* mutations. Characterising models of *PRPF8*-linked RP is of academic interest given that *PRPF8* is expressed ubiquitously yet mutations cause a tissue-specific phenotype.

Chapter 2. Materials and Methods

2.1 Patient Information and Ethics

All skin fibroblasts used in this study were obtained with informed consent according to the protocols approved by Yorkshire & the Humber Research Ethics Committee (REC ref. no. 03/362).

2.2 iPSC Culture

iPSC cultures were maintained on growth factor reduced Matrigel™ coated 6 well plates in media (mTESR™1 plus) at 37°C and 5% CO₂ for 5 days before passaging. Coating was applied by incubating plates overnight at 4 °C with 83 µg/ml Matrigel solution. Media was aspirated and replaced every second day during culture. Cells were passaged by aspirating media, followed by a quick wash with 1 ml phosphate buffered saline (PBS), and then released by incubating with 1 ml Versene (0.02% EDTA) for approximately 5 minutes. Once iPSC colonies were 'rounded up', 2 ml media was added to the well and cells were removed from the base of the well by gentle pipetting. The suspension was centrifuged at 300 RCF for 5 minutes. The supernatant was aspirated, and cells were resuspended in fresh media. Cells were passaged onto fresh Matrigel™ coated plates. For cryopreservation, cells were resuspended in freezing media (90% foetal bovine serum (FBS), 10% dimethyl sulfoxide and 10-µM ROCK inhibitor (Y-27632)) and stored in cryovials. Cryovials were stored at -80°C in Mr. Frosty™ Freezing Container for at least 4 hours before transfer to liquid nitrogen storage.

2.3 Spontaneous Differentiation of iPSCs to RPE

iPSCs were grown to form a confluent layer of cells in 6 well plates. Then the media was changed to RPE maintenance media (500 ml Advanced RPMI 1640, 10% knockout serum, 10 ml B27, 5 ml GlutaMAX and 5 ml penicillin streptomycin). Media was changed as required, approximately 3-5 times per week for the first 4 weeks and twice a week thereafter. Media was partially replaced; 1 ml was left in the well and 2 ml fresh media was added. Successful differentiation was apparent after approximately 6 weeks, when RPE patches began to appear in wells. These were maintained until suitable for purification.

2.4 Directed Differentiation of iPSC to RPE

Differentiation was performed as previously described (Regent *et al.*, 2019). In brief, RP13 patient-derived and RP13-Cas9 iPSCs were grown on 6 well plates coated with growth factor reduced Matrigel™, as described in (2.2). Cells were derived from three male donors. Cells were incubated at 37 °C, 5% CO₂, and fed every second day with 2 ml mTeSR™ Plus per well. Once iPSCs achieved 80-95% confluency, mTeSR™ Plus media was replaced with 3ml of differentiation medium (**Figure 2.1**) (DMEM/F-12, 50 µM β-mercaptoethanol, 1X MEM NEAA, 1X penicillin streptomycin, 20% knockout serum replacement and 10 mM nicotinamide). Differentiation media were partially changed every second day. On day 8 media composition was adjusted, from day 8-14 nicotinamide was omitted from and 100 ng/ml Activin A was added. From day 14-42, nicotinamide was omitted and 3 µM CHIR99021 was added. RPE patches formed during this time and were manually excised using a scalpel and transferred to a falcon tube containing differentiation media. Next, media was aspirated, and patches were washed quickly with PBS. Then patches were dissociated by incubation at 37 °C with TrypLE Select (10X) for approximately 20 minutes followed by passage through a 40 µm cell strainer. TrypLE Select was neutralised with RPE media and cells were centrifuged for 5 minutes at 300 RCF. Media was aspirated and replaced with fresh RPE maintenance media (DMEM/F-12, 50 µM β-mercaptoethanol, 1X MEM NEAA, 1X penicillin streptomycin, and 4% knockout serum replacement). iPSC-RPE cells were counted using a haemocytometer and plated at density of 1.5×10^5 / cm² on 6 well plates coated with growth factor reduced Matrigel™ in 3 ml RPE maintenance media. Media was partially replaced every 2-3 days until cells regained pigmentation. Then cells were dissociated using TrypLE Select (10X) as described and plated onto 24-well and 12-well PET 0.4 µm pore transwell ThinCerts™ (Greiner Bio-One, 662631) at a density of 1.5×10^5 cells / cm².

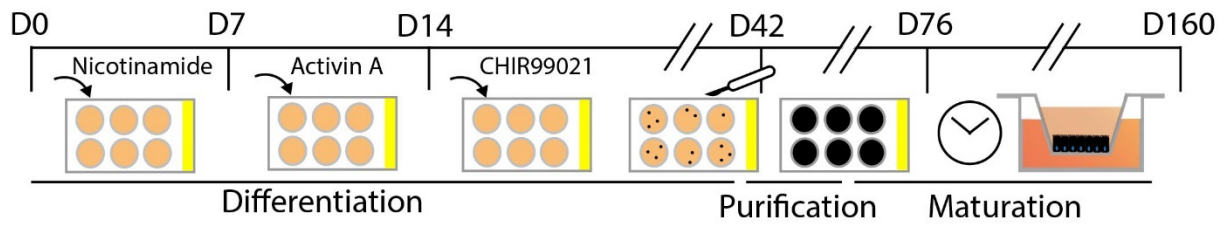


Figure 2.1: Schematic illustrating iPSC differentiation to RPE, purification and maturation on transwell inserts.

2.5 Measurement of Transepithelial Electrical Resistance (TEER)

TEER was measured using a Millicell ERS-2 Voltohmmeter (Millipore, MERS00002). Resistance measurements (Ω) were taken from a transwell insert containing RPE maintenance media only as well as inserts coated with RPE cells. The short and long electrode tips of the electrode were inserted into the apical and basolateral transwell chambers, respectively. To calculate resistance of the cell monolayer the resistance of the blank transwell was subtracted from the resistance reading of the transwells containing cells. Resistance (Ω) was then multiplied by the transwell surface area (cm^2) value to calculate the final TEER value in $\Omega \cdot \text{cm}^2$.

2.6 Transduction of iPSC-RPE Cells with Adeno-Associated Virus

PRPF31-CMV-AAV[7m8] particles were generated by the group of Professor Robin Ali and kept at -80 degrees. AAV[7m8] is a serotype that has superior transduction efficiency in iPSC-derived retinal organoids and RPE (Garita-Hernandez *et al.*, 2020). The *PRPF31* expression is driven by the cytomegalovirus (CMV) promoter as indicated in (**Figure 2.2**) and provided in full (**Supplementary Information 1**). Prior to transduction, 10 μl aliquots containing 1.18×10^{11} vector genomes (vg) were prepared in PBS and stored at -80 until use. Before use, each aliquot was thawed at room temperature and added to RPE maintenance media. The number of vector genomes required was calculated using the following equation: *Multiplicity of Infection (MOI)* = $\frac{\text{Number of Vector Genomes}}{\text{Number of Cells}}$. For example, treatment of one small transwell at an MOI of 1×10^5 : $1 \times 10^5 \text{ MOI} \times 1.5 \times 10^5 \text{ cells} = 1.5 \times 10^{10} \text{ vector genomes}$. One aliquot of AAV (1.18×10^{11} vector genomes) is sufficient to transduce ~ 7 small transwells at this MOI. The vector genomes were added to the apical portion of the transwell to a total volume of 40 μl . Eight hours later, an additional 250 μl maintenance media was added. 24 hours following application of vector genomes, media was replaced with maintenance media.

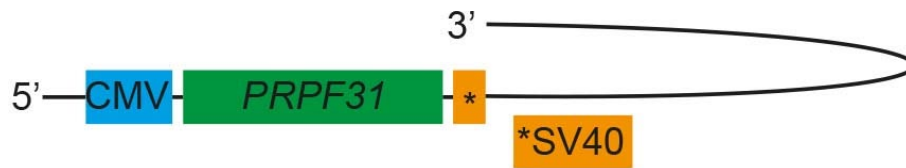


Figure 2.2: Cartoon illustrating functional regions of the *PRPF31*-AAV. CMV promoter is blue, *PRPF31* is in green, and the SV40 polyadenylation sequence is in orange.

2.7 Assessment of Transduction Efficiency by Quantitative Polymerase Chain Reaction (qPCR)

RPE were washed with PBS, mechanically removed from the plate using a cell scraper and then centrifuged. Cell pellets were kept on ice prior to RNA extraction. Cells were lysed using the RNA lysis buffer provided with the Promega Reliaprep™ RNA Cell Mini Miniprep system. RNA was extracted by following the manufacturer's instructions. In brief, following DNase digestion the lysate was passed through a column that binds nucleotides. The column was washed before the RNA was eluted in nuclease-free H₂O. Following this the mixture was treated with Turbo DNase (thermo). In brief, the mixture was incubated with TurboDNase enzyme at 37 °C before adding inactivation reagent. The mixture was centrifuged at high speed and the supernatant that contains RNA was removed using a pipette. RNA was either used immediately for cDNA synthesis or stored at -80 until cDNA synthesis was possible.

The RNA quality was evaluated using a NanoDrop 2000 Spectrophotometer and the concentration was measured using the Qubit™ RNA broad range assay kit. 1 µg of RNA was reverse transcribed into cDNA using the Promega GoScript™ Reverse Transcription system, following manufacturer's instructions.

Quantitative PCR (qPCR) was used to assess viral RNA expression using control (WT1) and patient (RP11S1) derived RPE cells. Cells were collected 2 weeks after viral transduction. The reaction was prepared using GoTaq® qPCR Master Mix and GoScript Reverse Transcriptase kit. Complementary DNA was prepared from 500 ng of RNA, qPCR primers used are detailed in (**Table 5**). The plates were run on a QuantStudio 7Flex Real-Time PCR system. The standard cycling program was used, a hot-start activation of 95°C for 5 minutes, followed by 45 PCR cycles with a 10 second denaturation step at 95°C, 30 second annealing step at 60°C and 30

second extension step at 72°C. Following amplification, a melt-curve analysis was performed from 72°C to 95°C.

Three independent experiments were done per condition and each experiment was repeated in triplicate. Control reactions that used water were run without cDNA and with water alongside the samples, were included to check for primer-dimers and possible contamination. For each experiment the average quantification cycle (C_q) was determined and used to estimate amplicon abundance. The expression of PRPF31 was normalised to GAPDH and converted to fold change using the $\Delta\Delta C_t$ method. In brief, this compares the number of PCR reaction cycles that happened before fluorescent signal was detected (C_t). The change in control gene C_t value (ΔC_t) is subtracted from the ΔC_t of the target gene to generate a $\Delta\Delta C_t$ value. This quantity is expressed in terms of PCR reaction cycles, each of which doubles amplicon abundance. The $\Delta\Delta C_t$ value is converted to fold change using the formula: fold change = $2^{-\Delta\Delta C_t}$.

Table 5 (next page): Oligonucleotide sequences of the PCR primers, guide RNAs (gRNA), and single stranded oligodeoxynucleotide (ssODN) used in this study. Off-target primers flank off-target sequences, these sequences are provided alongside the primer sequences.

Materials and Methods

Primers	Pan-PRPF31 CAGGGGCAGCAGCTGTCCGA GCCGGCCACACCCATGATCT	
	Virally Expressed PRPF31 AAGGTCAAGGGCGAGAAGAG GGGAGGTGTGGGAGGTTTT	
	Endogenous PRPF31 CTCAAGGTCAAGGGCGAGAA CAGAACCCGATCCTAGCCC	
	GFP CTGCTGCCCAGACAACCAC TCACGAACTCCAGCAGGAC	
	GAPDH GGTCACAGGCCAACCGCCTC CTCGTAGACGGTCGGGGGCA	
	PRPF8 genome cleavage detection TGGGGATGTGGGGATAGCA TAGGAAGGGGGCCTCATACTCC	
Off-target Primers and corresponding off-target sequences	PRPF8 Off-target 1 AACCACATACCCTCCCAACC ATGACCTTCCTTCTCCCTGG	Off-target Sequence 1 AGTTCTAGCACCAGATGCCC
	PRPF8 Off-target 2 CCTGTCTCTCCACGTGTTCT TGCTGAGATGGACATGGTGT	Off-target Sequence 2 AGTCCTACCACTACGTGCCC
	PRPF8 Off-target 3 GTGGTCATGATCTCGGTCCT CAGGGTGTGTGGGGTTCC	Off-target Sequence 3 AGTTCTACCACGTGGGACCC
	PRPF8 Off-target 4 GGCTAGTTCATTTTGTGTTGCA TCCCAGATTCTATACTCAGCC	Off-target Sequence 4 AGTTCTTCCACTAGGGGCCC
	PRPF8 Off-target 5 GCCTTCTCAGAAACCAGCT GACACTTCTACAGCATCAACCT	Off-target Sequence 5 AGTTTTACCAGGAGGTGCTC
Guide RNAs (gRNAs)	PRPF8 gRNA 1 GAGAGGGCCTGTGCACCTCG TGG	
	PRPF8 gRNA 2 CCCCAAAGAGTTCTACCACG AGG	
	PRPF8 gRNA 3 AGTTCTACCACGAGGTGCAC AGG	
Single Stranded oligodeoxynucleotide	PRPF8 P2309H GAAACGGTCAGGCATACAGGTCCTCCCGATCCGCAGAGTAAACCT CCCCCTCCTGCAGGAGAGCAAAGTTGAGGAAGTGAGAGGGTCTGT GCACCTCGTGGTAGAACTCTTTGGGGTTCCGCCAGCTG	

2.8 Assessment of Transduction Efficiency by Western Blot

RPE cells were washed twice with PBS then mechanically detached. Cells were centrifuged and kept on stored at -80 °C until further use. 50 µl ice lysis buffer (used previously in (Buskin *et al.*, 2018)) was added to cells collected from 2 transwells of a 12 well plate (~1 x 10⁶ cells) . Cells pellets were resuspended and kept on ice for 15 min, subsequently cells were vortexed for 15 minutes at 4°C. Next, cells were sonicated for three 5 second intervals at 0.5 W. Finally, the lysate was centrifuged at 1000 x RCF for 5 minutes and the protein fraction was collected. Protein concentration was determined using the Pierce BCA Assay by following manufacturer's instructions. In brief, this is a colorimetric assay that measures unknown protein concentration using a standard curve that is derived from protein standards. 10 µg protein per sample was linearised by 5-minute incubation at 95°C in the presence of NuPAGE™ lithium dodecyl sulphate (LDS) Sample Buffer (4x) and NuPAGE™ Sample Reducing Agent (10x). This process denatures the tertiary structure of proteins that might otherwise affect their interaction with the gel (Bolt™ 4-12% Bis-Tris Plus, Invitrogen). Linearised proteins were separated according to molecular weight using gel electrophoresis. This is possible because the LDS sample buffer endows the linearised protein with an overall negative charge.

Next the protein was transferred from the gel to a polyvinylidene difluoride (PVDF; iBlot® 2 PVDF Mini Stacks, Invitrogen) membrane using iBlot™ 2 Gel Transfer device and iBlot™ 2 Transfer Stacks. In brief, the gel is placed on the PVDF membrane, and these two layers are sandwiched within the Transfer Stack. The LDS coating gives the linearised protein an overall negative charge and so when the gel transfer device passes a current across the laminate this causes linearised protein to migrate from the gel to the PVDF membrane.

Next, the PVDF membrane was blocked using 5% w/v Marvel dried milk powder dissolved in Tris-Buffered Saline and Tween 20 (TBS-T) buffer. The membrane was submerged in the mixture and agitated for 1 hour. Protein from the milk powder binds to the membrane and reduces non-specific interaction of antibodies with the membrane that would confound results.

Following this, the PVDF was similarly incubated overnight at 4°C with TBS-T, 2% Marvel and an antibody that recognises the C-terminal domain of PRPF31. This antibody recognises the C-

terminus of PRPF31 that is present in both the wildtype and mutant protein isoform. It was made in-house by the Luhrmann group (Buskin *et al.*, 2018). This solution was then discarded, and the membrane was washed for 5 minutes three times, in 5% Marvel/TBS-T. Subsequently the PVDF membrane was submerged in 5% milk and TBST that contained a secondary antibody that was conjugated to horseradish peroxidase (HRP). The membrane was incubated and agitated for 1 hour at ambient temperature. Next the membrane was washed 3 times for 5 minutes in 5% Marvel and TBS-T. Finally, SuperSignal West Pico PLUS (ThermoFisher) chemiluminescent substrate applied to the membrane, shortly before the chemiluminescent signal was measured using a blot imager. In brief, the HRP-conjugate catalyses a bioluminescent reaction within the substrate. Therefore, the level of fluorescence is proportional to the amount of target protein present in a sample.

2.9 Mutation Validation

Genomic DNA was extracted from iPSCs using QIAamp DNA mini kit according to manufacturer's instructions. In brief, this involves lysing the cells using a cell lysis buffer. The mixture is centrifuged using a spin column that binds DNA. The spin column is washed to remove contaminants from the column. Finally, the DNA bound to the column is eluted in nuclease free water.

Primers were designed to amplify the sequence around the *PRPF8* H2309P mutation site. Forward (5'-TGGGGATGTGGGGATAGCA) and reverse (5'-GGAGTATGAGCCCCCTTCCTA) primers were selected as they produced single clean bands on analysis. For the PCR reaction, DNA was amplified using these primers at a concentration of 10 μ M, 10 μ M dNTPs, 5X GoTaq Reaction Buffer and GoTaq DNA polymerase (5 μ g/ μ l). The reaction cycled 35 times using a GeneFlow SensoQuest. Temperature changes during each cycle ensured denaturation (95°C), annealing (55°C) and synthesis (72°C) of a double stranded DNA fragment. Following this the PCR product was analysed using 2% agarose gel with GelRed™ Nucleic Acid Stain. A 1000 base pair ladder was run alongside all samples. The same fragment was used for both mutation screening and genomic cleavage detection.

PCR reaction product was purified using QIAquick PCR purification kit according to manufacturer's instructions. The concentration of DNA was quantified using a Qubit® 2.0

300 nM gRNA was incubated with 20 µl nuclease-free water, 3 µl NEBuffer 3.1 and 1 µM Cas9 Nuclease for ten minutes at 25°C. Then 3 µl of 30 nM PCR product was added and the mixture was incubated at 37°C for 15 minutes. Next 1 µl Proteinase K was added and the mixture was incubated at ambient temperature for 10 minutes. Finally, the product was analysed using 2% agarose gel containing GelRed™ Nucleic Acid Stain. DNA ladders were run alongside all samples. A total of three gRNAs with different target sequences were tested (**Figure 2.4**). However, clear results were only obtained for one gRNA following a repeat experiment. The on-target score of gRNA3 is 22/100, with 0 being no off-target effects (Doench *et al.*, 2016).

gRNA 1 (containing mutation)
GAGAGGGCCTGTGCACCTCG TGG (CCA CGAGGTGCACAGGCCCTCTC)

gRNA 2
CCCCAAAGAGTTCTACCACG AGG

gRNA 3
AGTTCTACCACGAGGTGCAC AGG

Figure 2.4: Guide RNA (gRNA) sequences that were tested using genomic cleavage detection. Two gRNAs contain the residue mutated in PRPF8 linked RP (red A). TGG and AGG codons are the PAM site recognised by Cas9. gRNA 1 is complimentary to anti-sense strand whereas gRNA 2 and gRNA are complimentary to the sense strand.

2.11 CRISPR/Cas9 Mediated Homology Directed Repair in RP13-1B iPSCs

iPSCs were cultured in mTeSR1 supplemented with 10 µM SCR7 pyrazine for 24 hours prior to nucleofection. SCR7 pyrazine is a DNA ligase inhibitor that inhibits non-homologous end joining and promotes homology directed repair of double stranded DNA breaks (Hu *et al.*, 2018). Prior to nucleofection, gRNA was synthesised using the GeneArt™ in vitro gRNA synthesis kit. Immediately before nucleofection 200 picomoles of gRNA was incubated with 100 picomoles Cas9 True Cut V2 (ThermoFisher). 1×10^6 iPSCs derived from RP13-1B (clone 3) were dissociated by incubation with StemPro Accutase (ThermoFisher) for 5 minutes. Cells were centrifuged (5 minutes 300 RCF) before being resuspended in a mixture of 100 µl 4D nucleofector P3 media (Lonza), 100 picomoles Cas9-gRNA ribonucleoprotein and 200 picomoles of the single stranded donor oligonucleotides (ssODN; sequence in **Table 5**). The mixture was transferred to a 100 µl Nucleocuvette Vessel using a Pasteur pipette, to minimise stress of cell transfer. Cells were nucleofected using a 4D-Nucleofector system (Lonza) using

parameters optimised for H9 ESCs. Then, 400 μ l of mTeSR media supplemented with 10 μ M SCR7 and 10 μ M Rock inhibitor (Y27632) was added to the nucleocuvette. Using a Pasteur pipette the suspension was added to 5 x 10 cm petri dishes that had been coated with Matrigel and filled with mTeSR supplemented with 10 μ M SCR7 and 10 μ M Y27632. The suspension was added in increasing volumes (one drops in the first plate, two drops in the second etc.). This was to ensure that the yield of cells was sufficient. Plates were then cultured for 5-7 days before colonies were passaged. Colonies that arose before this likely arose from multiple cells.

Single cell suspension was cultured following nucleofection with Cas9/gRNA ribonucleoprotein

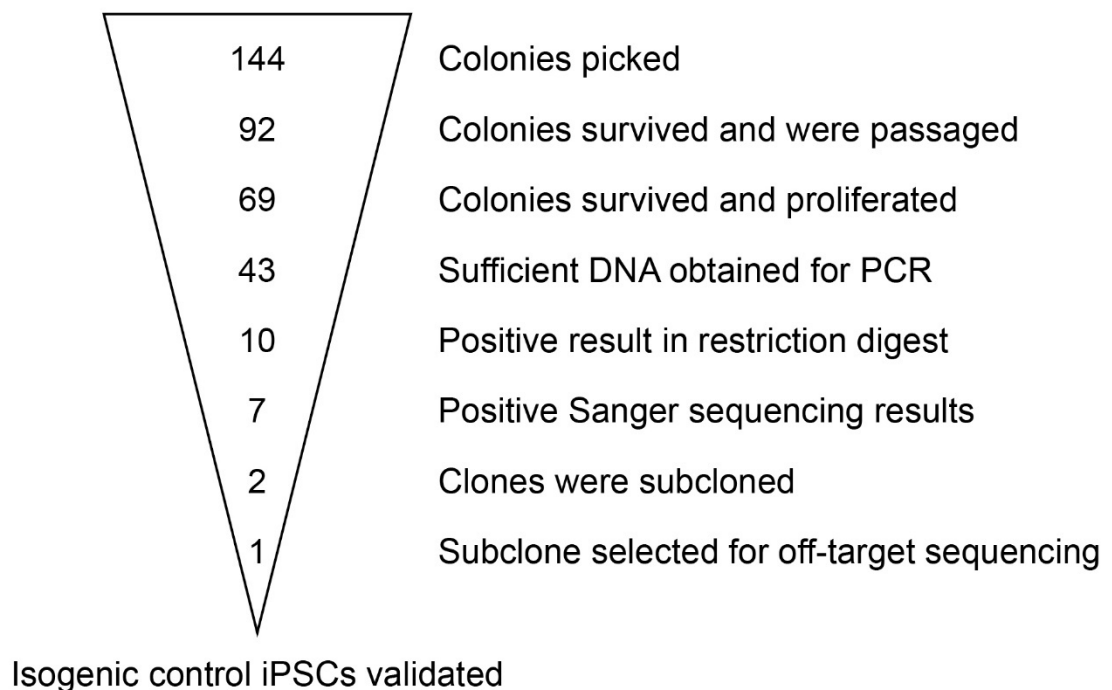


Figure 2.3: Schematic showing how one corrected iPSC clone was isolated following nucleofection with Cas9/gRNA ribonucleoprotein. 144 clones, each thought to arise from a single cell, were collected. These were then genotyped using a restriction digest and subsequent Sanger sequencing to identify 7 successfully edited iPSC clones. Of these, one was selected for in depth validation with off-target sequencing, chromosomal copy number evaluation, and confirmation of pluripotent status.

Colonies were mechanically transferred from 10 cm petri dishes to 24 well plates that were coated with Matrigel as described in (2.2). 144 colonies were picked, 92 of these proliferated successfully (Figure 2.5). Once colonies began to reach confluency they were passaged together, and samples were collected for DNA extraction. Due to variability in the rate of

growth between clones, not enough cells were obtained for passage and/or DNA extraction from all 92 clones. 69 colonies survived and were expanded (**Figure 2.5**). These were passaged and cultured for DNA extraction, samples were taken daily to ensure that enough cells were obtained for both DNA extraction and passaging. Once samples of all 69 clones were collected, DNA extraction was performed using a Wizard SV 96 Genomic DNA purification system (Promega). Quality of the DNA was assessed using a Nanodrop spectrophotometer.

For 29/69 clones, 200 ng of DNA was used and for 14/69 100 ng DNA was used to generate *PRPF8* amplicons (**Figure 2.5**). For 26/69 clones the DNA was of insufficient quality to perform PCR. The c.6926A>C *PRPF8* mutation removes an ApaLi restriction site (identified using NEBcutter V2.0 <http://nc2.neb.com/NEBcutter2/>), this feature was used to identify edited clones. PCR was performed using *PRPF8* sequencing primers as used in the genomic cleavage detection assay (35 cycles, 58 °C annealing temperature). The amplicon (602 base pairs) was incubated with 10 units ApaLi (New England Biolabs) in 1x Cutsmart buffer for one hour at 37 degrees. The mixture was separated on a 2% agarose gel. Two fragments of length 206 and 396 indicate cleavage at the ApaLi site 5'-GTGCAC-3'. A homogenous population of edited cells is indicated by the absence of a 602 bp band and presence of two bands of approximately 200 and 400 bp length. The gel was imaged using GelDoc. *PRPF8* amplicon from candidate clones was purified using the PCR Purification Kit (Qiagen) and sequenced using the Eurofins TubeSeq service. Other RP13 iPSCs were edited by Dr Chunbo Yang using the same technique.

2.12 Assessment of Pluripotency by PluriTest Assay

Two million iPSCs from each Cas9 corrected cell line were transported to ThermoFisher Scientific (USA) on dry ice. In brief, RNA was extracted from the cells and analysed using a GeneChip® microarray of 36,000 transcripts and variants. The transcriptome was analysed using PluriTest™ algorithm to generate a Pluripotency and Novelty Score.

2.13 Assessment of Chromosomal Stability

RP13-iPSCs (3 clones per donor) were screened for commonly occurring chromosomal abnormalities using the hPSC Genetic Analysis Kit (StemCell Technologies, #07550) according to the manufacturer's instructions. More specifically, the test looks for chromosomal amplifications and deletions in regions frequently observed *in vitro* (Martins-Taylor and Xu,

2012). Results were analysed using a specially designed online application (www.stemcell.com/geneticanalysisapp) using the $\Delta\Delta\text{CT}$ method to determine the relative fold gene expression. The application uses a machine learning algorithm to detect significant changes in fold-expression.

A second assay was performed on the Cas9 corrected cell lines. 2 million iPSCs from each Cas9 corrected cell line were transported to ThermoFisher Scientific (USA) on dry ice. In brief, genomic DNA was extracted from the cells and used in a microarray assay. The microarray is created by synthesising oligonucleotide probes directly onto the glass using photolithographic technology. The sample genome is used to generate complementary RNA using a T7 RNA polymerase in the presence of biotinylated ribonucleotides. After hybridisation of cRNA with the GeneChip, the array is stained with streptavidin-phycoerythrin before fluorescence is measured using a confocal scanner. The chromosomal copy number of each gene was determined using a control sample.

2.14 Analysis by Immunohistochemistry

iPSC-RPE cells grown on 24-well ThinCerts™ were washed with PBS and incubated with 4% paraformaldehyde (PFA) for 20 minutes at room temperature. PFA was then removed, cells were rinsed twice with PBS before culture surface was cut out and stored in PBS at 4 °C until required. Transwell culture surface was isolated and placed on Superfrost+ microscope slide (CellPath, MBB-0102-54A). Pigmentation of RPE cells was removed using Melanin Bleach Kit as per manufacturer's instructions. RPE cells were blocked in PBS supplemented with 10% donkey serum and 0.3% Triton-X100 (Sigma, T8787), for 1 hour at room temperature. For Ezrin, cells were not bleached Triton X-100 was substituted for a 5-minute incubation at -20 °C with methanol, prior to blocking. This was found to positively impact quality of the results and the likeness to other reports. The RPE cells were incubated with primary antibodies overnight at 4°C, antibody information is presented in **Table 6**. Following three washing with PBS, RPE cells were incubated with secondary antibodies diluted in antibody dilution (PBS and 1% donkey serum) with Hoescht for 1 hour at room temperature. Then, iPSC-RPE cells were washed 3X for 5 minutes with PBS before mounting with Vectashield and sealed with a #1 coverslip. RPE cells were imaged using an AxioImager upright microscope with Apotome

structured illumination fluorescence using 20x, 40x and 63x oil objectives (Zeiss, Germany). Images were processed using Zen imaging software (Zeiss).

2.14.1 Cilia Length and Frequency measurements in RPE Cells

Cells were blocked in 1% non-fat milk in PBS for 30 minutes then stained with ARL13B primary antibody. Images were obtained using a Nikon A1R confocal microscope with ×100 oil objective lens controlled by NIS Elements AR 4.20.01 (Nikon) software. Optical sections were generated through structured processing using NIS Elements AR 4.20.01 (Nikon) software. Images were deconvoluted using the deconvolution wizard and batch processor in Huygens software (Scientific Volume Imaging). ARL13B objects (cilia) were segmented automatically in Huygens and the object analyser was used to calculate ARL13B object (cilia) length and number. A minimum of 500 cilia from at least 3 non-overlapping fields of view were analysed per sample. Nuclei were counted manually, and ciliary incidence was calculated using number of ARL13B objects as a measure of cilia number.

2.15 Phagocytosis Assay by Flow Cytometry

Bovine POSs were obtained from a commercial vendor (InVision BioResources). In brief, bovine eyes were dissected using a scalpel under dim red light. The retina was homogenised, filtered, and ultracentrifuged. The POS separated into an orange-pink band which was collected, washed and aliquoted in DMEM supplemented with 2.5% sucrose. POS aliquots were stored at -80 °C until labelling.

2.15.1 Fluorescent Labelling of POS

Purified bovine POS were centrifuged for 4 minutes at 2600 RCF and then the supernatant was aspirated. Next the POS pellet was resuspended in 10 ml RPE maintenance media supplemented with 0.4 mg/ml FITC (Sigma). The mixture was protected from light and incubated on a shaker for one hour at room temperature. Following this, the mixture was centrifuged for 4 minutes at 2600 RCF and then the supernatant was aspirated. The pellet was resuspended in 500 µl PBS, this process was repeated twice. After the third PBS wash FITC-POS were counted using a haemocytometer. FITC-POS were then resuspended in 2.5% sucrose and PBS before storage at -80 °C.

2.15.2 Phagocytic Challenge and Preparation for Flow Cytometry

RPE cells were treated with 3×10^6 POS-FITC per transwell (20 POS per RPE cell) and incubated for 4 h at 37 °C, consistent with previous optimisation of this assay (Westenskow *et al.*, 2012). Two control experiments were performed using the control (WT1) cell line. In the first control experiment, RPE cells were challenged with the same number of non-stained POS and incubated for the same time. In the second control, RPE cells were challenged with POS-FITC and incubated for 4 hours at 4°C. At this low temperature, phagocytosis does not take place and fluorescence is the result of non-phagocytic processes.

Cells were rinsed with PBS and were detached from the wells using 200 µL of TrypLE Select (10x) for 20 minutes. TrypLE Select (10x) was removed and the cells were resuspended in FACS buffer (PBS with 2% FBS) and 5 mM Draq 5 to identify cells. After 5 minutes, the cells were centrifuged and treated with FACS buffer and 0.2% Trypan blue, to quench fluorescence of extracellular POS-FITC. After 10-minute incubation, the cells were washed several times. Cell pellets were resuspended in FACS buffer (PBS with 2% FBS) and transferred to FACS tubes. Samples were analysed immediately on an LSR Fortessa flow cytometer and at least 10,000 events were collected per sample. Results were analysed using FCS express software.

2.16 Transmission Electron Microscopy

Transwells of RPE cells were washed with PBS and fixed overnight with 2% glutaraldehyde in 0.1 M sodium cacodylate buffer at 4 °C. The samples were post-fixed in 1% osmium tetroxide, dehydrated in gradient acetone, and embedded in epoxy resin. Ultrathin sections of 70 nm thickness were picked up on copper grids, stained with uranyl acetate and lead citrate and imaged using a Philips CM100 transmission electron microscope with high-resolution digital image capture. For iPSC-RPE, ten cuboidal cells were images per sample at a magnification of 5000x. Sample identifications were created using a random number generator, images were then sent to researchers who were blind to *PRPF8* mutation. Melanosomes and vacuoles were counted manually by first importing the images into Microsoft PowerPoint. All other measurements were acquired using tools in Microscopy Image Browser (MIB, University of Helsinki).

2.17 Serial Block Face Scanning Electron Microscopy (SBF-SEM)

Cells were fixed overnight in 2% glutaraldehyde in 0.1M sodium cacodylate buffer. Once fixed, the samples were processed using the heavy metal staining protocol adapted from (Deerinck *et al.*, 2018). Briefly, samples were incubated in a series of heavy metal solutions -3% potassium ferrocyanide in 2% osmium tetroxide, 10% thiocarbohydrazide, 2% osmium tetroxide again, 1% uranyl acetate overnight, and finally lead aspartate solution. Between each step the samples were rinsed thoroughly in several changes of deionised water. Samples were dehydrated through a graded series of acetone and then impregnated with increasing concentrations of Taab 812 hard resin, with several changes of 100% resin. The samples were embedded in 100% resin and left to polymerise at 60°C for a minimum of 36 hours. The resin blocks were trimmed to approximately 0.75 mm by 0.5 mm and glued onto an aluminium pin. To reduce sample charging within the SEM, the block was painted with silver glue and sputter-coated with a 5 nm layer of gold. The pin was placed into a Zeiss Sigma SEM incorporating the Gatan 3view system, which allows sectioning of the block *in situ* and the collection of a series of images in the z-direction. Multiple regions of interest were imaged at $\times 2000$ magnification, 3000×1500 -pixel scan, which gave a pixel resolution of ~ 15 nm. Section thickness was 100 nm in the z-direction. In the resulting z-stacks, cilia were identified and segmented manually using MIB. Measurements were exported from MIB to excel for data processing and statistical analysis was performed in GraphPad Prism. Selected segmentations were imported into Amira (FEI) for construction of the 3D models.

2.18 Data Analysis

Statistical analysis was performed using Prism (GraphPad, USA). To compare variables and statistical significance between groups data was first tested normality. If data was normally distributed then either ANOVA, two-tailed Student's t-test, or paired t-test was used. Otherwise, non-parametric tests were used. Data was plotted as mean with error bars that represent standard error of the mean (SEM) unless indicated otherwise. Additional information such as that regarding N values is presented in figure legends, a minimum of 3 biological replicates were used throughout. Statistical significance was established as indicated by asterisks * $p < 0.05$, ** $p < 0.01$, *** $p < 0.001$, and **** $p < 0.0001$. Significance was defined as a p-value less than 0.05.

	SOURCE	IDENTIFIER
Antibodies		
Goat polyclonal anti-ZO-1	St John's Laboratory	STJ140055
Mouse monoclonal anti-Ezrin	Sigma-Aldrich	E8897
Rabbit polyclonal anti-collagen IV	Abcam	ab6586
Goat anti-PRPF31 N-terminus	Sigma	SAB2500828
Rabbit anti-PRPF31 C-terminus	Gift from Dr Sina Mozaffari-Jovin	
Mouse anti-HSPA2	Antibodies-online GmbH	ABIN561382
Mouse anti-GAPDH	Santa Cruz Biotechnology	
Rabbit polyclonal anti-ARL13B	Proteintech	17711-1-AP
Donkey anti-Goat Alexa 488	Life Technologies	A11055
Donkey anti-Mouse Alexa 488	Life Technologies	A21202
Donkey anti-Rabbit Alexa 546	Life Technologies	A10040
Rabbit Anti-Mouse Immunoglobulins/HRP	Agilent Dako	P0260
Polyclonal Rabbit Anti-Goat Immunoglobulins/HRP,	Agilent Dako	P0449
Chemicals, peptides, and recombinant proteins		
Knockout™ Serum Replacement	ThermoFisher Scientific	10828028
Nicotinamide	Sigma Aldrich	N0636
Activin A (E-Coli Derived)	PeproTech	120-14E
CHIR99021	Sigma-Aldrich	SML1046
TrypLE Select (10X)	ThermoFisher Scientific	A1217701
Versene Solution (EDTA)	ThermoFisher Scientific	15040066
mTesR™ Plus	StemCell Technologies	100-0276
Corning® Matrigel® Basement Membrane Matrix Growth Factor Reduced	VWR	734-0269
Melanin Bleach Kit	Polysciences	24909-1
TURBO™ DNase (2 U/μL)	ThermoFisher Scientific	AM2238
Critical commercial assays		
KaryoStat™	ThermoFisher Scientific	905403
PluriTest™	ThermoFisher Scientific	905402
Software		
Huygens Software	Scientific Volume Imaging	https://svi.nl/Huygens-Software
Microscopy Image Browser	Belevich et al., 2016	http://mib.helsinki.fi/
GraphPad Prism 9	GraphPad	https://www.graphpad.com/
Zen Pro	Zeiss	https://www.zeiss.com/microscopy/int/products/microscope-software/zen.html

RStudio		https://www.rstudio.com/
---------	--	---

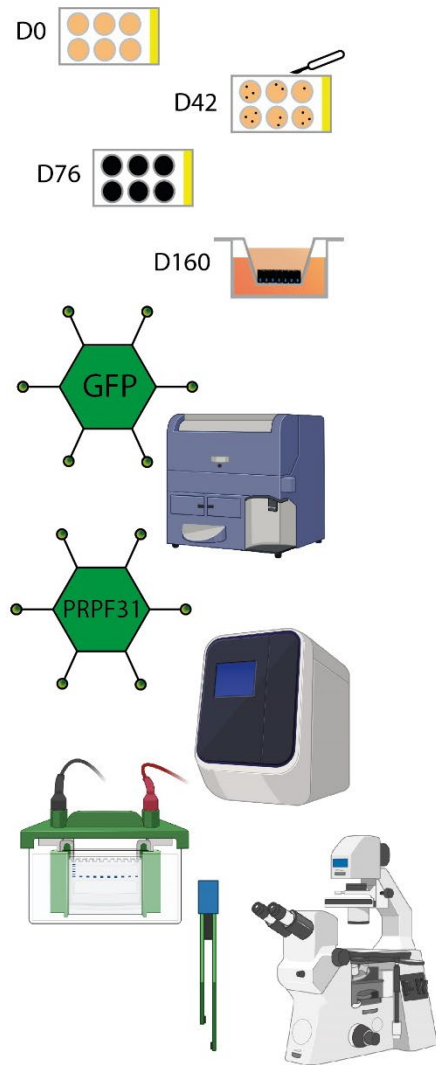
Table 6: Key Resources used in this study

2.19 Summary of Methods

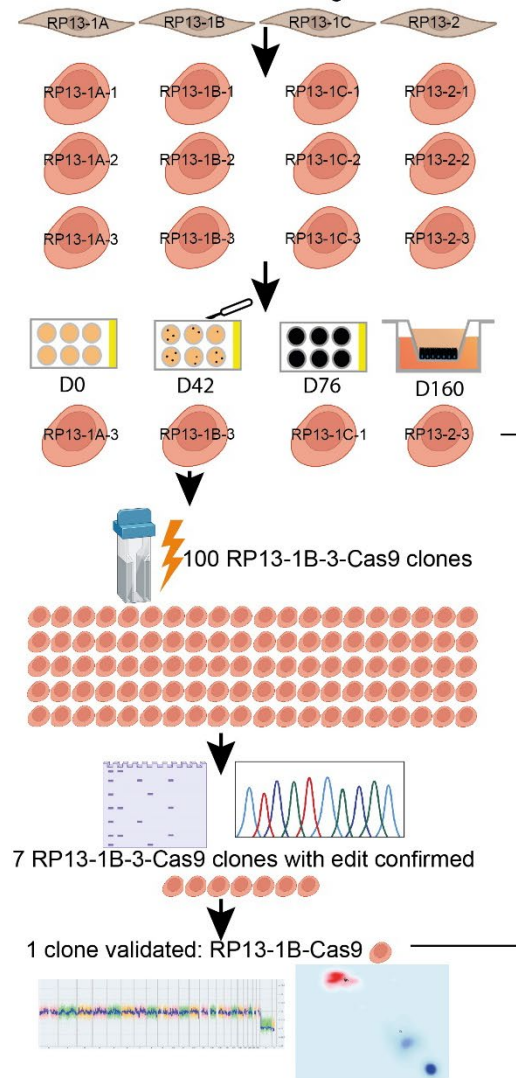
Provided below is a summary of the methods used throughout this thesis. The three results chapters are presented as three separate columns in which the methods used in each result chapter are presented (**Figure 2.6**).

Materials and Methods

3) Evaluating the Potential of *PRPF31*-AAV Gene Therapy



4) Generating Isogenic Controls of RP13 Patient-Derived iPSCs Using CRISPR/Cas9



5) Characterisation of RP13 and RP13-Cas9 iPSC-RPE Cells

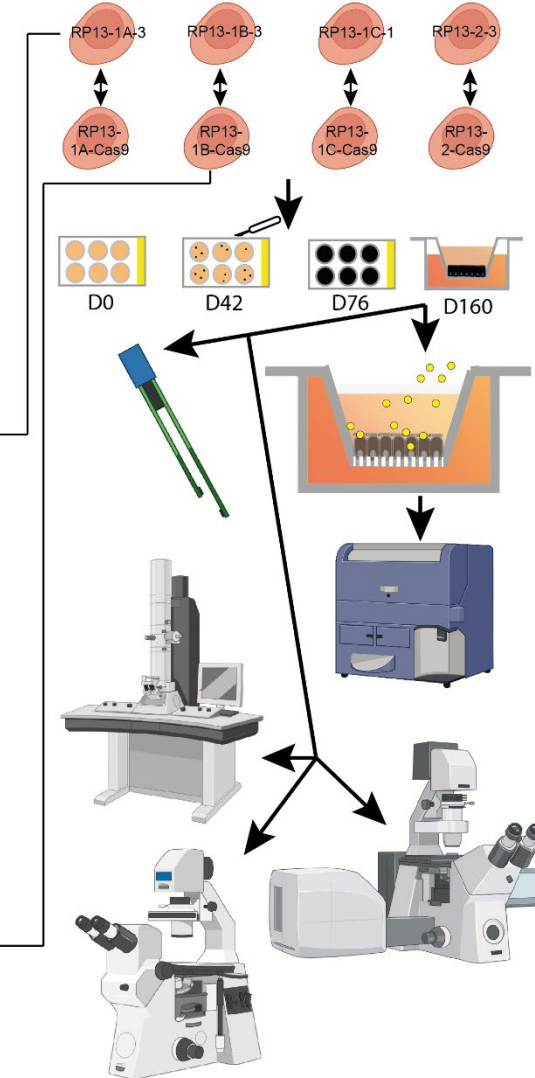


Figure 2.4: Schematic outlining the different work stands of the project. The left column illustrates Chapter 3, in which induced pluripotent stem cell-derived retinal pigment epithelium (iPSC-RPE) are differentiated and then transduced with adeno-associated virus encoding green fluorescent protein GFP-AAV or *PRPF31* (*PRPF31*-AAV). The effect of these viruses was assessed using flow cytometry, quantitative PCR (qPCR), western blot, transepithelial electrical resistance (TEER), and immunofluorescence microscopy. The middle column illustrates the 12 iPSC lines that were differentiated in Chapter 4 as well as the subsequent nucleofection and selection of an isogenic control. The right column is a schematic of the work carried out in Chapter 5. In brief, the iPSC lines that differentiated efficiently in Chapter 4 and the respective isogenic controls were differentiated to iPSC-RPE both groups of cells were then compared against to another in a range of assays using flow cytometry, TEER, transmission electron microscopy (TEM), confocal microscopy, and immunofluorescence microscopy.

Chapter 3. Evaluating the Potential of *PRPF31*-AAV Gene Therapy

3.1 Introduction

Retinitis pigmentosa (RP) is the most common form of inherited vision loss, affecting 1 in 4000 people (Hartong, Berson and Dryja, 2006). Up to 40% of cases are the result of autosomal dominant inheritance (adRP), where a mutation is inherited from one parent (Hartong, Berson and Dryja, 2006). Rhodopsin is the gene most commonly linked to adRP, accounting for around 25% of cases (Hartong, Berson and Dryja, 2006). The second most common is *PRPF31* which account for 5-10% of adRP cases (Xu *et al.*, 2012; Sullivan *et al.*, 2013; Whewey *et al.*, 2020). A wide range of mutations in *PRPF31* can lead to RP (RP11) with over 170 variants identified to date (Rose and Bhattacharya, 2016; Whewey *et al.*, 2020).

Mutations in *PRPF31* occur throughout all regions of the gene (Whewey *et al.*, 2020). A review of genotype-phenotype data suggests that nonsense mutations in *PRPF31* cause earlier disease onset (Whewey *et al.*, 2020). Interestingly, the presence of a mutation is not sufficient to predict disease onset. In asymptomatic individuals, *PRPF31* expression is higher than in symptomatic individuals (Rivolta *et al.*, 2006). This variable *PRPF31* expression is controlled by regulatory factors such as *CNOT3* and *MSR1* repeats (Rose *et al.*, 2017). Collectively, these data suggest that haploinsufficiency is the primary mechanism by which *PRPF31* mutations cause RP11.

In theory, haploinsufficiency can be rescued through supplementation of the missing gene. However, this approach was not used clinically until Luxturna was approved by the FDA in 2017. Luxturna is an AAV2 capsid containing the *RPE65* gene driven by a CAG promoter. The CAG promoter is a hybrid promoter caused by fusing elements of the CMV and chicken β -actin promoters. This was proof that gene supplementation can treat genetic disease. More so, Luxturna supplements *RPE65* to the RPE cells of patients with Leber congenital amaurosis type 2 (LCA2), an inherited retinal disease. This suggests the RPE cells of patients with RP11 can be supplemented with *PRPF31* to prevent vision loss. Indeed, a recent report gave evidence to support this by using a CRISPR/Cas9 *PRPF31*^{+/-} iPSC-RPE model (Brydon *et al.*, 2019).

There are several reports of stem cell derived RPE cells being transduced with AAVs (**Table 7**). All these use variants of the AAV2 capsid that is approved as part of Luxturna. Some of these variants, such as AAV2-Anc80 and AAV2-[7m8], have improved transduction efficiency over earlier versions. A range of promoters have also been tested; most are broadly active. The CMV promoter can be used unmodified, spliced with a portion of the chicken β -actin promoter to create a CAG promoter, or modified by incorporating elements of the Ubiquitin C enhancer to create the CASI promoter. By comparing studies that use different combinations of these elements some modified AAV2 capsids in combination with broad spectrum promoters can achieve ~70% GFP+ cells following transduction with ~100,000 vector genomes / cell (AKA multiplicity of infection (MOI)) of GFP-AAV (**Table 7**). However, this is variable between studies, with only 12% transduction being reported in (Garita-Hernandez *et al.*, 2020). Therefore, it is important to determine the transduction efficiency before investigating the potential of therapeutic AAVs such as PRPF31-AAV.

Article	Goncalves-Cordero et al., 2018	Brydon et al., 2019	Garita-Hernandez et al., 2020
Tissue	Mouse ESC-RPE	Human iPSC-RPE	Human iPSC-RPE
Serotype(s) Tested	AAV2/2, AAV2/9, AAV2/8, AAV2/8(Y733F), AAV2/5, and AAV2-ShH10	AAV2/2, AAV2/5, and AAV2/Anc80	AAV2, AAV2-[7m8], AAV8, and AAV9
Optimal Serotype	AAV2/5 and AAV2/ShH10	AAV2/Anc80	AAV2-[7m8]
Promoter(s) Tested	CMV	CMV and CASI	CAG
Optimal Promoter	CMV	CASI	CAG
Target Gene(s)	<i>GFP</i>	<i>Prpf31</i> and <i>GFP</i>	<i>GFP</i>
MOI(s) Tested	167,000	25,000-100,000	200,000
Optimal MOI	167,000	50,000-100,000	200,000
GFP-AAV Incubation Period(s)	1 week	2, 4, and 8 weeks	4 weeks
% GFP+ RPE Cells	up to 71%	up to 80%	up to 12%

Table 7: Table with details of the adeno-associated viruses (AAVs) and transduction protocols used to transduce retinal pigment epithelium (RPE) cells derived from either embryonic or induced pluripotent stem cells (ESCs, or iPSCs, respectively). Results from three articles (Gonzalez-Cordero *et al.*, 2018; Brydon *et al.*, 2019; Garita-Hernandez *et al.*, 2020) are presented/ Each study tested multiple variants of the AAV2 capsid in combination with one or more broad spectrum promoters. All studies included an AAV encoding green fluorescent protein (GFP-AAV) which allows comparison of transduction efficiency across studies. MOI = multiplicity of infection or vector genomes per cell. The GFP-AAV incubation period indicates the time between addition of AAV and analysis of GFP signal.

There is emerging evidence that *PRPF31* mutations cause production of mutant PRPF31 protein that accumulates in the cytoplasm of RPE cells (Bryant *et al.*, 2019; Valdés-Sánchez *et al.*, 2019; Georgiou *et al.*, 2022). Whilst all RP11 is thought to be caused by haploinsufficiency there is now evidence that mutant *PRPF31* protein could add to disease severity. However, perhaps due to limited patient numbers, there is no clinical data suggesting distinct *PRPF31* mutations cause different disease severities. Given the potential toxicity of mutant protein it is not clear how efficacious gene supplementation will be in those patients. If the mechanism is not just haploinsufficiency, those patients are less likely to benefit from gene supplementation.

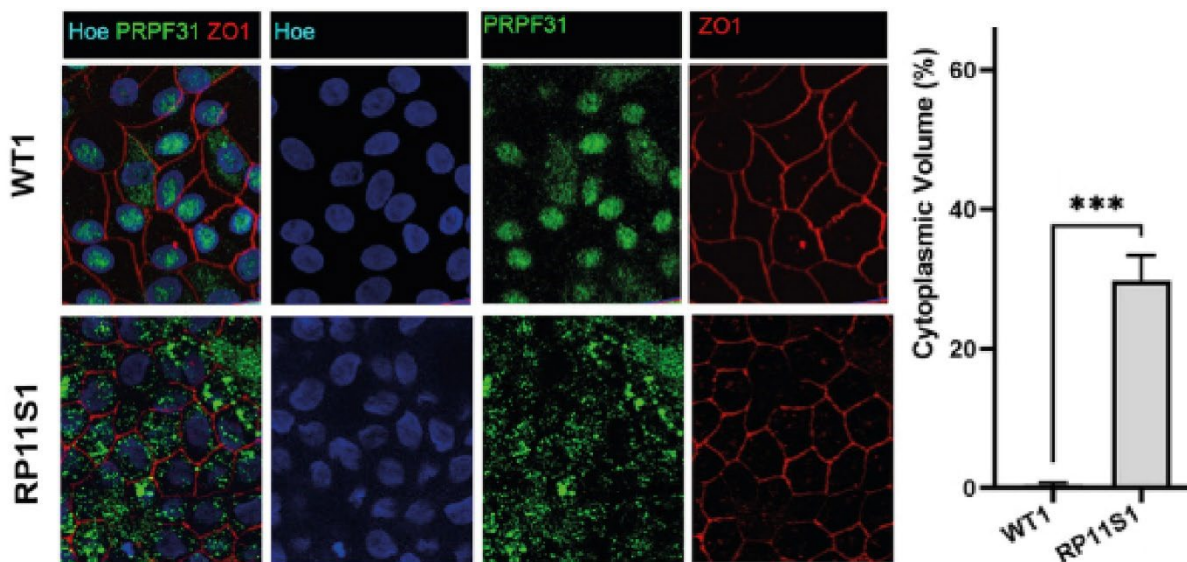


Figure 3.1: Immunofluorescence images showing cytoplasmic localisation of pre-mRNA processing factor 31 (PRPF31) in patient -derived retinal pigment epithelium (RPE) cells. RPE cells derived from an individual without RP (WT1, wildtype) and an individual with a severe form of RP caused by PRPF31 mutation (RP11S1) were immunostained with anti-PRPF31 N terminus (green) and anti-zona occludens 1 (ZO1, red) antibodies. Cell nuclei were counterstained using hoescht (blue). Quantitative analysis showed PRPF31 localised mainly in the nucleus of control RPE cells, whereas in RP11S1-RPE cells, PRPF31 protein was in the cytoplasm in an aggregate- like pattern. Data taken from Georgiou *et al.*, 2022.

This chapter builds on a previous report by the Lako group that characterised iPSC-RPE cells derived from an RP11 patient (RP11S1) with c.1115_1125 del11 *PRPF31* mutations (Buskin *et al.*, 2018). A mutant PRPF31 protein accumulates in the cytoplasm of RP11S1 iPSC-RPE cells

and may contribute to disease (**Figure 3.1**) (Georgiou *et al.*, 2022). However, there is no clinical evidence to support the hypothesis that some symptomatic *PRPF31* genotypes are more severe than others. Given the reported haploinsufficiency and our recent work showing reduced protein expression and inability of mutant protein to be incorporated in the spliceosome, we hypothesised that overexpression of PRPF31 in RPE cells would reduce the cellular and functional RP11 RPE phenotypes. In this chapter, RP11S1 iPSC-RPE cells were transduced with *PRPF31*-AAV before being characterised. This report shows that *PRPF31*-AAV rescued *PRPF31* expression, cilia length and phagocytic function in RP11S1 iPSC-RPE cells, corroborating data obtained following *PRPF31*-AAV transduction of *PRPF31*^{+/-} iPSC-RPE cells (Brydon *et al.*, 2019). These results suggest that *PRPF31* gene therapy could be used to treat RP11 patients who express mutant PRPF31 protein as well as those who do not.

3.2 Aims

The chapter aims to characterise the effect of *PRPF31*-AAV transduction on RP11S1 iPSC-RPE cells by:

- Optimising AAV transduction efficiency using *GFP*-AAV
- Determining whether *PRPF31*-AAV can upregulate *PRPF31* transcript in RP11 iPSC-RPE
- Examining whether *PRFP31*-AAV can upregulate PRPF31 protein in RP11 iPSC-RPE
- Investigating whether *PRFP31*-AAV can rescue the RP11 iPSC-RPE phenotype
 - Is cilia length or cilia incidence restored?
 - Is photoreceptor outer segment phagocytosis rescued?
 - Are cytoplasmic aggregates reduced?
- Exploring whether there is a toxic effect of AAV transduction on iPSC-RPE

3.3 AAV2-[7m8] (AAV) Transduces iPSC-RPE

Previously, iPSC-RPE cells derived from RP11 patients were characterised (Buskin *et al.*, 2018). The results showed that the cells harbouring *PRPF31* mutations had reduced phagocytic ability, TEER (Section 2.5) and cilia length- relative to wildtype controls (Buskin *et al.*, 2018). A follow up study then identified the presence of cytoplasmic aggregates within these same cells (Georgiou *et al.*, 2022). This study aims to rescue this phenotype by supplementing RP11S1 iPSC-RPE cells with additional *PRPF31* using AAV technology.

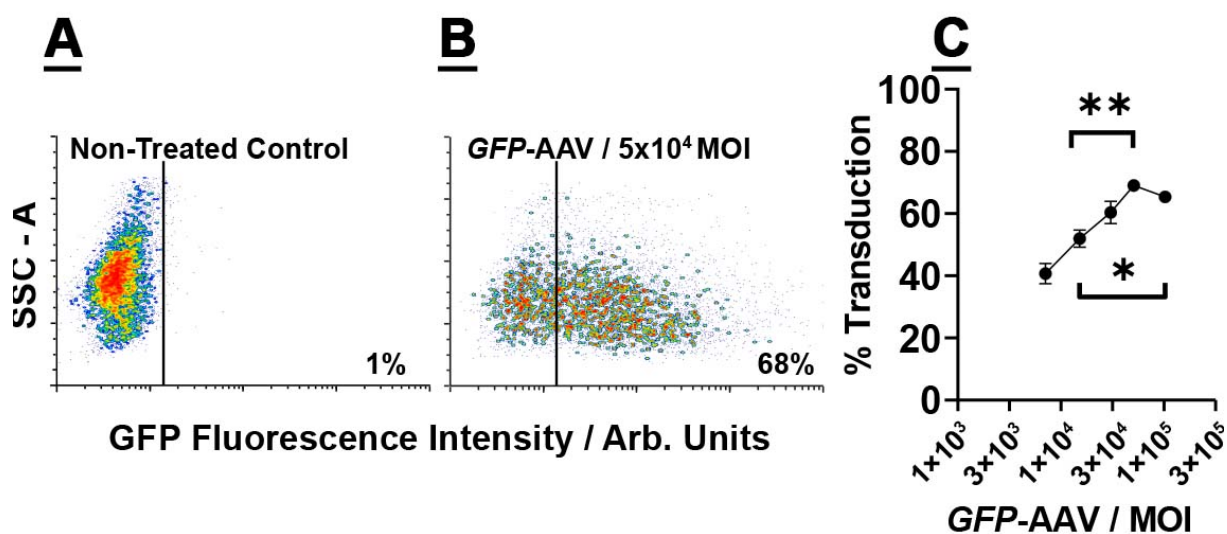


Figure 3.2: Efficiency of adeno-associated virus serotype [7m8] encoding green fluorescent protein (*GFP-AAV2*-[7m8]) transduction in F018 (wild type) induced pluripotent stem cell derived retinal pigment epithelium (iPSC-RPE) cells. A) Flow cytometry scatter plot showing side scatter (SSC-A; cell granularity) and GFP fluorescence in non-treated iPSC-RPE cells. B) Similar iPSC-RPE cells treated with a multiplicity of infection (MOI) of 5×10^4 *GFP-AAV2*-[7m8]. The black line in the plots is the fluorescence threshold. The number in the bottom right of the plots is the percentage of cells which are fluorescent. C) Line graph showing average percentage transduction at five MOIs of *GFP-AAV2*-[7m8], MOI is plotted on a logarithmic scale. Data was analysed using one-way ANOVA and post-hoc Tukey multiple comparisons. To avoid over-plotting, two results of multiple comparisons are shown: 5×10^4 MOI and 1×10^5 MOI had a significantly greater transduction efficiency than 2.5×10^4 MOI. Statistical significance is indicated by *, $p < 0.05$ and **, $p < 0.01$. Results are mean \pm standard error of the mean (SEM) and $n = 3$ experiments per condition, where n are discrete transwells derived from the same donor. A minimum of 10,000 events per experiment were collected.

Wildtype iPSC-RPE cells were transduced with a range of *GFP-AAV2*-[7m8] (*GFP-AAV*) doses to measure transduction efficiency. Transduction efficiency was quantified two weeks later using flow cytometry. This showed that the AAV2-[7m8] serotype (herein referred to as AAV) is significantly more efficient at 5×10^4 MOI and 1×10^5 MOI than 2.5×10^4 MOI (Section 2.6)

(**Figure 3.2**). On each transwell insert there are 1.5×10^5 cells and so this equates to 7.5×10^9 and 1.5×10^{10} vector genomes per transwell, respectively. The toxicity of these transductions was not assessed but this could have been achieved for example, by measuring release of lactate dehydrogenase.

3.4 PRPF31-AAV Increases PRPF31 mRNA Expression

After using GFP-AAV to assess the transduction efficiency of the AAV2-[7m8] serotype in wildtype iPSC-RPE cells, we investigated whether PRPF31-AAV2-[7m8] (PRPF31-AAV) could upregulate PRPF31. RP11S1 iPSC-RPE cells were transduced with either PRPF31-AAV or GFP-AAV at 5×10^4 MOI or 1×10^5 MOI (7.5×10^9 and 1.5×10^{10} vector genomes per transwell).

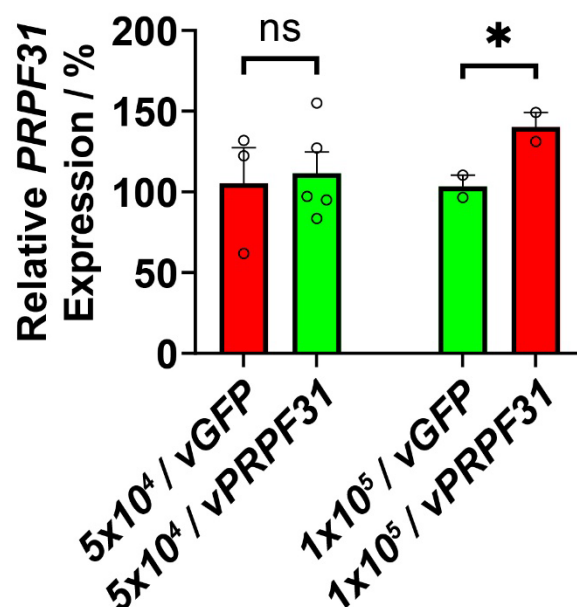


Figure 3.3: Expression level of PRPF31 in induced pluripotent stem cell derived retinal pigment epithelium (iPSC-RPE) measured using quantitative PCR (qPCR) following treatment with adeno associated viruses encoding either green fluorescent protein (GFP-AAV) or PRPF31, (PRPF31-AAV). This experiment was performed using iPSCs derived from an individual with retinitis pigmentosa type 11, caused by PRPF31 mutation, referred to as RP11S1. Treatment with an MOI PRPF31-AAV at a multiplicity of infection (MOI) 5×10^4 did not affect PRPF31 expression. Treatment with 1×10^5 MOI PRPF31-AAV increased PRPF31 expression by 37%. Statistical significance was assessed using an unpaired t-test and indicated using ns, not significant and *, $p < 0.05$. Results are mean \pm standard error of the mean (SEM) of three independent experiments ($n = 3$ where n is an experiment that transduces one transwell) with three repeat observations per experiment.

PRPF31 expression was determined using qPCR and the results show that 1×10^5 MOI *PRPF31*-AAV increased *PRPF31* expression by 37% (Figure 3.3). And so subsequently, all future transductions performed on RP11S1 iPSC-RPE cells used an MOI of 1×10^5 .

3.5 *PRPF31*-AAV Does Not Affect PRPF31 Protein Expression

After confirming *PRPF31*-AAV could upregulate *PRPF31* RNA, we investigated whether this was translated at the protein level. iPSC-RPE cells were transduced with *PRPF31*-AAV and collected for western blot analysis after 14 days.

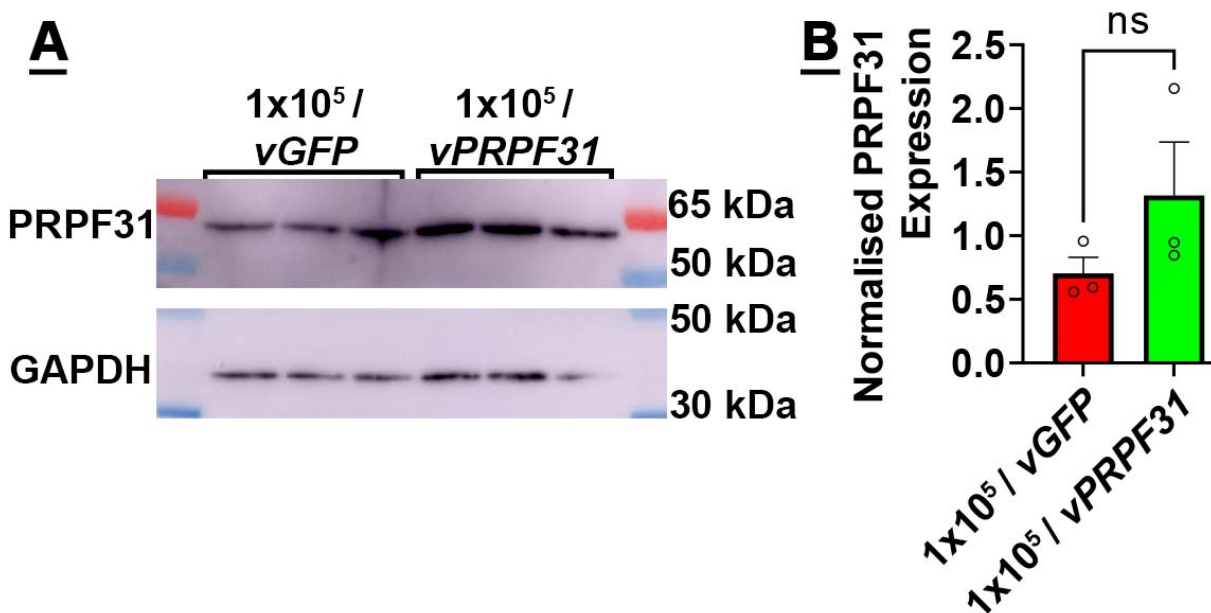


Figure 3.4: PRPF31 western blot following adeno associated virus (AAV) transduction in induced pluripotent stem cell derived retinal pigment epithelium (iPSC-RPE) cells and quantification. Cells originally derived from an individual with retinitis pigmentosa type 11, caused by *PRPF31* mutation, referred to as RP11S1. A) Western blot showing expression of full length PRPF31 and GAPDH which was used as a loading control. Above the blot are labels showing which lysates come from cells treated with AAV encoding green fluorescent protein (GFP-AAV) or *PRPF31* (*PRPF31*-AAV). Both AAVs were administered at a multiplicity of infection (MOI) of 1×10^5 vectors per cell. B) Bar chart showing the expression of PRPF31 relative to GAPDH (87% increase following *PRPF31*-AAV transduction). Statistical significance was assessed using Student's unpaired t-test, ns indicates not significant. Results are mean \pm standard error of the mean (SEM) of 3 independent experiments (separate transductions).

Expression of PRPF31 was normalised to GAPDH and result was analysed statistically (**Figure 3.4**). *PRPF31*-AAV treatment did not lead to a statistically significant increase in PRPF31 protein expression, although there was a trend for increased expression (87% increase).

3.6 Cilia Length but not Cilia Incidence is Rescued by *PRPF31*-AAV

As western blot provides a semi-quantitative assessment of protein expression, we investigated whether their evidence of phenotypic rescue in RP11S1 iPSC-RPE cells. Previous characterisation of RP11 iPSC-RPE cells identified reduced cilia length and incidence as a feature of the disease (Buskin *et al.*, 2018).

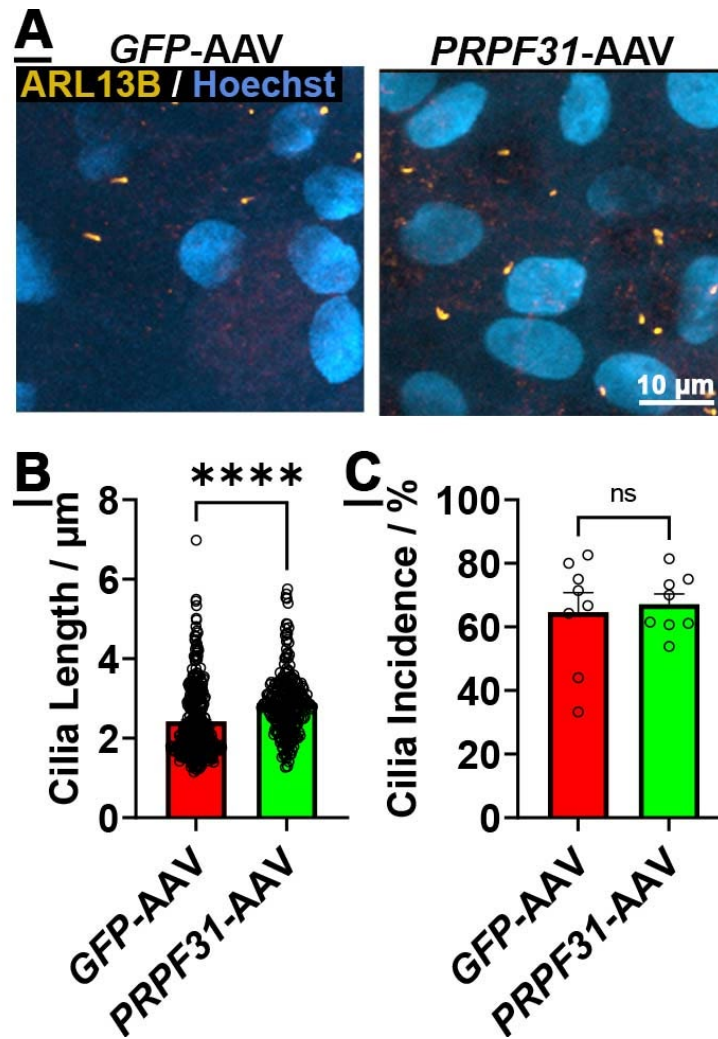


Figure 3.5: Quantification of cilia length and incidence using ADP ribosylation factor like GTPase 13B (ARL13B) immunofluorescent images. A) Example immunofluorescent image of induced pluripotent stem cell derived retinal pigment epithelium (iPSC-RPE) treated with adeno-associated virus (AAV) encoding either green fluorescent protein (*GFP-AAV*) or *PRPF31-AAV*. Both AAVs were administered at a multiplicity of infection (MOI) of 1×10^5 vectors per cell. Cells originally derived from an individual with retinitis pigmentosa type 11, caused by *PRPF31* mutation, referred to as RP11S1. B) Bar chart showing average cilia length per sample, $n > 250$ per sample where n is number of cilia. C) Bar chart showing average cilia incidence per sample. $n = 8$ where n is fields of view. Statistical significance was assessed

using Student's unpaired t-test and indicated with ns, not significant and ****, $p < 0.0001$. Results are mean \pm standard error of the mean (SEM).

Cilia length and incidence were determined through quantitative analysis of ARL13B immunofluorescence microscopy. The results show that cilia length increased following *PRPF31*-AAV treatment, but cilia incidence was unaffected (**Figure 3.5**).

3.7 iPSC-RPE Phagocytic Function is Rescued by *PRPF31*-AAV

Given the positive effect of *PRPF31*-AAV treatment on cilia length we continued evaluation of the treatment by assessing iPSC-RPE phagocytic function. This is a key function of the RPE *in vivo* that is necessary for photoreceptor survival.

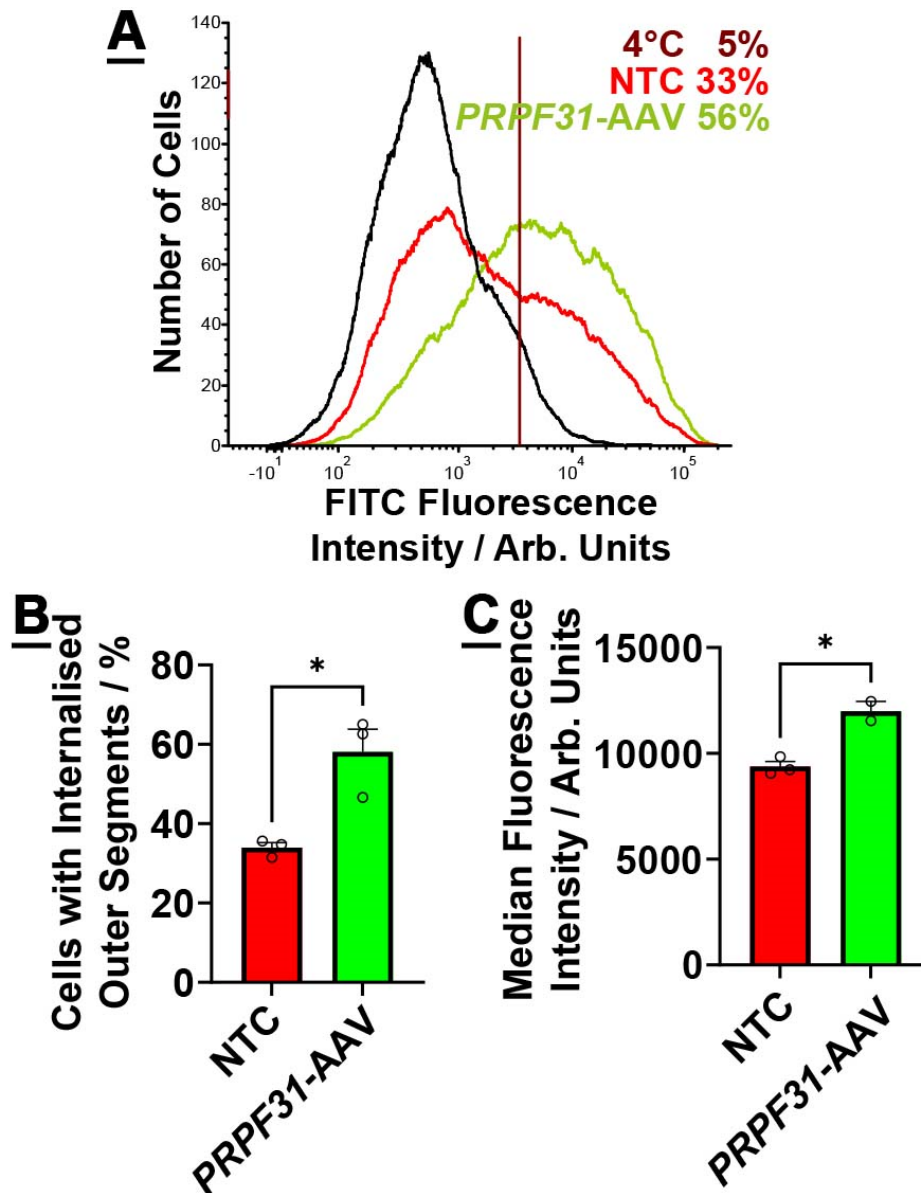


Figure 3.6: Effect of adeno-associated virus (AAV) encoding *PRPF31* (*PRPF31-AAV*) transduction on induced pluripotent stem cell derived retinal pigment epithelium (iPSC-RPE) phagocytosis of fluorescein isothiocyanate (FITC)-labelled photoreceptor outer segments (POS). Cells were originally derived from an individual with retinitis pigmentosa type 11, caused by *PRPF31* mutation, referred to as RP11S1. A) Flow cytometry histogram showing number of cells across a range of FITC fluorescence intensities. Cells challenged at 4 °C were used as a non-phagocytic control. This allowed identification of a fluorescence level associated with phagocytosis (black vertical line). The percentage of phagocytic cells treated without (red) and with *PRPF31-AAV* treatment (green) could then be calculated. Results shown are three merged experiments. B) Bar chart showing the percentage of RP11S1 cells that phagocytosed POS with and without *PRPF31-AAV* treatment. C) Bar chart showing the median fluorescence intensity of phagocytic iPSC-RPE cells following POS challenge. Statistical significance was assessed using Student's t-test, significance is indicated by *,

$p < 0.05$. Results are mean \pm standard error of the mean (SEM) of three independent transduction experiments.

Phagocytic cells were identified as those which with a higher FITC fluorescence than the non-phagocytic control. Cells challenged at 4 °C were used as the non-phagocytic control, as phagocytosis is dramatically reduced at this temperature. RP11S1 iPSC-RPE phagocytic function improved following *PRPF31*-AAV transduction. This is evident from the increased proportion of cells which internalised POS (cells that were fluorescent) as well as the increased fluorescence intensity of those cells (**Figure 3.6**).

3.8 *PRPF31*-AAV Treatment Reduces Protein Aggregation

Previous characterisation of RP11 iPSC-RPE has shown that heat-shock protein A2 (HSPA2) and mutant PRPF31 aggregate in the cytoplasm of RP11S1 iPSC-RPE cells (Georgiou *et al.*, 2022). To determine whether these aggregates are affected by *PRPF31*-AAV transduction, localization of HSPA2 and PRPF31 was determined by immunofluorescence microscopy, was performed with assistance from Dr Maria Georgiou.

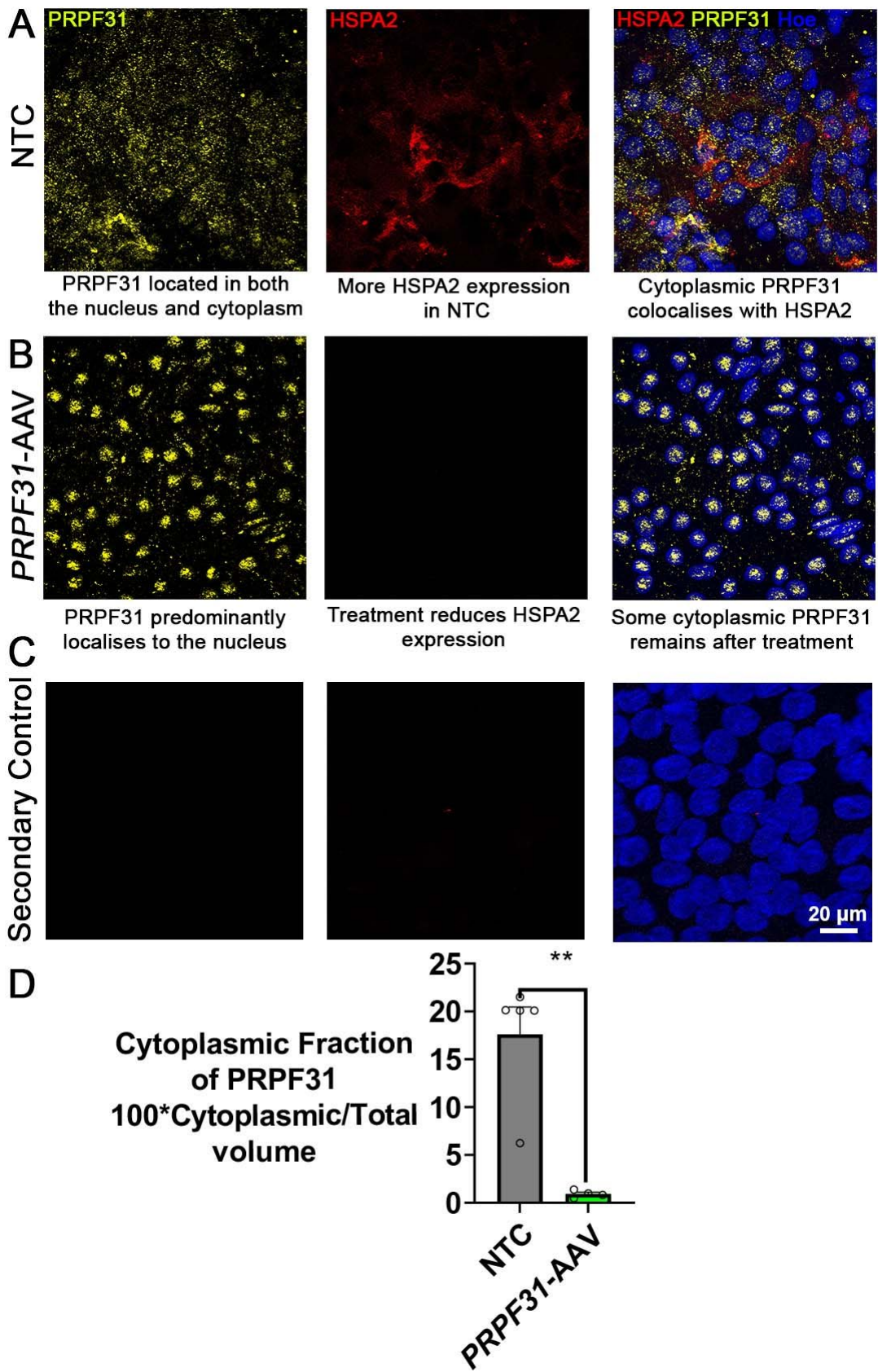


Figure 3.7: Representative images showing cytoplasmic aggregates present within the cytoplasm of induced pluripotent stem cell derived retinal pigment epithelium (iPSC-RPE) cells. Cells were originally derived from an individual with retinitis pigmentosa type 11, caused by *PRPF31* mutation, referred to as RP11S1. A) Images from non-treated control (NTC) iPSC-RPE cells shows PRPF31 protein (yellow) colocalises with heat shock protein A2 (HSPA2) (red) in the cytoplasm. B) After transduction with adeno-associated virus encoding *PRPF31* (*PRPF31*-AAV), there is a decrease in cytoplasmic signal and increased amount of PRPF31 in the nuclei. C) Secondary control showing minimal signal is caused by incubation with secondary antibodies. D) Bar chart showing the relative level of PRPF31 in the cytoplasm compared to the nucleus in non-treated and *PRPF31*-AAV treated iPSC-RPE. N= 5 where n are non-overlapping fields of view. Statistical significance was assessed using Student's t-test, significance is indicated by **, $p < 0.01$. Results are mean \pm standard error of the mean (SEM).

This suggests that the location of PRPF31 shifts from predominantly cytoplasmic to predominantly nuclear (**Figure 3.7**). HSPA2 was reduced following *PRPF31*-AAV treatment although some cytoplasmic aggregates persisted.

3.9 AAV Treatment Reduces Barrier Function but does not Cause Cell Death

After investigating the effect of *PRPF31*-AAV transduction on the RP11 iPSC-RPE phenotype, we assessed AAV-associated toxicity. This was done by measuring apoptosis using caspase 3 immunofluorescence microscopy. In addition, measurements of barrier function with TEER were interpreted as evidence of cellular stress. Caspase 3 is translated as a proenzyme and is activated during apoptosis. The active form caspase 3 can translocate into the nucleus whereas the inactive form localises to the cytoplasm (Georgiou *et al.*, 2022). Caspase 3 staining was performed with Dr Maria Georgiou who assisted with staining, image acquisition and image processing. These experiments were performed 4 weeks after AAV transduction, following a discussion with Professor Robin Ali, who's group works extensively with this technology (Gonzalez-Cordero *et al.*, 2018).

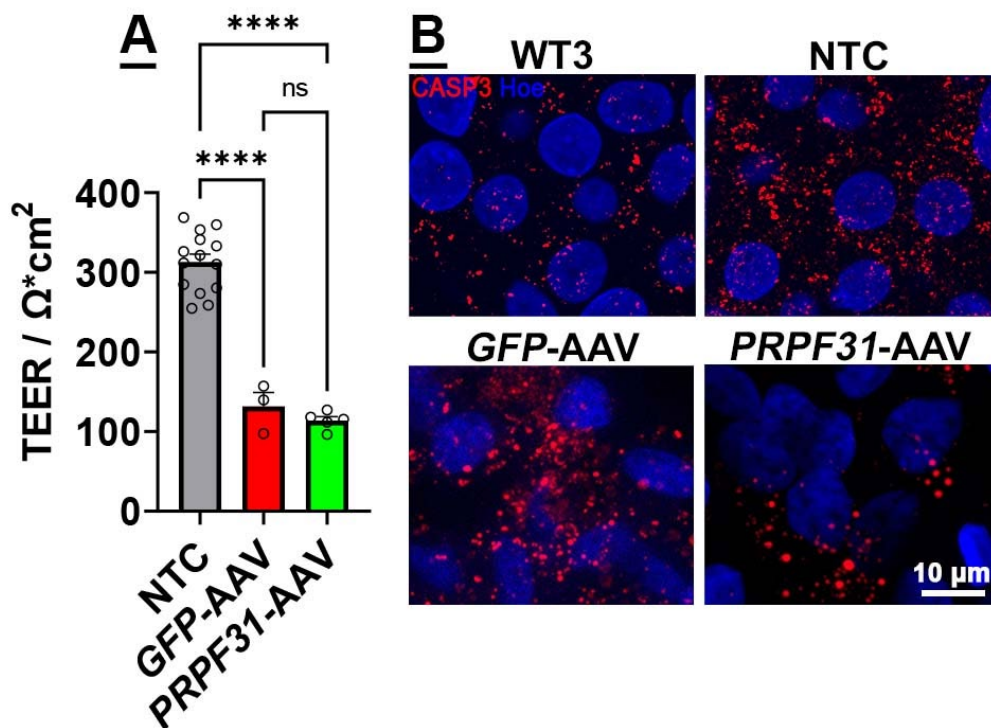


Figure 3.8: Adeno-associated virus (AAV) treatment negatively affects barrier function but does not induce apoptosis of induced pluripotent stem cell derived retinal pigment epithelium cells. Cells were originally derived from an individual with retinitis pigmentosa type 11, caused by PRPF31 mutation, referred to as RP11S1. A) Transepithelial electrical resistance (TEER) of RP11S1 iPSC-RPE was significantly reduced decreased 4 weeks after

transduction with AAV encoding green fluorescent protein (*GFP-AAV*) and *PRPF31* (*PRPF31-AAV*) transduction compared to the non-treated control (NTC). Statistical significance was assessed using one-way ANOVA followed by Tukey's post-hoc test for multiple comparisons, significance is indicated by *, $p < 0.05$, **, $p < 0.01$, ***, $p < 0.001$, ****, $p < 0.0001$. Results are mean \pm standard error of the mean (SEM). N is at least 3 for all conditions where n are transwell inserts that were transduced in independent experiments. B) Immunofluorescent staining of caspase 3 before and after AAV transduction. There is no increase in nuclear caspase 3 following AAV transduction. WT3 are iPSC-RPE cells derived from an individual with no history of retinal disease.

These results suggest that there is an impact of PRPF31-AAV treatment on the barrier function of iPSC-RPE 4 weeks after transduction (Figure 3.8 A). This is likely the result of cell stress rather than cell death, as there was no increase in nuclear caspase 3 staining (Figure 3.8 B).

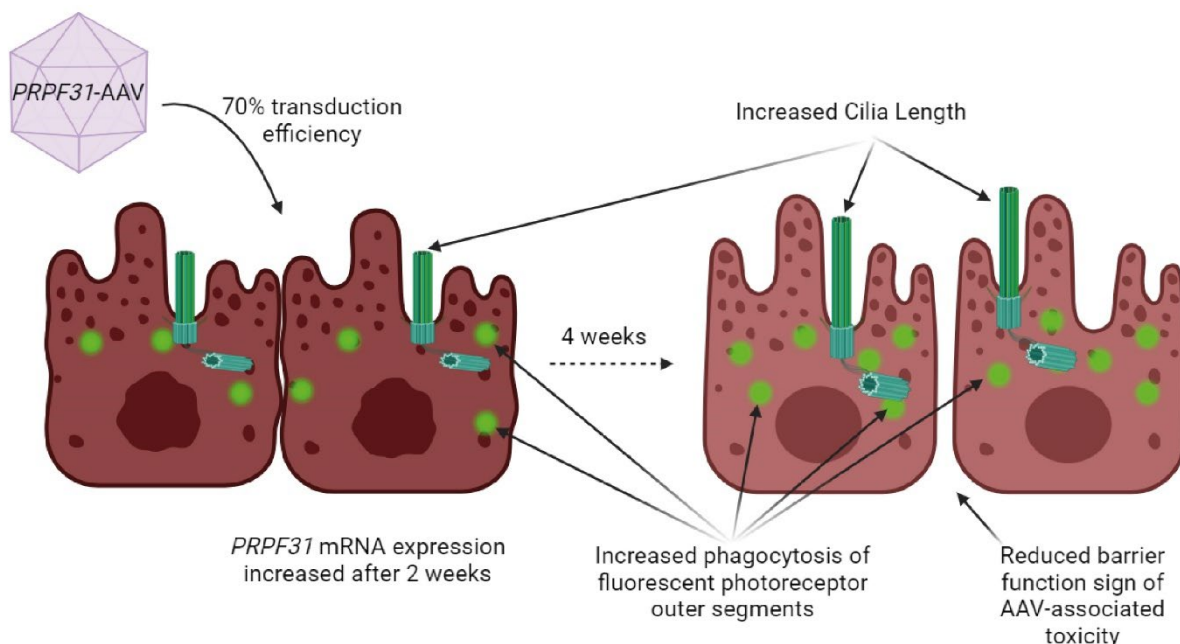


Figure 3.9: Schematic showing a summary of findings in this chapter. Patient derived cells are characterised by short cilia that protrude from the apical cell surface and a low ability to phagocytose fluorescently labelled photoreceptor outer segments (POS, green circles). *PRPF31*-AAV transduced 70% of the cells, an increase in *PRPF31* mRNA expression was detected after 2 weeks. After 4 weeks, an increase in cilia length and increase in POS phagocytosis was observed. In addition, the transepithelial electrical resistance (a measure of barrier function) reduced in comparison to untreated cells.

In summary, *PRPF31*-AAV treatment does cause cell stress. Nonetheless, there are several experimental pieces of evidence suggesting this treatment has a functional benefit on RP11 iPSC-RPE (Figure 3.9).

3.10 Discussion

In 2017 and 2018 Luxturna™ was approved for sale in the USA and Europe, respectively. It is now the longest available gene therapy and is used to treat *RPE65*-linked Leber congenital amaurosis (LCA2). Luxturna™ supplements RPE cells with *RPE65*, thereby restoring function and preventing loss of vision. This has a significant effect on the lives of patients, their families, and others affected by inherited retinal degeneration. Given RPE cells are the primary affected cell type in RP11, and like LCA2 this is caused by genetic haploinsufficiency, AAV supplementation of *PRPF31* is a promising treatment. A previous report evaluated this using a *PRPF31*^{+/-} iPSC-RPE model of RP11 (Brydon *et al.*, 2019). This study builds on these results by evaluating the efficacy of *PRPF31*-AAV in RP11 patient derived cells that express mutant PRPF31 protein.

This chapter uses patient derived iPSC-RPE cells that harbour an 11 base pair deletion in exon 11 of *PRPF31*. These cells, RP11S1 iPSC-RPE, were previously characterised by the Lako group (Buskin *et al.*, 2018; Georgiou *et al.*, 2022). This work builds on these studies by investigating whether this phenotype is ameliorated by *PRPF31*-AAV transduction. AAV2 efficiently transduces iPSC-RPE cells, as has been shown previously (Gonzalez-Cordero *et al.*, 2018; Brydon *et al.*, 2019). This study used the AAV2-[7m8], an AAV2 variant with superior transduction efficiency in the native murine retina (Dalkara *et al.*, 2013).

Firstly, control iPSC-RPE cells were transduced using a GFP-AAV construct. Next, flow cytometry was used to assess transduction efficiency of several MOIs and to identify the optimal AAV dose. When iPSC-RPE derived from a control cell line (F018) were treated with GFP-AAV at an MOIs of 50,000 and 100,000 then analysed 2 weeks later, 70% of the cells were GFP positive. This is comparable to transduction efficiencies obtained using AAV2/5 and AAV2/ShH10 in mouse ESC-RPE and AAV2/Anc80 in human iPSC-RPE (**Table 7**). It is significantly better than the 12% transduction efficiency previously reported for the AAV2-[7m8] in combination with iPSC-RPE cells (Garita-Hernandez *et al.*, 2020). This discrepancy could be caused by differences in cell culture conditions, such as the density and time at which iPSC-RPE cells are plated at 450,000 cells / cm² and left for 12 weeks before transduction.

However, in (Garita-Hernandez *et al.*, 2020) cells were plated at 200,000 cells / cm² and were immediately transduced.

After identifying two doses that transduced a majority of the iPSC-RPE cells the focus shifted to using *PRPF31*-AAV with RP11 patient-derived cells. RP11S1 iPSC-RPE cells were transduced with two different doses of *GFP* and *PRPF31*-AAV. Quantitative PCR showed that *PRPF31* was upregulated after treatment with 100,000 MOI and so this concentration was selected for future experiments. After observing mRNA upregulation, PRPF31 protein expression was evaluated by western blot. Despite mRNA upregulation there was no statistically significant change in protein expression. However, a small increase in protein may not be detected as western blot is a semi-quantitative measure of protein expression. An alternative, more sensitive, technique such as mass spectrometry may be capable of resolving this change. ARL13B immunofluorescence microscopy was performed with *PRPF31*-AAV transduced RP11S1 cells. Phenotypic characterisation was performed four weeks after treatment to provide time for transcription, translation, functional integration of PRPF31, and subsequent functional changes in cell biology. ARL13B immunofluorescence microscopy showed that cilia length but not cilia incidence was rescued, in agreement with a similar study using *PRPF31*^{+/-} iPSC-RPE cells (Brydon *et al.*, 2019). 70% of iPSC-RPE cells were ciliated regardless of treatment condition, this may reflect the presence of some mitotic cells in the RPE monolayer, as previously seen in rat RPE cells (Al-Hussaini *et al.*, 2008). The mean ARL13B object length increased by an average of 0.5 µm. A change this size is theoretically resolvable using confocal microscopy and as many cilia were measured (n>250), this result is unlikely to be a technical artefact (Schermelleh, Heintzmann and Leonhardt, 2010). Cilia function regulates RPE maturation and phagocytic ability (May-Simera *et al.*, 2018a). To determine whether restoration of cilia length was sufficient to rescue phagocytic ability a phagocytosis assay was performed. This showed that phagocytic ability increased after *PRPF31*-AAV treatment, in agreement with a similar observation made using iPSC-RPE cells with only one functional copy of *PRPF31* (Brydon *et al.*, 2019). This is significant as RPE phagocytosis of POS is likely a cause of vision loss in RP11. Restoration of phagocytosis *in vivo* would likely be of significant clinical benefit.

Recently the formation of cytoplasmic protein aggregates has been implicated in the aetiology of RP11 (Georgiou *et al.*, 2022). Moreover, removal of these aggregates through rapamycin treatment was shown to be beneficial (Georgiou *et al.*, 2022). To determine whether aggregation was affected by *PRPF31*-AAV treatment, HSPA2 and PRPF31 localisation was assessed by immunofluorescent microscopy. This showed that there was a shift in the localisation of PRPF31 from the cytoplasm to the nucleus and suggests the degree of aggregation is reduced but not eliminated following *PRPF31*-AAV treatment. Future studies could address this issue by combining *PRPF31*-AAV transduction with pharmacological clearance of PRPF31 aggregates (Georgiou *et al.*, 2022). This combined therapeutic approach may be more efficacious than either treatment alone.

Barrier function of the RPE is important for maintenance of the blood-retina-barrier, and this function is affected in RP11 (Buskin *et al.*, 2018). To determine whether barrier function is restored following *PRPF31*-AAV treatment, TEER was measured. TEER significantly reduced following both *GFP*- and *PRPF31*-AAV treatment. This shows that barrier function is disrupted for at least 4 weeks following AAV transduction and suggests AAV transduction leads to cell stress. To determine whether AAV transduction causes cell death, immunofluorescent staining of caspase-3 was performed. No cytoplasmic-nuclear translocation occurred following AAV transduction, suggesting that apoptosis was not induced (Luo *et al.*, 2010). Nonetheless, there was an improvement in cell function. Future studies could use additional methods such as a lactate dehydrogenase assay to assess cell health following transduction. The result is consistent with those obtained in mice treated with *CMV-GFP-AAV* (Xiong *et al.*, 2019). Interestingly, this study also reported RPE-specific promoters caused less toxicity than those which are broadly active. This could inform design of future gene therapies that target the RPE with reduced risk of damage or inflammation.

PRPF31-AAV transduction ameliorated the phenotype of RP11 patient-derived iPSC-RPE. This corroborates a previous report that characterised the effect of *PRPF31*-AAV transduction on CRISPR/Cas9 engineered *PRPF31* heterozygous knockout iPSCs (Brydon *et al.*, 2019). Whilst the studies used iPSCs with different genetic backgrounds and different AAV serotypes, both achieved ~70% transduction efficiency and rescued both phagocytic ability and cilia length

(Table 7). Overall, this is encouraging for those affected by RP11 as this is evidence that *PRPF31*-AAV is effective against diverse RP11 genotypes. Future studies should identify whether all genetic variants benefit equally from *PRPF31*-AAV treatment or whether some may benefit from a combination of therapies (Nazlamova *et al.*, 2021; Georgiou *et al.*, 2022). Continued development of *PRPF31* gene supplementation could then be carried out by developing a large mammal or non-human primate model to confirm the functional benefit *in vivo* before progressing into the clinic.

Chapter 4. Generating Isogenic Controls of RP13 Patient-Derived iPSCs Using CRISPR/Cas9 Technology

4.1 Introduction

As an unlimited source of patient-derived cells that have the potential to recapitulate diseases at a molecular, cellular, and functional level; induced pluripotent stem cells (iPSCs) are an excellent tool for use in *in vitro* disease modelling (Shi *et al.*, 2017). However, genetic variability between iPSC lines is a source of concern in the field (**Figure 4.1**) (Kyttälä *et al.*, 2016). This variability could confound results in studies where a small number of iPSC lines is used, because this genetic variability is not present in non-iPSC derived models e.g., immortalised cell lines or animal siblings.

The advent of highly sensitive techniques such as RNA-Seq and “shotgun” proteomics has shown that genetic variation in iPSCs is both transcribed and translated (Kilpinen *et al.*, 2017; Mirauta *et al.*, 2018). We plan to use both techniques for characterisation of iPSC-derived retinal pigment epithelium (RPE). As genetic variation within our lines could confound our results, we adopted CRISPR/Cas9 technology to rigorously control genetic background. This

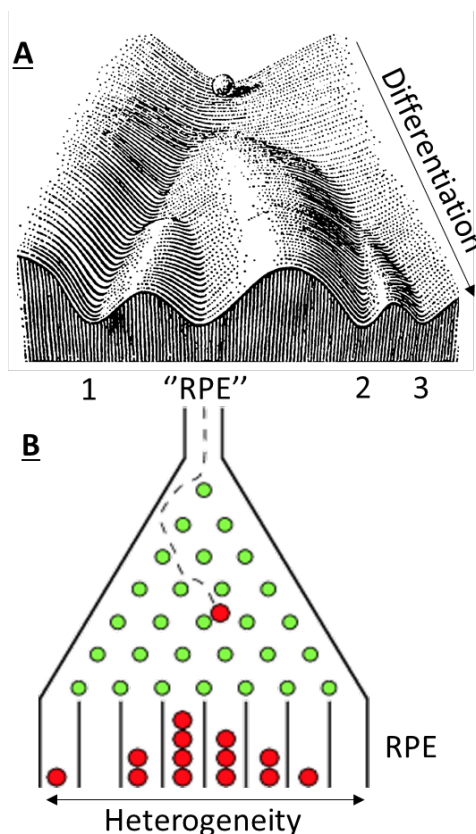


Figure 4.1: Cartoon to illustrate heterogeneity amongst iPSCs. A) Waddington's epigenetic landscape (1957), a conceptual drawing of cell differentiation. During development, cells become increasingly committed to a particular fate. Waddington postulated that differentiation is analogous to a marble rolling down a hill.

B) Marble falling down a Galton board. Highly sensitive techniques such as RNA-Seq and “shotgun” proteomics can detect genetic variation across iPSC-derived cultures, such as RPE. The lanes at the base of the board are analogous to this variability.

approach could also be used to generate isogenic iPSC-derived transplants that have a low risk of rejection.

Inherited genetic variation is the largest source of innate variation between iPSC lines. However, genetic and epigenetic variation can be acquired after cells are obtained from patients (**Figure 4.2**), reviewed in (Liang and Zhang, 2013). For example, copy number variations (CNVs) and DNA methylation variability can arise during somatic cell induced reprogramming and culture (Laurent *et al.*, 2011; Lister *et al.*, 2011).

Non-genetic factors such as differentiation protocol, laboratory methods, and post-differentiation passage number can all create variation between genetically identical (isogenic) tissues (Kokkinaki, Sahibzada and Golestaneh, 2011; Volpato *et al.*, 2018; Mellough, Collin, *et al.*, 2019). There is also evidence to suggest that variation arises during maturation of iPSC-derived cells (Kaya *et al.*, 2019). These non-genetic variables should be controlled where possible to reduce potential effects.

The aim of this project was to create an isogenic control of a RP13 iPSC line. The generation of isogenic controls will allow insight into the effect *PRPF8* mutations have on the transcriptome and proteome of iPSC-derived RPE.

Variability in iPSC-derived Cells

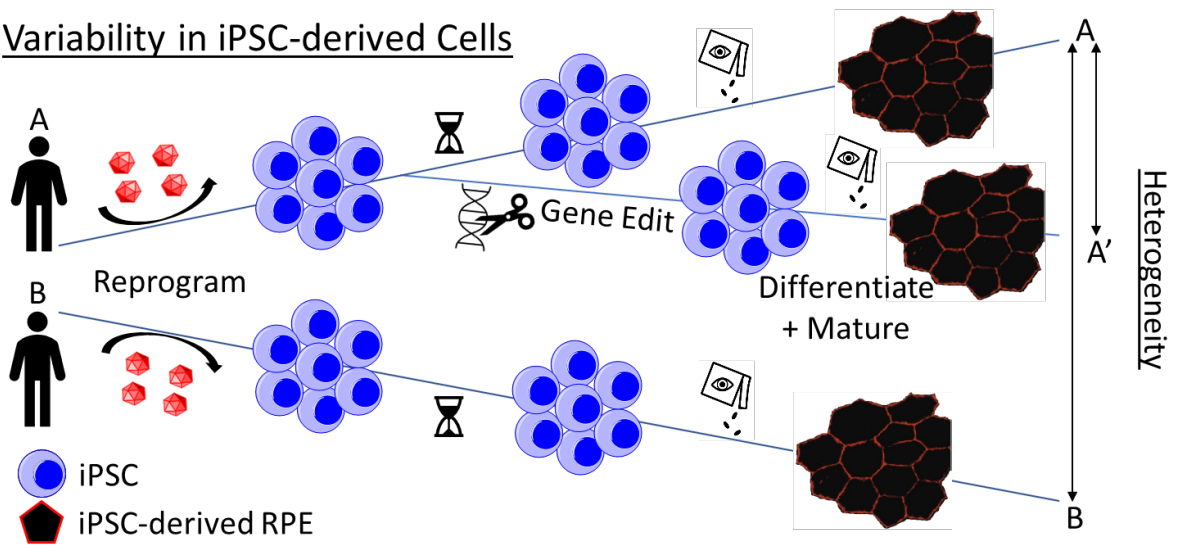


Figure 4.2: Cartoon illustrating how heterogeneity is acquired by iPSC-derived samples. Genetic variability arises between donors, during somatic cell reprogramming, and prolonged cell culture. Non-genetic variability can arise during differentiation and maturation. Gene editing technology can create cells with a shared genetic background (sample A and sample A'). Results obtained using these are less likely to be the result of genetic variation, such as that which exists between sample A and sample B. Black double-ended arrows indicate the degree of heterogeneity between samples.

4.2 Aims

The main aim of this chapter is to fully characterise the PRPF8-iPSC lines, generate isogenic controls and assess the impact of gene editing on the genomic stability

- Before I joined the project, fibroblasts of four RP13 patients were obtained by Mr Martin McKibbin (Leeds University) and reprogrammed to generate 3 iPSC clones per patient by Dr Chunbo Yang.
- Confirm *PRPF8* mutations
- Confirm genetic stability of iPSC clones
- Identify clones that differentiate most efficiently to RPE
- Identify gRNA that selectively recognises *PRPF8* target site
- Use CRISPR/Cas9 technology to edit *PRPF8* mutation of the RP13-1B iPSC clone that efficiently differentiates into RPE
- Isolate edited cell population
- Assess efficacy of gene editing

4.3 RP13 Patient Background

Before I joined the project, fibroblasts were obtained from RP13 patients (**Table 8**) and gifted by Mr Martin McKibbin (University of Leeds). These were reprogrammed into iPSCs by Dr Chunbo Yang. Following reprogramming, three iPSC clones were expanded and characterised, since variability in differential potential can arise during the reprogramming process. Propagating three clones increases the likelihood of identifying iPSCs that efficiently differentiate into retinal tissue is increased.

It is also emerging that there is variability between iPSC lines that is likely due to genomic variation between cell lines (Kilpinen *et al.*, 2017). Furthermore, this appears to translate into differences between iPSC-derived RPE cultures using lines derived from multiple healthy donors (Miyagishima *et al.*, 2016). To address these potential limitations, CRISPR/Cas9 technology was employed to eliminate genetic variation between patient and control cell lines.

Lab Identifier	Initials	Sex	Age at Biopsy	Gene	RefSeq Transcript ID	Heterozygous Mutation	Amino Acid	Age of onset	Clinical notes
PRPF8 1a	GM	Male	80	PRPF8	NM_006445.4	c.6926A>C	H2309P	first decade	Early onset cataracts. Reading aged 80.
PRPF8 1b	IM	Male	57	PRPF8	NM_006445.4	c.6926A>C	H2309P	first decade	Unilateral cataract surgery
PRPF8 1c	MS	Female	36	PRPF8	NM_006445.4	c.6926A>C	H2309P	first decade	Unilateral cataract surgery
PRPF8 2	SM	Male	18	PRPF8	NM_006445.4	c.6926A>C	H2309P	8	VA 6/12 and 6/60. Marked cystoid macular oedema in both eyes. Mid-peripheral spiculation. Visual field of 10 degrees.(Towns et al 2010)

Table 8: The cell lines used throughout this study were derived from four patients. This table describes the clinically relevant information of those patients.

These results show that the RP phenotypes between the patients share similarities in the age of onset, all patients were diagnosed within the first decade of life. Three of the patients had also undergone cataract surgery before the biopsy was taken. Patient 2 was 18 at the time of biopsy, it is not known whether patient 2 went on to develop cataract later in life. The clinical notes of patient 2 suggest that this individual has additional retinal pathology in the form of cystoid macular oedema. No differences in disease severity were identified by Mr Martin McKibbin.

4.4 RP13 Patient-Derived iPSCs do not acquire genomic abnormalities during the reprogramming and expansion process

The generation of iPSC cultures from fibroblasts increases the probability of chromosomal amplifications and deletions. Research has shown that there are genomic hot spots where these events occur most frequently, and these mutations can affect stem cell properties. For example, chromosome 20q amplification can affect TGF β signalling and differentiation (Markouli *et al.*, 2019). Quantitative PCR of these hot spot regions using hiPSC ScoreCard assay was performed on genomic DNA from the iPSC clones to determine whether chromosomal amplifications or deletions were present. This is important as chromosomal aberrations could confound subsequent experiments. For this reason, the hiPSC ScoreCard is used by other groups working on similar projects (Reid *et al.*, 2021).

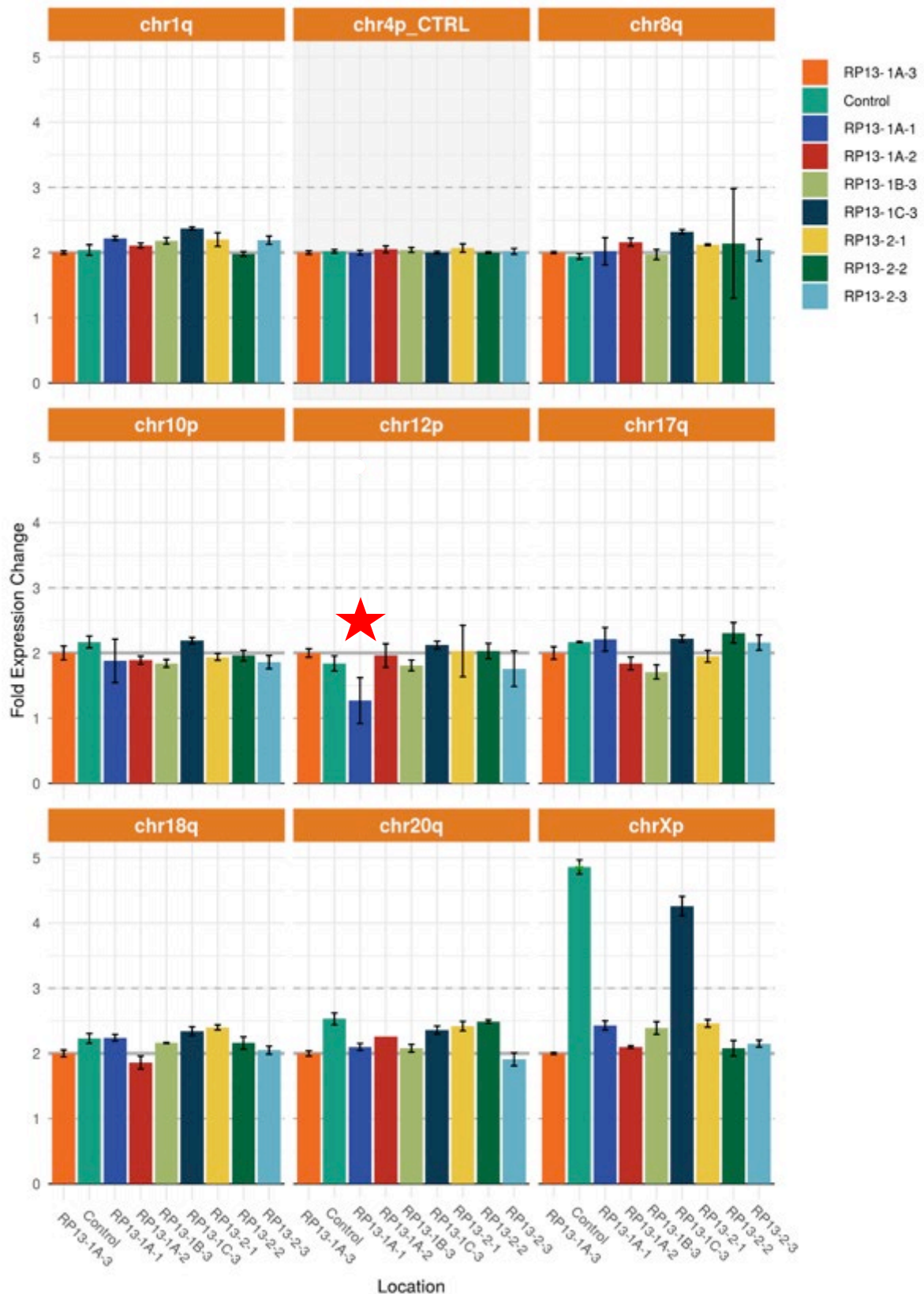


Figure 4.3: Chromosomal copy number is plotted along the y-axis; the cell line is shown on the x-axis. Each graph shows a chromosomal locus that is frequently mutated and/or deleted during iPSC reprogramming and culture. For example, ChrXp shows the number of copies of the X chromosome. Therefore, patient RP13-1C is confirmed as being female as the copy number of X chromosomes is double that of the other patients. Error bars indicate SEM from three biological replicates (n = 3). Significance was determined using a machine-learning algorithm incorporated into the online analysis application.

One limitation of this assay was the limitation on the number of samples which can be run at one time. One patient from family 1 (RP13-1A) and the de-novo case (RP13-2) were selected, and all the iPSC clones were analysed. It was possible to analyse two more samples and for this RP13-1C-3 and RP13-1B-3 were selected, based on a visual assessment of their differentiation efficiency.

Due to high variability in the results obtained from the reference DNA supplied with the kit, results were normalised to the results from RP13-1A (clone 3). This confirmed that RP13-1C was derived from a female and showed that there is a chromosomal deletion in chromosome 12 of RP13-1A (clone 1) (**Figure 4.3**). The y-axis indicates fold expression change of a given chromosomal region, if there is amplification or deletion of a region this will be reflected by a change in expression as determined by qPCR. These results led to RP13-1A (clone 1) being discontinued whilst all other lines were deemed suitable for further study.

4.5 RP13 Patient-Derived iPSCs and RP13-Cas9 iPSCs Differentiate into RPE

To account for iPSC clonal variability, we differentiated two iPSC clones of RP13-1A and three iPSC clones of RP13-1B, RP13-1C and RP13-2. All lines harbour the same H2309P mutation in *PRPF8* (**Table 8**). This experiment assessed the differentiation capacity of the clones that were generated during the reprogramming of iPSCs, under the same differentiating conditions. We observed that there was variability in how clones differentiated and selected the clone that differentiated most efficiently for use throughout the rest of the study (**Figure 4.4** and **Table 9**).

Donor/Clone	<i>PRPF8</i> ^{H2309P/+}	<i>PRPF8</i> ^{+/+}
RP13-1A-3	RP13-1A	RP13-1A-Cas9
RP13-1B-3	RP13-1B	RP13-1B-Cas9
RP13-1C-1	RP13-1C	RP13-1C-Cas9
RP13-2-3	RP13-2	RP13-2-Cas9

Table 9: Table showing the induced pluripotent stem cell (iPSC) clones that differentiated most efficiently into retinal pigment epithelium (iPSC-RPE). Clone numbers are redundant following this experiment and so the cells are referred to as either RP13-X or RP13-X-Cas9 to distinguish between edited and unedited cells, respectively, where X denotes the original donor of the cells.

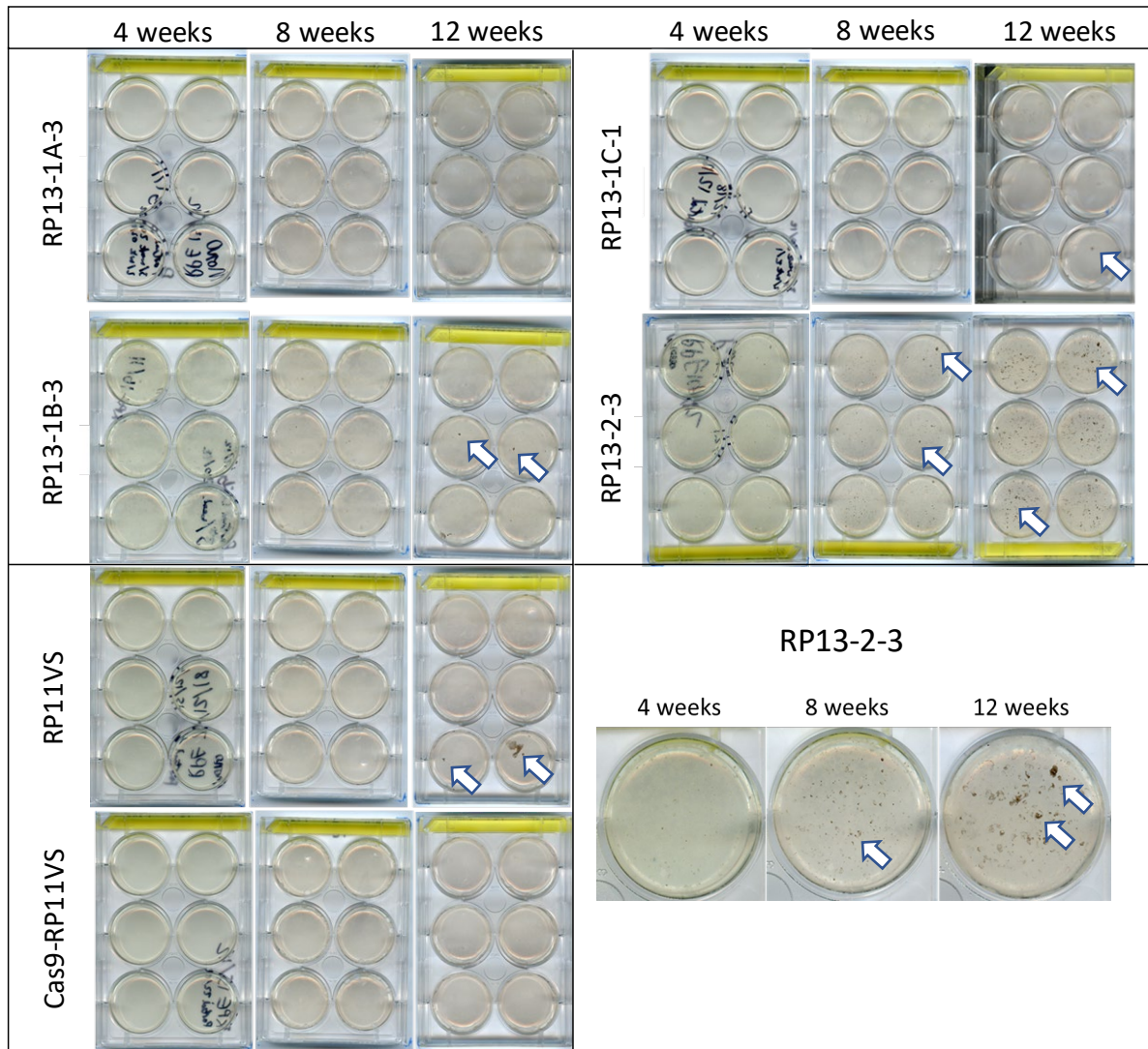
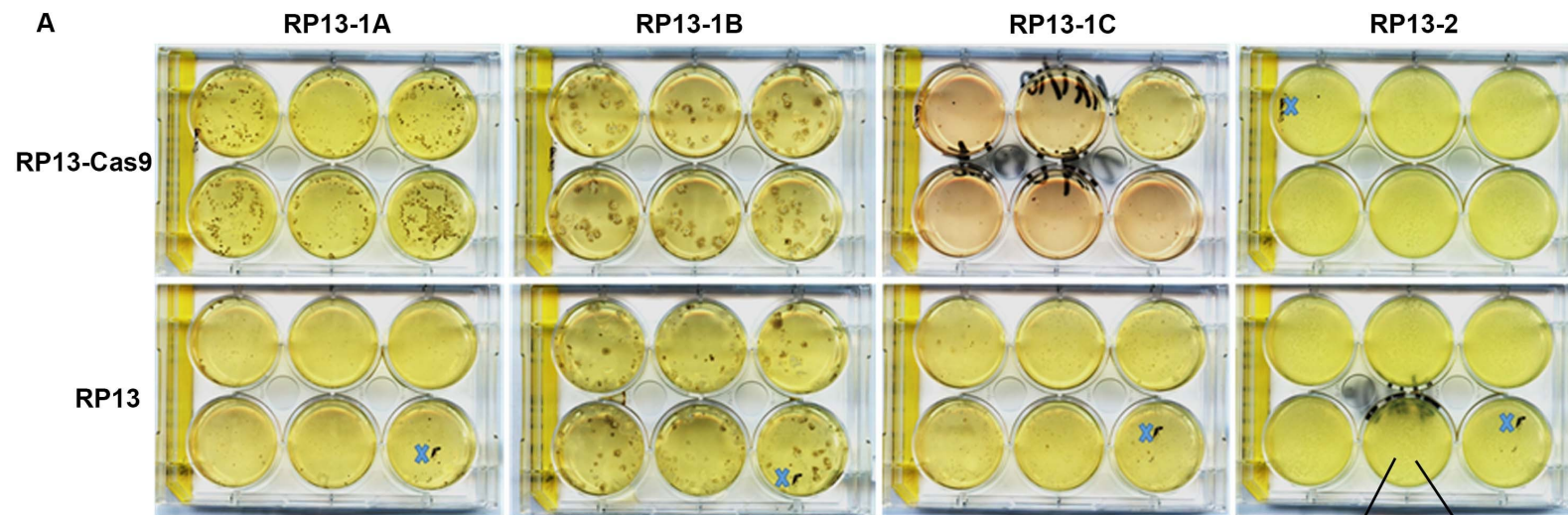


Figure 4.4: Photographs to illustrate progression of RPE differentiation over 12 weeks. The top 4 sequences show differentiation of RPE from clones of each patient. The clone that differentiated most efficiently is shown. Two sequences in the bottom left show differentiation of PRPF31 lines RP11VS and Cas9-RP11VS. The bottom right sequence shows the emergence of RPE colonies within one well. White arrow indicates patches of pigmented cells.



To differentiate iPSCs to RPE, iPSCs were seeded onto 6 well plates and grown to 80% confluency. Next, the media was changed from iPSC maintenance media to RPE differentiation media. This differentiation phase takes three to four months. After this, the RPE colonies that arise (**Figure 4.4** and **Figure 4.5**) must be excised and plated, usually in a 24 well format (**Figure 4.6**). It takes approximately 2 weeks for the excised cells to reach confluency. This process is repeated two or three times (4-6 weeks) to expand the RPE cultures until there are enough cells for the planned experiments. If the cells are expanded beyond this, it may result in them being unable to mature into a monolayer of pigmented cells. Finally, the cells are plated onto transwell inserts and 12 well plates. The cells are left to mature into a monolayer of pigmented cells that have a transepithelial resistance of $\sim 200 \Omega/\text{cm}^2$. In total the differentiation and maturation take 6 months.

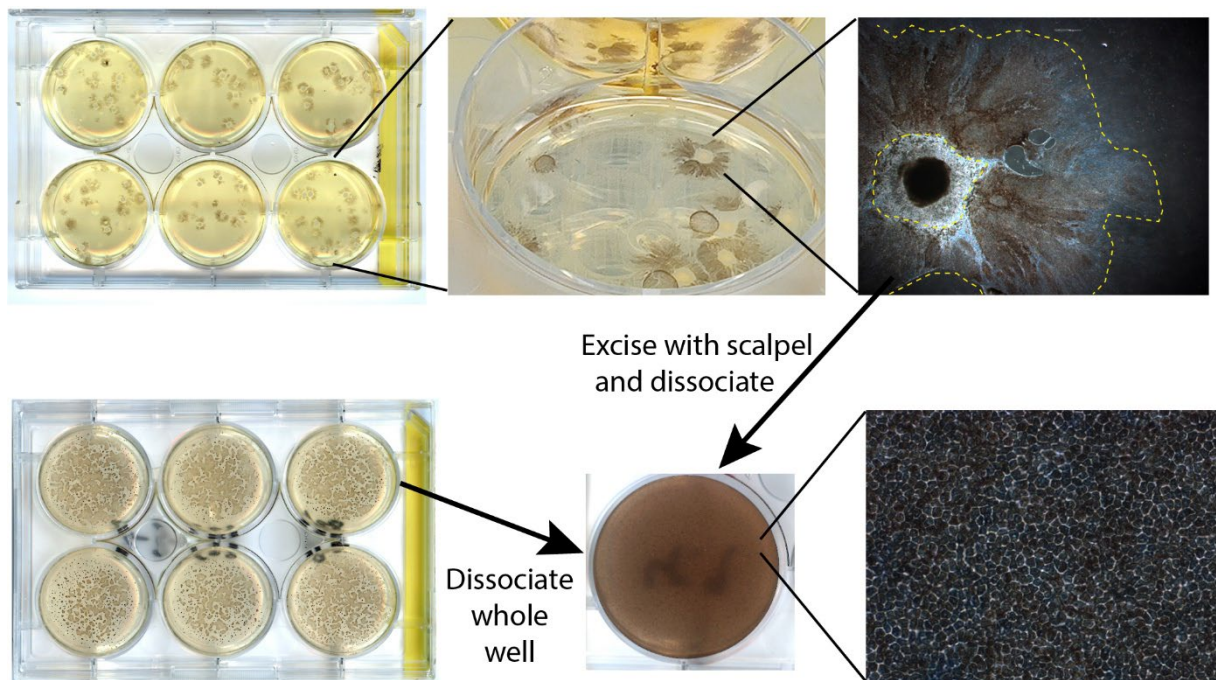


Figure 4.6: Photographs showing iPSC-RPE differentiation and purified iPSC-RPE cells. Two images of 6 well plates show different distributions of differentiated cells. Where non-RPE cells are clearly visible (top row), the non-RPE cells are excised with a scalpel (dotted yellow line, top right) to purify the iPSC-RPE population. In some instances, this is not possible (bottom left) and so no excision is performed. In both cases, the iPSC-RPE cells are dissociated before being plated and left to mature to form an even iPSC-RPE monolayer.

All RP13 lines gave rise to RPE cells in at least one clone (**Figure 4.4**). There was variability in the efficiency of differentiation, for example RPE patches arose in RP13-1A-3 cultures within the first month. There was also variability in how well the cultures expanded and matured. For example, despite the modest appearance of patches (**Figure 4.4**) in RP13-1B-3, these cells expanded and matured into RPE more efficiently than the other lines. As RP13-1A-3, RP13-1B-3, RP13-1C-1, and RP13-2-3 each differentiated most efficiently, these clones were selected for further study.

On the second attempt at differentiation that began in January 2020 we tested a new differentiation protocol that involved the addition of small molecules to the media at set timepoints throughout the first weeks of the protocol (Regent *et al.*, 2019). Preliminary results suggested that this increased the efficiency of the differentiation. However, these differentiations were terminated before the efficiency could be assessed due to COVID-19 lockdown (March 2020). New differentiations were initiated in August 2020 using a guided differentiation protocol (Regent *et al.*, 2019). Images taken after 6 weeks (**Figure 4.5**) show generally improved differentiation efficiency compared to that achieved using the spontaneous differentiation protocol (**Figure 4.4**). The possible exception to this observation was decreased efficiency for line RP13-2-3, as more pigmentation can be seen in **Figure 4.4** bottom right panel compared to **Figure 4.5** right hand panel. However, phase contrast microscopy (**Figure 4.5**) shows that whilst pigmentation is not obvious in these cultures, a proportion of cells displayed epithelial morphology. The end

For successful editing with CRISPR/Cas9, the gRNA must recognise and stimulate efficient cleavage of the target sequence (**Section 1.3**). To determine whether the gRNA recognises and stimulates cleavage of the of the *PRPF8* 2309 codon, a 600 nucleotide *PRPF8* amplicon was generated from genomic DNA. Incubation of the amplicon with the Cas9/gRNA resulted in the formation of two products (400 and 200 nucleotides). To confirm that this was the result of the ribonucleoprotein recognising the *PRPF8* mutation, all permutations of the reaction components were performed. In brief, the Cas9 protein is incubated with the gRNA to form a Cas9-gRNA ribonucleoprotein. The gRNA anneals to the target site and guides the Cas9 restriction enzyme to the cut site. The Cas9 protein interacts with the PAM site, causing a

conformational change in the protein that creates a double-stranded DNA (dsDNA) break at the cut site (Barrangou *et al.*, 2007).

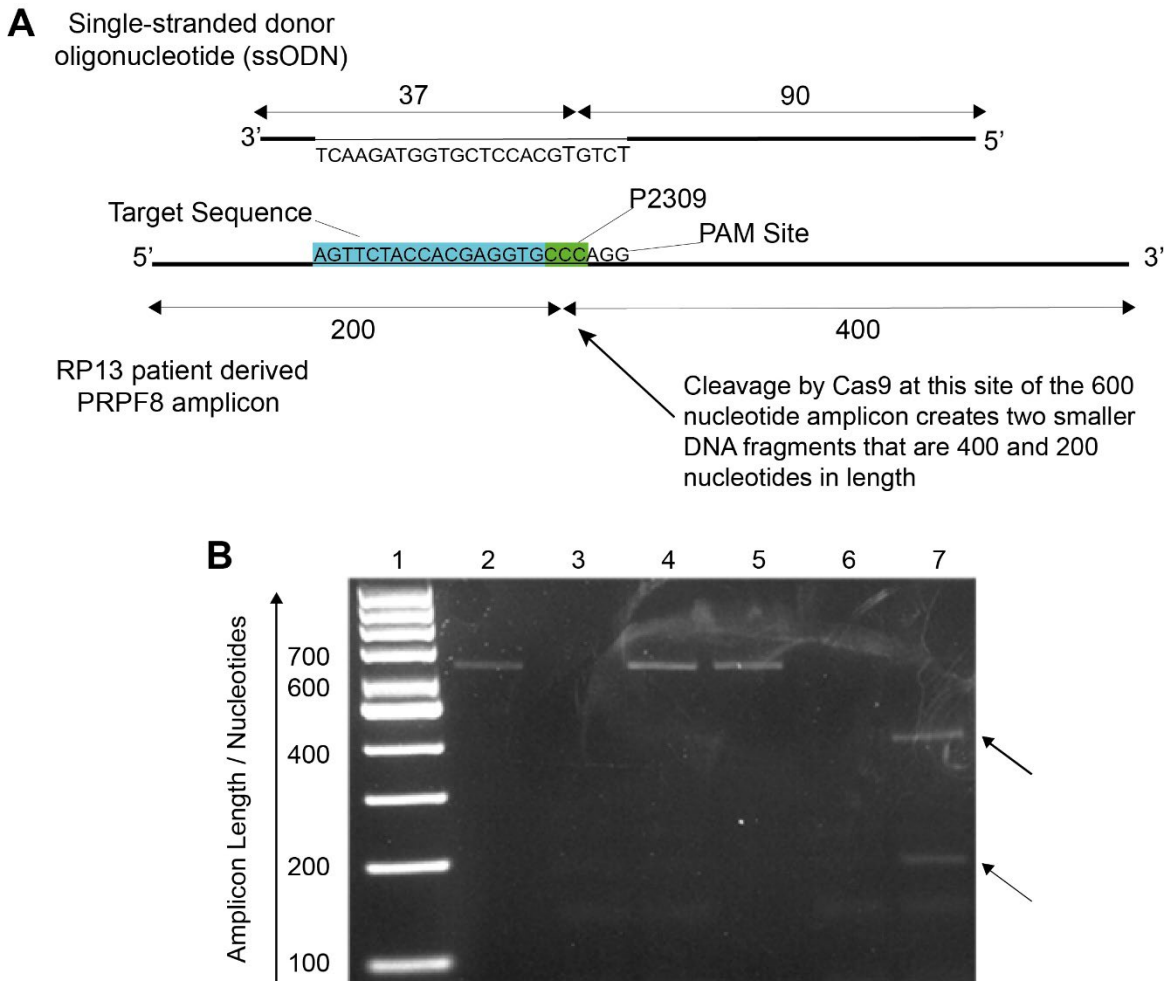


Figure 4.7: Schematic of gRNA and single stranded donor oligonucleotide (ssODN) design and in vitro cleavage detection of PRPF8 amplicon. A) cartoon of 600 bp PCR fragment used for genomic cleavage detection. On the RP13 patient derived amplicon the gRNA target sequence, 2309 codon, and protospacer adjacent motif (PAM) site are labelled. On the ssODN, nucleotides that are intended to cause edits are in bold. Recognition of the target site by Cas9/gRNA leads to cleavage of the RP13 patient derived amplicon into two, 400 bp and 200 bp long fragments (black arrows). B) lanes numbers correspond to the following reaction components: 1) 1 kb DNA ladder 2) PRPF8 amplicon only 3) Guide RNA (gRNA) only 4) PRPF8 amplicon and gRNA 5) Cas9 protein and PRPF8 amplicon 6) Cas9 protein and gRNA 7) Cas9 protein, gRNA and PRPF8 amplicon. On-target cleavage of the ~600 bp amplicon produces two products of ~400 bp and ~200 bp. Cleavage was only detected when amplicon was incubated with cas9/gRNA duplex.

Figure 4.7 shows that the gRNA was effective in stimulating specific cleavage of the *PRPF8* amplicon. Most dsDNA breaks are repaired by non-homologous end joining (NHEJ) which often results in the insertion or deletion of nucleotides. For gene editing, a second less efficient repair mechanism is exploited: homology directed repair (HDR). This process

normally uses the homologous chromosome as a template to repair dsDNA breaks. This process can be exploited by using a single stranded donor oligonucleotide (ssODN) that can act as template instead of the homologous chromosome. The ssODN can be designed to edit the PAM site, to prevent cleavage of edited sites **Figure 4.7**. In addition, the ssODN can be introduced to the cell along with the Cas9/gRNA ribonucleoprotein. The advantage of this is shorter incubation of genomic DNA. Longer incubation, for example with viral transfection of the Cas9 gene and gRNA, increases the chance of non-specific dsDNA cleavage. The architecture of the ssODN incorporated an asymmetric design, the centre of which lies upstream of the cut site, as this has been shown to enhance HDR efficiency (Richardson *et al.*, 2016). A pharmacological inhibitor of NHEJ (SCR7) was used in parallel to further enhance HDR efficiency (Hu *et al.*, 2018).

To generate Cas9 isogenic controls, iPSCs were dissociated into a single cell suspension before nucleofection in the presence of Cas9/gRNA duplexes and the ssODN. This procedure facilitates rapid entry of these molecules into the nucleus. Following nucleofection, the cells were plated at a low density so that iPSC colonies arose from approximately single cells. This ensured genetically homogenous colonies could be isolated and expanded in a 24 well plate format. Subsequently, DNA from each clone was isolated and used to generate *PRPF8* amplicons. These amplicons were incubated with a second restriction enzyme that can discriminate the mutant/wild type sequence.

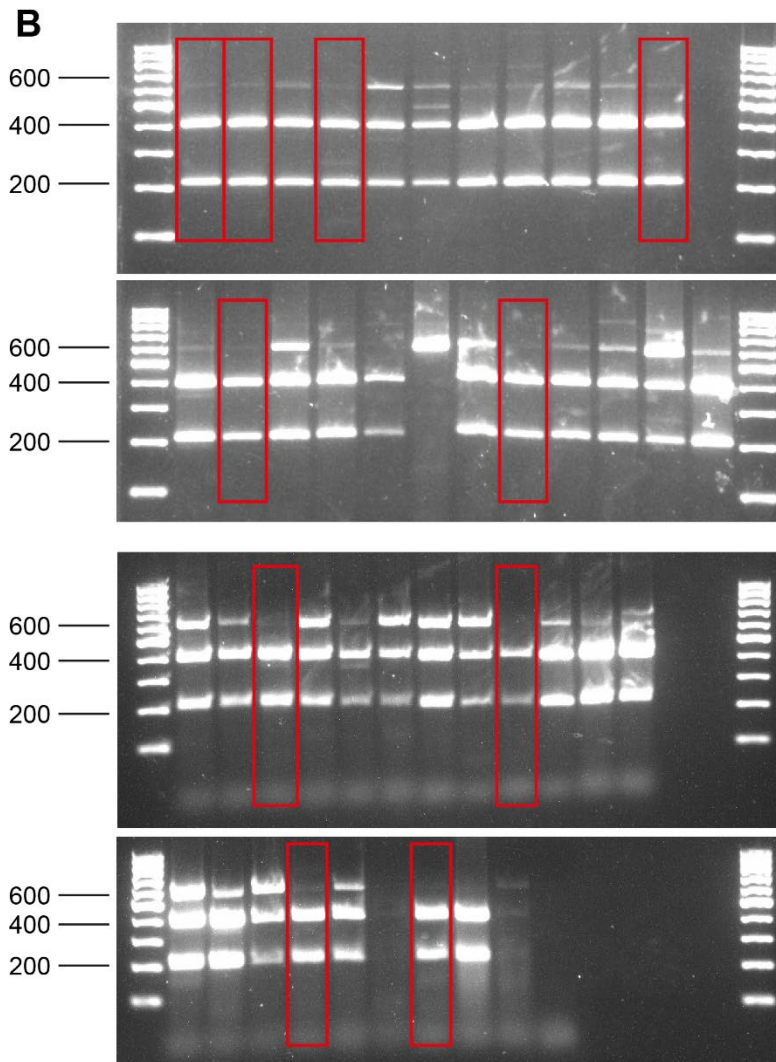
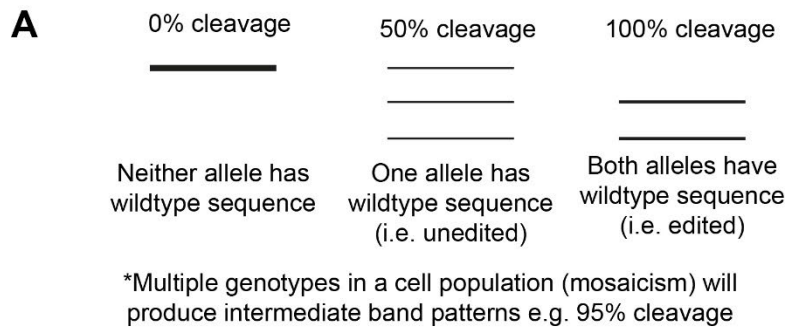


Figure 4.8: Restriction digest of *PRPF8* following nucleofection with Cas9/gRNA. iPSC colonies that grew following nucleofection were passaged into individual wells, cultured and then DNA was isolated from each culture. *PRPF8* amplicons (600 bp) were generated by using the polymerase chain reaction (PCR). These amplicons were incubated with a restriction endonuclease that recognises the wildtype/edited sequence. (A) The restriction enzyme does not cleave the unedited sequence. Upon recognition of the wildtype/edited sequence, the amplicon is cleaved to produce two bands (400 bp and 200 bp). (B) Gel showing cleavage of *PRPF8* amplicon generated from forty two iPSC colonies. The red boxes indicate samples that are homozygous for the wildtype/edited allele.

Cleavage of 50% of the amplicon indicates cells contain a heterozygous mutation, whilst 100% cleavage indicates the H2309P mutation has successfully been edited (**Figure 4.8**; 10/43 clones). Cleavage of between 50-100% of the amplicon indicates incomplete cleavage and could be generated by polyclonal iPSC colonies. To confirm successful editing Sanger sequencing was used, the sequencing results suggested 7 clones had undergone successful editing (**Figure 4.9**). Sequencing results of parallel experiments using RP13 1A-3, 1C-1 and 2-3 that were performed by Dr Chunbo Yang are given alongside those of RP13-1B-3, as these lines are studied in Chapter 5.

4.6 Lack of Off-Targeting Effects in the Gene Edited Isogenic Controls

Two RP13-1B clones (originally derived from RP13-1B-3) underwent further subcloning after identifying successful gene editing. This was to ensure a genetically homogenous population. Subcloning was performed by dissociating the iPSC clone into a single cell suspension and then culturing a sample of these in isolation from each other. After *PRPF8* sequences of these subclones were confirmed one subclone was selected for further characterisation based on the signal-to-noise ratio of the sequence chromatogram. DNA from this clone was used for analysis of off-target sequences. To determine whether the gRNA/Cas9 ribonucleoprotein selectively cleaved the target site and no other regions, we sequenced the *PRPF8* target site in RP13 (**Figure 4.9**), RP13-Cas9 (**Figure 4.10**) and sites with high sequence homology to the target site (**Figure 4.11** and **Table 5**). These off-target sites were identified using an online tool (<https://www.thermofisher.com/uk/en/home/life-science/genome-editing/geneart-crispr/geneart-crispr-search-and-design-tool.html>) that identifies sequences with fewer than 5 nucleotide mismatches to the target sequence (sequences provided in **Table 5**). This analysis returned 5 possible off-target regions. We also confirmed that the *PRPF8* mutation, H2309P, was present in both patient specific iPSC and the genetically edited isogenic controls. Dr Chunbo Yang performed *PRPF8* sequencing for RP13-1A (originally clone 3), RP13-1C (originally clone 1) and RP13-2 (originally clone 3). I sequenced the *PRPF8* region of RP13-1B (originally clone 3). Dr Chunbo Yang generated amplicons of the off-target regions, I purified the amplicons and sent them for analysis using the Eurofins Genomics TubeSeq service. Results for all cell lines are included as they will be used for the duration of the project.

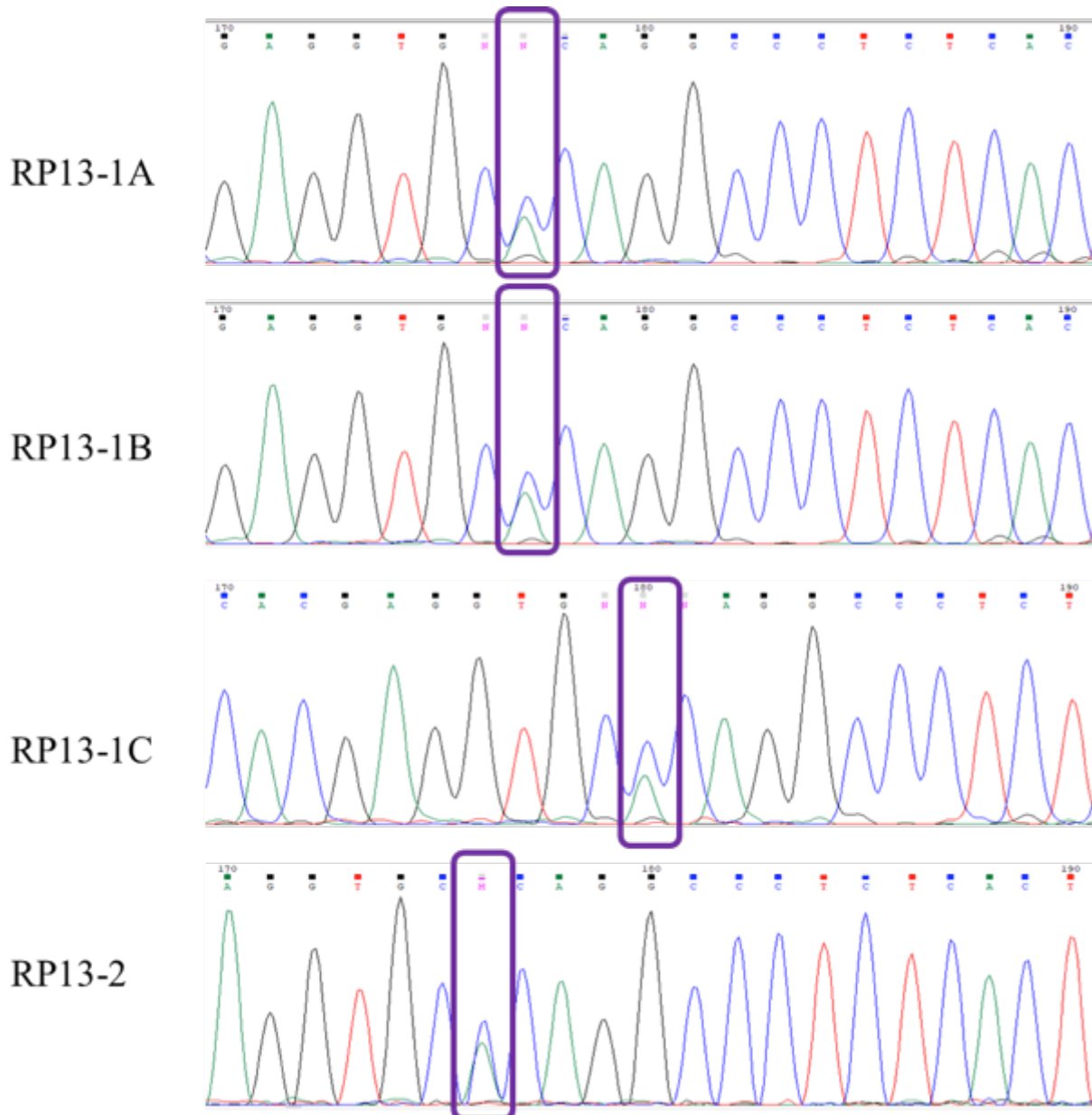


Figure 4.9: The heterozygous H2309P PRPF8 mutation is present in all four patient lines (RP13-1A(-3), RP13-1B(-3), RP13-1C(-1), and RP13-2(-3)). Line colour indicates nucleotide in sequence. Sequences were aligned with a PRPF8 reference sequence. The affected nucleotide (c.6926A>C) is indicated by a purple box. The CCC codon present in 50% of the DNA codes for proline, whereas CAC codes for histidine.

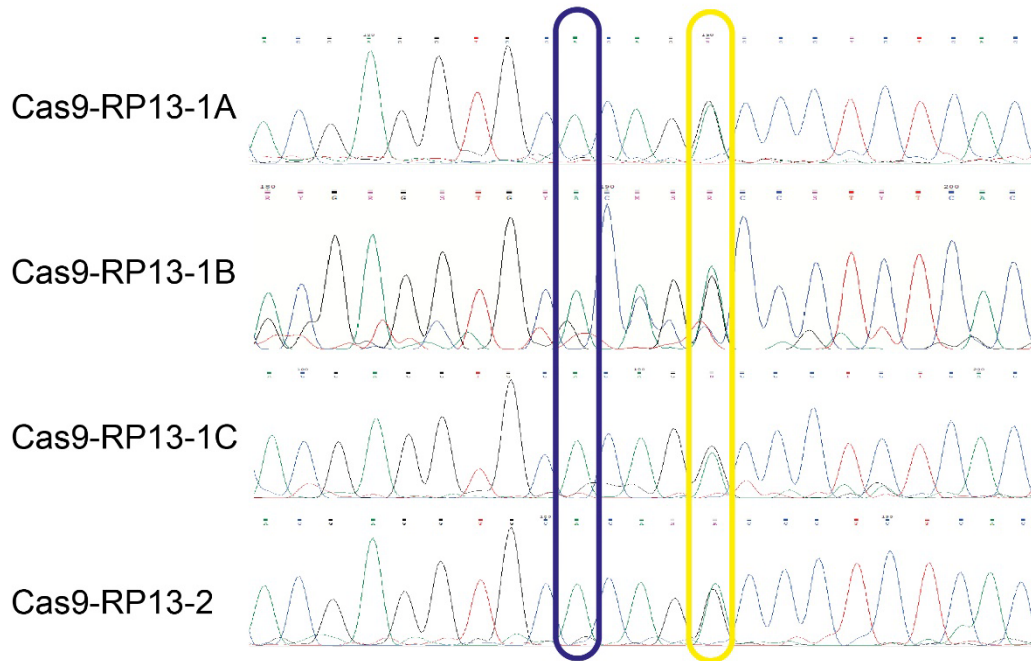


Figure 4.10: The pathogenic PRPF8 mutation present in all patient lines was edited to the wildtype sequence. Edited pathogenic mutation and PAM site are indicated by purple and yellow ovals, respectively. The left box of each sequence shows the homozygous adenine residue. The right box shows a heterozygous silent mutation in the PAM site, indicating successful editing by CRISPR/Cas9.

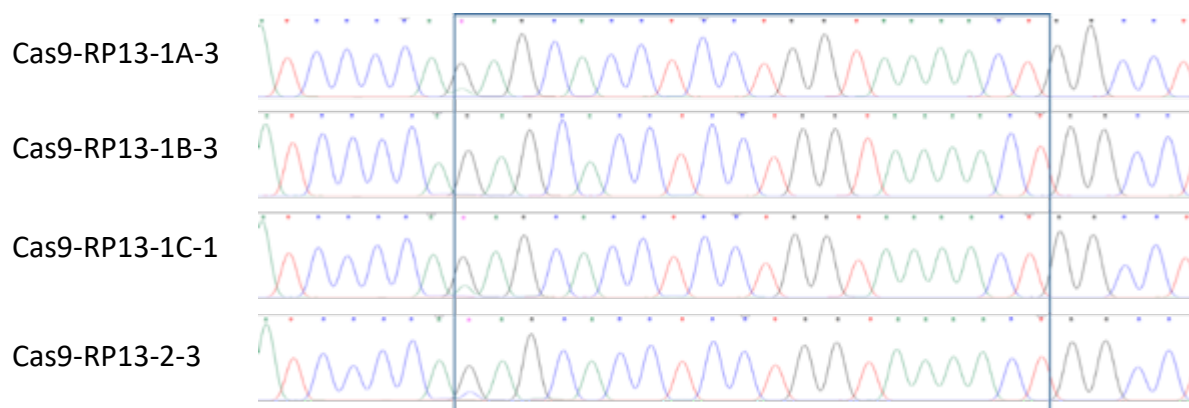


Figure 4.11: Sequences of possible off-target gRNA/cas9 cleavage sites. Five possible sites were identified by Dr Chunbo Yang, using the Invitrogen TrueDesign Genome Editor (<https://www.thermofisher.com/uk/en/home/life-science/genome-editing/geneart-crispr/geneart-crispr-search-and-design-tool.html>). This online tool identifies potential off-target restriction sites based on homology to the target site (<5 mismatches). These were sequenced to determine whether DNA double stranded breaks had occurred at sites away from the target sequence. One example is shown in this figure *ITIH4* (NG_016006), and further information on all 5 regions is shown in Table 6. There is no evidence of insertions, deletions or homology directed repair. The site of each possible off-target sequence is indicated by a blue box. The PCR reaction was performed by Dr Chunbo Yang, I purified the amplicon and sent them for sequencing.

Figure 4.9 shows the c.6926A>C mutation present in all RP13 cell lines. The sequence was corrected following Cas9-mediated gene editing (**Figure 4.10**). By sequencing regions of the genome with high sequence homology to the *PRPF8* target site (**Figure 4.11** and **Table 5**) we have provided evidence that this editing was highly specific and so these edited cell lines are suitable for further characterisation.

4.7 Gene Edited Cells are Pluripotent and Have Not Acquired Genomic Instabilities During Gene Editing and Culture

Following this we sent samples of each edited iPSC line (**Table 9**) for genetic analysis by ThermoFisher Scientific (<https://www.thermofisher.com/uk/en/home/life-science/stem-cell-research/stem-cell-services/karyostat-karyotyping-service.html>). Two assays were performed, the first was a qPCR based assay (<https://www.stemcell.com/hpsc-genetic-analysis-kit.html>) that looked for amplifications and deletions within genomic DNA, similar to previously done (**Figure 4.3**). The reason for changing the assay was to increase experimental power. Previously we screened the genome at 11 hot spots, whereas this second assay screened all 36,000 refseq genes (**Figure 4.12**).

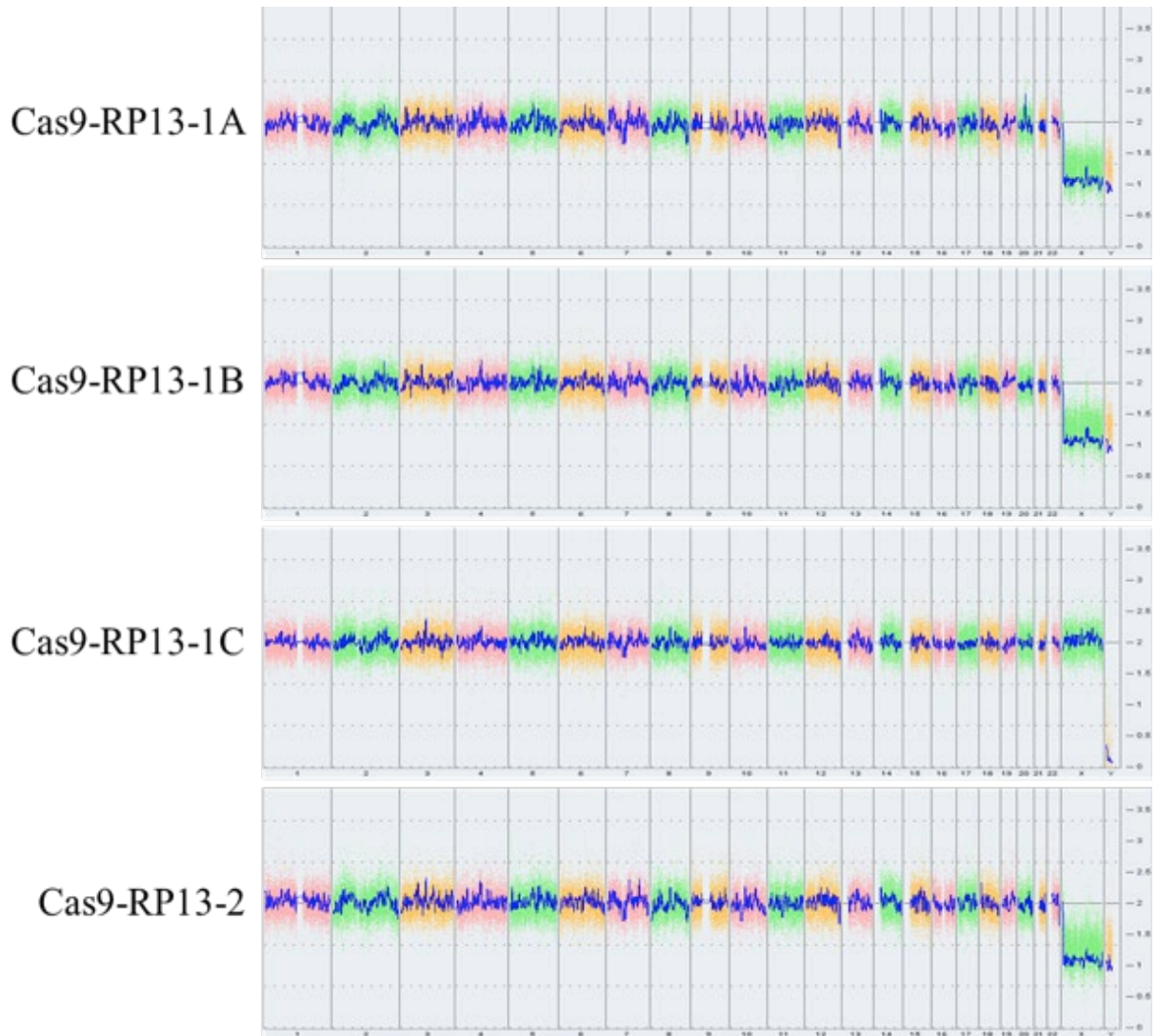
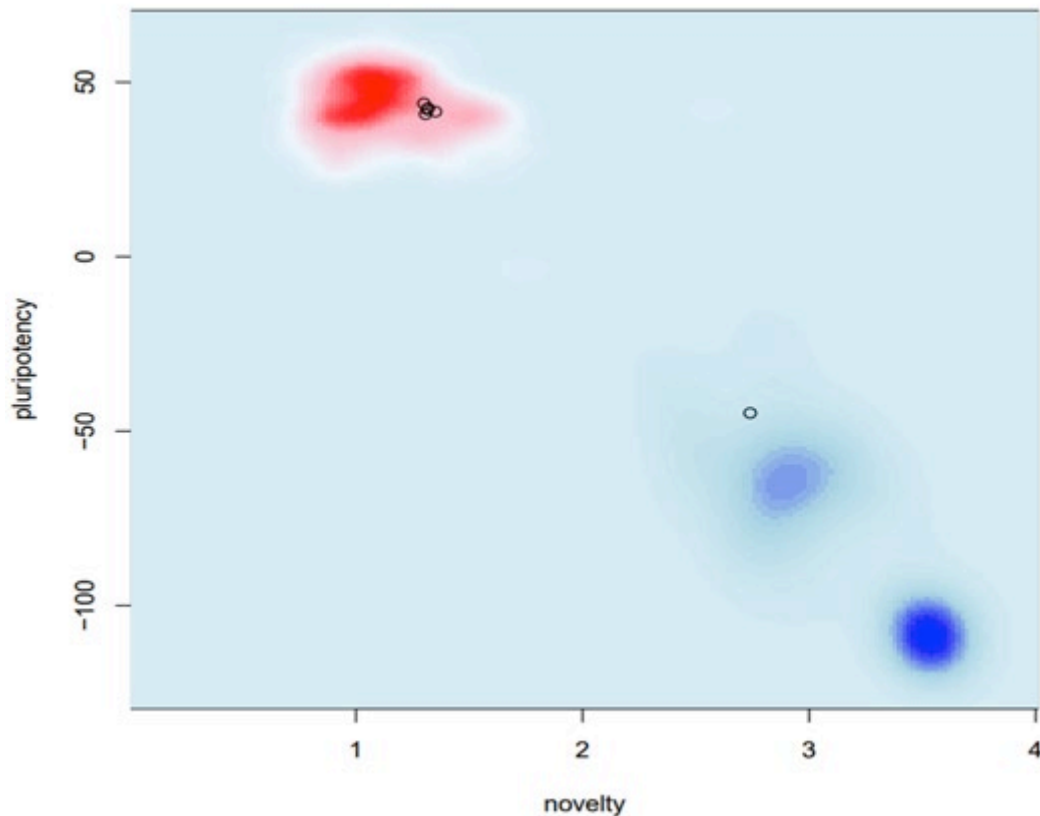


Figure 4.12: The right y-axis corresponds to the copy number ($n = 3$) produced by each probe on the microarray. A value of 2 represents a normal copy number state. A value of 3 represents chromosomal gain and a value of 1 represents a chromosomal loss. The pink, green and yellow colours indicate the raw signal for each chromosome probe, while the blue signal represents the normalized probe signal which is used to identify copy number. A copy number of 2 indicates a normal ploidy, unless the locus is within the X chromosome in which case cell line derived from males are expected to have a copy number of 1. Colours are for illustrative purposes only, to distinguish individual chromosomes from one another.

Alongside this, the transcriptome of each line was analysed and its similarity to other pluripotent cell types determined (**Figure 4.13**). This was achieved using a PluriTest assay that generates two transcriptome scores: pluripotency score and novelty score (Bunney *et al.*, 2011) (<https://www.thermofisher.com/uk/en/home/life-science/stem-cell-research/stem-cell-services/pluritest-characterization-service.html>). The first is an indication of how similar

the transcriptome is to a reference library that includes >250 stem cell data sets. Partially differentiated cells may have a positive pluripotency score but cannot be reconstructed with data from well-characterised stem cell lines. Partially differentiated cells would have a high novelty score, which is an indication of how well the data set could be reconstructed using the reference data set.



Sample ID	PluriTest Result	Pluripotency Score	Novelty Score
Cas9-RP13-1A	Pass	40.83	1.31
Cas9-RP13-1B	Pass	41.53	1.35
Cas9-RP13-1C	Pass	42.15	1.31
Cas9-RP13-2	Pass	43.92	1.30
iPSC Control	Pass	42.50	1.32
non-iPSC	Fail	-44.83	2.74

Figure 4.13: Pluripotency plot that provides a visual representation of the results in table below. The red and blue areas show the distribution of the pluripotent (red) and non-pluripotent (blue) reference data sets. The distribution of the samples (scores in Table 1; n = 3) can be seen (black circles). A non-iPSC sample was included in this experiment to serve as a negative control for non-pluripotency. Table shows results of transcriptome analysis using an algorithm that integrates gene expression data to determine pluripotency status. Samples are screened against samples in a stem cell database and given a pluripotency

score and novelty score. A positive pluripotency score indicates that the transcriptome has features resembling other pluripotent cell types. A low novelty score indicates that other patterns within the transcriptome can be explained by a database of pluripotent stem cell types.

This shows that all four Cas9 edited lines are pluripotent and free of genomic abnormalities. This corroborates data generated by Dr Chunbo Yang showing that the unedited lines are pluripotent.

4.8 Discussion

iPSCs can serve as an unlimited source of cells that share the same genetic background of the patients they are derived from. They can differentiate *in vitro* and be used to study pathology of diseases, such as PRPF-linked RP. Genetic variability between lines restricts the application of iPSC technology. This chapter provides evidence to show generation of an RP13 isogenic control line that can be used for effective disease modelling.

All RP13 patient- derived iPSCs were screened for *PRPF8* mutations, chromosomal amplifications and chromosomal deletions that might arise during reprogramming of fibroblasts to iPSCs (**Figure 4.3**). This was to identify aneuploidy that could arise during prolonged cell culture. Three clones from each of four RP13 lines were confirmed to harbour H2309P *PRPF8* mutations (**Figure 4.9**). Of the RP13 clones, 92% lacked chromosomal amplifications or deletions and so were suitable for further study (**Figure 4.3**). These iPSC clones were differentiated in parallel using a spontaneous differentiation protocol (Regent *et al.*, 2019). This did not incorporate small molecules to guide differentiation. The efficiency of differentiation was modest across all lines, with some variation between lines (**Figure 4.4**). There was variation between clones of the same line, and between wells of the same clone. The differentiation efficiency was estimated and used to identify one clone from each line that would then undergo CRISPR/Cas9 mediated gene editing.

CRISPR/Cas9 gene- editing requires identification of a gRNA that efficiently recognises the *PRPF8* mutant site. This was identified using an *in vitro* screen, with gRNA efficiency is indicated by absence of a 600 base pair amplicon and presence of two fragments (400 and 200 base pairs long; **Figure 4.7**). This was also proof-of-concept that the ribonucleoprotein

nuclease platform could cleave *PRPF8*. We favoured a ribonucleoprotein rather than a viral expression platform due to its shorter biological half-life and thus reduced risk of multiple cutting events. Viral expression of the Cas9 and guide RNA would introduce a template into the cells that can be translated for weeks, whereas ribonucleoproteins exist in cells for a matter of hours (Chen, Smeeckens and Wu, 2016). The gRNA/Cas9 ribonucleoprotein was introduced to RP13 1B iPSCs following nucleofection. The gRNA guided Cas9 to cleave double-stranded DNA and form double-stranded breaks (DSBs) at the target site. There are two mechanisms of DSB repair: non-homologous end joining (NHEJ), and homology directed repair (HDR). Gene editing exploits the latter, less efficient, mechanism of DSB repair. Several steps were taken to augment a HDR mediated DSB repair response. The first was the use of a single stranded donor oligonucleotide (ssODN). The ssODN has a deliberately asymmetric design that has been shown to facilitate HDR. Lastly, a pharmacological inhibitor of NHEJ further increased HDR mediated DSB repair.

RP13 1B iPSCs were recovered and then dissociated into single cells. Low volumes of this mixture were added to 10 cm petri dishes and colonies began to appear after 1 week. These colonies arose from near single cells and were expanded to allow DNA extraction. The c.6926C>A edit creates an ApaL1 restriction site (wildtype sequence/cut site: G/TGCAC) that allows easy identification of edited clones (**Figure 4.8**). In brief, a *PRPF8* amplicon with an off-centre restriction site was created. Following incubation of the amplicon with ApaL1 edited clones could be identified as those in which all the amplicon was digested to produce two fragments (**Figure 4.8**). Results of the restriction digest were confirmed by Sanger sequencing to reveal that 16% of clones were successfully edited (**Figure 4.10**). The literature reports similar events to have efficiencies that range from less than 1% to almost 50% (Liang *et al.*, 2017). Systematic quantification suggests that efficiency varies with nuclease platform, cell type, and target gene (Miyaoka *et al.*, 2016), and that 16% efficiency is remarkably high. Personal communication with colleagues using the same cell type and nuclease platform (Dr A. Rozanska and Dr C. Yang) suggests that this high efficiency was the result of favourable target sequence properties.

Following confirmation that the gene edit was successful, two clones were selected based on relative signal-to-noise ratio in the Sanger sequencing results. Varying clarity is caused by sample contamination and genetic heterogeneity. To reduce the risk of mosaicism within the selected clones we performed subcloning. The clones were dissociated into single cells and plated at a low density, colonies arose 1 week later and were isolated and cultured. Successful gene editing was confirmed in these subclones (as in **Figure 4.10**). Subsequently, one subclone was selected for off-target sequencing. Off-target sequences are regions of the reference genome with fewer than 5 mismatched bases to the gRNA. There was no evidence of NHEJ (predominant mechanism of DSB repair) in these regions (**Figure 4.11**). This result corroborates a growing body of literature reporting precise gene editing using the CRISPR/Cas9 system (Barrangou *et al.*, 2007; Liang *et al.*, 2015; Xu *et al.*, 2018).

Once it was confirmed that the gene editing event was specific it was important to confirm the pluripotent status of the edited iPSCs. To do this, a transcriptomic analysis of the edited lines was performed. The results were analysed using the PluriTest™ algorithm to generate a Pluripotency and Novelty score. In brief this compares the transcriptome to a library of pluripotent and partially differentiated cells to determine an undifferentiated pluripotent status (**Figure 4.13**). Concurrently we obtained a detailed analysis of chromosomal copy number. Copy number variations can arise during prolonged iPSC culture (Laurent *et al.*, 2011) and therefore, potentially during the gene editing procedure. To determine whether CNVs were acquired, we obtained the chromosomal copy number of 36,000 genes. This showed that there were no chromosomal deletions or amplifications in the edited cells. This result corroborates the previous CNV screen which suggested the unedited iPSCs had not acquired any CNVs (**Figure 4.3** and **Figure 4.12**).

The aim of this study was to generate an isogenic control line. As the edited line underwent nucleofection and was twice propagated from a single cell, there is a risk that single-nucleotide polymorphisms were acquired. We could have isolated an unedited cell population following nucleofection. However, acquiring an unedited cell population would likely increase genetic heterogeneity, as prolonged culturing of the control line would increase risk of SNPs and CNVs (Laurent *et al.*, 2011). The level of genetic similarity could not be assessed using next

generation sequencing as doing so would be uneconomical. The edited cells retained pluripotent status and have a much higher genetic similarity to the patient line. Therefore, despite the lack of information regarding SNPs the edited cells are a more suitable control than an iPSC line derived from an unaffected individual.

The isogenic control line has been produced and it will be differentiated into RPE before being characterised alongside the patient-derived line. This will allow robust identification of transcriptomic, proteomic, and phenotypic changes in iPSC derived RPE that are caused by the c.6926A>C *PRPF8* mutation. This will provide insight into the disease pathology and could elucidate to new treatment options. These results also have an implication with regards to development of autologous cell therapy for RP. The 16% of *PRPF8* gene editing efficiency is relatively high, with reports of editing efficiency at some targets being well below 1% (Miyaoaka *et al.*, 2016). It is also more efficient than the 13% editing efficiency reported in iPSCs from a patient with an RP-causing *RPGR* mutation (Bassuk *et al.*, 2016). This suggests that production of gene-edited autologous transplants for RP13 would be more efficient than similar products targeting other mutations. Thus, RP13 is a form of RP where autologous gene edited transplants are more producible.

This the first RP13 iPSC model and the use of isogenic controls will increase the ability of our experiments to detect transcriptomic and proteomic changes caused by *PRPF8* mutations.

Chapter 5. Characterisation of RP13 and RP13-Cas9 iPSC-RPE Cells

5.1 Introduction

Retinitis pigmentosa (RP) is an inherited retinal dystrophy affecting 1 in 4000 people worldwide (Hartong, Berson and Dryja, 2006). There are over 100 genes implicated in RP onset (Hartong, Berson and Dryja, 2006). Most of these genes encode proteins that are critical to retinal function. This project focuses on *PRPF8*, a gene encoding a core component of the spliceosome that does not have a clear retinal function. Mutations in the spliceosome components thioredoxin-like 4A (*TXNL4A*) (MIM #608572) and splicing factor 3B, subunit 4 (*SF3B4*) (MIM #154400) also cause disease in humans and affect craniofacial development. Mutations in genes that regulate splicing can affect different tissues. For example, TAR DNA-binding protein (*TARDBP*) (MIM #612069) and fused in sarcoma (*FUS*) (MIM #608030) are genes that regulate splicing of a range of mRNAs. Mutations in these genes cause amyotrophic lateral sclerosis which causes degeneration of motor neurons. It is not clear why mutations in these ubiquitously expressed genes cause tissue specific disease in humans.

PRPF8 is one of several genes associated with RP that encode core components of the spliceosome (Hartong, Berson and Dryja, 2006). It is unclear why mutations in ubiquitously expressed genes required for splicing cause a retinal phenotype. Mice harbouring homozygous *Prpf8*^{H2309P/H2309P} mutations exhibit profound RPE dysfunction including loss of polarity, altered phagocytic ability, and decreased adhesion (Farkas *et al.*, 2014). These results suggested that RPE are the primary affected cell type (Graziotto *et al.*, 2011; Farkas *et al.*, 2014). Given that no patients with homozygous mutations have been reported and homozygous mutations may not faithfully recapitulate disease, this chapter characterises iPSC-RPE harbouring heterozygous mutations in *PRPF8*.

In 2018 the Lako group characterised iPSC-RPE cells derived from patients with *PRPF31*-linked RP (Buskin *et al.*, 2018). This confirmed that iPSC technology could recapitulate the *PRPF*-linked RP retinal phenotype. Induced pluripotent stem cell derived-RPE cells that harbour mutations in *PRPF31* exhibit loss of polarity, reduced phagocytic ability, and changes to ciliary structure (Buskin *et al.*, 2018). In addition, there was global disruption in alternative splicing across all tissues (**Figure 5.1**). Enrichment analysis of the alternatively spliced transcripts in the

RPE identified RNA splicing and cellular respiration as the most significantly enriched gene ontology (GO) biological processes and adherens junction and mitochondrial inner membrane in the top five most significantly enriched GO cellular components (**Figure 5.1**). In retinal organoids, splicing related GO biological processes were also highly enriched as well as several cilia-related GO cellular components (microtubule, centrosome, centriole, microtubule organising centre part).

This chapter builds on this previous report by the Lako group. The results presented use the CRISPR/Cas9 gene-edited iPSCs that were generated in chapter 4. These cells serve two functions: 1) to reduce genetic variability that could confound results and 2) to assess gene editing as a treatment of *PRPF8*-linked RP. Similarities including a change to ciliary structure and a loss of epithelial polarity between the RP11-RPE and RP13-RPE phenotypes are identified as reproducible features of *PRPF8*-associated RP.

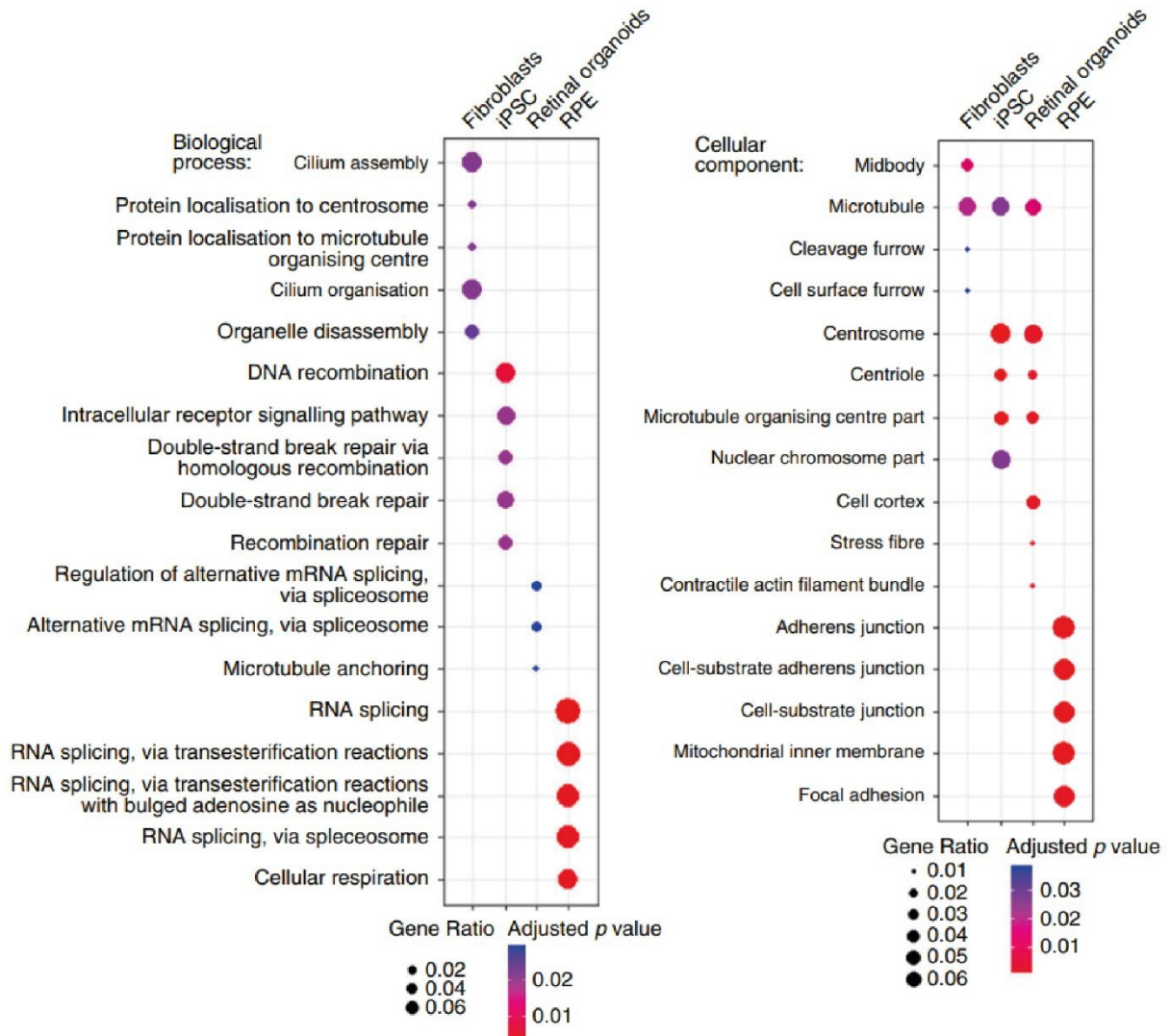


Figure 5.1 Dot plots showing enrichment analysis of genes that were alternatively spliced in fibroblasts, iPSCs, retinal organoids, and RPE cells harbouring *PRPF31* mutations. The top five A) Gene ontology (GO) biological processes and B) GO cellular components identified in each cell type are plotted. The size of the point (gene ratio) shows the fraction of the category that is represented in the data set. The colour of the points (adjusted P-value) indicates the likelihood that the result was obtained due to chance. Figure taken from Buskin et al., 2018.

5.2 Aims

This chapter aims to validate the differentiation of iPSCs into RPE and identify differences between RP13 and RP13-Cas9 iPSC-RPE cells using:

- Brightfield and immunofluorescence microscopy to assess iPSC-RPE cell morphology
- Transepithelial electrical resistance (TEER) to evaluate barrier function
- Immunofluorescence microscopy to assess of RPE polarity
- Flow cytometry to assess phagocytosis of photoreceptor outer segments (POS)
- Transmission electron microscopy (TEM) to quantify cell ultrastructure
- Confocal fluorescence microscopy and serial block face scanning electron microscopy (SBF-SEM) to investigate cilia structure

5.3 RP13 and RP13-Cas9 iPSC-RPE cells have characteristics of human RPE

Previously in chapter 4, iPSCs from four RP13 patients were differentiated into iPSC-RPE cells carrying a heterozygous *PRPF8* mutation alongside paired isogenic controls (**Table 9**). RP13-1C iPSCs differentiated with poor efficiency and as a result could not be characterised. As both RP13-1C and RP13-1C-Cas9 differentiated with poorer efficiency compared to all other iPSC lines, this effect appears to be caused by donor dependent variation. To explain further, differences in the genetic background of this individual make the derived iPSCs less amenable to iPSC-RPE differentiation. Following successful differentiation, iPSC-RPE cells derived from RP13-1A (originally clone 3), RP13-1B (originally clone 3), RP13-2 (originally clone 3), and the respective isogenic controls were purified and then seeded onto porous transwell inserts that both promote maturation and facilitate imaging. Following a 12-week maturation period, cell morphology and barrier function were assessed to validate differentiation of RP13 and RP13-Cas9 iPSC-RPE cells.

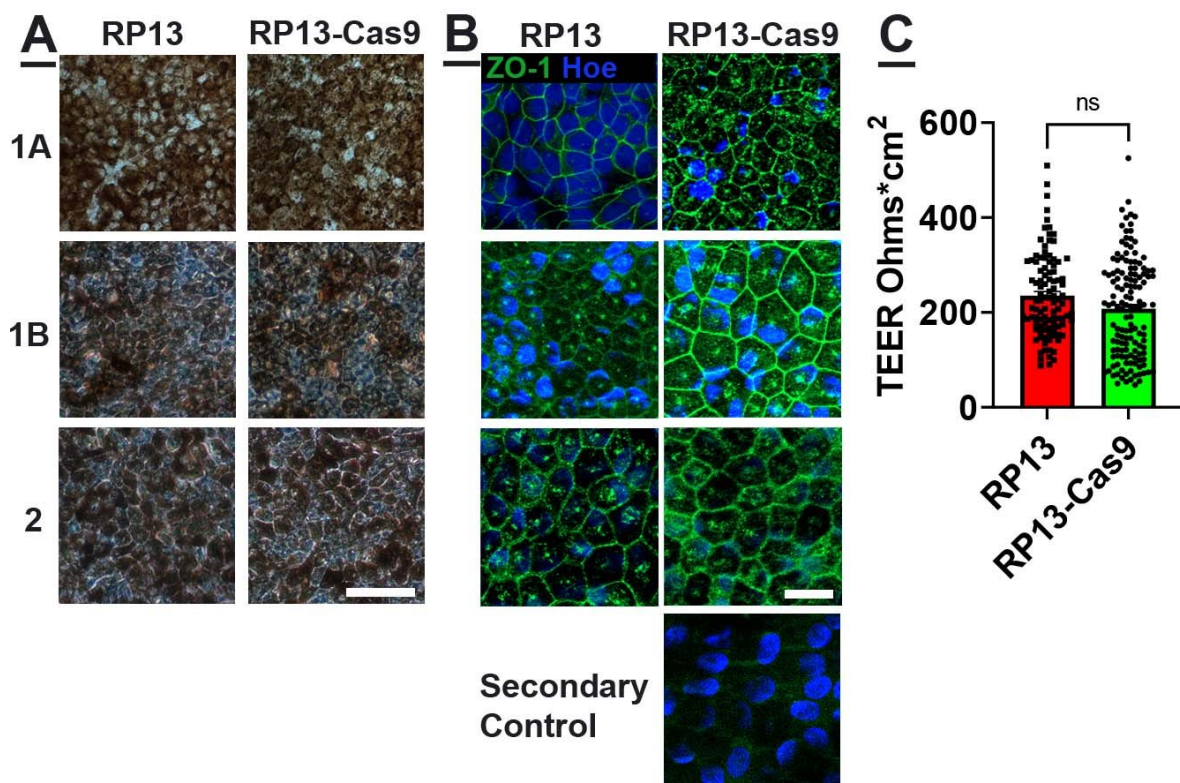


Figure 5.2: RP13 and RP13-Cas9 iPSC-RPE cell cultures form monolayers of pigmented epithelial cells. A) Brightfield images of iPSC-RPE cell monolayers show pigmented cells with cobblestone morphology, scale bar is 50 μm and $n = 3$. B) ZO-1 immunofluorescent images

of iPSC-RPE cells shows the presence of tight junctions between adjacent cells and hexagonal cell morphology, scale bar is 20 μm and $n = 3$. C) TEER values of RP13 ($235 \pm 9 \Omega \cdot \text{cm}^2$, $n = 102$) and RP13-Cas9 iPSC-RPE ($214 \pm 10 \Omega \cdot \text{cm}^2$, $n = 118$) were not significantly different ($p = 0.12$). Statistical significance was determined using 2-tailed Student's t-test. N was defined as one transwell insert, results are mean \pm SEM.

There were no obvious changes in cell morphology apparent using brightfield microscopy (Figure 5.2 A). This was corroborated by immunofluorescent staining of ZO-1, a marker of cell borders, which showed hexagonal cell morphology in both RP13 and RP13-Cas9 iPSC-RPE (Figure 5.2 B). The ZO-1 staining appeared less intense in RP13 compared to RP13-Cas9. To determine whether there was a functional change in barrier function between RP13 and RP13-Cas9, electrical resistance of the tissue was quantified using transepithelial electrical resistance (TEER). These results suggested that there was no effect of *PRPF8* mutation on RPE barrier function (Figure 5.2 C). After confirming normal cell morphology, we proceeded with further functional assessment using flow cytometry.

5.4 *PRPF8* Mutation Does not Impact Photoreceptor Outer Segment Phagocytosis *in-vitro*

One of the key RPE functions *in vivo* is daily phagocytosis of POS which occurs in time with the light-dark cycle. Disruption of this process has long been associated with inherited retinal disease (Bok and Hall, 1971).

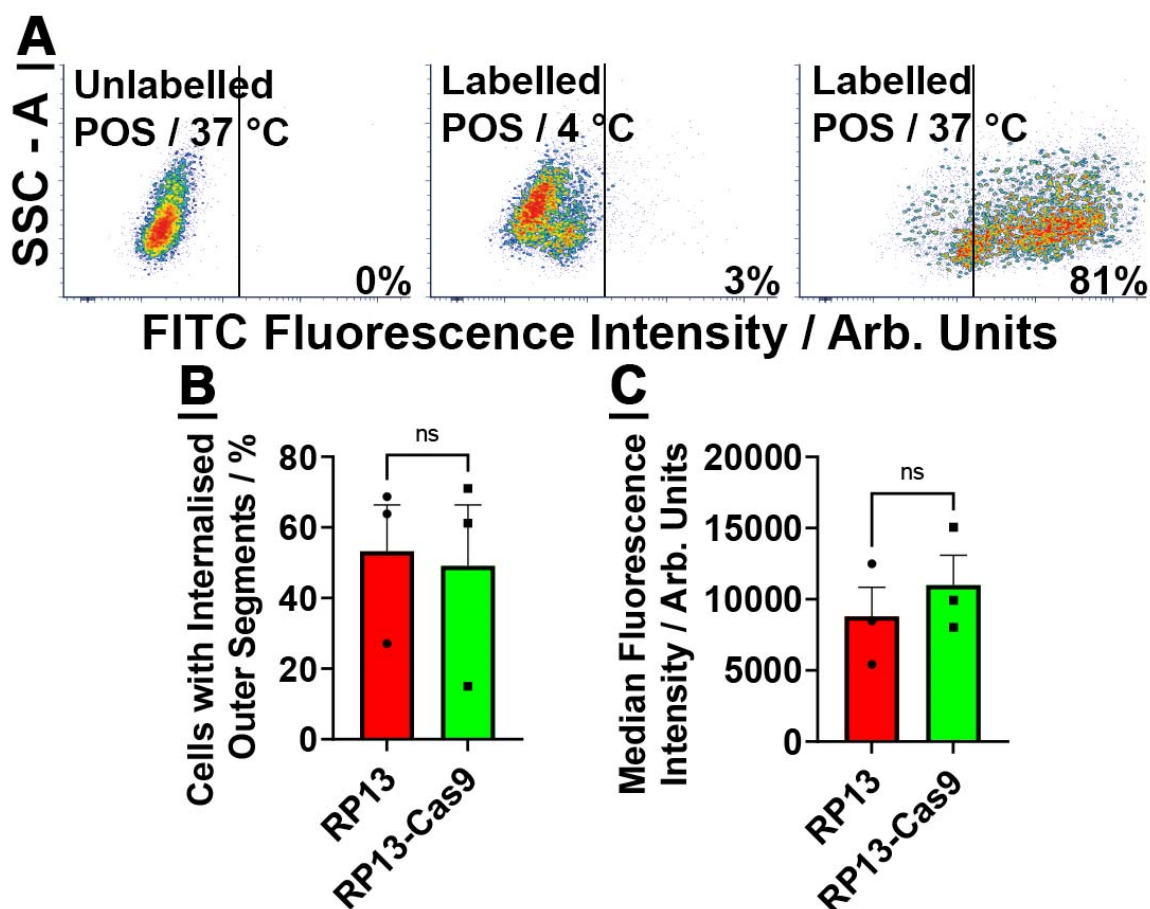


Figure 5.3: Quantified phagocytosis of FITC-labelled photoreceptor outer segments (POS) by iPSC-RPE cells. A) Flow cytometry scatter plots showing side scatter (SSC-A; cell granularity) and FITC fluorescence across three conditions. iPSC-RPE cells challenged with unlabelled POS then incubated at 37 °C (left), labelled POS then incubated at 4 °C (middle), and labelled POS then incubated at 37 °C. Numbers in the bottom right of each plot indicate the percentage of cells identified as phagocytic. B) Bar chart showing average percentage of RP13 and RP13-Cas9 iPSC-RPE cells that phagocytosed fluorescently labelled POS after incubation at 37 °C. C) Bar chart showing average median fluorescence intensity of the same cell populations. Results are mean \pm SEM, N = 3 where n is the number of independent experiments. A minimum of 10,00 observations were recorded per experiment.

To establish the level of fluorescence that was caused by phagocytosis of photoreceptor outer segments, two controls experiments were performed. The first control challenged RPE cells at 37 °C with unlabelled POS, this was used during the analysis to determine whether the fluorescence observed was caused by the FITC-labelling of POS. The second control challenged iPSC-RPE cells with fluorescently labelled POS at 4 °C. This was used to identify fluorescence that was not caused by phagocytosis of the FITC dye e.g., FITC that passively entered the cells.

This fluorescence was deemed to be background signal and can be seen in the middle panel of **(Figure 5.3 A)**. The level of fluorescence identified in these control experiments was not caused by phagocytosis, and this information was used to identify true phagocytic events. On average, 71% of the iPSC-RPE cell population phagocytosed fluorescent POS, but there was no statistically significant difference between RP13 and RP13-Cas9 **(Figure 5.3 B, Table 9)** excluding RP13-1C and RP13-1C-Cas9). The median fluorescence intensity (MFI) is proportional to the number of labelled POS phagocytosed per cell. Quantification of MFI suggested that there was no significant difference in the number of POS phagocytosed per cell between RP13 and RP13-Cas9 iPSC-RPE **(Figure 5.3 C)**.

5.5 Ultrastructural Analysis of RP13 and RP13-Cas9 iPSC-RPE cells

Following validation of iPSC-RPE cell function, we performed transmission electron microscopy (TEM) of iPSC-RPE cells derived from three RP13 patients (RP13-1A-3, RP13-1B-3, and RP13-2-3) and the respective isogenic controls **(Table 9)**. All cells possessed typical RPE organelles such as melanosomes, mitochondria, and extracellular material. Samples were processed for TEM and imaged by Mr Ross Laws before being analysed by a BSc (Miss Chia Beh) and MRes student (Mr Abhijit Saxena), who were blind to cell identity.

5.5.1 Cell Area

Cell area was quantified to determine whether there was a significant effect of *PRPF8* mutation on cell size. It could also be used as a way of normalising measurements between samples.

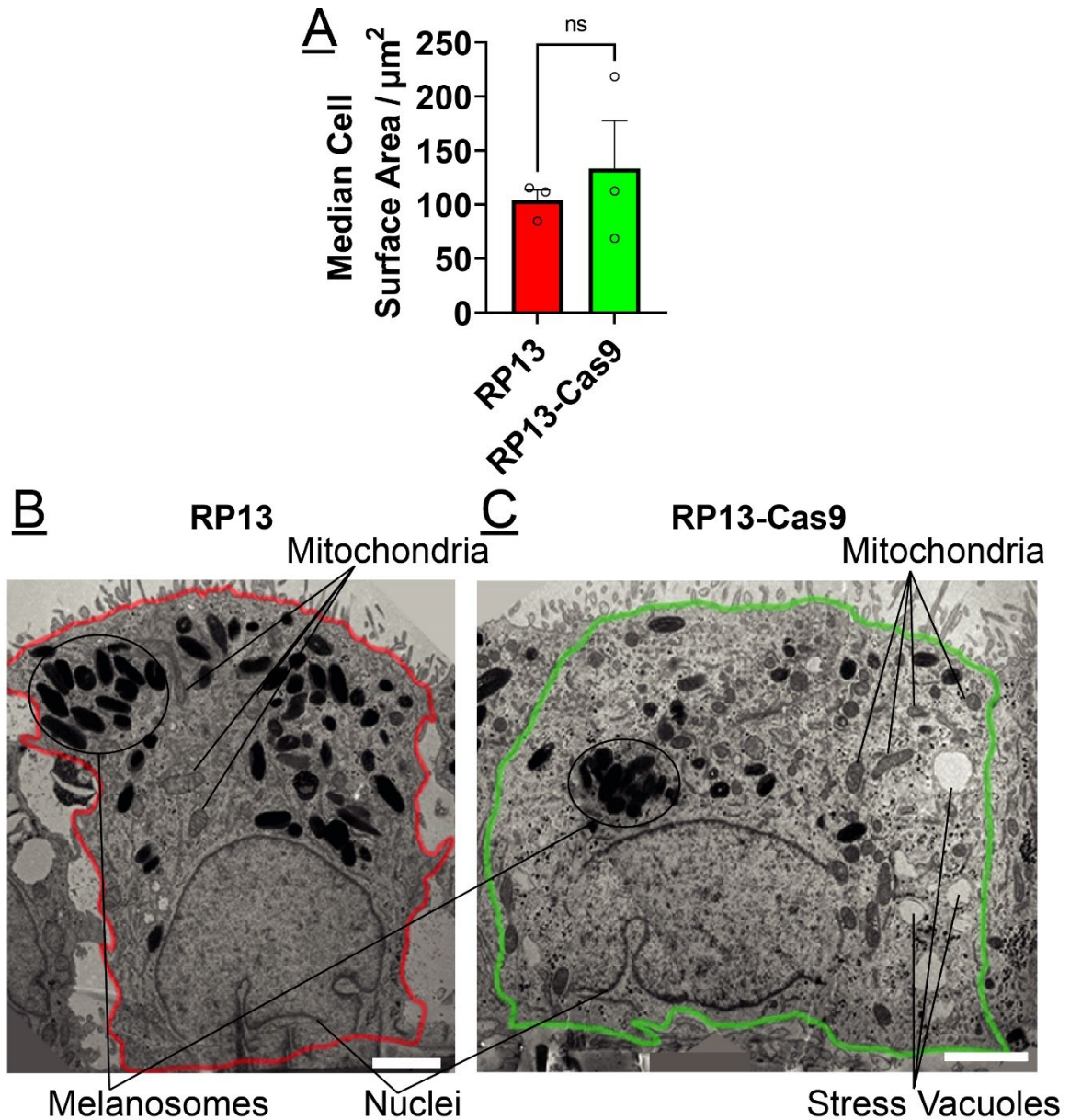


Figure 5.4: Quantification of cross-sectional cell surface area and example transmission electron microscopy (TEM) images. **A)** The mean surface area of RP13 ($101 \pm 7 \mu\text{m}^2$) and RP13-Cas9 ($127 \pm 32 \mu\text{m}^2$) iPSC-RPE cells. $N = 3$ where n is the median value for each donor (RP13-1A, RP13-1B, RP13-2) for both RP13 and RP13-Cas9 samples. The median value was calculated using 10 whole cell images per donor. Results presented are mean \pm SEM of 3

donors. Significance was assessed using 2-tailed paired t-test. B) Example TEM images from RP13 with the cell membrane highlighted in red. Examples melanosomes, mitochondria and the nucleus are also labelled. C) RP13-Cas9 iPSC-RPE cells with the cell membranes highlighted in green. Example melanosomes, mitochondria and stress vacuoles are labelled. The basal membrane is visible in both B and C as the highlighted surface that traverses the bottom of the images. Scale bars are 2 μm .

The mean surface area across all iPSC-RPE cells was 114 μm^2 . There was no significant difference in surface area between RP13 (Figure 5.4 A and B) and RP13-Cas9 (Figure 5.4 A and C) iPSC-RPE cells. The whole cell images provided show other ultrastructural features such as mitochondria, melanosomes, and stress vacuoles in the context of a whole cell image. These structures are analysed in more detail throughout this chapter.

5.5.2 Melanosomes and Melanosome Complexes

Using a similar approach, we quantified the number of melanosomes and melanosome complexes present in RP13 and RP13-Cas9 iPSC-RPE cells. There are four stages of melanosome development and two types of melanosome complex. Melanosomes in stage one of development appear vesicular, electron-dense proteinaceous fibrils begin to grow in stage two of development. Melanin deposition on these fibrils increases in stage 3, making the fibrils highly electron dense. When sufficient melanin is deposited onto these fibrils, the fibrils cannot be distinguished from one another. This is the final stage, stage four, of melanosome development. Melanosomes may later be broken down by lysosomes, the intermediate structure is known as a melanolysosome. Melanosomes can also form complexes with lipofuscin, during aging these complexes tend to accumulate (Feeney, 1978). Within the six iPSC-RPE samples we identified stage III and stage IV melanosomes. In addition, we observed two types of melanosome complex: melanolysosomes and melanolipofuscin. These were identifiable from other cellular electron-dense bodies by their relatively high electron-density.

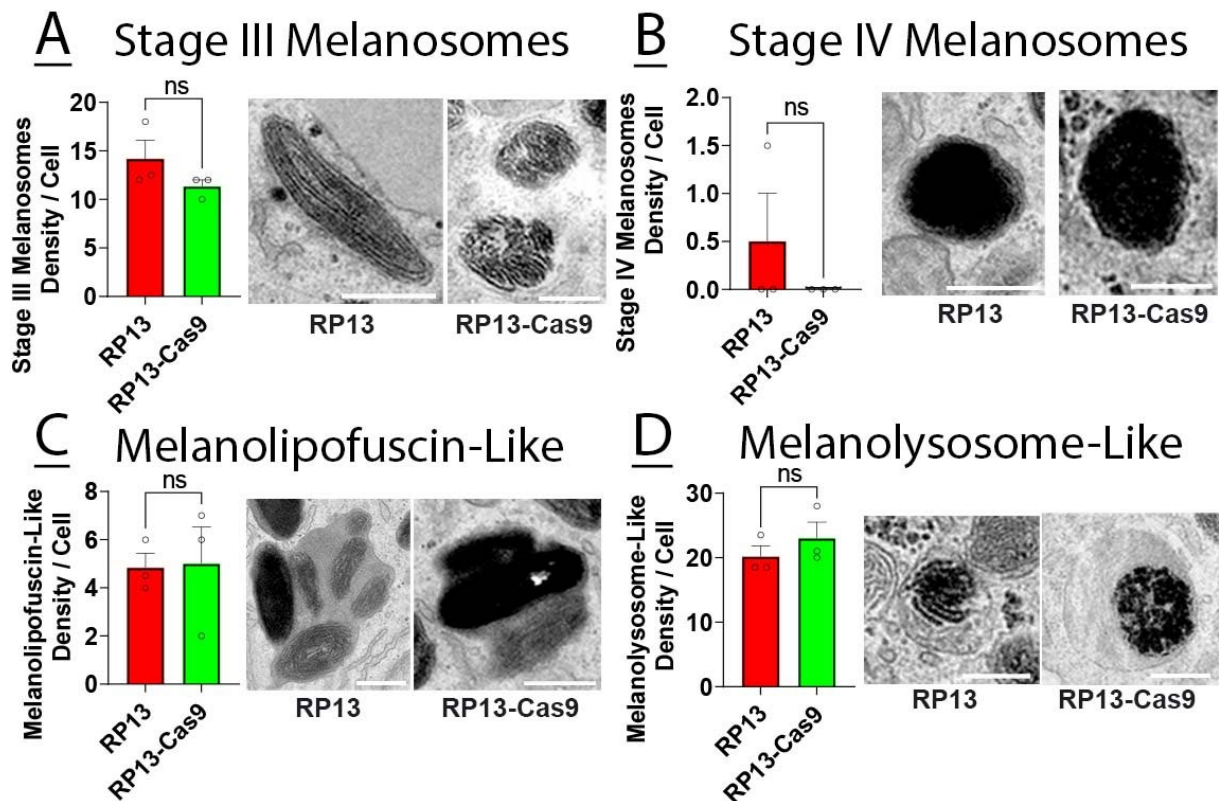


Figure 5.5: Quantification of melanosomes, melanosome-complexes, and example TEM images. A) Bar chart showing density of stage III melanosomes per cell in RP13 (14.2 ± 1.9) and RP13-Cas9 iPSC-RPE cells (11.3 ± 0.67). B) Bar chart showing density of stage IV melanosomes per cell in RP13 (0.5 ± 0.5) and RP13-Cas9 iPSC-RPE cells (0 ± 0). C) Bar chart showing density of melanolipofuscin-like complexes per cell in RP13 (4.8 ± 0.6) and RP13-Cas9 iPSC-RPE cells (5.0 ± 1.5). D) Bar chart showing density of melanolysosome-like complexes per cell in RP13 (20.2 ± 1.7) and RP13-Cas9 iPSC-RPE cells (23.0 ± 2.5). Two example images are presented on the right-hand side of each chart, scale bars are $0.5 \mu\text{m}$. Statistical significance was assessed using 2-tailed paired t-test, results are mean \pm SEM. $N = 3$ where n is the median value for each donor, calculated using 10 whole cell images per donor.

Melanosomes and melanosome complexes could be categorised by comparing to previous studies. Stage III melanosomes have a fibrillar structure, and this structure is not visible after melanosomes mature to stage IV (Raposo and Marks, 2007). Melanolipofuscin-like complexes were identified as one or more melanosomes surrounded by a less-electron-dense matrix (Feeney, 1978). Melanolysosome-like complexes were identified as melanosomes within membrane-delimited structures and/or showing evidence of degradation (Gouras *et al.*, 2011). Evidence of degradation includes disrupted structure of the melanosome, stage IV melanosomes have a homogenous electron-dense interior (**Figure 5.5 B**) whereas

melanosome-like structures have more heterogenous electron density in their interiors (Figure 5.5 D). Statistical analysis suggests there is no significant difference in the frequency of melanosomes or melanosome-complexes between RP13 and RP13-Cas9 iPSC-RPE cells (Figure 5.5).

5.5.3 Stress Vacuoles

Stress vacuoles are round electron-lucent objects present in the cytoplasm. They have previously been reported to be more frequent in the RPE cells of mice harbouring mutations in *PRPF8* (Graziotto *et al.*, 2011). To determine whether this effect is recapitulated in an iPSC-RPE cell model we counted the number of stress vacuoles per cell.

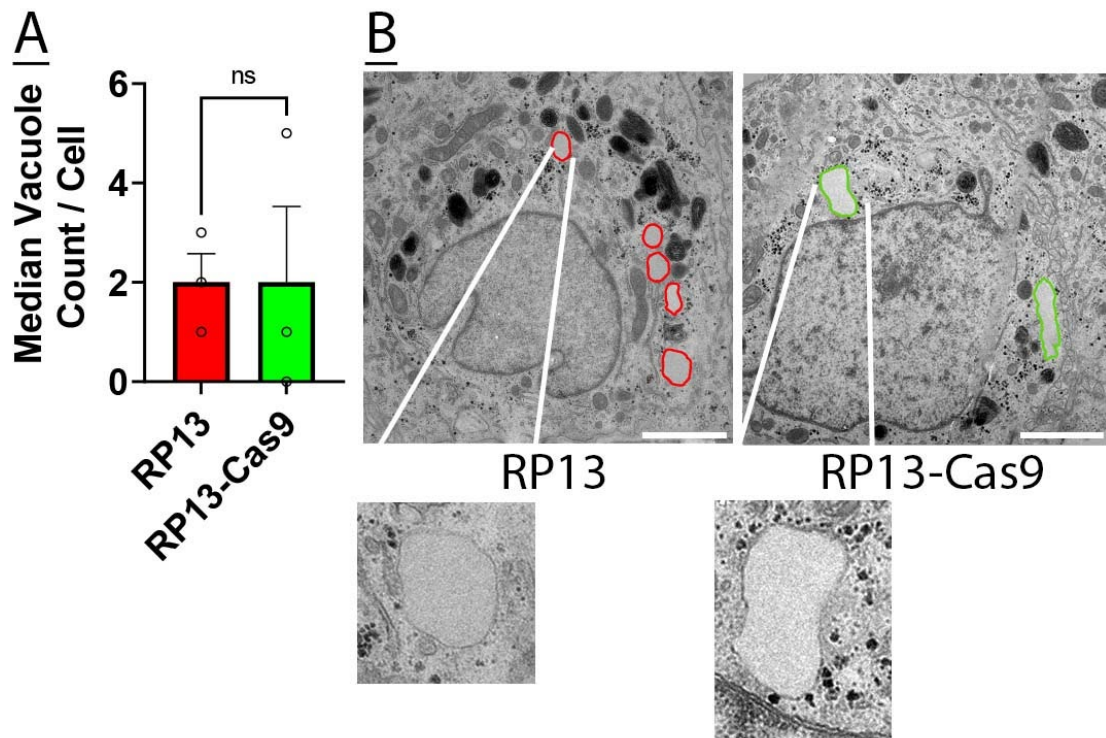


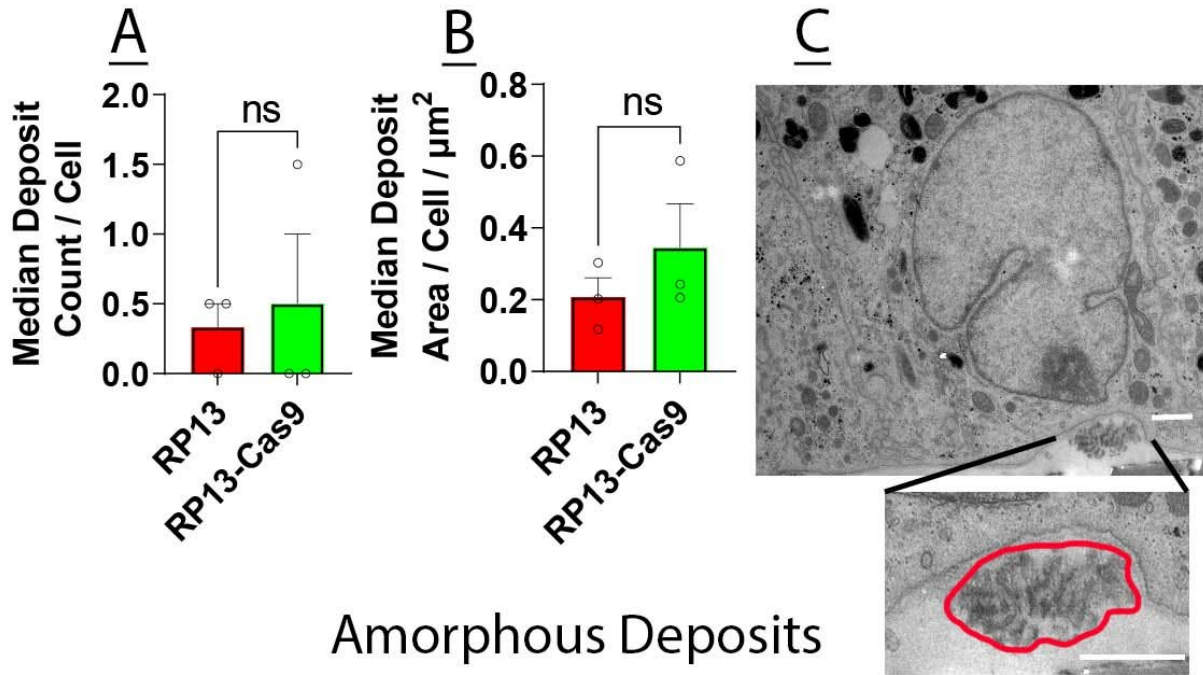
Figure 5.6: TEM image quantification of stress vacuoles and example TEM images. A) Bar chart showing median vacuole counts per cell for RP13 (2.0 ± 0.6) and RP13-Cas9 iPSC-RPE cells (2.0 ± 1.5). $N = 3$ where n is the median value for each donor, calculated using 10 whole cell images per donor. Statistical significance was assessed using 2-tailed paired t-test, results are mean \pm SEM. B) TEM images showing stress vacuoles (round, electron-lucent objects) in RP13 (red) and RP13-Cas9 (green) iPSC-RPE cells. High magnification images are provided below. Scale bars are 2 μ m.

Stress vacuoles are readily identifiable due to their large ($\sim 1 \mu\text{m}$ diameter) and electron-lucent appearance (**Figure 5.6 B**). Objects of a similar appearance that were not electron lucent were also present in some samples. Statistical analysis suggests that the number of stress vacuoles per cell does not differ between RP13 and RP13-Cas9 iPSC-RPE cells (**Figure 5.6 A**).

5.5.4 Basal Deposits

The extracellular matrix secreted by iPSC-RPE cells contains a number of protein components such as collagens and laminins that are important for cell adhesion (Strauss, 2005). These form part of the Bruch's membrane, a layer of extracellular material that separates the RPE from the choriocapillaris. We could identify two types of basal deposit: collagenous deposits, which have an obvious laminated structure and amorphous deposits. The area of these deposits as well as number was measured.

Collagenous Deposits



Amorphous Deposits

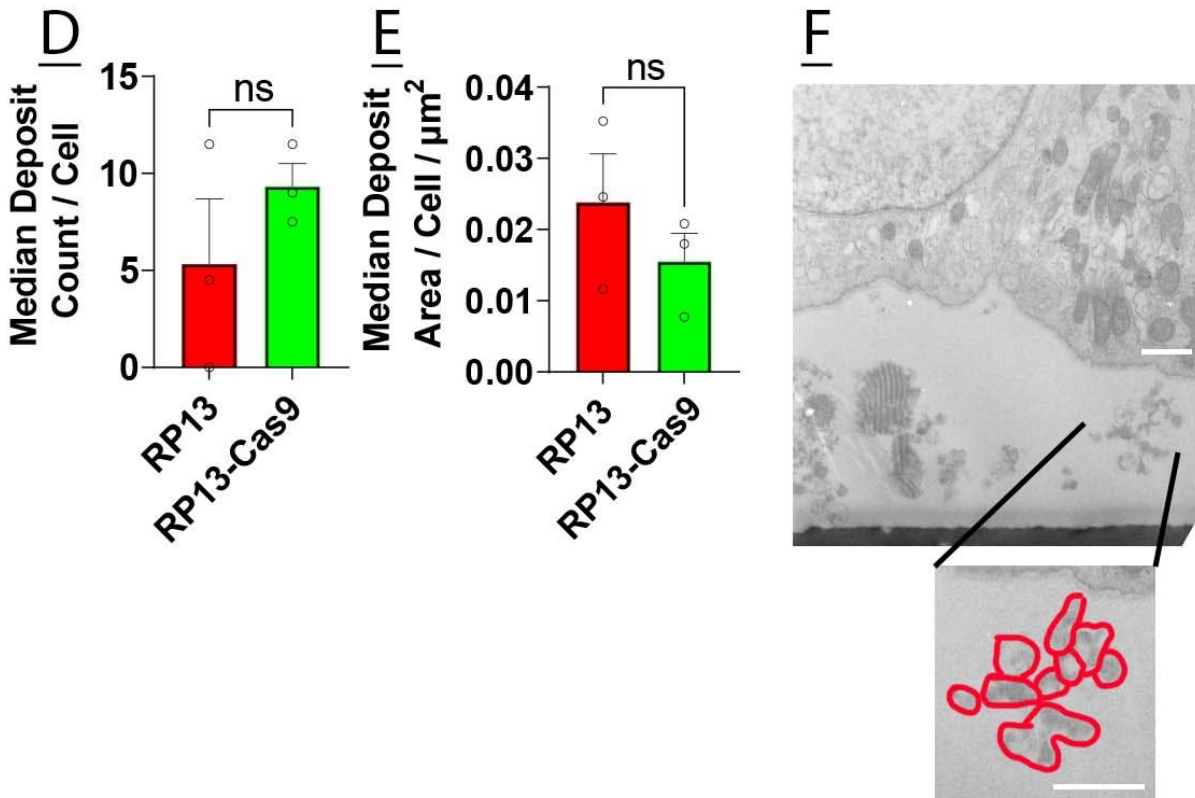


Figure 5.7: TEM image quantification of number and area of basal deposits, and example images. Bar charts showing the A) median number and B) median area of collagenous

deposits per cell in RP13 and RP13-Cas9 iPSC-RPE cells. C) TEM image of a collagenous deposit (outlined in red) with characteristic banded appearance. Bar charts showing the D) median number and median area E) of amorphous deposits per cell in RP13 and RP13-Cas9 iPSC-RPE cells. F) TEM image of an amorphous deposit (outlined in red), round electron dense structures. Results are mean \pm SEM, $n = 3$ where n is the median value for each donor, calculated using 10 whole cell images per donor. Significance was assessed using 2-tailed paired t-test. Scale bars are 1 μm .

We categorised and quantified the number and surface area of basal deposits per cell (**Figure 5.7**). This showed that collagenous deposits are larger but less abundant than amorphous deposits. Statistical analysis showed that there was no significant difference between the number or area of collagenous basal deposits (**Figure 5.7 A-C**). Nor was there a significant difference in the number or area of amorphous basal deposits (**Figure 5.7 D-F**).

5.5.5 Basal Membrane Linearity

The basal membrane of RPE cells has numerous infoldings to increase surface area and facilitate transport of nutrients and ions between RPE and the choriocapillaris. To determine whether basal membrane infolding is altered in an iPSC-RPE model we quantified linearity of the basal membrane.

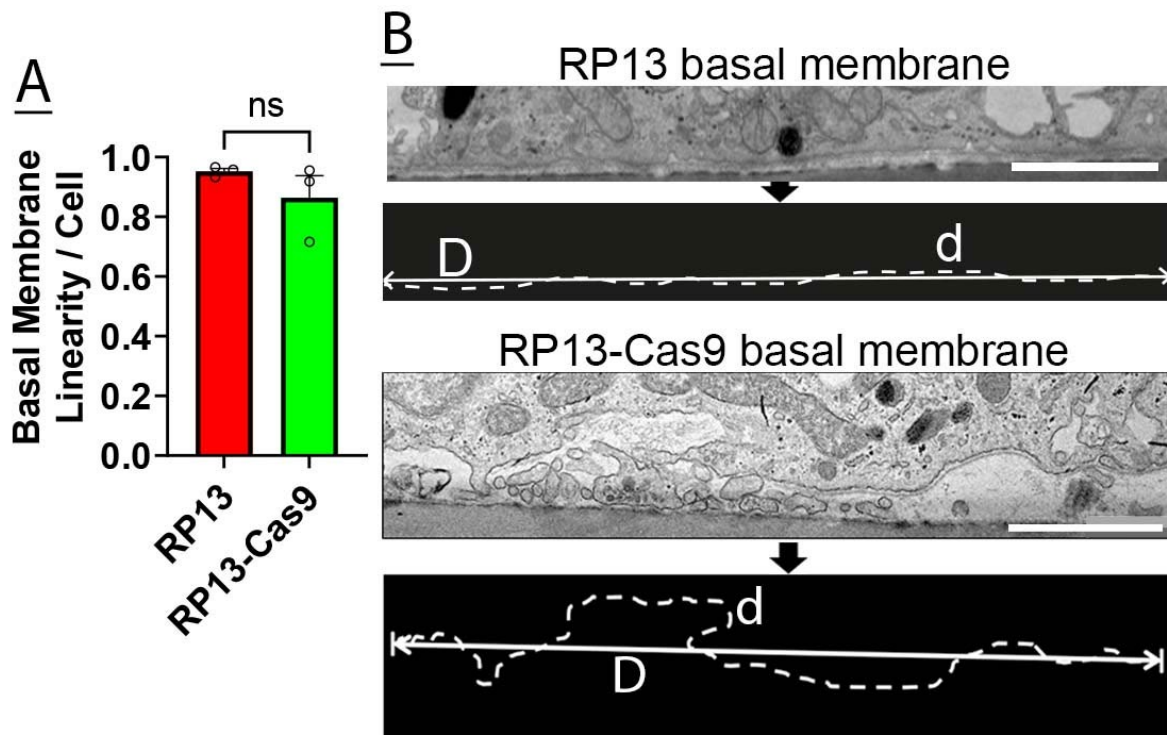


Figure 5.8: TEM image quantification of basal membrane linearity, example TEM image and diagrammatic explanation of measurement. **A)** Bar chart showing basal membrane linearity of RP13 (0.95 ± 0.01) and RP13-Cas9 (0.86 ± 0.07) iPSC-RPE cells. $N = 3$ where n is the median value for each donor, calculated using 10 whole cell images per donor. Statistical significance was assessed using 2-tailed paired t-test. **B)** TEM image showing infoldings of the basal cell membrane. The cell width was measured as a linear distance (D) and a freehand membrane trace (d), $linearity = (d/D)$. Scale bar is $2 \mu\text{m}$.

The average basal membrane linearity was 0.9 across RP13 and RP13-Cas9 iPSC-RPE cells. Linearity is calculated as the linear distance across the cell divided by the length of the basal membrane. A low linearity value indicates a higher degree of infolding, as illustrated (**Figure 5.8 B**). The data shows a trend towards more infolding in RP13-Cas9, but the difference was not statistically significant ($p = 0.39$) (**Figure 5.8 A**).

5.5.6 Mitochondrial Shape and Number

Mitochondria can be identified by their morphology and relative electron density. Each mitochondria have either a round or flat oval morphology and is more electron-dense than the surrounding cytoplasm but less electron dense than melanosomes. A subset of mitochondria has clearly defined cristae. These were used as a reference when evaluating which other objects in the image are mitochondria.

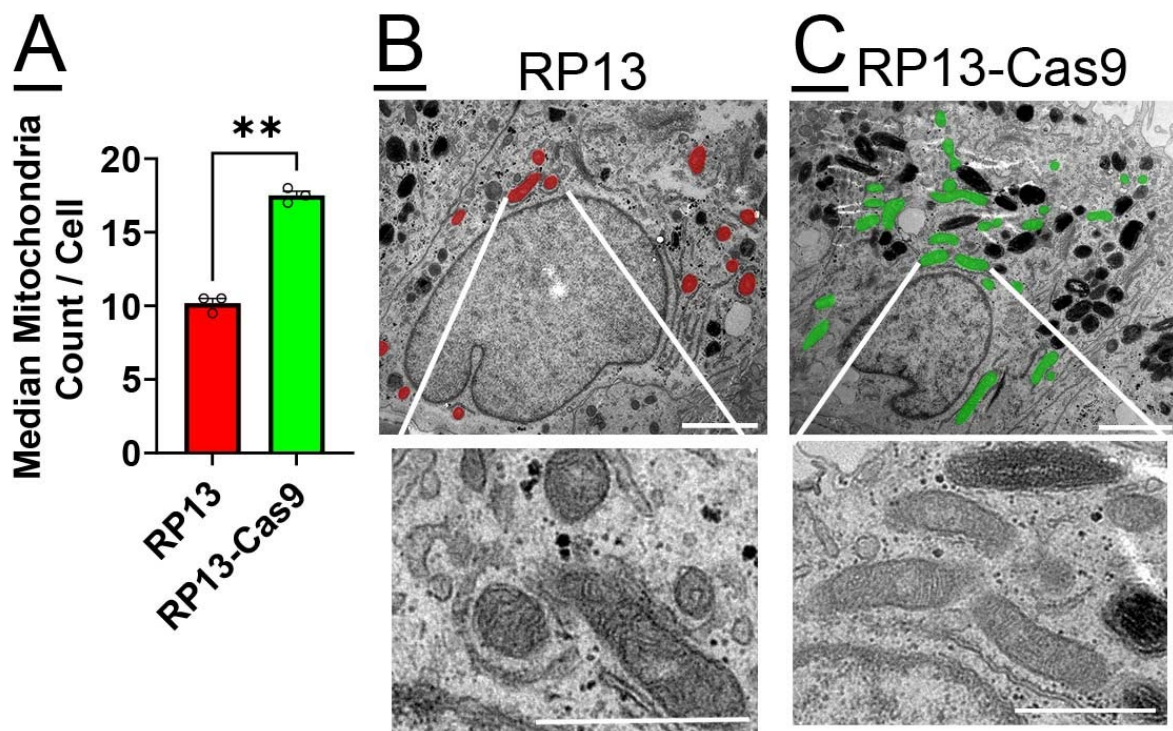


Figure 5.9: Quantification of mitochondrial number per cell and representative TEM images. A) Bar chart showing the number of mitochondria per cell was significantly ($p < 0.01$) lower in RP13 (10.4 ± 0.3) compared RP13-Cas9 iPSC-RPE cells (16.9 ± 0.7). $N = 3$ where n is the median value for each donor, calculated using 10 whole cell images per donor. Statistical significance was assessed using 2-tailed paired t-test. Results are mean \pm SEM. B) Example TEM image of RP13 and C) RP13-Cas9 iPSC-RPE cell with mitochondria highlighted in red and green, respectively. Scale bars are $2 \mu\text{m}$ in whole cell images and $1 \mu\text{m}$ in high resolution images of mitochondria.

In RP13-Cas9 iPSC-RPE cells there is an average of 16.9 ± 0.7 mitochondria per cell, whereas in RP13 iPSC-RPE cells there is an average of 10.4 ± 0.3 mitochondria per cell. The standardised

effect size (Cohen's *d*) is 7, suggesting an extreme effect that is unlikely to occur due to chance ($p < 0.01$) (Figure 5.9).

The mitochondria exhibit range of morphologies ranging from elongated too circular. To determine whether mitochondrial shape is affected in RP13 iPSC-RPE cells we measured mitochondrial aspect ratio.

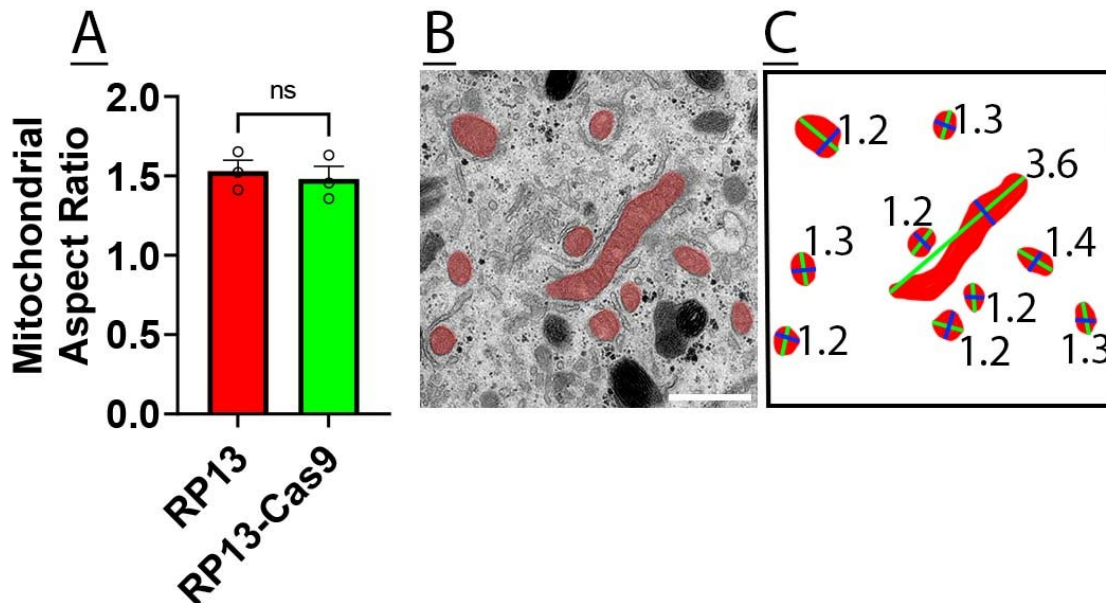


Figure 5.10: Quantification of mitochondrial aspect ratio, example TEM image and explanation of measurement. A) Bar chart showing median aspect ratio of mitochondria in RP13 (1.50 ± 0.06) and RP13-Cas9 (1.49 ± 0.06) iPSC-RPE cells. Statistical significance was assessed using 2-tailed paired t-test. $N = 3$ where n is the median value for each donor, calculated using 10 whole cell images per donor. B) Mitochondria (red) are identified by their double-membrane, and relative electron-density compared to the cytoplasm. C) Aspect ratio of mitochondria (red) was calculated by dividing the length of the major axis (green) by the minor axis (blue). Aspect ratios are written next to the mitochondria.

The mitochondrial aspect ratio is the length of the mitochondrial major axis divided by the mitochondrial minor axis (Figure 5.10 C). The average mitochondrial aspect ratio was not affected by *PRPF8* mutation (Figure 5.10 A). These results show that mitochondrial number is significantly reduced by *PRPF8* mutation, but shape is unaffected.

5.6 RP13 iPSC-RPE cells have Altered Ciliary Structure

We hypothesised that *PRPF8* mutation leads to mis-splicing that affects multiple cell compartments such as the RPE primary cilia, which is affected by RP11 causing mutations (Wheway *et al.*, 2015a; Buskin *et al.*, 2018). There are two ways that PRPF function links to the cilia. Knockdown of *PRPF8* and other RP-linked PRPFs was shown to reduce ciliogenesis in immortalised cell lines (Wheway *et al.*, 2015b). The same article also showed that these PRPFs localise to the base of the cilia (Wheway *et al.*, 2015b). Furthermore, a subsequent investigation by the Lako group showed that ciliary transcripts were highly enriched in the list of genes that were alternatively spliced in retinal organoids harbouring *PRPF31* mutations (**Figure 5.1**). Cilia are important for retinal function, as is evident from the large number of ciliary mutations that lead to retinal degeneration (Gerdes, Davis and Katsanis, 2009).

We assessed cilia structure using immunofluorescence microscopy then quantified cilia length and incidence. These are frequently used markers of cilia related disease.

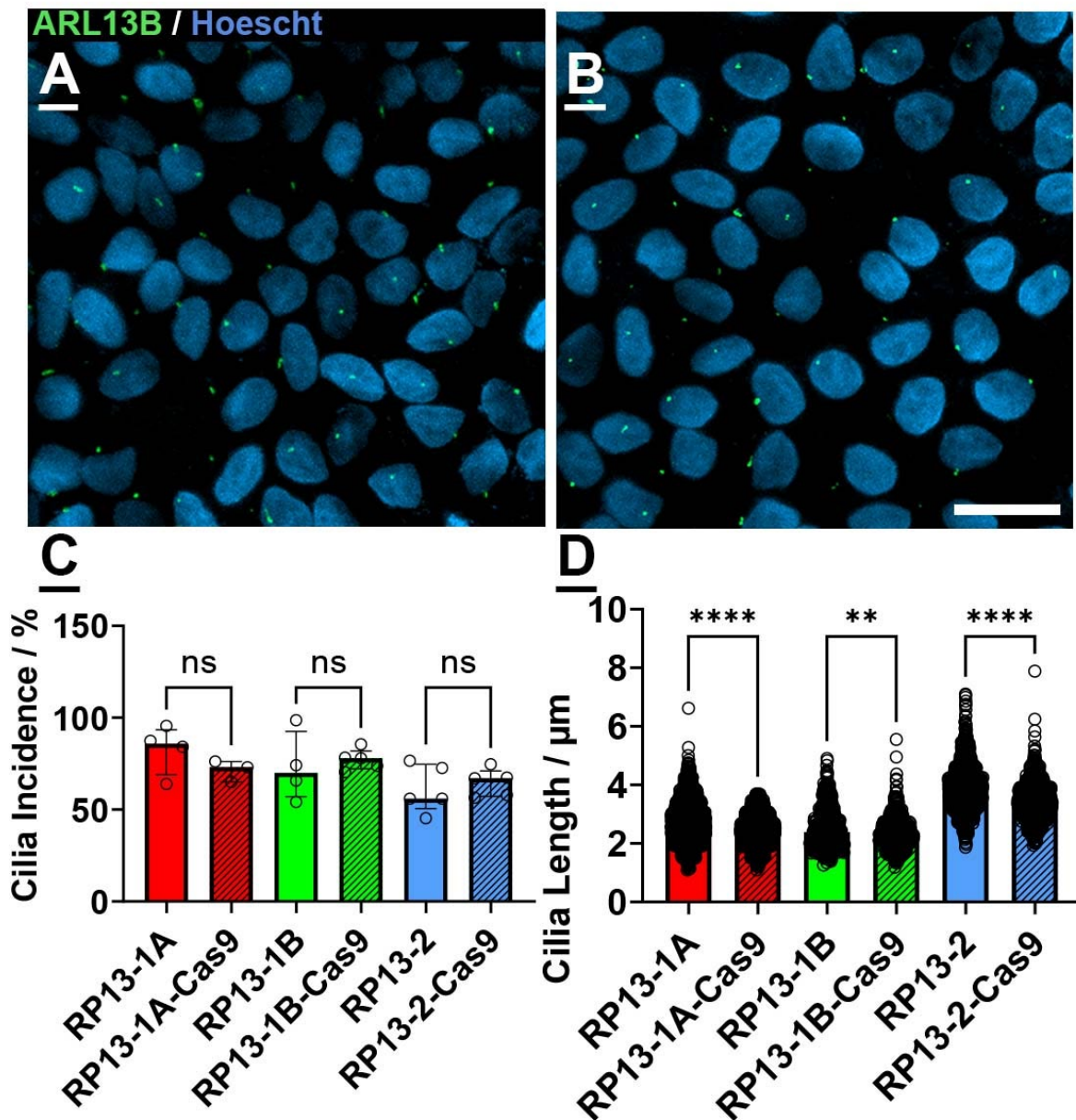


Figure 5.11: Quantification of cilia length and incidence using ARL13B immunofluorescent images. A) Example ARL13B immunofluorescent images of RP13 and B) RP13-Cas9 iPSC-RPE cells, ARL13B is green, and Hoescht/DNA is blue. C) Bar chart showing average cilia incidence per iPSC line. N = 5 where n is defined as fields of view (>100 cells) per donor D) Bar chart showing average cilia length per sample. N > 500 where n is defined as number of cilia. Statistical significance was assessed using 2-tailed Student's t-test. Results are mean \pm SEM. Scale bar is 20 μ m.

By taking the average result presented in (Figure 5.11 C) these results show that 75% of RP13 (RP13-1A-3, RP13-1B-3, RP13-2-3) and RP13-Cas9 iPSC-RPE cells have primary cilia, as determined using ARL13B immunofluorescence (Figure 5.11). There was no significant

difference in cilia incidence between RP13 and RP13-Cas9 iPSC-RPE cells (**Figure 5.11 C**). However, quantification of cilia length revealed a 10% increase in RP13 cilia length compared to RP13-Cas9 iPSC-RPE cells (**Figure 5.11 D**). These results suggest that iPSC-RPE cilia structure is affected by *PRPF8* mutation. To resolve ciliary structural changes at higher resolution we imaged iPSC-RPE cells using SBF-SEM. This technique generates backscattered electron microscopy images and allows visualisation of ciliary ultrastructure.

Cilia were identified by their ultrastructural features which are well documented (reviewed in (Fisch and Dupuis-Williams, 2011)). In brief, the ciliary axoneme protrudes from the apical cell surface. The ciliary membrane and cell surface membrane join at a small depression at the base of the cilia, known as the ciliary pocket. This region of membrane is linked to the base of the axoneme by distal appendages. These project from the distal (closest to the apical cell surface) portion of the basal body and are found adjacent to the subdistal appendages. The basal body is a barrel shaped structure that forms when the centriole docks to the cell surface membrane. It is formed by a ring of nine microtubule triplets. This distinctive ring structure makes the basal body particularly striking by electron microscopy and so it was often the first cilia marker identified.

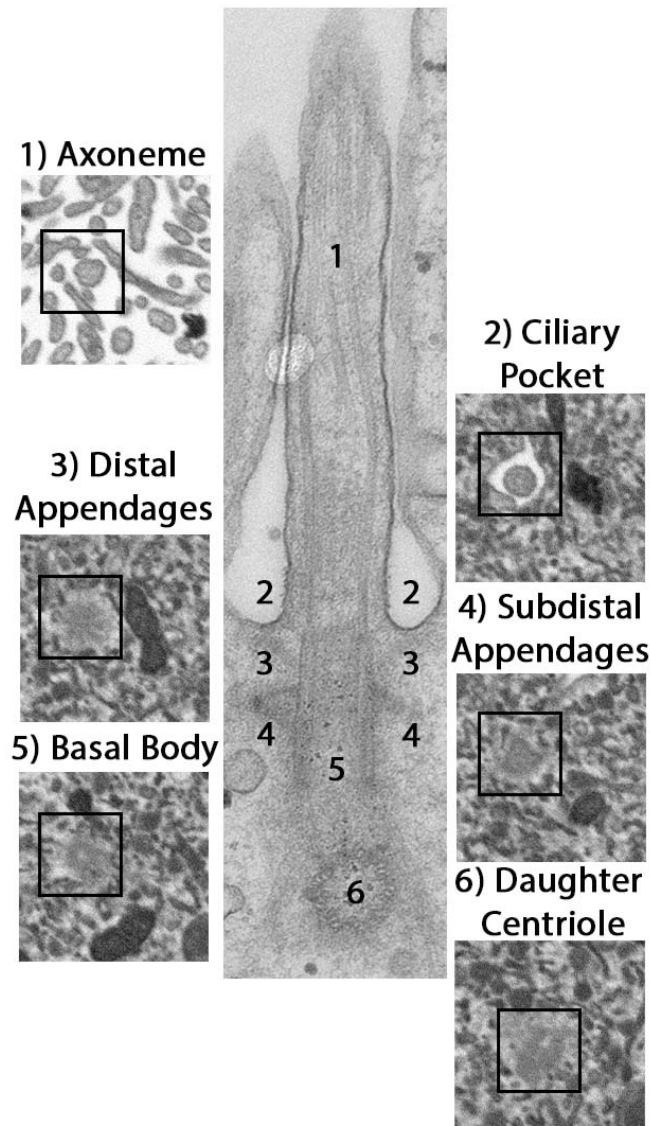


Figure 5.12: Comparison of iPSC-RPE ciliary ultrastructure visible using TEM and SBF-SEM. Central rectangular panel is a longitudinal TEM image of an iPSC-RPE cilium. Peripheral square panels show transverse sections of an iPSC-RPE cilium imaged using SBF-SEM. 1) The axoneme protrudes from the apical cell surface. Microtubules are visible by TEM but not SBF-SEM. The axoneme in TEM is truncated during processing whilst entire cilia are captured by SBF-SEM. 2) At the base of the cilium is a membrane depression called the ciliary pocket which is visible by TEM and SBF-SEM. 3) Distal appendages that link the basal body to the cell membrane are faintly visible by TEM as lines inclined at approximately 40°. By SBF-SEM these are occasionally visible as blurred lines originating from the basal body. 4) Subdistal appendages are conical structures attached to the basal body, and they are clearly visible by TEM and SBF-SEM. 5) The basal body and daughter centriole 6) are barrel-shaped structures formed by a ring of nine microtubule triplets. They are clearly visible using TEM and SBF-SEM, but microtubules are only visible by TEM. Also visible by TEM are connecting fibres between the basal body and daughter centriole.

Volume and length of iPSC-RPE cilia was measured using MIB (Belevich *et al.*, 2016). After analysing the data, 3D reconstructions of selected cilia were produced by Mr Ross Laws.

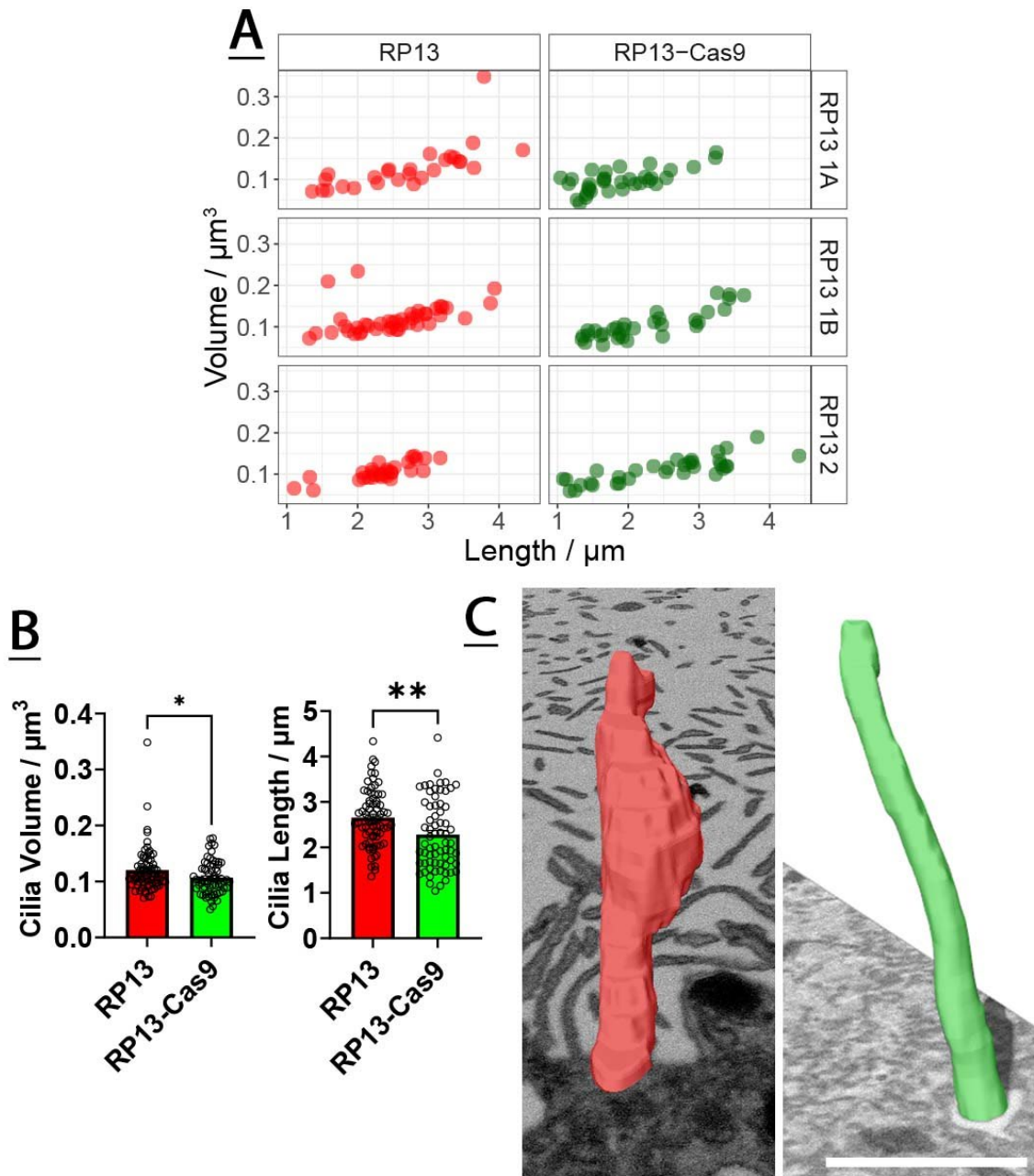


Figure 5.13: Analysis of ciliary volume and length and three-dimensional reconstruction of selected cilia using SBF-SEM data. A) Scatter plot of volume and length for RP13-1B (left, red) and RP13-1B-Cas9 (right, green) iPSC-RPE cilia. $N > 27$ for all cell lines, where n is the number of cilia analysed. **B)** Bar chart showing cilia volume and cilia length across all complete RP13 ($n = 73$) and RP13-Cas9 ($n = 67$) cilia analysed. Data was assessed for statistical significance using an unpaired t-test (p value < 0.05). **3-Dimensional**

reconstructions of RP13 (left, red) and RP13-Cas9 (right, green) iPSC-RPE cilia from SBF-SEM data. Scale bar is 1 μm .

Structural analysis of cilia by immunofluorescence microscopy showed cilia length is increased in RP13 (**Figure 5.11**). Ultrastructural characterisation of cilia using SBF-SEM revealed additional differences between RP13 (RP13-1A-3, RP13-1B-3, and RP13-2-3) and RP13-Cas9 iPSC-RPE cilia. Specifically, a subpopulation (3%) of RP13 cilia exhibit swelling within the axoneme that leads to a 2-fold increase in cilia volume or $0.03 \mu\text{m}^3$ increase in mean ciliary volume (**Figure 5.13**). This change in mean cilia volume was corroborated by an increase in cilia length, as was previously observed using confocal microscopy (**Figure 5.11**). Existence of the subpopulation was assessed using linear regression to produce diagnostic plots of fitted values, standardised residuals, leverage, and cook's distance. This suggested that those points within the subpopulation do not follow the same linear relation between length and volume as the rest of the data points.

5.7 Epithelial Polarisation is reduced in RP13 RPE

Retinal pigment epithelial cells are characteristically polarised with cilia located on the apical surface. Cilia both maintain and are maintained by cell polarity signalling pathways (Malicki and Johnson, 2017). This polarisation can be observed in the distribution of proteins across RPE cells. The apical surface can be identified by labelling proteins such as MerTK and Ezrin whilst the basal surface stains positively for Collagen IV and BEST1. This experiment was performed with Dr Maria Georgiou who assisted with immunofluorescent staining, image acquisition and image processing. We assessed polarisation of RP13 (RP13-1A-3, RP13-1B-3, and RP13-2-3) and RP13-Cas9 iPSC-RPE cells using Ezrin and Collagen IV immunofluorescence microscopy.

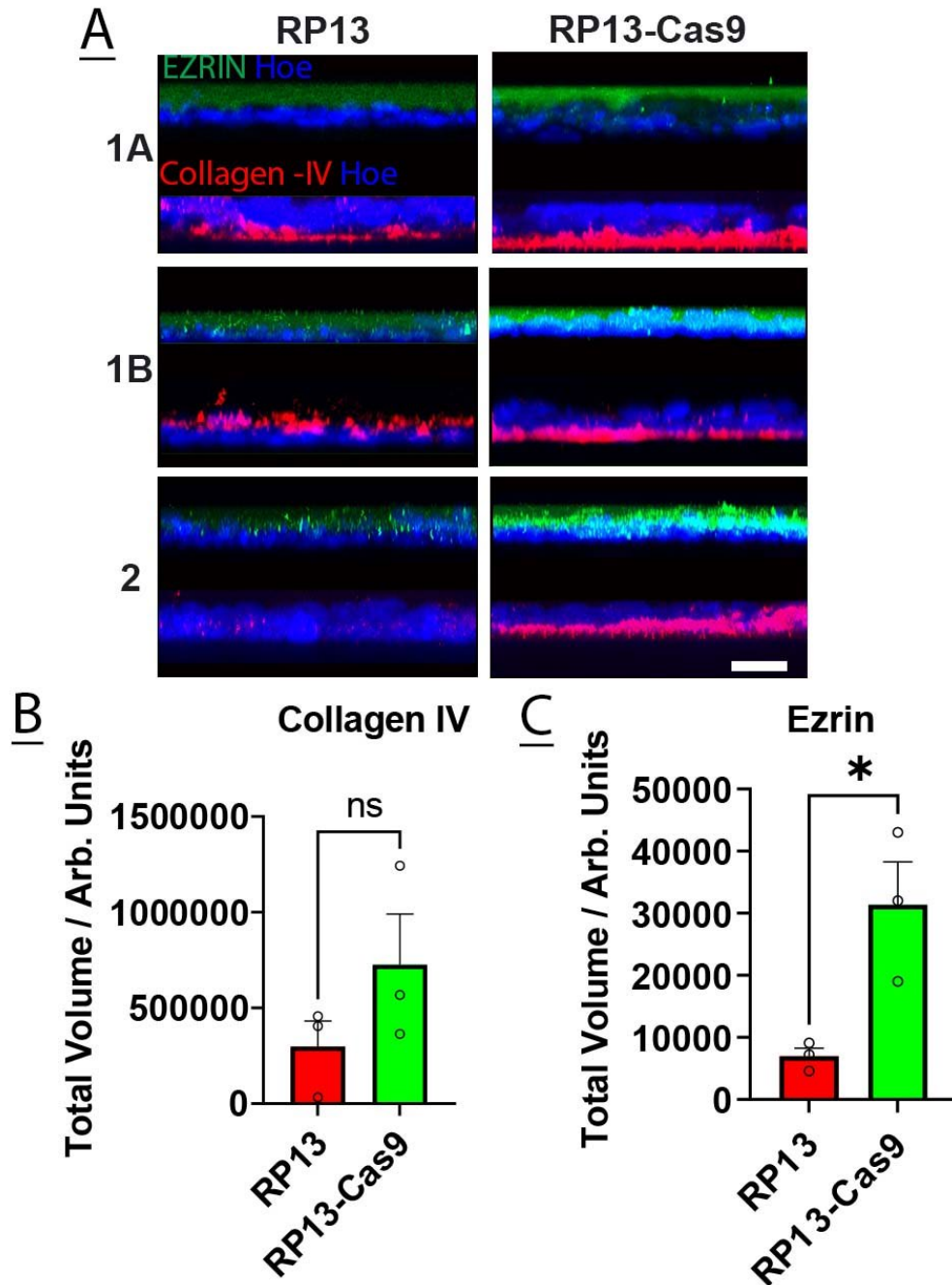


Figure 5.14: Assessment of epithelial polarity using immunocytochemistry of apical and basal polarity markers in induced pluripotent stem cell derived retinal pigment epithelium (iPSC-RPE) cells. A) Immunostaining for Ezrin (green) an apical surface marker and Collagen IV (red), a basal surface marker. In iPSC-RPE cells from all three donors, the intensity of Ezrin at the apical surface and Collagen IV at the basal surface are reduced in comparison to RP13-Cas9. Scale bar is 10 μ m. B) Bar chart showing volume of Collagen IV (measured in arbitrary units) in iPSC-RPE cell derived from patients with retinitis pigmentosa type 13 (RP13) and control cells generated using CRISPR/Cas9 (RP13-Cas9). C) Bar chart showing volume of Ezrin (measured in arbitrary units) in RP13 and RP13-Cas9 iPSC-RPE cells. Data is presented as the

mean \pm standard error of the mean (SEM). Statistical significance was assessed using Student's unpaired t-test, ns = not significant, * indicates $p < 0.05$.

This data shows the fluorescence intensity of Ezrin at the apical membrane is reduced in RP13 iPSC-RPE cells, when compared to RP13-Cas9. This suggests reduced localisation of the protein at this location (**Figure 5.14**). Similarly, the fluorescence intensity of collagen IV at the basal surface of RP13 iPSC-RPE cells is also reduced when compared to RP13-Cas9 (**Figure 5.14**).

5.8 Discussion

Retinitis pigmentosa affects 1 in 4000 people worldwide and has been linked to mutations in over 100 genes. Of these, six encode core components of the spliceosome. It is interesting that despite having a critical role in all nucleated cells, mutations in these genes cause a retinal phenotype. This study aims to discover more about how one of these genes, *PRPF8*, causes retinitis pigmentosa and to compare the cellular phenotype with that caused by mutations in *PRPF31* (Buskin *et al.*, 2018).

This chapter characterises iPSC-RPE cells derived from three RP13 patients and three paired isogenic controls that were generated using CRISPR/Cas9 (RP13-Cas9). iPSC-RPE cells derived from a fourth patient (RP13-1C) could not be characterised due to low differentiation efficiency. Following differentiation, iPSC-RPE cells were purified and matured as described in (**Section 2.4**). When RPE cells are passaged multiple times, TEER and cell morphology degenerates with subsequent passages (Singh *et al.*, 2013). This may be the early stages of an epithelial to mesenchymal transition, partly mediated by a repetitive loss of cell-to-cell contacts (Tamiya, Liu and Kaplan, 2010; Milyushina *et al.*, 2011). To preserve iPSC-RPE cell epithelial qualities, passage number and cell seeding density of RP13 and RP13-Cas9 iPSC-RPE cells were controlled. In addition, iPSC-RPE cells were cultured on transwells to promote polarisation and allow measurement of TEER. The mean TEER across 220 transwells was $224 \Omega \cdot \text{cm}^2$ and morphology appeared normal by both brightfield and fluorescence microscopy (**Figure 5.2**). Most iPSC-RPE cells could phagocytose photoreceptor outer segments in an *in vitro* assay (**Figure 5.3**). This suggests that the RP13 iPSC-RPE cells recapitulate native human RPE cell structure and function and are a physiologically relevant disease model (Quinn and Miller, 1992; Strauss, 2005). These results contrast the report of iPSC-RPE cells derived from

patients with RP11. In the previous report, patient-derived cells were shown to have a reduced TEER and phagocytosis of POS (Buskin *et al.*, 2018). As the control iPSC-RPE cells were derived from unaffected individuals as opposed to the isogenic controls used in this study, it is possible that these differences are caused by variation in the genetic background of the donors. Previous studies have shown this variability affects iPSC characteristics and therefore, are likely to also affect iPSC-RPE cells (Kilpinen *et al.*, 2017).

Following validation of iPSC-RPE cell maturation, we investigated cell ultrastructure and structure. This approach identified several similarities between the RP11 and RP13 iPSC-RPE cell phenotype, including mitochondria-associated changes (alternative splicing of mitochondrial transcripts in RP11 iPSC-RPE and decrease in mitochondria number in RP13 iPSC-RPE), structural changes to the cilia (change in cilia length detected using ARL13B immunofluorescence microscopy) and a loss of cell polarity (assessed using immunofluorescence microscopy of proteins known to have polarised distribution across RPE cells). Previous studies including a report characterising RP11 iPSC-RPE (Buskin *et al.*, 2018) have used qualitative analysis of TEM data which may only detect large changes in ultrastructure and is susceptible to unconscious bias. So, we designed a quantitative analysis approach that was performed by Miss Chia Beh (BSc) and Mr Abhijit Saxena (MRes), who were blind to cell identity. This overcame one limitation of previous TEM analyses, but the data is still limited to 2-dimensions when the actual subcellular structures exist in 3-dimensions. Whilst area measurements may not reflect the 3-dimensional ultrastructure, they allow for a more objective interpretation of the TEM data compared to qualitative analysis. TEM images of whole cell sections show a polarised distribution of organelles and microvilli on the apical cell surface (top of image) (**Figure 5.4**). Beneath the monolayer were deposits of extracellular material (**Figure 5.7**) that resemble those seen in mature human RPE (Curcio and Millican, 1999). Melanosomes and melanosome complexes were concentrated in the apical portion of the cells. A reduction in the number of type 4 melanosomes and increase in the number of melanolysosome-like vesicles has been associated with age-related macular degeneration (AMD) and a reduction in all melanosomes has been associated with oculocutaneous albinism (Cerniauskas *et al.*, 2020; George *et al.*, 2022). To determine whether similar changes in melanosome composition are present in RP13 iPSC-RPE, we performed an analysis of

melanosome subtypes and complexes present within RP13 and RP13-Cas9 iPSC-RPE cells but did not identify any statistically significant differences in abundance (**Figure 5.5**). Their presence within iPSC-RPE is evidence of a high degree of physiological similarity between iPSC-RPE cells and native human RPE cells.

We continued with quantitative ultrastructural characterisation, this time using the results of RNA-Seq analysis performed using RP11 iPSC-RPE cells to guide experimental design (**Figure 5.1**) (Buskin *et al.*, 2018). This experiment suggested that splicing mitochondrial transcripts was particularly affected in RP11 iPSC-RPE cells (Buskin *et al.*, 2018). To determine whether mitochondria are affected in both RP11 and RP13 iPSC-RPE cells we quantified mitochondrial number and structure. This showed that mitochondrial number was strongly reduced in RP13 cells, but mitochondrial shape was unaffected (**Figure 5.9**). These results contrast previous qualitative ultrastructural analysis of RP13 iPSC-RPE cells (Foltz *et al.*, 2018; Arzalluz-Luque *et al.*, 2021). However, the qualitative analysis used in these papers is unlikely to detect to a quantitative change such as this. This result is similar to an observation made in RPE cells of AMD patients. Quantitative analysis of mitochondria in RPE cells from 65 donors showed that mitochondrial number is reduced in AMD (Feher *et al.*, 2006). This finding suggests the existence of a shared disease mechanism between RP13 and AMD. In addition, RPE cells from AMD patients have been shown to express lower levels of several mitochondrial proteins such as ATPase subunits required for oxidative phosphorylation (Nordgaard *et al.*, 2008). Future experiments could confirm mitochondrial involvement by quantifying expression of these proteins in RP13 and RP13-Cas9 iPSC-RPE cells.

Another key finding from the RP11 iPSC-RPE characterisation was *PRPF31* mutations caused a reduction in cilia length and cilia incidence (Buskin *et al.*, 2018). This ciliary phenotype was also reflected in RNA-Seq analysis of alternatively spliced transcripts and SBF-SEM of ciliary ultrastructure. To determine whether this is a common feature between RP11 and RP13 iPSC-RPE cells we performed quantitatively analysed ARL13B immunofluorescent images of RP13 iPSC-RPE cells. The results showed that RP13 cilia are 10% longer but frequency is unaffected (**Figure 5.11**). This corroborates previous experiment looking at the effect of mutant PRPF8 on cilia frequency (Shen *et al.*, 2022). An increase or decrease in cilia length is indicative of ciliary

stress (Avasthi and Marshall, 2012). As cilia length is affected in both RP11 and RP13 iPSC-RPE, these results are consistent with the hypothesis that there are common disease mechanisms between RP11 and RP13. To determine whether ciliary ultrastructure was similarly affected in both RP11 and RP13-iPSC-RPE cells we performed quantitative analysis of RP13 iPSC-RPE cilia. The results revealed a small subpopulation (5%) of cilia with pronounced swelling (**Figure 5.13**). These resemble those observed in RP11 iPSC-RPE cells, they were present in 2/3 RP13 patient derived iPSC-RPE cells (Buskin *et al.*, 2018). The lack of swollen cilia detected in RP13-2, the patient with a suspected *de novo* mutation in *PRPF8* could be due to the small number of cilia analysed. Alternatively, it could suggest that the presence and/or frequency of ciliary swelling is dependent on the shared genetic background of patients 1A and 1B. The previous observation of similar swelling suggests that there are common disease mechanisms between RP11 and RP13 (Buskin *et al.*, 2018).

Cell polarity is an important feature of RPE cells, POS are phagocytosed at the apical surface whilst small molecules and ions are actively transported across the basal surface. This polarity was reduced in both RP11 iPSC-RPE cells and RP13 murine RPE cells (Farkas *et al.*, 2014; Buskin *et al.*, 2018). To determine whether polarity is also lost in RP13 iPSC-RPE cells we performed immunofluorescence microscopy of Ezrin (an apical cell surface marker) and Collagen IV (a basal cell surface marker). The results showed that fluorescence intensity of both Ezrin and Collagen IV at their respective subcellular locations was reduced in RP13 iPSC-RPE cells compared to RP13-Cas9 (**Figure 5.14**). This suggests that epithelial polarity of RP13 RPE cells is reduced in comparison to controls, as seen before in RP13 mice (Farkas *et al.*, 2014).

We were able to recapitulate several of the features seen in RP13 mice and RP11 iPSC-RPE cells. Cilia swelling was detected in both RP11 and RP13 iPSC-RPE using SBF-SEM, albeit at a low frequency in RP13. In addition there was a loss of epithelial polarisation in RP11 and RP13 iPSC-RPE as well as in a mouse model of RP13. However, there were functional and ultrastructural limitations of the RP13 iPSC-RPE model. Native RPE cells phagocytose POS and actively transport ions and nutrients across the Bruch's membrane between the retina and choriocapillaris *in vivo*. Transport of small molecules and ions between the RPE and the circulation is facilitated by infoldings in the basal RPE cell membrane that increase the rate of

transport. In addition, the RPE transports small molecules such as 11-*cis* retinal to the adjacent photoreceptors.

In the mouse retina, POS phagocytosis occurs rhythmically, in synchrony with the light-dark cycle. Peak phagocytosis occurs 2 hours after light onset. In both RP11 and RP13 mice fewer POS were phagocytosed during this phagocytic peak compared to wildtype controls (**Figure 5.15**). Then 8 hours after light onset the RPE cells of RP13 mice (but not RP11) phagocytosed more POS compared to controls (**Figure 5.15**). This was interpreted as a loss of phagocytic *rhythmicity*, perhaps secondary to circadian cycle disruption. A small circadian effect is apparent in RP13 mice wheel running times (Shakhmantsir et al., 2020). Phagocytosis of POS *in vitro* does not follow the same time course, instead, peak phagocytosis occurs 4 hours after POS challenge (Westenskow *et al.*, 2012). To measure peak phagocytosis *in vitro*, we assessed cells 4 hours after POS challenge. The comparable degree of phagocytosis between RP13 and control cells corroborates previous reports made using RP13 iPSC-RPE cells (Foltz *et al.*, 2018; Arzalluz-Luque *et al.*, 2021). The reason why there was reduced phagocytosis in RP13 mice but not RP13 iPSC-RPE cells could be because the phagocytic peak that occurs *in vivo* is dependent on an interaction between RPE cells and photoreceptor cells.

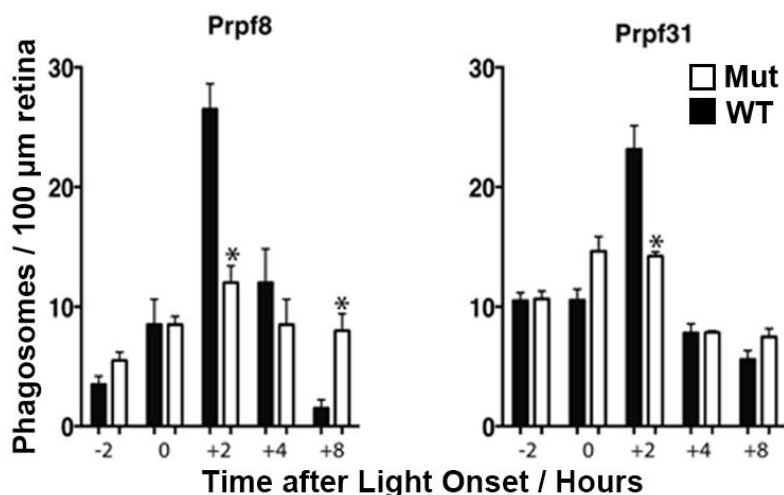


Figure 5.15: The rhythmicity of phagocytosis is affected in RP13 mice. Phagocytosis was assessed before and after light onset using TEM. Data are expressed as means \pm SD, n = 2. *P<0.05. Results taken from (Farkas *et al.*, 2014).

Transport of small molecules and ions by RPE cells is not recapitulated in a transwell culture system, as there is not the same biochemical gradient either side of the cells. Potentially the

reason basal infoldings are reduced *in vivo* but not *in vitro* is because the infoldings that develop *in vitro* are less complex than those seen *in vivo* (Hayes *et al.*, 2019). This is supported by the observation that the basal membrane of iPSC-RPE cells is close to linear. Similarly, the materials identified beneath iPSC-RPE cells have been observed in human retinal samples alongside other components (Curcio and Millican, 1999). Formation of native RPE basal deposits may depend on phagocytosis of POS and presence of the Bruch's membrane (Amin *et al.*, 2004). This would explain why basal deposits accumulate beneath the RPE *in vivo* but not *in vitro* (Farkas *et al.*, 2014). Similarly, we did not observe an increase in stress vacuoles as was observed in RP13 mice RPE cells. Two reports of RPE cell ultrastructure in Briard dogs (that inherit *RPE65* mutations) identified large (1 μm diameter) intracellular inclusions (Riis RC, 1983; Wrigstad, Narfström and Nilsson, 1994). However, one group identified lipid within the inclusions whilst the other reported an electron-lucent interior. This variable electron-density of similar inclusions was also observed in RPE cells of *RPE65*^{-/-} mice (Redmond *et al.*, 1998). The authors proposed that histological processing led to variable removal of lipids from samples. Further characterisation of the inclusions in *RPE65*^{-/-} mice, identified them as retinyl ester storage particles (Imanishi *et al.*, 2004). As formation of retinyl ester storage particles is dependent on an interaction between RPE cells and photoreceptors, formation may not be recapitulated by RPE cells grown *in vitro*. Therefore, the reason why we did not observe an increase in the number of stress vacuoles could be because formation is impaired *in vitro*.

By using iPSCs and isogenic controls from three donors we controlled for the high variability that has been associated with iPSC-based models. From our results, it appears that the biggest limitation of iPSC-RPE cells comes from a lack of interaction with other retinal components that means cell maturation is limited. When necessary, disease modelling studies could overcome this by studying human-iPSC RPE xenografts or by developing co-culture methods. Despite this, there is considerable progress being in the development of iPSC-RPE cell replacement therapy. The poor differentiation efficiency of RP13-1C to iPSC-RPE suggests that production of autologous cell therapies could be challenging. A possible solution is to use hypoimmune iPSC lines as an allogenic source of donor tissue that can be produced on an industrial scale (Deuse *et al.*, 2019; Han *et al.*, 2019). Results from the iPSCs that differentiated efficiently suggest that there are conserved features between RP11 and RP13 iPSC-RPE

phenotypes, indicating a similar mechanisms of action between these two forms of RP. Namely, the involvement of mitochondria, changes cilia structure, and loss of polarity. Further characterisation of this model is ongoing in the lab and aims to elucidate the impact of *PRPF8* mutation on mRNA splicing. For example, “how does *PRPF8* mutation impact splicing of retinal transcripts?” will be assessed by sequencing the iPSC-RPE transcriptome using next-generation and/or long read sequencing. To ask “do these events occur in all RPE cells, or a fraction?” will require analysis by single cell RNA-Seq. To answer “does the mutant *PRPF8* protein differentially interact with some RNAs?” will be assessed by crosslinking RNA with protein and immunoprecipitating (CLIP) *PRPF8* before sequencing the bound RNA. Finally, to understand the functional impact of those alternative splicing events at the protein level we will perform proteomic analysis by mass spectrometry.

Chapter 6. Conclusions and Future Directions

Retinal degenerative diseases vary in the way vision is affected, the age at which vision loss begins, and the rate at which vision is lost. However, there are commonalities between all individuals who lose their sight. Loss of sight affects an individual's ability to function independently of others and this often impacts their mental health. Some support is provided by the government and relevant charities such as a reduced cost of public transport or the provision of guide dogs. This support is valuable to many people but there is still a significant impact of vision loss on an individual's ability to work, travel, and interact with others.

Retinitis pigmentosa is an inherited retinal disease that affects 1 in 4000 people worldwide and is one of the leading causes of vision loss in individuals younger than 60 years (Hartong et al., 2006). Due to the early age of onset individuals experience disability for a longer period of time and this impacts each individual's ability to work. There are additional medical expenses, amounting to around \$7,000 per person per year (Frick *et al.*, 2012; Watanabe *et al.*, 2023). In the UK the total wellbeing costs caused by inherited retinal disease was estimated to be 196 million pounds and the total economic costs was estimated to be 327 million pounds (Galvin *et al.*, 2020). As around 50% of individuals with an inherited retinal disease are diagnosed with RP, the economic impact of RP on individuals and on society is significant (Galvin *et al.*, 2020).

The age of symptom onset is highly variable between individuals. Some patients are diagnosed in childhood whilst others experience no symptoms until the fourth decade of life. Typically, the first symptom patients experience is a loss of dark adaptation and vision in low levels of light. This progresses to a loss of peripheral vision which in some cases is followed by loss of central vision. There are over 100 genes that have been linked to RP with up to 40% of these transferred through autosomal dominant inheritance (Hartong et al., 2006). Of these genes, the second most common cause of RP is mutations in pre-mRNA processing factors (**Figure 6.1**). There are six PRPFs implicated in RP, with the most common mutations found in *PRPF31* and *PRPF8* which cause RP11 and RP13, respectively. All these PRPFs encode components of the spliceosome, a multi-megadalton ribonucleoprotein that splices nascent RNA into

messenger RNA (mRNA). PRPFs are expressed ubiquitously throughout the body, and it is unknown why mutations in these genes give rise to a retinal phenotype.

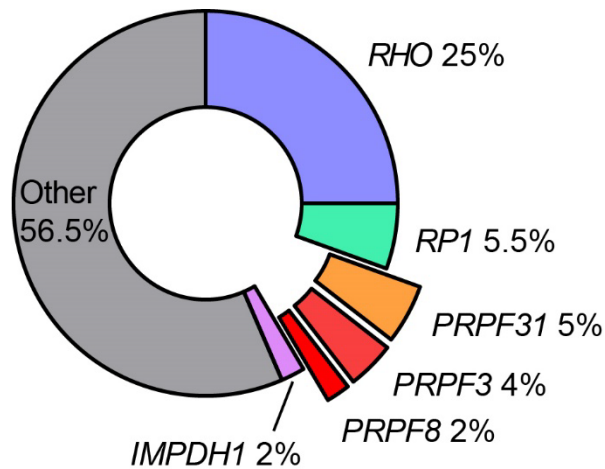


Figure 6.1: Pie chart showing the most common causes of autosomal dominant retinitis pigmentosa (adRP). Collectively, pre-mRNA processing factors (PRPFs) (PRPF31, PRPF3, and PRPF8) are the second most common cause of adRP, making up 11% of the total population. Data was obtained from Hartong, Berson, and Dryja (2006).

Over the last 30 years, significant progress has been made in understanding the genetic basis and pathology of inherited retinal disease. This has led to the anticipation of personalised therapies for retinal diseases such as RP. Interest in personalised therapies increased further since the FDA and EMA approval of Luxturna® in 2018. This is an advanced therapy for patients with biallelic mutations in the *RPE65* gene that mean effectively no functional protein can be produced. This causes progressive vision loss that starts in early childhood. Luxturna® is an adeno-associated virus (AAV) that has been engineered to increase the expression of *RPE65*. Subretinal injection facilitates transduction of the primary affected cell type, retinal pigment epithelium (RPE) cells.

The approval of Luxturna suggests that AAV treatment of other inherited retinal diseases such as RP11 and RP13 is possible. The successful design of such personalised therapies is only possible if the mechanism of disease is sufficiently well understood. Whilst small animals such as mice and rats are useful for studying inherited retinal disease, they possess several limitations. For example, there are differences in retinal biology between mice/rats and humans as well as ethical standards that limit the number of animals that can be sacrificed for

each project. Studies using primary cell cultures overcome issues of species-specific biology but access to such material is extremely limited, particularly when studying rare diseases.

It is because of these limitations that iPSC technology is being widely adopted for the study of inherited retinal disease. Two key advantages of iPSCs are that they are an almost unlimited source of cells and can effectively recapitulate human retinal biology. These properties make iPSC models interesting from a drug discovery perspective as they can be produced on an industrial scale. However, iPSCs are limited by donor variability (genetic variability between iPSC donors). Disease modelling studies typically use a small number of iPSC lines, and this donor variability can confound results. Fortunately, technological advancements mean that this genetic variability can be controlled, as described in this study.

Mutations in *PRPF31* are thought to cause RP11 by reducing the level of functional protein expressed in RPE cells. Given this, supplementation of affected cells with additional *PRPF31* should prevent retinal degeneration. This approach was evaluated using iPSC-RPE cells that harbour *PRPF31* mutations, as were previously characterised by members of the Lako lab (Buskin et al., 2018). These RP11 iPSC-RPE cells were transduced with adeno-associated viruses that had been engineered to express *PRPF31*. A myriad of AAV serotypes exist, for this project, we used an AAV2 variant called AAV2-[7m8]. There are multiple reports of the AAV2-7m8] serotype having superior transduction efficiency in retinal cells, including retinal pigment epithelium (RPE) cells (Dalkara et al., 2013; Hickey et al., 2017). A cytomegalovirus (CMV) promoter was used to drive high expression of exogenous *PRPF31*. This approach is different from the chicken beta-actin promoter used in both Luxturna® and a similar project also investigating the potential of *PRPF31*-AAV (Brydon et al., 2019). Both promoters drive high expression in a broad range of cell types. However, one possible limitation of the CMV promoter is that over time transcription can be silenced due to methylation (Brooks et al., 2004). All three approaches use AAV2-derived serotypes. Despite differences in experimental design and disease genotype, both this study and a similar one report similar results (Brydon et al., 2019). Specifically, both studies found that *PRPF31*-AAV treatment rescued cilia length and phagocytic function. This rescue of phagocytic function is particularly interesting as photoreceptor outer segment (POS) phagocytosis by RPE cells is affected in multiple retinal

diseases and could be the primary functional defect that causes vision loss. Thus, this study provided *in vitro* data supporting the efficacy of *PRPF31*-AAV treatment for RP. However, there remain several questions that require *in vivo* studies. Most obviously, does *PRPF31*-AAV treatment reduce vision loss in animal models of *PRPF31*-linked RP? And how can AAV efficacy be improved? This will require future studies to continue optimising AAV transduction efficiency (e.g., AAV serotype and delivery regime) and sustained expression (e.g., promoter and enhancer) of the viral gene. Previous studies have shown that the CMV promoter is silenced through methylation in multiple cell types (Brooks *et al.*, 2004). Similarly, silencing of the chicken β -actin promoter has been observed, although to a lesser extent (Dou *et al.*, 2021). Potentially, endogenous promoters such as the *RPE65* promoter will be more effective at sustaining expression over long periods. Optimising treatment of *PRPF31*-linked RP *in vivo* will provide hope not only to those directly affected by RP11 but also to those affected by other inherited retinal diseases caused by a reduction in functional gene expression.

The second component of this study is to create a disease model of *PRPF8*-linked RP, also known as RP13. Given that *PRPF8* is a core component of the spliceosome it will be interesting to perform a transcriptomic analysis as part of the extended characterisation of this model. This will identify whether RP13 mutations affect splicing and if so, which transcripts are most affected. To prevent donor variability from confounding these results, isogenic control iPSC lines were generated using CRISPR/Cas9. The edit was confirmed by Sanger sequencing and the editing process did not affect RPE differentiation or cell potency. At 16%, the efficiency of Cas9-mediated editing at the affected *PRPF8* sequence was remarkably high. The efficiency of off-target edits was not quantified. However, in a panel of five sites that had fewer than five nucleotide mismatches with the target sequence, there were no off-target events detected in the iPSC clone that was assessed. This suggests that this location in *PRPF8* is a promising candidate to assess therapeutic gene editing. For example, high editing efficiency is conducive to the production of autologous transplants that are edited *ex vivo*. Another therapeutic approach could be to perform *in vivo* DNA editing using prime editing technology (Anzalone *et al.*, 2019; Kim *et al.*, 2020). This is of significant interest because, if successful, would have a permanent effect on retinal biology in treated individuals. These are new approaches that

require evaluation but have the potential to benefit those affected by a range of retinal and non-retinal diseases.

The Cas9-edited (RP13-Cas9) and unedited (RP13) iPSCs were differentiated in parallel into iPSC-RPE cells, allowed to mature, and then characterised. Characterisation of the RP13 iPSC-RPE disease model revealed an overlapping phenotype caused by *PRPF8* and *PRPF31* mutations. Both the RP11 and RP13 iPSC-RPE phenotypes include a loss of apical-basal polarity also observed in mice harbouring *Prpf8* and *Prpf31* mutations (Farkas et al., 2014) as well as iPSC-RPE derived from a patient with syndromic disease caused by *CEP290* mutation and *BBS8*^{-/-} (May-Simera et al., 2018b) (**Figure 6.2**). In addition, a change in cilia length and the presence of ciliary swelling was detected by SBF-SEM in iPSC-RPE harbouring both *PRPF8* and *PRPF31* mutations.

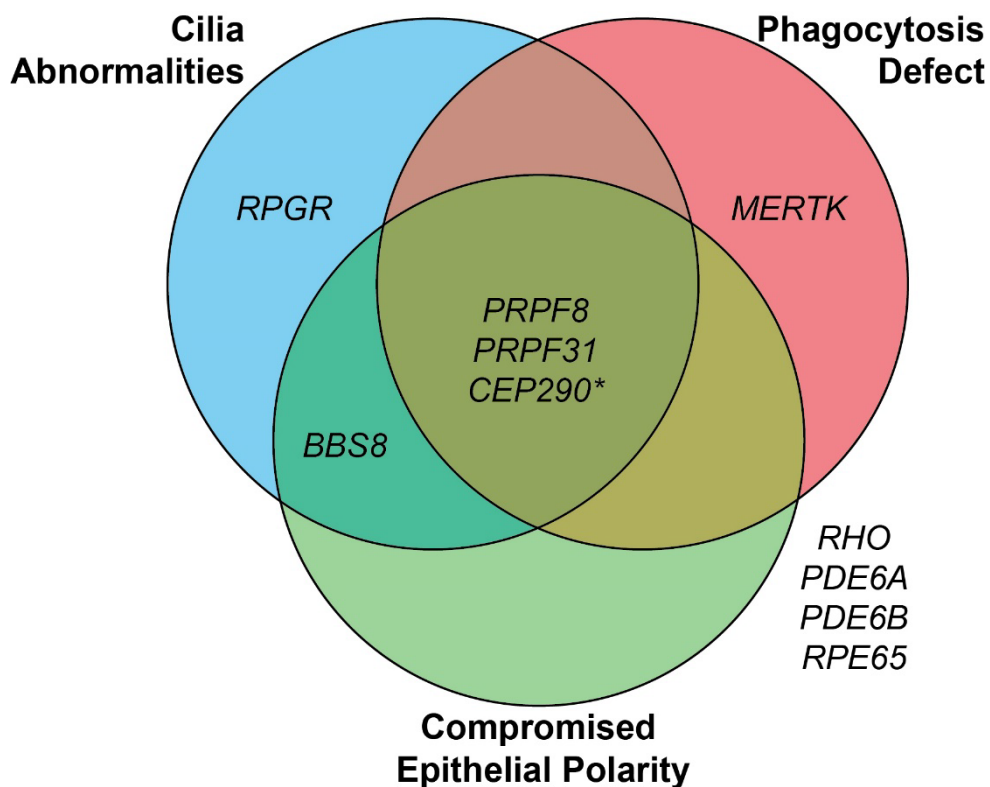


Figure 6.2: Venn diagram illustrating overlapping disease mechanisms observed in induced pluripotent stem cell-derived retinal pigment epithelial cells derived from patients with *PRPF8* mutations and other models of retinitis pigmentosa. The genes that are affected in those models are shown in the Venn-diagram. The asterisk indicates that retinitis pigmentosa caused by the *CEP290* mutation studied causes a syndromic disease affecting multiple tissues (Joubert syndrome).

Changes to cilia structure have also been linked to several other RP-associated genes including RPGR, BBS8, and CEP290 (Patnaik *et al.*, 2015; May-Simera *et al.*, 2018b) (**Figure 6.2**). The cilia regulates RPE maturation and epithelial cell polarity (May-Simera *et al.*, 2018a), but cilia function is also dependent on the maintenance of this polarity.

Therefore, it is not clear which comes first is without further study. It is also important to note that whilst changes to cilia structure, epithelial polarity, and POS phagocytosis are observed in some models of RP they are not observed in all. For example, mutations in genes that encode components of the visual cycle of photoreceptor-specific genes do not affect the RPE in these ways (**Figure 6.2**).

There are also several differences between the RP11 and RP13 iPSC-RPE models. Most strikingly was the lack of effect that the *PRPF8* mutation has on the phagocytosis of photoreceptor outer segments (POS). This could indicate that the effect *PRPF8* mutations have on phagocytosis is not the same as that caused by *PRPF31* mutations. The POS phagocytosis defect associated with *PRPF8* mutations may be more difficult to recapitulate using iPSC-RPE than previously thought, perhaps because of the circadian dependency of this defect (Farkas *et al.*, 2014; Shakhmantsir *et al.*, 2020). The effect of *Prpf31* mutations on POS phagocytosis in mice cause a reduction in the amount of phagocytosis done by the RPE (Farkas *et al.*, 2014). However, *Prpf8* mutations have a more complex effect than that seen in mice with *Prpf31* mutations. In *Prpf8* mice, there is both a reduction and an increase in the amount of phagocytosis relative to wildtype RPE at different times after light onset (Farkas *et al.*, 2014). This could suggest that the phagocytosis defect in murine RPE harbouring *Prpf8* mutations affects the light-stimulated shedding of POS rather than the ability of RPE to phagocytose.

Despite this, the RP13 iPSC-RPE model can be used to discover new treatments for RP13. Chapter 3 demonstrated how the iPSC-RPE can be transduced using an AAV to restore a key cellular function. The results of chapter 4 indicate that the *PRPF8* mutation site is amenable to editing using the Cas9 protein. Ongoing work related to this project suggests that supplementation with additional *PRPF8* may not improve disease. Furthermore, the high frequency of indels associated with Cas9-mediated double-stranded DNA breaks mean this approach is unlikely to translate in vivo. However, viral delivery of the prime editing system

could overcome limitations of the original Cas9 system (Anzalone et al., 2019). It would be interesting to test this prime editing approach using the iPSC-RPE model from chapter 5. If prime editing can efficiently rescue the RP13 phenotype in iPSC-RPE this would warrant clinical evaluation of this approach. If effective, such a treatment would likely involve one or two medical procedures that have a positive and long term effect on a patients vision. In conclusion, this thesis provides evidence supporting the use of iPSCs for the discovery of advanced therapies in the treatment of PRPF-linked RP.

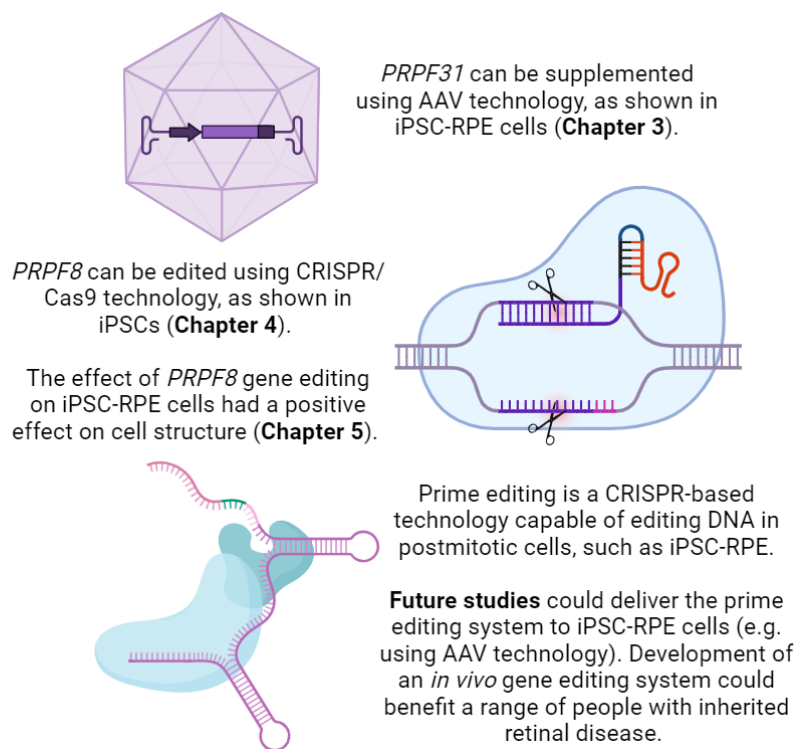


Figure 6.3: Schematic summarising work completed in the three results chapters of this thesis and describing how this work could be continued to develop a possible therapy for *PRPF8*-linked RP using prime editing.

References

- Abelson, J. (2008) *Is the spliceosome a ribonucleoprotein enzyme?*, *Nature Structural and Molecular Biology*. Nature Publishing Group. doi: 10.1038/nsmb1208-1235.
- Acland, G. M. *et al.* (2001) 'Gene therapy restores vision in a canine model of childhood blindness', *Nature Genetics*, 28(1), pp. 92–95. doi: 10.1038/ng0501-92.
- Agafonov, D. E. *et al.* (2016) 'Molecular architecture of the human U4/U6.U5 tri-snRNP', *Science*, 351(6280), pp. 1416–20. doi: 10.1126/science.aad2085.
- Ait-Ali, N. *et al.* (2015) 'Rod-Derived Cone Viability Factor Promotes Cone Survival by Stimulating Aerobic Glycolysis', *Cell*, 161(4), pp. 817–832. doi: 10.1016/J.CELL.2015.03.023.
- Ajuh, P. *et al.* (2000) 'Functional analysis of the human CDC5L complex and identification of its components by mass spectrometry', *EMBO Journal*, 19(23), pp. 6569–6581. doi: 10.1093/emboj/19.23.6569.
- Al-Hussaini, H. *et al.* (2008) 'Mature retinal pigment epithelium cells are retained in the cell cycle and proliferate in vivo', *Molecular Vision*, 14, pp. 1784–1791. Available at: <http://www.molvis.org/molvis/v14/a210> (Accessed: 6 February 2021).
- Amin, S. *et al.* (2004) 'Modulation of Sub-RPE Deposits In Vitro: A Potential Model for Age-Related Macular Degeneration', *Investigative Ophthalmology & Visual Science*, 45(5), pp. 1281–1288. doi: 10.1167/IOVS.03-0671.
- Anderson, D. H., Fisher, S. K. and Steinberg, R. H. (1978) 'Mammalian cones: disc shedding phagocytosis, and renewal', *Investigative Ophthalmology and Visual Science*, 17(2), pp. 117–133. Available at: <http://www.ncbi.nlm.nih.gov/pubmed/415019> (Accessed: 26 June 2019).
- Anzalone, A. V. *et al.* (2019) 'Search-and-replace genome editing without double-strand breaks or donor DNA', *Nature* 2019 576:7785, 576(7785), pp. 149–157. doi: 10.1038/s41586-019-1711-4.
- Arzalluz-Luque, Á. *et al.* (2021) 'Mutant PRPF8 Causes Widespread Splicing Changes in

Spliceosome Components in Retinitis Pigmentosa Patient iPSC-Derived RPE Cells', *Frontiers in Neuroscience*, 15, p. 276. doi: 10.3389/FNINS.2021.636969/BIBTEX.

Avasthi, P. and Marshall, W. F. (2012) 'Stages of ciliogenesis and regulation of ciliary length', *Differentiation*, 83(2), p. S30. doi: 10.1016/j.diff.2011.11.015.

Bainbridge, J. W. B. *et al.* (2008) 'Effect of Gene Therapy on Visual Function in Leber's Congenital Amaurosis', *New England Journal of Medicine*, 358(21), pp. 2231–2239. doi: 10.1056/nejmoa0802268.

Ballios, B. G., Pierce, E. A. and Huckfeldt, R. M. (2021) 'Gene editing technology: Towards precision medicine in inherited retinal diseases'. doi: 10.1080/08820538.2021.1887903.

Barrangou, R. *et al.* (2007) 'CRISPR provides acquired resistance against viruses in prokaryotes', *Science*, 315(5819), pp. 1709–1712. doi: 10.1126/science.1138140.

Bassuk, A. G. *et al.* (2016) 'Precision Medicine: Genetic Repair of Retinitis Pigmentosa in Patient-Derived Stem Cells', *Scientific Reports 2016 6:1*, 6(1), pp. 1–6. doi: 10.1038/srep19969.

Batten, M. L. *et al.* (2004) 'Lecithin-retinol Acyltransferase is Essential for Accumulation of All-trans-Retiny Ester in the Eye and in the Liver', *Journal of Biological Chemistry*, 279(11), pp. 10422–10432. doi: 10.1074/jbc.M312410200.

Baylor, D. (1996) 'How photons start vision', *Proceedings of the National Academy of Sciences of the United States of America*, 93(2), pp. 560–565. doi: 10.1073/pnas.93.2.560.

Baylor, D. A. and Burns, M. E. (1998) 'Control of rhodopsin activity in vision', *Eye (Basingstoke)*, 12(3), pp. 521–525. doi: 10.1038/eye.1998.140.

Baylor, D. A., Lamb, T. D. and Yau, K. W. (1979) 'Responses of retinal rods to single photons.', *The Journal of Physiology*, 288(1), pp. 613–634. doi: 10.1113/jphysiol.1979.sp012716.

Baylor, D. A., Nunn, B. J. and Schnapf, J. L. (1984) 'The photocurrent, noise and spectral sensitivity of rods of the monkey *Macaca fascicularis*.', *The Journal of Physiology*, 357(1), pp. 575–607. doi: 10.1113/jphysiol.1984.sp015518.

Bazan, N. G. (2006) 'Cell survival matters: docosahexaenoic acid signaling, neuroprotection and photoreceptors', *Trends in Neurosciences*, 29(5), pp. 263–271. doi: 10.1016/j.tins.2006.03.005.

Beavo, J. A. (1995) 'Cyclic nucleotide phosphodiesterases: Functional implications of multiple isoforms', *Physiological Reviews*, 75(4), pp. 725–748. doi: 10.1152/physrev.1995.75.4.725.

Behzadnia, N. *et al.* (2007) 'Composition and three-dimensional EM structure of double affinity-purified, human prespliceosomal A complexes', *EMBO Journal*, 26(6), pp. 1737–1748. doi: 10.1038/sj.emboj.7601631.

Belevich, I. *et al.* (2016) 'Microscopy Image Browser: A Platform for Segmentation and Analysis of Multidimensional Datasets', *PLOS Biology*, 14(1), p. e1002340. doi: 10.1371/JOURNAL.PBIO.1002340.

Berson, E. L. *et al.* (1993) 'A Randomized Trial of Vitamin A and Vitamin E Supplementation for Retinitis Pigmentosa', *Archives of Ophthalmology*, 111(6), pp. 761–772. doi: 10.1001/archophth.1993.01090060049022.

Berson, E. L. *et al.* (2010) 'Clinical trial of lutein in patients with retinitis pigmentosa receiving vitamin A', *Archives of Ophthalmology*, 128(4), pp. 403–411. doi: 10.1001/archophthalmol.2010.32.

Bertram, K., Agafonov, D. E., Liu, W. T., *et al.* (2017) 'Cryo-EM structure of a human spliceosome activated for step 2 of splicing', *Nature*, 542(7641), pp. 318–323. doi: 10.1038/nature21079.

Bertram, K., Agafonov, D. E., Dybkov, O., *et al.* (2017) 'Cryo-EM Structure of a Pre-catalytic Human Spliceosome Primed for Activation', *Cell*, 170(4), pp. 701–713.e11. doi: 10.1016/j.cell.2017.07.011.

Bessonov, S. *et al.* (2008) 'Isolation of an active step I spliceosome and composition of its RNP core', *Nature*, 452(7189), pp. 846–850. doi: 10.1038/nature06842.

Bok, D. (1993) 'The retinal pigment epithelium: A versatile partner in vision', *Journal of Cell Science*, 106(SUPPL. 17), pp. 189–195. doi: 10.1242/jcs.1993.supplement_17.27.

Bok, D. and Hall, M. O. (1971) 'The role of the pigment epithelium in the etiology of inherited retinal dystrophy in the rat', *Journal of Cell Biology*, 49(3), pp. 664–682. doi: 10.1083/jcb.49.3.664.

Bornancin, F., Pfister, C. and Chabre, M. (1989) 'The transitory complex between photoexcited rhodopsin and transducin: Reciprocal interaction between the retinal site in rhodopsin and the nucleotide site in transducin', *European Journal of Biochemistry*, 184(3), pp. 687–698. doi: 10.1111/j.1432-1033.1989.tb15068.x.

Bowne, S. J. *et al.* (2013) *Mutations in the small nuclear riboprotein 200 kDa gene (SNRNP200) cause 1.6% of autosomal dominant retinitis pigmentosa*, *Molecular Vision*. Available at: <http://www.molvis.org/molvis/v19/2407> (Accessed: 5 February 2019).

Boye, S. E. *et al.* (2013) 'A comprehensive review of retinal gene therapy', *Molecular Therapy*, 21(3), pp. 509–519. doi: 10.1038/mt.2012.280.

Brooks, A. R. *et al.* (2004) 'Transcriptional silencing is associated with extensive methylation of the CMV promoter following adenoviral gene delivery to muscle', *Journal of Gene Medicine*, 6(4), pp. 395–404. doi: 10.1002/jgm.516.

Brown, E. E. *et al.* (2019) 'Mitochondrial oxidative stress in the retinal pigment epithelium (RPE) led to metabolic dysfunction in both the RPE and retinal photoreceptors', *Redox Biology*, 24(March), p. 101201. doi: 10.1016/j.redox.2019.101201.

Bryant, L. *et al.* (2019) 'Clinical science Identification of a novel pathogenic missense mutation in PRPF31 using whole exome sequencing: a case report', *Br J Ophthalmol*, 103, pp. 761–767. doi: 10.1136/bjophthalmol-2017-311405.

Brydon, E. M. *et al.* (2019) 'AAV-Mediated Gene Augmentation Therapy Restores Critical Functions in Mutant PRPF31+/- iPSC-Derived RPE Cells', *Molecular Therapy - Methods and Clinical Development*, 15, pp. 392–402. doi: 10.1016/j.omtm.2019.10.014.

Buhr, E. D. *et al.* (2015) 'Neuropsin (OPN5)-mediated photoentrainment of local circadian oscillators in mammalian retina and cornea', *Proceedings of the National Academy of Sciences of the United States of America*, 112(42), pp. 13093–13098. doi: 10.1073/pnas.1516259112.

Bujakowska, K. *et al.* (2009) 'Study of gene-targeted mouse models of splicing factor gene Prpf31 implicated in human autosomal dominant retinitis pigmentosa (RP)', *Investigative Ophthalmology and Visual Science*, 50(12), pp. 5927–5933. doi: 10.1167/iovs.08-3275.

Bunney, P. E. *et al.* (2011) 'A bioinformatic assay for pluripotency in human cells', *Nature Methods*, pp. 315–317. doi: 10.1016/j.physbeh.2017.03.040.

Bunt Milam, A. H. and Saari, J. C. (1983) 'Immunocytochemical localization of two retinoid-binding proteins in vertebrate retina', *Journal of Cell Biology*, 97(3), pp. 703–712. doi: 10.1083/jcb.97.3.703.

Buskin, A. *et al.* (2018) 'Human iPSC-derived RPE and retinal organoids reveal impaired alternative splicing of genes involved in pre-mRNA splicing in PRPF31 autosomal dominant retinitis pigmentosa', *Nature Communications*. doi: 10.1101/232397.

Cao, H. *et al.* (2011) 'Temporal and tissue specific regulation of RP-Associated splicing factor genes PRPF3, PRPF31 and PRPC8-implications in the pathogenesis of RP', *PLoS ONE*. Edited by R. Roberts, 6(1), pp. 1–10. doi: 10.1371/journal.pone.0015860.

Caprara, C. and Grimm, C. (2012) 'From oxygen to erythropoietin: Relevance of hypoxia for retinal development, health and disease', *Progress in Retinal and Eye Research*, 31(1), pp. 89–119. doi: 10.1016/j.preteyeres.2011.11.003.

Cerniauskas, E. *et al.* (2020) 'Complement modulation reverses pathology in Y402H-retinal pigment epithelium cell model of age-related macular degeneration by restoring lysosomal function', *Stem Cells Translational Medicine*, 9(12), pp. 1585–1603. doi: 10.1002/sctm.20-0211.

Chen, C. H. *et al.* (2002) 'Functional and physical interactions between components of the Prp19p-associated complex', *Nucleic Acids Research*, 30(4), pp. 1029–1037. doi:

10.1093/nar/30.4.1029.

Chen, C. H. *et al.* (2006) 'Functional links between the Prp19-associated complex, U4/U6 biogenesis, and spliceosome recycling', *Rna*, 12(5), pp. 765–774. doi: 10.1261/rna.2292106.

Chen, H. R. *et al.* (1999) 'Snt309p modulates interactions of Prp19p with its associated components to stabilize the Prp19p-associated complex essential for pre-mRNA splicing', *Proceedings of the National Academy of Sciences of the United States of America*, 96(10), pp. 5406–5411. doi: 10.1073/pnas.96.10.5406.

Chen, W., Smeekens, J. M. and Wu, R. (2016) 'Systematic study of the dynamics and half-lives of newly synthesized proteins in human cells', *Chemical Science*, 7(2), pp. 1393–1400. doi: 10.1039/C5SC03826J.

Chen, Xue *et al.* (2014) 'PRPF4 mutations cause autosomal dominant retinitis pigmentosa', *Human Molecular Genetics*, 23(11), pp. 2926–2939. doi: 10.1093/hmg/ddu005.

Choudhary, P. *et al.* (2017) 'Directing Differentiation of Pluripotent Stem Cells Toward Retinal Pigment Epithelium Lineage', *Stem Cells Translational Medicine*, 6(2), pp. 490–501. doi: 10.5966/sctm.2016-0088.

Cideciyan, A. V. *et al.* (2000) 'Rod and cone visual cycle consequences of a null mutation in the 11-cis-retinol dehydrogenase gene in man', *Visual Neuroscience*, 17(5), pp. 667–678. doi: 10.1017/S0952523800175029.

Collin, J. *et al.* (2019) 'Deconstructing Retinal Organoids: Single Cell RNA-Seq Reveals the Cellular Components of Human Pluripotent Stem Cell-Derived Retina', *Stem Cells*, 37(5), pp. 593–598. doi: 10.1002/stem.2963.

Cong, L. *et al.* (2013) 'Multiplex Genome Engineering Using CRISPR/Cas Systems', *Science*, 339(5891), pp. 819–822. doi: 10.1126/science.1159689.

Curcio, C. A. and Millican, C. L. (1999) 'Basal linear deposit and large drusen are specific for early age-related maculopathy', *Archives of Ophthalmology*, 117(3), pp. 329–339. doi:

10.1001/archophth.117.3.329.

D'Cruz, P. M. *et al.* (2000) 'Mutation of the receptor tyrosine kinase gene Mertk in the retinal dystrophic RCS rat', *Human Molecular Genetics*, 9(4), pp. 645–651. doi: 10.1093/HMG/9.4.645.

Dalkara, D. *et al.* (2013) 'In vivo-directed evolution of a new adeno-associated virus for therapeutic outer retinal gene delivery from the vitreous', *Science Translational Medicine*, 5(189), pp. 189ra76-189ra76. doi: 10.1126/scitranslmed.3005708.

Deckert, J. *et al.* (2006) 'Protein Composition and Electron Microscopy Structure of Affinity-Purified Human Spliceosomal B Complexes Isolated under Physiological Conditions', *Molecular and Cellular Biology*, 26(14), pp. 5528–5543. doi: 10.1128/mcb.00582-06.

Deerinck, T. J. *et al.* (2018) 'High-performance serial block-face SEM of nonconductive biological samples enabled by focal gas injection-based charge compensation', *Journal of Microscopy*, 270(2), pp. 142–149. doi: 10.1111/JMI.12667.

Deuse, T. *et al.* (2019) 'Hypoimmunogenic derivatives of induced pluripotent stem cells evade immune rejection in fully immunocompetent allogeneic recipients', *Nature Biotechnology*, 37(3), pp. 252–258. doi: 10.1038/s41587-019-0016-3.

Doench, J. G. *et al.* (2016) 'Optimized sgRNA design to maximize activity and minimize off-target effects of CRISPR-Cas9', *Nature Biotechnology*, 34(2), pp. 184–191. doi: 10.1038/nbt.3437.

Dou, Y. *et al.* (2021) 'The CAG promoter maintains high-level transgene expression in HEK293 cells', *FEBS Open Bio*, 11(1), pp. 95–104. doi: 10.1002/2211-5463.13029.

Doudna, J. A. and Charpentier, E. (2014) 'The new frontier of genome engineering with CRISPR-Cas9', *Science*, 346(6213). doi: 10.1126/science.1192272.

Ebert, A. D. *et al.* (2009) 'Induced pluripotent stem cells from a spinal muscular atrophy patient', *Nature*, 457(7227), pp. 277–280. doi: 10.1038/nature07677.

Eiraku, M. *et al.* (2011) 'Self-organizing optic-cup morphogenesis in three-dimensional culture', *Nature*, 472(7341), pp. 51–58. doi: 10.1038/nature09941.

Evans, M. J. and Kaufman, M. H. (1981) 'Establishment in culture of pluripotential cells from mouse embryos', *Nature*, 292(5819), pp. 154–156. doi: 10.1038/292154a0.

Evans, R. J. *et al.* (2010) 'The retinitis pigmentosa protein RP2 links pericentriolar vesicle transport between the Golgi and the primary cilium', *Human Molecular Genetics*, 19(7), pp. 1358–1367. doi: 10.1093/hmg/ddq012.

Farjo, K. M. *et al.* (2009) 'The 11-cis-retinol dehydrogenase activity of RDH10 and its interaction with visual cycle proteins', *Investigative Ophthalmology and Visual Science*, 50(11), pp. 5089–5097. doi: 10.1167/iovs.09-3797.

Farkas, M. H. *et al.* (2014) 'Mutations in Pre-mRNA processing factors 3, 8, and 31 cause dysfunction of the retinal pigment epithelium', *American Journal of Pathology*, 184(10), pp. 2641–2652. doi: 10.1016/j.ajpath.2014.06.026.

Feeney, L. (1978) 'Lipofuscin and melanin of human retinal pigment epithelium. Fluorescence, enzyme cytochemical, and ultrastructural studies', *Investigative Ophthalmology and Visual Science*, 17(7), pp. 583–600. Available at: <https://iovs.arvojournals.org/article.aspx?articleid=2175722> (Accessed: 22 February 2022).

Feher, J. *et al.* (2006) 'Mitochondrial alterations of retinal pigment epithelium in age-related macular degeneration', *Neurobiology of Aging*, 27(7), pp. 983–993. doi: 10.1016/j.neurobiolaging.2005.05.012.

Fesenko, E. E., Kolesnikov, S. S. and Lyubarsky, A. L. (1985) 'Induction by cyclic GMP of cationic conductance in plasma membrane of retinal rod outer segment', *Nature*, 313(6000), pp. 310–313. doi: 10.1038/313310a0.

Finn, J. T., Grunwald, M. E. and Yau, K. W. (1996) 'Cyclic nucleotide-gated ion channels: An extended family with diverse functions', *Annual Review of Physiology*, 58(1), pp. 395–426. doi: 10.1146/annurev.ph.58.030196.002143.

Fisch, C. and Dupuis-Williams, P. (2011) 'Ultrastructure of cilia and flagella - back to the future!', *Biology of the Cell*, 103(6), pp. 249–270. doi: 10.1042/bc20100139.

Flaxman, S. R. *et al.* (2017) 'Global causes of blindness and distance vision impairment 1990–2020: a systematic review and meta-analysis', *The Lancet Global Health*, 5(12), pp. e1221–e1234. doi: 10.1016/S2214-109X(17)30393-5.

Foltz, L. P. *et al.* (2018) 'Functional Assessment of Patient-Derived Retinal Pigment Epithelial Cells Edited by CRISPR/Cas9', *International Journal of Molecular Sciences*, 19(12). doi: 10.3390/IJMS19124127.

Foltz, L. P. and Clegg, D. O. (2017) 'Rapid, directed differentiation of retinal pigment epithelial cells from human embryonic or induced pluripotent stem cells', *Journal of Visualized Experiments*, 2017(128), p. 56274. doi: 10.3791/56274.

Frick, K. D. *et al.* (2012) 'Health services utilization and cost of retinitis pigmentosa', *Archives of Ophthalmology*, 130(5), pp. 629–634. doi: 10.1001/archophthalmol.2011.2820.

Futterman, S. and Saari, J. C. (1977) 'Occurrence of 11 cis retinal binding protein restricted to the retina', *Investigative Ophthalmology and Visual Science*, 16(8), pp. 768–771. Available at: <http://www.ncbi.nlm.nih.gov/pubmed/560359> (Accessed: 26 June 2019).

Futterman, S., Saari, J. C. and Blair, S. (1977) 'Occurrence of a binding protein for 11 cis retinal in retina', *Journal of Biological Chemistry*, 252(10), pp. 3267–3271. doi: 10.1016/s0021-9258(17)40382-6.

Galvin, O. *et al.* (2020) 'The impact of inherited retinal diseases in the republic of ireland (ROI) and the United Kingdom (UK) from a cost-of-illness perspective', *Clinical Ophthalmology*, 14, pp. 707–719. doi: 10.2147/OPHTH.S241928.

Gao, H. and Hollyfield, J. G. (1992) *Aging of the human retina.*, *Investigative ophthalmology & visual science*. [Association for Research in Vision and Ophthalmology, etc.]. Available at: <http://www.ncbi.nlm.nih.gov/pubmed/1730530> (Accessed: 26 June 2019).

Garcia-Gonzalo, F. R. and Reiter, J. F. (2017) 'Open Sesame: How transition fibers and the transition zone control ciliary composition', *Cold Spring Harbor Perspectives in Biology*, 9(2). doi: 10.1101/cshperspect.a028134.

Garita-Hernandez, M. *et al.* (2020) 'AAV-mediated gene delivery to 3D retinal organoids derived from human induced pluripotent stem cells', *International Journal of Molecular Sciences*, 21(3), p. 994. doi: 10.3390/ijms21030994.

Gaudelli, N. M. *et al.* (2017) 'Programmable base editing of A•T to G•C in genomic DNA without DNA cleavage', *Nature* 2017 551:7681, 551(7681), pp. 464–471. doi: 10.1038/nature24644.

George, A. *et al.* (2022) 'In vitro disease modeling of oculocutaneous albinism type 1 and 2 using human induced pluripotent stem cell-derived retinal pigment epithelium', *Stem Cell Reports*, 17(1), pp. 173–186. doi: 10.1016/j.stemcr.2021.11.016.

Georgiou, M. *et al.* (2022) 'Activation of autophagy reverses progressive and deleterious protein aggregation in PRPF31 patient-induced pluripotent stem cell-derived retinal pigment epithelium cells', *Clinical and Translational Medicine*, 12(3), p. e759. doi: 10.1002/CTM2.759.

Gerdes, J. M., Davis, E. E. and Katsanis, N. (2009) 'The Vertebrate Primary Cilium in Development, Homeostasis, and Disease', *Cell*, 137(1), pp. 32–45. doi: 10.1016/J.CELL.2009.03.023.

Ghossoub, R. *et al.* (2011) 'The ciliary pocket: a once-forgotten membrane domain at the base of cilia', *Biology of the Cell*, 103(3), pp. 131–144. doi: 10.1042/bc20100128.

Goetz, S. C. and Anderson, K. V. (2010) 'The primary cilium: A signalling centre during vertebrate development', *Nature Reviews Genetics*, 11(5), pp. 331–344. doi: 10.1038/nrg2774.

Gonzalez-Cordero, A. *et al.* (2018) 'Assessment of AAV Vector Tropisms for Mouse and Human Pluripotent Stem Cell-Derived RPE and Photoreceptor Cells', *Human Gene Therapy*, 29(10), pp. 1124–1139. doi: 10.1089/hum.2018.027.

Gorczyca, W. A. *et al.* (1995) 'Guanylyl cyclase activating protein: A calcium-sensitive regulator of phototransduction', *Journal of Biological Chemistry*, 270(37), pp. 22029–22036. doi: 10.1074/jbc.270.37.22029.

Gottschalk, A. *et al.* (1999) *Identification by mass spectrometry and functional analysis of novel proteins of the yeast [U4/U6·U5] tri-snRNP*, *EMBO Journal*. doi: 10.1093/emboj/18.16.4535.

Gouras, P. *et al.* (2011) 'A novel melano-lysosome in the retinal epithelium of rhesus monkeys', *Experimental Eye Research*, 93(6), pp. 937–946. doi: 10.1016/j.exer.2011.10.011.

Gozani, O., Feld, R. and Reed, R. (1996) 'Evidence that sequence-independent binding of highly conserved U2 snRNP proteins upstream of the branch site is required for assembly of spliceosomal complex A', *Genes and Development*, 10(2), pp. 233–243. doi: 10.1101/gad.10.2.233.

Gozani, O., Potashkin, J. and Reed, R. (1998) 'A Potential Role for U2AF-SAP 155 Interactions in Recruiting U2 snRNP to the Branch Site', *Molecular and Cellular Biology*, 18(8), pp. 4752–4760. doi: 10.1128/mcb.18.8.4752.

Grainger, R. J. and Beggs, J. D. (2005) 'Prp8 protein: At the heart of the spliceosome', *Rna*, pp. 533–557. doi: 10.1261/rna.2220705.

Graziotto, J. J. *et al.* (2011) 'Three gene-targeted mouse models of RNA splicing factor RP show late-onset RPE and retinal degeneration', *Investigative Ophthalmology and Visual Science*, 52(1), pp. 190–198. doi: 10.1167/iovs.10-5194.

Gurdon, J. B. (1962) 'The developmental capacity of nuclei taken from intestinal epithelium cells of feeding tadpoles.', *Journal of embryology and experimental morphology*, 10(4), pp. 622–640. doi: 10.1242/dev.10.4.622.

Haeseleer, F. *et al.* (1998) 'Molecular characterization of a novel short-chain dehydrogenase/reductase that reduces all-trans-retinal', *Journal of Biological Chemistry*, 273(34), pp. 21790–21799. doi: 10.1074/jbc.273.34.21790.

Haeseleer, F. *et al.* (2002) 'Dual-substrate specificity short chain retinol dehydrogenases from the vertebrate retina', *Journal of Biological Chemistry*, 277(47), pp. 45537–45546. doi: 10.1074/jbc.M208882200.

Hamm, H. E. (1998) 'The many faces of G protein signaling', *Journal of Biological Chemistry*, 273(2), pp. 669–672. doi: 10.1074/jbc.273.2.669.

Han, X. *et al.* (2019) 'Generation of hypoimmunogenic human pluripotent stem cells', *Proceedings of the National Academy of Sciences of the United States of America*, 116(21), pp. 10441–10446. doi: 10.1073/pnas.1902566116.

Hargrave, P. A. (2001) *Rhodopsin structure, function, and topography: The Friedenwald lecture, Investigative Ophthalmology and Visual Science*. [Association for Research in Vision and Ophthalmology, etc.]. Available at: <https://iovs.arvojournals.org/article.aspx?articleid=2162649> (Accessed: 6 June 2019).

Hartmuth, K. *et al.* (2002) 'Protein composition of human prespliceosomes isolated by a tobramycin affinity-selection method', *Proceedings of the National Academy of Sciences of the United States of America*, 99(26), pp. 16719–16724. doi: 10.1073/pnas.262483899.

Hartong, D. T., Berson, E. L. and Dryja, T. P. (2006) *Retinitis pigmentosa, Lancet*. doi: 10.1016/S0140-6736(06)69740-7.

Haselbach, D. *et al.* (2018) 'Structure and Conformational Dynamics of the Human Spliceosomal Bact Complex', *Cell*, 172(3), pp. 454-464.e11. doi: 10.1016/J.CELL.2018.01.010.

Hauswirth, W. W. *et al.* (2008) 'Treatment of Leber congenital amaurosis due to RPE65 mutations by ocular subretinal injection of adeno-associated virus gene vector: Short-term results of a phase I trial', *Human Gene Therapy*, 19(10), pp. 979–990. doi: 10.1089/hum.2008.107.

Hayes, M. J. *et al.* (2019) 'Remodeling of the basal labyrinth of retinal pigment epithelial cells with osmotic challenge, age, and disease', *Investigative Ophthalmology and Visual Science*, 60(7), pp. 2515–2524. doi: 10.1167/iovs.19-26784.

He, W., Cowan, C. W. and Wensel, T. G. (1998) 'RGS9, a GTPase accelerator for phototransduction', *Neuron*, 20(1), pp. 95–102. doi: 10.1016/S0896-6273(00)80437-7.

Heng, H. H. Q., Wang, A. and Hu, J. (1998) 'Mapping of the human HPRP3 and HPRP4 genes encoding U4/U6-associated splicing factors to chromosomes 1q21.1 and 9q31-q33', *Genomics*, 48(2), pp. 273–275. doi: 10.1006/geno.1997.5181.

Herzel, L. *et al.* (2017) 'Splicing and transcription touch base: Co-transcriptional spliceosome assembly and function', *Nature Reviews Molecular Cell Biology*, 18(10), pp. 637–650. doi: 10.1038/nrm.2017.63.

Hsu, P. D., Lander, E. S. and Zhang, F. (2014) 'Development and applications of CRISPR-Cas9 for genome engineering', *Cell*, 157(6), pp. 1262–1278. doi: 10.1016/j.cell.2014.05.010.

Hu, Z. *et al.* (2018) 'Ligase IV inhibitor SCR7 enhances gene editing directed by CRISPR-Cas9 and ssODN in human cancer cells', *Cell and Bioscience*, 8(1). doi: 10.1186/s13578-018-0200-z.

Huranová, M. *et al.* (2009) 'A mutation linked to retinitis pigmentosa in HPRP31 causes protein instability and impairs its interactions with spliceosomal snRNPs', *Human Molecular Genetics*, 18(11), pp. 2014–2023. doi: 10.1093/hmg/ddp125.

Hurley, J. B., Spencer, M. and Niemi, G. A. (1998) 'Rhodopsin phosphorylation and its role in photoreceptor function', *Vision Research*, 38(10), pp. 1341–1352. doi: 10.1016/S0042-6989(97)00459-8.

Idelson, M. *et al.* (2009) 'Directed Differentiation of Human Embryonic Stem Cells into Functional Retinal Pigment Epithelium Cells', *Cell Stem Cell*, 5(4), pp. 396–408. doi: 10.1016/j.stem.2009.07.002.

Iiri, T., Farfel, Z. and Bourne, H. R. (1998) 'G-protein diseases furnish a model for the turn-on switch', *Nature*, 394(6688), pp. 35–38. doi: 10.1038/27831.

Imanishi, Y. *et al.* (2004) 'Noninvasive two-photon imaging reveals retinyl ester storage structures in the eye', *Journal of Cell Biology*, 164(3), pp. 373–383. doi:

10.1083/jcb.200311079.

Iwasaki, Y. *et al.* (2016) 'Differentiation/purification protocol for retinal pigment epithelium from mouse induced pluripotent stem cells as a research tool', *PLoS ONE*, 11(7), p. 158282. doi: 10.1371/journal.pone.0158282.

Jacobson, S. G. *et al.* (2012) 'Gene therapy for leber congenital amaurosis caused by RPE65 mutations: Safety and efficacy in 15 children and adults followed up to 3 years', *Archives of Ophthalmology*, 130(1), pp. 9–24. doi: 10.1001/archophthalmol.2011.298.

Jang, H. *et al.* (2021) 'Application of prime editing to the correction of mutations and phenotypes in adult mice with liver and eye diseases', *Nature Biomedical Engineering*, 6, pp. 181–194. doi: 10.1101/2021.01.08.425835.

Jurica, M. S. and Moore, M. J. (2003) 'Pre-mRNA splicing: Awash in a sea of proteins', *Molecular Cell*, 12(1), pp. 5–14. doi: 10.1016/S1097-2765(03)00270-3.

Kahlert, M. and Hofmann, K. P. (1991) 'Reaction rate and collisional efficiency of the rhodopsin-transducin system in intact retinal rods', *Biophysical Journal*, 59(2), pp. 375–386. doi: 10.1016/S0006-3495(91)82231-7.

Kajiwara, K., Berson, E. L. and Dryja, T. P. (1994) 'Digenic retinitis pigmentosa due to mutations at the unlinked peripherin/RDS and ROM1 loci', *Science*, 264(5165), pp. 1604–1608. doi: 10.1126/science.8202715.

Kamao, H. *et al.* (2014) 'Characterization of human induced pluripotent stem cell-derived retinal pigment epithelium cell sheets aiming for clinical application', *Stem Cell Reports*, 2(2), pp. 205–218. doi: 10.1016/j.stemcr.2013.12.007.

Kasus-Jacobi, A. *et al.* (2005) 'Functional characterization of mouse RDH11 as a retinol dehydrogenase involved in dark adaptation in Vivo', *Journal of Biological Chemistry*, 280(21), pp. 20413–20420. doi: 10.1074/jbc.M413789200.

Kawamura, S. (1993) 'Rhodopsin phosphorylation as a mechanism of cyclic GMP

phosphodiesterase regulation by S-modulin', *Nature*, 362(6423), pp. 855–857. doi: 10.1038/362855a0.

Kaya, K. D. *et al.* (2019) 'Transcriptome-based molecular staging of human stem cell-derived retinal organoids uncovers accelerated photoreceptor differentiation by 9-cis retinal', *Molecular Vision*, 25, pp. 663–678. Available at: /pmc/articles/PMC6857775/?report=abstract (Accessed: 26 June 2020).

Kevany, B. M. and Palczewski, K. (2010) 'Phagocytosis of retinal rod and cone photoreceptors', *Physiology*, 25(1), pp. 8–15. doi: 10.1152/physiol.00038.2009.

Kilpinen, H. *et al.* (2017) 'Common genetic variation drives molecular heterogeneity in human iPSCs', *Nature*, 546(7658), pp. 370–375. doi: 10.1038/nature22403.

Kim, H. K. *et al.* (2020) 'Predicting the efficiency of prime editing guide RNAs in human cells', *Nature Biotechnology* 2020 39:2, 39(2), pp. 198–206. doi: 10.1038/s41587-020-0677-y.

Kim, S. *et al.* (2014) 'Highly efficient RNA-guided genome editing in human cells via delivery of purified Cas9 ribonucleoproteins', *Genome Research*, 24(6), pp. 1012–1019. doi: 10.1101/gr.171322.113.

Kim, T. S. *et al.* (2005) 'Delayed dark adaptation in 11-cis-retinol dehydrogenase-deficient mice: A role of RDH11 in visual processes in vivo', *Journal of Biological Chemistry*, 280(10), pp. 8694–8704. doi: 10.1074/jbc.M413172200.

Kiser, P. D., Golczak, M. and Palczewski, K. (2014) 'Chemistry of the retinoid (visual) cycle', *Chemical Reviews*, 114(1), pp. 194–232. doi: 10.1021/cr400107q.

Kokkinaki, M., Sahibzada, N. and Golestaneh, N. (2011) 'Human induced pluripotent stem-derived retinal pigment epithelium (RPE) cells exhibit ion transport, membrane potential, polarized vascular endothelial growth factor secretion, and gene expression pattern similar to native RPE', *Stem Cells*, 29(5), pp. 825–835. doi: 10.1002/stem.635.

Kolb, H., Fernandez, E. and Nelson, R. (2016) 'The Organization of the Retina and Visual

- System', *Webvision*, pp. 1–31. Available at: <http://www.ncbi.nlm.nih.gov/books/NBK11504/>.
- Kumar, S. R. *et al.* (2016) 'Clinical development of gene therapy: results and lessons from recent successes', *Molecular Therapy - Methods and Clinical Development*, 3, p. 16034. doi: 10.1038/mtm.2016.34.
- Kurtovic-Kozaric, A. *et al.* (2015) 'PRPF8 defects cause missplicing in myeloid malignancies', *Leukemia*, 29(1), pp. 126–136. doi: 10.1038/leu.2014.144.
- Kyttälä, A. *et al.* (2016) 'Genetic Variability Overrides the Impact of Parental Cell Type and Determines iPSC Differentiation Potential', *Stem Cell Reports*, 6(2), pp. 200–212. doi: 10.1016/j.stemcr.2015.12.009.
- Lange, C. A. K. and Bainbridge, J. W. B. (2012) 'Oxygen sensing in retinal health and disease', *Ophthalmologica*, 227(3), pp. 115–131. doi: 10.1159/000331418.
- Laurent, L. C. *et al.* (2011) 'Dynamic changes in the copy number of pluripotency and cell proliferation genes in human ESCs and iPSCs during reprogramming and time in culture', *Cell Stem Cell*, 8(1), pp. 106–118. doi: 10.1016/j.stem.2010.12.003.
- Lee Ann, R. A. (2012) *Clinical Anatomy and Physiology of the Visual System*, *Clinical Anatomy and Physiology of the Visual System*. Elsevier/Butterworth-Heinemann. doi: 10.1016/C2009-0-56108-9.
- Lee, G. *et al.* (2009) 'Modelling pathogenesis and treatment of familial dysautonomia using patient-specific iPSCs', *Nature*, 461(7262), pp. 402–406. doi: 10.1038/nature08320.
- Liang, G. and Zhang, Y. (2013) *Genetic and epigenetic variations in iPSCs: Potential causes and implications for application*, *Cell Stem Cell*. NIH Public Access. doi: 10.1016/j.stem.2013.07.001.
- Liang, X. *et al.* (2015) 'Rapid and highly efficient mammalian cell engineering via Cas9 protein transfection', *Journal of Biotechnology*, 208, pp. 44–53. doi: 10.1016/j.jbiotec.2015.04.024.
- Liang, X. *et al.* (2017) 'Enhanced CRISPR/Cas9-mediated precise genome editing by improved

design and delivery of gRNA, Cas9 nuclease, and donor DNA', *Journal of Biotechnology*, 241, pp. 136–146. doi: 10.1016/j.jbiotec.2016.11.011.

Lim, L. S. *et al.* (2012) 'Age-related macular degeneration', *The Lancet*, 379(9827), pp. 1728–1738. doi: 10.1016/S0140-6736(12)60282-7.

Linder, B. *et al.* (2011) 'Systemic splicing factor deficiency causes tissue-specific defects: A zebrafish model for retinitis pigmentosa', *Human Molecular Genetics*, 20(2), pp. 368–377. doi: 10.1093/hmg/ddq473.

Linder, B. *et al.* (2014) 'Identification of a PRPF4 loss-of-function variant that abrogates U4/U6.U5 Tri-snRNP integration and is associated with retinitis pigmentosa', *PLoS ONE*, 9(11). doi: 10.1371/journal.pone.0111754.

Lister, R. *et al.* (2011) 'Hotspots of aberrant epigenomic reprogramming in human induced pluripotent stem cells', *Nature*, 471(7336), pp. 68–73. doi: 10.1038/nature09798.

Liu, S. *et al.* (2015) 'A composite double-/single-stranded rna-binding region in protein Prp3 supports tri-snRNP stability and splicing', *eLife*, 4(JULY 2015). doi: 10.7554/eLife.07320.

Liu, T. *et al.* (2012) 'A Novel Missense SNRNP200 Mutation Associated with Autosomal Dominant Retinitis Pigmentosa in a Chinese Family', *PLoS ONE*. Edited by U. Pandey, 7(9), p. e45464. doi: 10.1371/journal.pone.0045464.

Luo, M. *et al.* (2010) 'Nuclear entry of active caspase-3 is facilitated by its p3-recognition-based specific cleavage activity', *Cell Research*, 20(2), pp. 211–222. doi: 10.1038/cr.2010.9.

Lützelberger, M. *et al.* (2009) 'The N-terminus of Prp1 (Prp6/U5-102 K) is essential for spliceosome activation in vivo', *Nucleic Acids Research*, 38(5), pp. 1610–1622. doi: 10.1093/nar/gkp1155.

MacDonald, P. N. and Ong, D. E. (1988) 'A lecithin: Retinol acyltransferase activity in human and rat liver', *Biochemical and Biophysical Research Communications*, 156(1), pp. 157–163. doi: 10.1016/S0006-291X(88)80818-0.

Maeda, A. *et al.* (2005) 'Role of photoreceptor-specific retinol dehydrogenase in the retinoid cycle in vivo', *Journal of Biological Chemistry*, 280(19), pp. 18822–18832. doi: 10.1074/jbc.M501757200.

Maeda, A. *et al.* (2006) 'Effects of potent inhibitors of the retinoid cycle on visual function and photoreceptor protection from light damage in mice', *Molecular Pharmacology*, 70(4), pp. 1220–1229. doi: 10.1124/mol.106.026823.

Maeder, C., Kutach, A. K. and Guthrie, C. (2009) 'ATP-dependent unwinding of U4/U6 snRNAs by the Brr2 helicase requires the C terminus of Prp8', *Nature Structural and Molecular Biology*, 16(1), pp. 42–48. doi: 10.1038/nsmb.1535.

Maguire, A. M. *et al.* (2008) 'Safety and Efficacy of Gene Transfer for Leber's Congenital Amaurosis', *New England Journal of Medicine*, 358(21), pp. 2240–2248. doi: 10.1056/nejmoa0802315.

Maita, H. *et al.* (2005) 'Association of PAP-1 and Prp3p, the products of causative genes of dominant retinitis pigmentosa, in the tri-snRNP complex', *Experimental Cell Research*, 302(1), pp. 61–68. doi: 10.1016/j.yexcr.2004.08.022.

Makarov, E. M. *et al.* (2002) 'Small nuclear ribonucleoprotein remodeling during catalytic activation of the spliceosome', *Science*, 298(5601), pp. 2205–2208. doi: 10.1126/science.1077783.

Makarova, O. V. *et al.* (2002) 'Protein 61K, encoded by a gene (PRPF31) linked to autosomal dominant retinitis pigmentosa, is required for U4/U6·U5 tri-snRNP formation and pre-mRNA splicing', *EMBO Journal*, 21(5), pp. 1148–1157. doi: 10.1093/emboj/21.5.1148.

Makarova, O. V. *et al.* (2004) 'A subset of human 35S U5 proteins, including Prp19, function prior to catalytic step 1 of splicing', *EMBO Journal*, 23(12), pp. 2381–2391. doi: 10.1038/sj.emboj.7600241.

Makino, E. R. *et al.* (1999) 'The GTPase activating factor for transducin in rod photoreceptors is the complex between RGS9 and type 5 G protein β subunit', *Proceedings of the National*

Academy of Sciences of the United States of America, 96(5), pp. 1947–1952. doi: 10.1073/pnas.96.5.1947.

Malicki, J. J. and Johnson, C. A. (2017) 'The Cilium: Cellular Antenna and Central Processing Unit', *Trends in Cell Biology*, 27(2), pp. 126–140. doi: 10.1016/j.tcb.2016.08.002.

Maniatis, T. and Reed, R. (2002) 'An extensive network of coupling among gene expression machines', *Nature*, 416(6880), pp. 499–506. doi: 10.1038/416499a.

Mao, Y. and Finnemann, S. C. (2012) 'Essential diurnal Rac1 activation during retinal phagocytosis requires $\alpha\beta 5$ integrin but not tyrosine kinases focal adhesion kinase or Mer tyrosine kinase', *Molecular Biology of the Cell*, 23(6), pp. 1104–1114. doi: 10.1091/mbc.E11-10-0840.

Maréchal, A. *et al.* (2014) 'PRP19 Transforms into a Sensor of RPA-ssDNA after DNA Damage and Drives ATR Activation via a Ubiquitin-Mediated Circuitry', *Molecular Cell*, 53(2), pp. 235–246. doi: 10.1016/j.molcel.2013.11.002.

Markouli, C. *et al.* (2019) 'Gain of 20q11.21 in Human Pluripotent Stem Cells Impairs TGF- β -Dependent Neuroectodermal Commitment', *Stem Cell Reports*, 13(1), pp. 163–176. doi: 10.1016/j.stemcr.2019.05.005.

Martin, G. R. (1981) 'Isolation of a pluripotent cell line from early mouse embryos cultured in medium conditioned by teratocarcinoma stem cells', *Proceedings of the National Academy of Sciences of the United States of America*, 78(12 II), pp. 7634–7638. doi: 10.1073/pnas.78.12.7634.

Martins-Taylor, K. and Xu, R. H. (2012) 'Concise review: Genomic stability of human induced pluripotent stem cells', *Stem Cells*, 30(1), pp. 22–27. doi: 10.1002/stem.705.

May-Simera, H. L. *et al.* (2018a) 'Primary Cilium-Mediated Retinal Pigment Epithelium Maturation Is Disrupted in Ciliopathy Patient Cells', *Cell Reports*, 22(1), pp. 189–205. doi: 10.1016/j.celrep.2017.12.038.

May-Simera, H. L. *et al.* (2018b) 'Primary Cilium-Mediated Retinal Pigment Epithelium Maturation Is Disrupted in Ciliopathy Patient Cells', *Cell Reports*, 22(1), pp. 189–205. doi: 10.1016/j.celrep.2017.12.038.

Mayerle, M. and Guthrie, C. (2016) 'Prp8 retinitis pigmentosa mutants cause defects in the transition between the catalytic steps of splicing', *Rna*, 22(5), pp. 793–809. doi: 10.1261/rna.055459.115.

Mellough, C. B. *et al.* (2014) 'Lab generated retina: Realizing the dream', *Visual Neuroscience*, 31(4–5), pp. 317–332. doi: 10.1017/S095252381400008X.

Mellough, C. B., Bauer, R., *et al.* (2019) 'An integrated transcriptional analysis of the developing human retina', *Development (Cambridge)*, 146(2), p. dev169474. doi: 10.1242/dev.169474.

Mellough, C. B., Collin, J., *et al.* (2019) 'Systematic Comparison of Retinal Organoid Differentiation from Human Pluripotent Stem Cells Reveals Stage Specific, Cell Line, and Methodological Differences', *Stem Cells Translational Medicine*, 8(7), pp. 694–706. doi: 10.1002/sctm.18-0267.

Micheal, S. *et al.* (2018) 'Variants in the PRPF8 Gene are Associated with Glaucoma', *Molecular Neurobiology*, 55(5), pp. 4504–4510. doi: 10.1007/s12035-017-0673-5.

Milyushina, L. A. *et al.* (2011) 'Phenotypic plasticity of retinal pigment epithelial cells from adult human eye in vitro', *Bulletin of Experimental Biology and Medicine*, 151(4), pp. 506–511. doi: 10.1007/s10517-011-1368-y.

Mirauta, B. A. *et al.* (2018) 'Population-scale proteome variation in human induced pluripotent stem cells', *bioRxiv*, p. 439216. doi: 10.1101/439216.

Miyagishima, K. *et al.* (2016) 'In Pursuit of Authenticity: iPSC derived RPE for clinical applications', *STEM CELLS Translational Medicine*, pp. 381–388.

Miyaoka, Y. *et al.* (2016) 'Systematic quantification of HDR and NHEJ reveals effects of locus,

nuclease, and cell type on genome-editing', *Scientific Reports*, 6. doi: 10.1038/srep23549.

Moiseyev, G. *et al.* (2003) 'Retinyl esters are the substrate for isomerohydrolase', *Biochemistry*, 42(7), pp. 2229–2238. doi: 10.1021/bi026911y.

Molla-Herman, A. *et al.* (2010) 'The ciliary pocket: An endocytic membrane domain at the base of primary and motile cilia', *Journal of Cell Science*, 123(10), pp. 1785–1795. doi: 10.1242/jcs.059519.

Morizur, L. *et al.* (2020) 'Human pluripotent stem cells: A toolbox to understand and treat retinal degeneration', *Molecular and Cellular Neuroscience*, 107, p. 103523. doi: 10.1016/J.MCN.2020.103523.

Mozaffari-Jovin, S. *et al.* (2013) 'Inhibition of RNA helicase Brr2 by the C-terminal tail of the spliceosomal protein Prp8', *Science*, 341(6141), pp. 80–84. doi: 10.1126/science.1237515.

Nag, T. C. and Wadhwa, S. (2012) 'Ultrastructure of the human retina in aging and various pathological states', *Micron*, 43(7), pp. 759–781. doi: 10.1016/j.micron.2012.01.011.

Nakano, T. *et al.* (2012) 'Self-formation of optic cups and storable stratified neural retina from human ESCs', *Cell Stem Cell*, 10(6), pp. 771–785. doi: 10.1016/j.stem.2012.05.009.

Nazlamova, L. *et al.* (2021) 'A CRISPR and high-content imaging assay compliant with ACMG/AMP guidelines for clinical variant interpretation in ciliopathies', *Human Genetics*, 140(4), pp. 593–607. doi: 10.1007/S00439-020-02228-1/FIGURES/3.

Nickells, R. W. (1999) 'The First Steps in Seeing', *Archives of Ophthalmology*, 117(4), p. 550. doi: 10.1001/archophth.117.4.550.

Nordgaard, C. L. *et al.* (2008) 'Mitochondrial proteomics of the retinal pigment epithelium at progressive stages of age-related macular degeneration', *Investigative Ophthalmology and Visual Science*, 49(7), pp. 2848–2855. doi: 10.1167/iovs.07-1352.

O'Grady, L. *et al.* (2022) 'Heterozygous variants in PRPF8 are associated with neurodevelopmental disorders', *American Journal of Medical Genetics Part A*. doi:

10.1002/AJMG.A.62772.

O'Toole, E. T. *et al.* (2003) 'Three-dimensional organization of basal bodies from wild-type and δ -tubulin deletion strains of *Chlamydomonas reinhardtii*', *Molecular Biology of the Cell*, 14(7), pp. 2999–3012. doi: 10.1091/mbc.E02-11-0755.

Orban, T., Palczewska, G. and Palczewski, K. (2011) 'Retinyl ester storage particles (retinosomes) from the retinal pigmented epithelium resemble lipid droplets in other tissues', *Journal of Biological Chemistry*, 286(19), pp. 17248–17258. doi: 10.1074/jbc.M110.195198.

Palczewska, G. *et al.* (2010) 'Noninvasive multiphoton fluorescence microscopy resolves retinol and retinal condensation products in mouse eyes', *Nature Medicine*, 16(12), pp. 1444–1450. doi: 10.1038/nm.2260.

Palczewski, K. *et al.* (1994) 'Molecular cloning and characterization of retinal photoreceptor guanylyl cyclase-activating protein', *Neuron*, 13(2), pp. 395–404. doi: 10.1016/0896-6273(94)90355-7.

Palczewski, K. (1997) 'GTP-binding-protein-coupled receptor kinases - Two mechanistic models', *European Journal of Biochemistry*, 248(2), pp. 261–269. doi: 10.1111/j.1432-1033.1997.00261.x.

Papasaikas, P. and Valcárcel, J. (2016) 'The Spliceosome: The Ultimate RNA Chaperone and Sculptor', *Trends in Biochemical Sciences*, 41(1), pp. 33–45. doi: 10.1016/j.tibs.2015.11.003.

Parker, R. O. and Crouch, R. K. (2010) 'Retinol dehydrogenases (RDHs) in the visual cycle', *Experimental Eye Research*, 91(6), pp. 788–792. doi: 10.1016/j.exer.2010.08.013.

Patnaik, S. R. *et al.* (2015) 'The Role of RPGR and Its Interacting Proteins in Ciliopathies', *Journal of Ophthalmology*, 2015. doi: 10.1155/2015/414781.

Pena, V. *et al.* (2007) *Structure of a Multipartite Protein-Protein Interaction Domain in Splicing Factor Prp8 and Its Link to Retinitis Pigmentosa*, *Molecular Cell*. Cell Press. doi: 10.1016/j.molcel.2007.01.023.

Pugh, E. N. and Lamb, T. D. (1993) 'Amplification and kinetics of the activation steps in phototransduction', *BBA - Bioenergetics*, 1141(2–3), pp. 111–149. doi: 10.1016/0005-2728(93)90038-H.

Pugh, E. N. and Lamb, T. D. (2000) 'Chapter 5 Phototransduction in vertebrate rods and cones: Molecular mechanisms of amplification, recovery and light adaptation', *Handbook of Biological Physics*, 3(C), pp. 183–255. doi: 10.1016/S1383-8121(00)80008-1.

Quinn, R. H. and Miller, S. S. (1992) 'Ion transport mechanisms in native human retinal pigment epithelium', *Investigative Ophthalmology and Visual Science*, 33(13), pp. 3513–3527.

Radu, R. A. *et al.* (2008) 'Retinal pigment epithelium-retinal G protein receptor-opsin mediates light-dependent translocation of all-trans-retinyl esters for synthesis of visual chromophore in retinal pigment epithelial cells', *Journal of Biological Chemistry*, 283(28), pp. 19730–19738. doi: 10.1074/jbc.M801288200.

Raposo, G. and Marks, M. S. (2007) 'Melanosomes - Dark organelles enlighten endosomal membrane transport', *Nature Reviews Molecular Cell Biology*. Nature Publishing Group, pp. 786–797. doi: 10.1038/nrm2258.

Rattner, A., Smallwood, P. M. and Nathans, J. (2000) 'Identification and characterization of all-trans-retinol dehydrogenase from photoreceptor outer segments, the visual cycle enzyme that reduces all-trans-retinal to all-trans-retinol', *Journal of Biological Chemistry*, 275(15), pp. 11034–11043. doi: 10.1074/jbc.275.15.11034.

Redmond, T. M. *et al.* (1998) 'Rpe65 is necessary for production of 11-cis-vitamin A in the retinal visual cycle', *Nature Genetics*, 20(4), pp. 344–351. doi: 10.1038/3813.

Redmond, T. M. *et al.* (2005) 'Mutation of key residues of RPE65 abolishes its enzymatic role as isomerohydrolase in the visual cycle', *Proceedings of the National Academy of Sciences of the United States of America*, 102(38), pp. 13658–13663. doi: 10.1073/pnas.0504167102.

Regent, F. *et al.* (2019) 'Automation of human pluripotent stem cell differentiation toward retinal pigment epithelial cells for large-scale productions', *Scientific Reports*, 9(1), pp. 1–11.

doi: 10.1038/s41598-019-47123-6.

Reid, J. C. *et al.* (2021) 'Human pluripotent stem cells identify molecular targets of trisomy 12 in chronic lymphocytic leukemia patients', *Cell Reports*, 34(11). doi: 10.1016/j.celrep.2021.108845.

Richardson, C. D. *et al.* (2016) 'Enhancing homology-directed genome editing by catalytically active and inactive CRISPR-Cas9 using asymmetric donor DNA', *Nature Biotechnology*, 34(3), pp. 339–344. doi: 10.1038/nbt.3481.

Riis RC, A. G. (1983) 'The Briard Problem', *Proc Am Coll Vet Ophth*, pp. 62–75. Available at: https://repository.upenn.edu/vet_papers (Accessed: 21 February 2022).

Ripps, H. (2008) 'The color purple: milestones in photochemistry', *The FASEB Journal*, 22(12), pp. 4038–4043. doi: 10.1096/fj.08-1202ufm.

Rivolta, C. *et al.* (2006) 'Variation in retinitis pigmentosa-11 (PRPF31 or RP11) gene expression between symptomatic and asymptomatic patients with dominant RP11 mutations', *Human Mutation*, 27(7), pp. 644–653. doi: 10.1002/humu.20325.

Robinton, D. A. and Daley, G. Q. (2012) 'The promise of induced pluripotent stem cells in research and therapy', *Nature*, pp. 295–305. doi: 10.1038/nature10761.

Rose, A. M. *et al.* (2016) 'Transcriptional regulation of PRPF31 gene expression by MSR1 repeat elements causes incomplete penetrance in retinitis pigmentosa', *Scientific Reports 2016 6:1*, 6(1), pp. 1–9. doi: 10.1038/srep19450.

Rose, A. M. *et al.* (2017) 'Gene of the month: PRPF31', *Journal of Clinical Pathology*, 70(9), pp. 729–732. doi: 10.1136/jclinpath-2016-203971.

Rose, A. M. and Bhattacharya, S. S. (2016) 'Variant haploinsufficiency and phenotypic non-penetrance in PRPF31-associated retinitis pigmentosa', *Clinical Genetics*, 90(2), pp. 118–126. doi: 10.1111/CGE.12758.

Saari, J. C. *et al.* (2002) 'Analysis of the visual cycle in cellular retinol-binding protein type I

(CRBPI) knockout mice', *Investigative Ophthalmology and Visual Science*, 43(6), pp. 1730–1735. Available at: <http://www.ncbi.nlm.nih.gov/pubmed/12036972> (Accessed: 26 June 2019).

Sahel, J. A. *et al.* (2021) 'Partial recovery of visual function in a blind patient after optogenetic therapy', *Nature Medicine* 2021 27:7, 27(7), pp. 1223–1229. doi: 10.1038/s41591-021-01351-4.

Sander, J. D. and Joung, J. K. (2014) 'CRISPR-Cas systems for editing, regulating and targeting genomes', *Nature Biotechnology*, 32(4), pp. 347–350. doi: 10.1038/nbt.2842.

Schermelleh, L., Heintzmann, R. and Leonhardt, H. (2010) 'A guide to super-resolution fluorescence microscopy', *Journal of Cell Biology*, 190(2), pp. 165–175. doi: 10.1083/JCB.201002018.

Schnetkamp, P. P. M. (1989) 'NaCa or NaCaK exchange in rod photoreceptors', *Progress in Biophysics and Molecular Biology*, 54(1), pp. 1–29. doi: 10.1016/0079-6107(89)90007-2.

Schnetkamp, P. P. M. (1995) 'Calcium homeostasis in vertebrate retinal rod outer segments', *Cell Calcium*, 18(4), pp. 322–330. doi: 10.1016/0143-4160(95)90028-4.

Schwarz, N. *et al.* (2017) 'Arl3 and RP2 regulate the trafficking of ciliary tip kinesins', *Human Molecular Genetics*, 26(13), pp. 2480–2492. doi: 10.1093/hmg/ddx143.

Sell, S. (2010) 'On the stem cell origin of cancer', *American Journal of Pathology*, 176(6), pp. 2584–2594. doi: 10.2353/ajpath.2010.091064.

Shakhmantsir, I. *et al.* (2020) 'RNA Splicing Factor Mutations That Cause Retinitis Pigmentosa Result in Circadian Dysregulation', *Journal of Biological Rhythms*, 35(1), pp. 72–83. doi: 10.1177/0748730419887876.

Shen, X. L. *et al.* (2022) 'LUBAC regulates ciliogenesis by promoting CP110 removal from the mother centriole', *The Journal of cell biology*, 221(1). doi: 10.1083/jcb.202105092.

Shi, Y. *et al.* (2017) 'Induced pluripotent stem cell technology: A decade of progress', *Nature*

Reviews Drug Discovery, 16(2), pp. 115–130. doi: 10.1038/nrd.2016.245.

Simon, A. *et al.* (1995) 'The retinal pigment epithelial-specific 11-cis retinol dehydrogenase belongs to the family of short chain alcohol dehydrogenases', *Journal of Biological Chemistry*, 270(3), pp. 1107–1112. doi: 10.1074/jbc.270.3.1107.

Singh, R. *et al.* (2013) 'Functional analysis of serially expanded human iPS cell-derived RPE cultures', *Investigative Ophthalmology and Visual Science*, 54(10), pp. 6767–6778. doi: 10.1167/iovs.13-11943.

Sprang, S. R. (1997) 'G protein mechanisms: Insights from structural analysis', *Annual Review of Biochemistry*, 66(1), pp. 639–678. doi: 10.1146/annurev.biochem.66.1.639.

Srivastava, M. *et al.* (2012) 'An inhibitor of nonhomologous end-joining abrogates double-strand break repair and impedes cancer progression', *Cell*, 151(7), pp. 1474–1487. doi: 10.1016/j.cell.2012.11.054.

Stadtfield, M. and Hochedlinger, K. (2010) 'Induced pluripotency: History, mechanisms, and applications', *Genes and Development*, pp. 2239–2263. doi: 10.1101/gad.1963910.

Staley, J. P. and Guthrie, C. (1998) 'Mechanical devices of the spliceosome: Motors, clocks, springs, and things', *Cell*, 92(3), pp. 315–326. doi: 10.1016/S0092-8674(00)80925-3.

Staněk, D. *et al.* (2008) 'Spliceosomal small nuclear ribonucleoprotein particles repeatedly cycle through Cajal bodies', *Molecular Biology of the Cell*. Edited by W. Bickmore, 19(6), pp. 2534–2543. doi: 10.1091/mbc.E07-12-1259.

Stecher, H. *et al.* (1999) 'Preferential release of 11-cis-retinol from retinal pigment epithelial cells in the presence of cellular retinaldehyde-binding protein', *Journal of Biological Chemistry*, 274(13), pp. 8577–8585. doi: 10.1074/jbc.274.13.8577.

Steinberg, R. H., Fisher, S. K. and Anderson, D. H. (1980) 'Disc morphogenesis in vertebrate photoreceptors', *Journal of Comparative Neurology*, 190(3), pp. 501–518. doi: 10.1002/cne.901900307.

Strauss, O. (2005) 'The retinal pigment epithelium in visual function', *Physiological Reviews*, 85(3), pp. 845–881. doi: 10.1152/physrev.00021.2004.

Suh, S. *et al.* (2022) 'Precision genome editing in the eye.', *Proceedings of the National Academy of Sciences of the United States of America*, 119(39), p. e2210104119. doi: 10.1073/PNAS.2210104119.

Sullivan, L. S. *et al.* (2013) 'Prevalence of Mutations in eyeGENE Proband With a Diagnosis of Autosomal Dominant Retinitis Pigmentosa', *Investigative Ophthalmology & Visual Science*, 54(9), pp. 6255–6261. doi: 10.1167/IOVS.13-12605.

Takahashi, K. *et al.* (2007) 'Induction of Pluripotent Stem Cells from Adult Human Fibroblasts by Defined Factors', *Cell*, 131(5), pp. 861–872. doi: 10.1016/j.cell.2007.11.019.

Takahashi, K. and Yamanaka, S. (2006) 'Induction of Pluripotent Stem Cells from Mouse Embryonic and Adult Fibroblast Cultures by Defined Factors', *Cell*, 126(4), pp. 663–676. doi: 10.1016/j.cell.2006.07.024.

Tamiya, S., Liu, L. H. and Kaplan, H. J. (2010) 'Epithelial-mesenchymal transition and proliferation of retinal pigment epithelial cells initiated upon loss of cell-cell contact', *Investigative Ophthalmology and Visual Science*, 51(5), pp. 2755–2763. doi: 10.1167/iovs.09-4725.

Tanackovic, G., Ransijn, A., Ayuso, C., *et al.* (2011) 'A missense mutation in PRPF6 causes impairment of pre-mRNA splicing and autosomal-dominant retinitis pigmentosa', *American Journal of Human Genetics*, 88(5), pp. 643–649. doi: 10.1016/j.ajhg.2011.04.008.

Tanackovic, G., Ransijn, A., Thibault, P., *et al.* (2011) 'PRPF mutations are associated with generalized defects in spliceosome formation and pre-mRNA splicing in patients with retinitis pigmentosa', *Human Molecular Genetics*, 20(11), pp. 2116–2130. doi: 10.1093/hmg/ddr094.

Taschner, M. and Lorentzen, E. (2016) 'The intraflagellar transport machinery', *Cold Spring Harbor Perspectives in Biology*, 8(10), p. a028092. doi: 10.1101/cshperspect.a028092.

Thomson, J. A. (1998) 'Embryonic stem cell lines derived from human blastocysts', *Science*, 282(5391), pp. 1145–1147. doi: 10.1126/science.282.5391.1145.

Towns, K. V. *et al.* (2010) 'Prognosis for splicing factor PRPF8 retinitis pigmentosa, novel mutations and correlation between human and yeast phenotypes', *Human Mutation*, 31(5), p. Online. doi: 10.1002/humu.21236.

Vaclavik, V. *et al.* (2010) *Variable phenotypic expressivity in a Swiss family with autosomal dominant retinitis pigmentosa due to a T494M mutation in the PRPF3 gene*, *Molecular Vision*. Available at: <http://www.molvis.org/molvis/v16/a53> (Accessed: 11 February 2019).

Valcárcel, J. *et al.* (1996) 'Interaction of U2AF65 RS region with pre-mRNA of branch point and promotion base pairing with U2 snRNA', *Science*, 273(5282), pp. 1706–1709. doi: 10.1126/science.273.5282.1706.

Valdés-Sánchez, L. *et al.* (2019) 'Retinal pigment epithelium degeneration caused by aggregation of PRPF31 and the role of HSP70 family of proteins', *Molecular Medicine*, 26(1), p. 1. doi: 10.1186/s10020-019-0124-z.

Venturini, G. *et al.* (2012) 'CNOT3 Is a Modifier of PRPF31 Mutations in Retinitis Pigmentosa with Incomplete Penetrance', *PLoS Genetics*, 8(11). doi: 10.1371/journal.pgen.1003040.

Verbakel, S. K. *et al.* (2018) 'Non-syndromic retinitis pigmentosa'. doi: 10.1016/j.preteyeres.2018.03.005.

Veske, A. *et al.* (1999) 'Retinal Dystrophy of Swedish Briard/Briard–Beagle Dogs Is Due to a 4-bp Deletion in RPE65', *Genomics*, 57(1), pp. 57–61. doi: 10.1006/GENO.1999.5754.

Vithana, E. N. *et al.* (2001) 'A human homolog of yeast pre-mRNA splicing gene, PRP31, underlies autosomal dominant retinitis pigmentosa on chromosome 19q13.4 (RP11)', *Molecular Cell*, 8(2), pp. 375–381. doi: 10.1016/S1097-2765(01)00305-7.

Volpato, V. *et al.* (2018) 'Reproducibility of Molecular Phenotypes after Long-Term Differentiation to Human iPSC-Derived Neurons: A Multi-Site Omics Study', *Stem Cell Reports*,

11(4), pp. 897–911. doi: 10.1016/j.stemcr.2018.08.013.

Volpato, V. and Webber, C. (2020) 'Addressing variability in iPSC-derived models of human disease: Guidelines to promote reproducibility', *DMM Disease Models and Mechanisms*. Company of Biologists Ltd. doi: 10.1242/dmm.042317.

Wahl, M. C., Will, C. L. and Lührmann, R. (2009) 'The Spliceosome: Design Principles of a Dynamic RNP Machine', *Cell*. Cell Press, pp. 701–718. doi: 10.1016/j.cell.2009.02.009.

Wald, G. (1968) 'The molecular basis of visual excitation', *Nature*, 219(5156), pp. 800–807. doi: 10.1038/219800a0.

Watanabe, K. *et al.* (2023) 'Quality of Life and Economic Impacts of Retinitis Pigmentosa on Japanese Patients: A Non-interventional Cross-sectional Study', *Advances in Therapy*, 40(5), pp. 2375–2393. doi: 10.1007/s12325-023-02446-9.

Wei, Q. *et al.* (2012) 'The BBSome controls IFT assembly and turnaround in cilia', *Nature Cell Biology*, 14(9), pp. 950–957. doi: 10.1038/ncb2560.

Weissman, I. L. (2000) 'Stem cells: Units of development, units of regeneration, and units in evolution', *Cell*. Cell Press, pp. 157–168. doi: 10.1016/S0092-8674(00)81692-X.

Westenskow, P. D. *et al.* (2012) 'Using flow cytometry to compare the dynamics of photoreceptor outer segment phagocytosis in iPS-derived RPE cells', *Investigative Ophthalmology and Visual Science*, 53(10), pp. 6282–6290. doi: 10.1167/iovs.12-9721.

Wheway, G. *et al.* (2015a) 'An siRNA-based functional genomics screen for the identification of regulators of ciliogenesis and ciliopathy genes', *Nature Cell Biology*, 17(8), pp. 1074–1087. doi: 10.1038/ncb3201.

Wheway, G. *et al.* (2015b) 'An siRNA-based functional genomics screen for the identification of regulators of ciliogenesis and ciliopathy genes', *Nature Cell Biology*, 17(8), pp. 1074–1087. doi: 10.1038/ncb3201.

Wheway, G. *et al.* (2020) 'Mutation spectrum of PRPF31, genotype-phenotype correlation in

retinitis pigmentosa, and opportunities for therapy', *Experimental Eye Research*. Academic Press, p. 107950. doi: 10.1016/j.exer.2020.107950.

Wickramasinghe, Vihandha O *et al.* (2015) 'Regulation of constitutive and alternative mRNA splicing across the human transcriptome by PRPF8 is determined by 5' splice site strength', *Genome Biology*, 16(1). doi: 10.1186/s13059-015-0749-3.

Wickramasinghe, Vihandha O. *et al.* (2015) 'Regulation of constitutive and alternative mRNA splicing across the human transcriptome by PRPF8 is determined by 5' splice site strength', *Genome Biology*, 16(1), p. 201. doi: 10.1186/s13059-015-0749-3.

Wilden, U., Hall, S. W. and Kuhn, H. (1986) 'Phosphodiesterase activation by photoexcited rhodopsin is quenched when rhodopsin is phosphorylated and binds the intrinsic 48-kDa protein of rod outer segments', *Proceedings of the National Academy of Sciences of the United States of America*, 83(5), pp. 1174–1178. doi: 10.1073/pnas.83.5.1174.

Wilkie, S. E. *et al.* (2008) 'Disease mechanism for retinitis pigmentosa (RP11) caused by missense mutations in the splicing factor gene PRPF31', *Molecular Vision*, 14, pp. 683–690. Available at: <http://www.ncbi.nlm.nih.gov/pubmed/18431455> (Accessed: 9 July 2019).

Will, C. L. *et al.* (2001) 'A novel U2 and U11/U12 snRNP protein that associates with the pre-mRNA branch site', *EMBO Journal*, 20(16), pp. 4536–4546. doi: 10.1093/emboj/20.16.4536.

Will, C. L. and Lührmann, R. (2011) 'Spliceosome structure and function', *Cold Spring Harbor Perspectives in Biology*, 3(7), pp. 1–2. doi: 10.1101/cshperspect.a003707.

Wilmut, I. *et al.* (1997) 'Viable offspring derived from fetal and adult mammalian cells', *Nature*, 385(6619), pp. 810–813. doi: 10.1038/385810a0.

Wrigstad, A., Narfström, K. and Nilsson, S. E. G. (1994) 'Slowly progressive changes of the retina and retinal pigment epithelium in briard dogs with hereditary retinal dystrophy', *Documenta Ophthalmologica 1994 87:4*, 87(4), pp. 337–354. doi: 10.1007/BF01203343.

Wrigstad, A., Nilsson, S. E. G. and Narfström, K. (1992) 'Ultrastructural changes of the retina

and the retinal pigment epithelium in briard dogs with hereditary congenital night blindness and partial day blindness', *Experimental Eye Research*, 55(6), pp. 805–818. doi: 10.1016/0014-4835(92)90007-F.

Wu, Q., Chen, C. and Koutalos, Y. (2006) 'All-trans retinol in rod photoreceptor outer segments moves unrestrictedly by passive diffusion', *Biophysical Journal*, 91(12), pp. 4678–4689. doi: 10.1529/biophysj.106.086728.

Xiong, W. *et al.* (2019) 'AAV cis-regulatory sequences are correlated with ocular toxicity', *Proceedings of the National Academy of Sciences of the United States of America*, 116(12), pp. 5785–5794. doi: 10.1073/PNAS.1821000116/-/DCSUPPLEMENTAL.

Xu, F. *et al.* (2012) 'Novel PRPF31 mutations associated with Chinese autosomal dominant retinitis pigmentosa patients', *Molecular Vision*, 18, pp. 3021–3028. Available at: <http://www.molvis.org/molvis/v18/a309>.

Xu, X. *et al.* (2018) 'Efficient homology-directed gene editing by CRISPR/Cas9 in human stem and primary cells using tube electroporation', *Scientific Reports*, 8(1), pp. 1–11. doi: 10.1038/s41598-018-30227-w.

Yin, J. *et al.* (2011) 'Mutant Prpf31 causes pre-mRNA splicing defects and rod photoreceptor cell degeneration in a zebrafish model for Retinitis pigmentosa', *Molecular Neurodegeneration*, 6(1), p. 56. doi: 10.1186/1750-1326-6-56.

Zhang, J. *et al.* (2017) 'Stem cell culture and differentiation in microfluidic devices toward organ-on-a-chip', *Future Science OA*, 3(2), p. FSO187. doi: 10.4155/fsoa-2016-0091.

Zhang, L. *et al.* (2007) 'Crystal structure of the C-terminal domain of splicing factor Prp8 carrying retinitis pigmentosa mutants', *Protein Science*, 16(6), pp. 1024–1031. doi: 10.1110/ps.072872007.

Zhang, X. *et al.* (2018) 'Structure of the human activated spliceosome in three conformational states', *Cell Research*, 28(3), pp. 307–322. doi: 10.1038/cr.2018.14.

Zhao, C. *et al.* (2009) 'Autosomal-Dominant Retinitis Pigmentosa Caused by a Mutation in SNRNP200, a Gene Required for Unwinding of U4/U6 snRNAs', *American Journal of Human Genetics*, 85(5), pp. 617–627. doi: 10.1016/j.ajhg.2009.09.020.

Zhao, X., Palczewski, K. and Ohguro, H. (1995) 'Mechanism of rhodopsin phosphorylation', *Biophysical Chemistry*, 56(1–2), pp. 183–188. doi: 10.1016/0301-4622(95)00031-R.

Zhong, Z. *et al.* (2016) 'Two novel mutations in PRPF3 causing autosomal dominant retinitis pigmentosa', *Scientific Reports*, 6. doi: 10.1038/srep37840.

Annex

Supplementary Information 1: Full sequence of the CMV-*PRPF31*-AAV provided by Dr Mark Basche from the group of Professor Robin Ali at University College London.

Confirmed by 1 read

Confirmed by 2 reads

CMV Promotor

PRPF31

SV40 PolyA

Deviation from expected

One deviation at the end of CMV promotor. Outside annotated features, likely a result of an inaccurate reference sequence.

```
ACAAGAGAATCGCTGCGCGCTCGCTCGCTCACTGAGGCCGCCGGCAAAGCCCGGGCGTCGGGCG
ACCTTTGGTCGCCCCGCCTCAGTGAGCGAGCGAGCGCGCAGAGAGGGAGTGGCCAACCTCCATCACT
GATGTAATACGACTCACTAGTGGGCAGATCTTGAATGCATCGCGCGCACCGTACGTCTCGAGGAAT
TCCTGCAGGATATCCTGCAGTAGTTATTAATAGTAATCAATTACGGGGTCATTAGTTCATAGCCCATA
TATGGAGTTCGCGTTACATAACTTACGGTAAATGGCCCGCCTGGCTGACCGCCCAACGACCCCCGC
CCATTGACGTCAATAATGACGTATGTTCCCATAGTAACGCCAATAGGGACTTTCCATTGACGTCAATG
GGTGGAGTATTTACGGTAAACTGCCCACTTGGCAGTACATCAAGTGTATCATATGCCAAGTACGCC
CCTATTGACGTCAATGACGGTAAATGGCCCGCCTGGCATTATGCCAGTACATGACCTTATGGGACTT
TCCTACTTGGCAGTACATCTACGTATTAGTCATCGCTATTACCATGGTGTATGCGGTTTTGGCAGTACA
TCAATGGGCGTGGATAGCGGTTTGACTCACGGGGATTTCCAAGTCTCCACCCATTGACGTCAATGG
GAGTTTGTGGCACCAAATCAACGGGACTTTCCAAAATGTCGTAACAACCTCCGCCCATGACGC
AAATGGGCGGTAGGCGTGTACGGTGGGAGGTCTATATAAGCAGAGCT[C>G]GTTTAGTGAACCGTC
AGATCCGCTAGCGCTACCGGACTCAGATCTCGAGCTCAAGCTTCTGAATTCTGCAGTCGACGGTACCG
CGGATGTCTCTGGCAGATGAGCTCTTAGCTGATCTCGAAGAGGCAGCAGAAGAGGAGGAAGGAGG
AAGCTATGGGGAGGAAGAAGAGGAGCCAGCGATCGAGGATGTGCAGGAGGAGACACAGCTGGAT
CTTCCGGGGATTGAGTCAAGACCATCGCCAAGCTATGGGATAGTAAGATGTTTGCTGAGATTATGA
TGAAGATTGAGGAGTATATCAGCAAGCAAGCCAAAGCTTCAGAAGTGTGGGACCAGTGGAGGCC
GCGCCTGAATACCGCGTCATCGTGGATGCCAACAACCTGACCGTGGAGATCGAAAACGAGCTGAAC
ATCATCCATAAGTTCATCCGGGATAAGTACTCAAAGAGATTCCTGAACTGGAGTCCTTGGTCCCCAA
```

TGCACTGGATTACATCCGCACGGTCAAGGAGCTGGGCAACAGCCTGGACAAGTGCAAGAACAATGA
GAACCTGCAGCAGATCCTACCAATGCCACCATCATGGTCGTCAGCGTCACCGCCTCCACCACCCAGG
GGCAGCAGCTGTCGGAGGAGGAGCTGGAGCGGCTGGAGGAGGCCTGCGACATGGCGCTGGAGCT
GAACGCCTCCAAGCACCGCATCTACGAGTATGTGGAGTCCCGGATGTCCTTCATCGCACCCAACCTGT
CCATCATTATCGGGGCATCCACGGCCGAAGATCATGGGTGTGGCCGGCGGCCTGACCAACCTCTC
CAAGATGCCCGCCTGCAACATCATGCTGCTCGGGGCCAGCGCAAGACGCTGTCGGGCTTCTCGTCT
ACCTCAGTGCTGCCCCACACCGGCTACATCTACCACAGTGACATCGTGCAGTCCCTGCCACCGGATCT
GCGGGCGAAAGCGGCCCGGCTGGTGGCCGCAAGTGCACTGGCAGCCCGTGTGGACAGTTTCCA
CGAGAGCACAGAAGGGAAGGTGGGCTACGAACTGAAGGATGAGATCGAGCGCAAATTCGACAAGT
GGCAGGAGCCGCGCCTGTGAAGCAGGTGAAGCCGCTGCCTGCGCCCCTGGATGGACAGCGGAAG
AAGCGAGGCGGCCGAGGTACCGCAAGATGAAGGAGCGGCTGGGGCTGACGGAGATCCGGAAGC
AGGCCAACCGTATGAGCTTCGGAGAGATCGAGGAGGACGCCTACCAGGAGGACCTGGGATTACGC
CTGGGCCACCTGGGCAAGTCGGGCAGTGGGCGTGTGCGGCAGACACAGGTAAACGAGGCCACCAA
GGCCAGGATCTCCAAGACGCTGCAGCGGACCCTGCAGAAGCAGAGCGTCGTATATGGCGGGAAGTC
CACCATCCGCGACCGCTCCTCGGGCACGGCCTCCAGCGTGGCCTTACCCCACTCCAGGGCCTGGAG
ATTGTGAACCCACAGGCGGCAGAGAAGAAGGTGGCTGAGGCCAACCAAGTATTTCTCCAGCATG
GCTGAGTTCTCAAGGTCAAGGGCGAGAAGAGTGGCCTTATGTCCACCTGACCTGCAGGTCATCAAG
CTTATCGATACCGTCGACCTCGAGGGGGGGCCGCGACTCTAGATCATAATCAGC**CATACCACATTTG**
TAGAGGTTTTACTTGCTTTAAAAAACCTCCACACCTCCCCCTGAACCTGAAACATAAAATGAATGCA
ATTGTTGTTGTTAACTTGTTTATTGCAGCTTATAATGGTTACAAATAAAGCAATAGCATCACAAATTC
ACAAATAAAGCATTTTTTCTACTGCATTCTAGTTGTGGTTGTCCAAACTCATCAATGTATCTTAAGGC
CTAGGTGAGCTCTGGTACCCTCTAGTCAAGGATCAGTGATGGAGTTGGCCACTCCCTCTCTGCGCGCT
CGCTCGCTCACTGAGGCCGGGCGACCAAAGGTCGCCCCGACGCCCGGGCTTTGCCCGGGCGGCCTCA
GTGAGCGAGCGAGCGCGCAGCTGCTGCATTAATGAATCGGCCAACGCGCGGGGAGAGGCGGTTTG
CGTATTGGGCGCTCTTCCGCTCTAGACTTAATTAAGGATCAATCACTGGCCGTGTTTTACAACGTC
GTGACTGGGAAAACCCTGGCGTTACCCAACCTAATCGCCTTGCAGCACATCCCCCTTTCGCCAGCTGG
CGTAATAGCGAAGAGGCCCGCACCGATCGCCCTTCCCAACAGTTGCGCAGCCTGAATGGCGAATGG
CGCCTGATGCGGTATTTTCTCCTTACGCATCTGTGCGGTATTTACACCCGCATATGGTGCACTCTCAGT
ACAATCTGCTCTGATGCCGCATAGTTAAGCCAGCCCCGACACCCGCCAACGCAGAGAAAAAAAAAAC
CCGCTGACGCGCCCTGACGGGCTTGCTGCTCCCAGCATCCGCTTACAGACAAGCTGTGACCGTCTCC

Conclusions and Future Directions

GGGAGCTGCATGTGTCAGAGGTTTTACCGTCATCACCGAAACGCGCGAGACGAAAGGGCCTCGTG
ATACGCCTATTTTTATAGGTTAATGTCATGATAATAATGGTTTCTTAGACGTCAGGTGGCACTTTTTCGG
GGAAATGTGCGCGGAACCCCTATTTGTTTATTTTTCTAAATACATTCAAATATGTATCCGCTCATGAGA
CAATAACCCTGATAAATGCTTCAATAATATTGAAAAAGGAAGAGTATGAGTATTCAACATTTCCGTGT
CGCCCTTATTCCCTTTTTTGCGGCATTTCCTTCTGTTTTTCTCACCCAGAAACGCTGGTGAAAGT
AAAAGATGCTGAAGATCAGTTGGGTGCACGAGTGGGTTACATCGAACTGGATCTCAACAGCGGTAA
GATCCTTGAGAGTTTTCGCCCCGAAGAAGTTTTCCAATGATGAGCACTTTTAAAGTTCTGCTATGTG
GCGCGGTATTATCCCGTATTGACGCCGGGCAAGAGCAACTCGGTCGCCGCATACACTATTCTCAGAA
TGACTTGGTTGAGTACTCACCAGTCACAGAAAAGCATCTTACGGATGGCATGACAGTAAGAGAATTA
TGCAGTGCTGCCATAACCATGAGTGATAAACTGCGGCCAACTTACTTCTGACAACGATCGGAGGAC
CGAAGGAGCTAACCGCTTTTTTGCACAACATGGGGGATCATGTAACCTGCCTTGATCGTTGGGAACC
GGAGCTGAATGAAGCCATACCAAACGACGAGCGTGACACCACGATGCCTGTAGCAATGGCAACAAC
GTTGCGCAAACCTATTAACCTGGCGAACTACTTACTCTAGCTTCCCGGCAACAATTAATAGACTGGATGG
AGGCGGATAAAGTTGCAGGACCACTTCTGCGCTCGGCCCTCCGGCTGGCTGGTTTATTGCTGATAA
ATCTGGAGCCGGTGAGCGTGGGTCTCGCGGTATCATTGCAGCACTGGGGCCAGATGGTAAGCCCTC
CCGTATCGTAGTTATCTACACGACGGGGAGTCAGGCAACTATGGATGAACGAAATAGACAGATCGT
GAGATAGGTGCCTCACTGATTAAGCATTGGTAACTGTCAGACCAAGTTTACTCATATATACTTTAGAT
TGATTTAAACTTCATTTTTAATTTAAAGGATCTAGGTGAAGATCCTTTTTGATAATCTCATGACCAA
AATCCCTAACGTGAGTTTTCGTCCACTGAGCGTCAGACCCCGTAGAAAAGATCAAAGGATCTTCTT
GAGATCCTTTTTTCTGCGCGTAATCTGCTGCTTGCAAACAAAAAACCACCGCTACCAGCGGTGGTT
TGTTTGCCGGATCAAGAGCTACCAACTTTTTCCGAAGGTAACCTGGCTTACAGCAGAGCGCAGATAC
CAAATACTGTTCTTCTAGTGTAGCCGTAGTTAGGCCACCACTTCAAGAACTCTGTAGCACCGCCTACA
TACCTCGCTCTGCTAATCCTGTTACCAGTGGCTGCTGCCAGTGGCGATAAGTCGTGTCTTACCGGGTT
GGACTCAAGACGATAGTTACCGGATAAGGCGCAGCGGTCCGGCTGAACGGGGGGTTCTGTGCACAC
AGCCCAGCTTGGAGCGAACGACCTACACCGAACTGAGATACCTACAGCGTGAGCTATGAGAAAGCG
CCACGCTTCCCGAAGGGAGAAAGGCGGACAGGTATCCGGTAAGCGGCAGGGTCGGAACAGGAGAG
CGCACGAGGGAGCTTCCAGGGGGAAACGCCTGGTATCTTTATAGTCCTGTCTGGGTTTTGCCACCTCT
GACTTGAGCGTCGATTTTTGTGATGCTCGTCAGGGGGGCGGAGCCTATGGAAAAACGCCAGCAACG
CGGCCTTTTTACGGTTCCTGGCCTTTGCTGGCCTTTGCTCACATGTTCTTCTGCGTTATCCCCTGA
TTCTGTGGATAACCGTATTACCGCCTTTGAGTGAGCTGATACCGCTCGCCGCAGCCGAACGACCGAG

CGCAGCGAGTCAGTGAGCGAGGAAGCGGAAGAGCGCCAATACGCAAACCGCCTCTCCCCGCGCGT
TGCCCGATTCATTAATGCAGCTGGCACGACAGGTTTCCCGACTGGAAAGCGGGCAGTGAGCGCAAC
GCAATTAATGTGAGTTAGCTCACTCATTAGGCACCCCAGGCTTTACACTTTATGCTTCCGGCTCGTAT
GTTGTGTGGAATTGTGAGCGGATAACAATTTACACAGGAAACAGCTATGACCATGATTACGCCAAG
CTCTAGACTTAATCGGCGCGCCGATTAAGGATCAATTCAGTGGCCGTCGTTTTACAACGTCGTGACTG
GGAAAACCCTGGCGTTACCCAACCTAATCGCCTTGCAGCACATCCCCCTTTCGCCAGCTGGCGTAATA
GCGAAGAGGCCCGCACCGATCGCCCTTCCCAACAGTTGCGCAGCCTGAATGGCGAATGGCGCCTGA
TGCGGTATTTTCTCCTTACGCATCTGTGCGGTATTTACACCCGCATATGCGGTGTGAAATACCGCACA
GATGCGTAAGGAGAAAATACCGCATCAGGAATTCCAACATCCAATAAATCATACAGGCAAGGCAAA
GAATTAGCAAAATTAAGCAATAAAGCCTCAGAGCATAAAGCTAAATCGGTTGTACCAAAAACATTAT
GACCCTGTAATACTTTTGCGGGAGAAGCCTTTATTTCAACGCAAGGATAAAAATTTTLAGAACCTCA
TATATTTTAAATGCAATGCCTGAGTAATGTGTAGGTAAAGATTCAAACGGGTGAGAAAGGCCGGAG
ACAGTCAAATCACCATCAATATGATATTCAACCGTTCTAGCTGATAAATTCATGCCGGAGAGGGTAGC
TATTTTTGAGAGGTCTCTACAAAGGCTATCAGGTCATTGCCTGAGAGTCTGGAGCAA